

**Part I. Slip Behavior of the San Andreas Fault Through  
Several Earthquake Cycles**

**Part II. A Structural Interpretation of the Aftershock  
“Cloud” of the 1992  $M_w$  7.3 Landers Earthquake**

Thesis by

**Jing Liu**

In Partial Fulfillment of the Requirements  
for the Degree of  
Doctor of Philosophy

California Institute of Technology

Pasadena, California

2003

(Defended January 31, 2003)

© 2003

Jing Liu

All Rights Reserved

For my grandmother whose maiden name is unknown to me and  
who died in the beginning period of my Ph. D. education  
and  
my daughter, Carisa  
who was born in the ending period of my thesis

## Acknowledgements

It is a privilege for me to study here at the Division of Geological and Planetary Science, California Institute of Technology, and to be around some of the finest minds in geology and geophysics, whom I would only read the names from prints if I had not come here. I have benefited from numerous people I met here in years. I wish I could thank each of them properly and without omissions.

My thanks go first to my thesis advisor, Kerry Sieh, whom I have learned much from both scientifically and personally. His influence on me and his guidance have been in many aspects, to name a few, his passionate love of science, his amazing scientific intuition, his astonishing meticulous work, his strong belief in clarity and simplicity, his humorous tolerance of ambiguity and his effective communication skills. I thank him for his enthusiasm, effort and patience in shaping me as a scientist. I also appreciate his understanding and support in my adventures with pregnancy and motherhood.

I would like to thank Tom Heaton, with whom I worked on one of my first-year propositions, for his advice and support. His personal style and scientific background differ from Kerry's. I feel lucky to be able to look at earthquake phenomena from both a geologist's and seismologist's perspective. I believe their complementary influences on me will help me to tap the essence of earthquakes. I also thank Egill Hauksson, whom I worked with on the Landers aftershock sequence, for enlightening discussions.

Thanks to my thesis committee members, Kerry Sieh, Joe Kirschvink, Tom Heaton, Brian Wernicke and Paul Tapponnier for taking the time to review my thesis. Extra thanks to Paul for his graceful acceptance of sitting on my committee and his enthusiasm and constructive comments. Critical reviews by Kerry Sieh and Yann Klinger, as well as their involvements in the study that leads to the main portion of this thesis, are appreciated. I also learned useful tricks in writing and editing from Theresa Lynn.

Various people have help with field work at one point or another. Yann Klinger has participated substantially in both hand-excavations and trench exposure documentation. Kerry Sieh and Charlie Rubin participated in the excavation of the first two hand-dug trenches, at about the 143<sup>rd</sup> anniversary of the great January 9, 1857 earthquake. Brandon Maehr assisted me throughout the field seasons with digging and surveying. Additional assistance was provided by Jim Nye, Christ Madden, Clay Stevens and Lingsen Zeng. O. C. Canto and Clay Stevens helped to digitize the trench logs. Their help is acknowledged and appreciated. I thank Johna Hurl, the Carrizo manager and people from Bureau of Land Management for their support in getting permission to excavate.

How fortunate I am to meet Jim Nye and Brandon Maehr when I was doing my field work in the Carrizo Plain! They provided me with beds, food, shelter from the wind and storms, a home outside the home. They entertained me with many conversations, which greatly deepened my understanding of American life and helped improve my language skills. Jim's intelligent talks, as well as his concern over my safety, are always appreciated. Brandon was my primary field assistant and gave me help whenever needed and always on short notice. He had removed at least half of the excavated 450 m<sup>3</sup> dirt by hand! No complaint even under the hottest sun. He was also a major participant in the 3-people survey team that logged over 10,000 measurements of survey points. Thank you so much.

The Caltech faculty and staff members provided a supportive environment. Special thanks to Bruce Murray for his encouragement; to Donna Sackett, Carolyn Porter, Marcia Hudson, Tess Puig and Erin Wilk for their caring and supportive gestures; to Jim O'Donnell, Susan Leising, Tony Soeller, Joanne Gilbertson, Ken Ou and Kimo Yap for their effective technical support.

Interactions with people in Kerry's group have been very fruitful. I met three postdocs of Kerry's throughout the years of my stay here, and I learned a lot from each of them. With Doug Yule, I started my first trench in southern California. I remember the adventure on the day Doug operated on a backhoe and I drove a stick-shift truck, both for the first time. At that time I did not even have many experiences with an automatic car! With Yann Klinger, I had some of the field work done together. Conversations on the long drives to and from the field, as well as at lunch

breaks at trench site, spanned a wide range of topics and they were fun. I must admit that my views on many things have been changed by him through the discussion. Congratulations, Yann. Eric Cowgill has kindly helped me through many discussion and group meetings. His sincerity and willingness to help amazed me much. Thank him for organizing our Friday lunch meetings. Discussion with other members of lunch meetings, Bruce Hsu, Danny H. Natawidjaja, Todd Ehlers, Nadine McQuarrie and others, are stimulating and joyful. I also thank Suefawn Barnett, our group administration assistant, for making my life easier.

My life was enriched by friends and fellow students. Many friends popped me up through some particularly difficult times. Kate Zhang, Lijie Han and Hui Zhang cheered me on and shared their personal experiences with me, and provided me with practical advice. Special thanks to Yuk Yung family and Lee family for delicious Thanksgiving dinners. I thank Greg Okin, for his comforting words when I was bewildered with organizing the weekly Geoclub seminars for a whole year literally all by myself. Thanks to Ronit Kessel and Julia Goreva for their much needed help with Geoclub tasks. I have enjoyed the company and benefited from the interactions with Anupama Venkataraman, Patricia Persaud, Liz Johnson, Edwin Schauble, Ulyana Dyudina, Chen Ji, Sidao Ni, Zhengrong Wang, Huirong Ai, Yin Tan, Zhimei Yan, Min Chen, Junjun Liu, Shengnian Luo, Mike Oskin, Jim Spotila, Mihai Ducea, Rob Brady, Slawek Tulaczky, Martha House, Liz Holt, Tanja Bosak, Elisabeth Nadin, Julie O'Leary. Many more people than those listed here have helped me one way or another. I apologize for the apparent omission.

My stay at Cal Tech serves as not only the drill process for my scientific pursuit, but also a journey of my self-discovering and spiritual growth. My scientific achievement may seem trivial to some people, but is something I feel proud of, because I know how many barriers that were so daunting in my way and how hard I have been trying to remove them. Throughout the process, I have changed dramatically. My experiences in U. S. have opened my mind to new possibilities. The impact is revolutionary. By the time I am leaving here, I have become a different person inside.

The support from my closely-tied family has been an invaluable resource. I thank my grandparents, parents, and sisters for their belief and pride in me. Thank my parents for giving me ample freedom and for their love, tolerance and patience as I rebelled in my adolescent years, a

period that I am sure was very painful for them. I grew up more independently than my sisters. This element of independence serves me well in my tackling various problems. Special thanks to my grandmother, whom I spent my first ten years with and whose character molded me. I devote this thesis to her because any of the achievement in my life originates from her.

This thesis would not have been possible without the love, friendship and support of my husband, Lingsen. I resort to you more than to anybody else, Lingsen, for encouragement and support. You are always there whenever I need help. Like air and water, your love, trust and support are ubiquitous that I sometime took them for granted. I am deeply grateful.

I cherish the moments that my daughter Carisa and I shared in the Carrizo Plain. Her presence, even though silent, made pregnant me not feel lonely down in the trenches alone, especially at the times when the only sound I heard is of wind blowing and birds occasionally flying by. Carisa also motivates me to work as efficiently as possible with her arrival. She has added joy and balance to my life. Child-raising experience also increases my awareness of challenges women in science in general have to face. In this sense, I appreciate the gifts of time and babysitting from my husband and my parents.

Through the efforts of two generations of my family, I have gotten to this point. I believe that Carisa will climb higher in this ladder and will have a brighter future than all of us.

## Abstract

Part I of this thesis addresses the question of how variable fault slip per event is through time. This question is important, because progress in understanding and forecasting large earthquakes depends critically on precise reconstruction of the variation of rupture magnitude with time. Well-documented examples of slip measurements of successive past earthquakes rarely span more than three earthquake cycles. The dearth of accurate measurements of serial slip is partly due to the obliteration of piercing lines that we can use to separate the offsets associated with individual earthquakes.

The special configuration of a series of channels offset across the San Andreas fault, near Wallace Creek has enabled me to determine the styles and the magnitudes of slip of the most recent 6 events at this locality. At the site, a feeder channel cuts a Pleistocene alluvial fan on the upstream side of the fault. On the downstream side, several small channels were offset dextrally from the source and sequentially abandoned. We opened a latticework of trenches across the offset channels on both sides of the fault. The trenches across the mouth of the upstream feeder channel exposed a set of nested channels; downstream trenches revealed several singular channels. The elevations, shapes, stratigraphy and ages of channels provide reliable information for correlating channels across the fault. 3-D excavations have allowed me to locate accurately the offset channel pairs and to determine the amounts of motion with small uncertainties. The dextral slips associated with the latest 6 events are, from the youngest to oldest,  $\sim 8$  m,  $\sim 7.5$  m,  $\sim 5.5$  m,  $\sim 1.5$  m,  $\sim 8.0$  m, and  $\sim 5.5$  m. The high occurrence of events with slip of about 7.5 m suggests that the magnitude of slip at a point along the fault does not result from a random process. But the slip is not as regular as predicted by characteristic models either. Thus, data at the site do not support perfectly characteristic behavior, but do show a significant degree of regularity.

Part II of the thesis demonstrates that Landers aftershocks constituted primarily a several-km-wide damage zone centered on the mainshock rupture plane. Most aftershocks probably did not occur on the same surfaces that had moved during the mainshock. Rather, the aftershock populations revealed the nature of the fractured medium around the principal faults, and the general structure of a fault zone.

## Table of Contents

Chapter 1	Introduction.....	1-1
1.1	Motivation.....	1-2
1.2	The study site.....	1-5
1.3	Organization of the thesis.....	1-7
1.4	References.....	1-9
Chapter 2	Channel Morphology and Stratigraphy Revealed in 3-D Excavations.....	2-1
2.1	Site description.....	2-2
2.2	Methods.....	2-6
2.3	Channel stratigraphy and morphology.....	2-10
2.3.1	Underlying Late Pleistocene alluvium.....	2-10
2.3.2	Downstream channels.....	2-10
2.3.2.1	General channel configurations.....	2-12
2.3.2.2	Channel <i>a</i> .....	2-13
2.3.2.3	Channel <i>b</i> .....	2-19
2.3.2.4	Channels <i>c</i> and <i>d</i> .....	2-26
2.3.2.5	Channels <i>e</i> , <i>f</i> , <i>g</i> and <i>h</i> .....	2-30
	Channel morphology and stratigraphy.....	2-30
	Relative ages of channels.....	2-37
2.3.2.6	Channels <i>i</i> , <i>j</i> , <i>k</i> and <i>l</i> .....	2-39
	Channel <i>k</i> .....	2-43
	Channel <i>l</i> .....	2-44
	Relative age of channel <i>k</i> and <i>l</i> .....	2-44
	Channel <i>j</i> .....	2-45
	Channel <i>i</i> .....	2-45
2.3.3	Upstream channels.....	2-46

2.3.3.1	General .....	2-46
2.3.3.2	Channel 1.....	2-49
2.3.3.3	Channel 2.....	2-55
2.3.3.4	Channel 4, 5 and 6.....	2-60
	Channel 4 .....	2-60
	Channel 5 .....	2-65
	Channel 6 .....	2-65
2.3.3.5	Channel 3.....	2-66
2.3.3.6	Channels 7, 8 and 9.....	2-68
	Channel 7 .....	2-68
	Channel 8 .....	2-70
	Channel 9 .....	2-71
2.4	Summary.....	2-73
2.5	References.....	2-75
Chapter 3	Interpretation of Slip per Event for the Last Several Earthquakes .....	3-1
3.1	Overview.....	3-2
3.2	Fault zone structure.....	3-2
3.3	Channel correlation.....	3-6
3.3.1	Recapitulation of basic channel geometries.....	3-6
3.3.2	General criteria for channel correlation.....	3-8
3.3.3	Channel pairs.....	3-11
3.3.3.1	Channel 1-a.....	3-11
3.3.3.2	Channel 2-b.....	3-14
3.3.3.3	Channel 3-c and channel 4-d.....	3-16
3.3.3.4	Channel 5-g.....	3-18
3.3.3.5	Tentative correlation of channel 6-h.....	3-20
3.3.3.6	Correlations between older channels.....	3-22
	Possible correlations with channel 7.....	3-22
	Possible correlations with channel 8.....	3-23

	Possible correlations with channel 9.....	3-23
3.4	Measurement of offsets.....	3-24
3.4.1	Minor offset on Fault 1 and Fault 2.....	3-26
3.4.2	Channel 1-a: 8 m-offset.....	3-28
3.4.3	Channel 2-b: 15.5 m-offset.....	3-30
3.4.4	Channel 3-c: 20.7 m-offset.....	3-34
3.4.5	Channel 4-d: 22 m-offset.....	3-39
3.4.6	Channel 5-g: 30 m-offset.....	3-41
3.4.7	Channel 6-h: 35.5 m offset.....	3-39
3.4.8	Non-brittle warping.....	3-43
3.5	Derivation of a rupture sequence at the site.....	3-45
3.5.1	Is each offset a single rupture event? .....	3-46
3.5.1.1	Offset WC1 and the 1857 earthquake.....	3-47
3.5.1.2	Offset WC2 and the penultimate rupture.....	3-48
3.5.1.3	Offsets WC3 and WC4.....	3-48
3.5.1.4	Offset WC5.....	3-50
3.5.1.5	Offset WC6.....	3-51
3.5.2	Summary.....	3-51
3.6	Radiocarbon constraints.....	3-52
3.6.1	Inheritance problem.....	3-56
3.6.2	Ages of the channels.....	3-57
3.6.2.1	Channel 1-a.....	3-57
3.6.2.2	Channel 2-b.....	3-58
3.6.2.3	Channel 3-c .....	3-58
3.6.2.4	Channel 4-d and 5-g .....	3-61
3.6.2.5	Channel 6-h.....	3-62
3.6.2.6	Dates of older channels.....	3-63
	Channel 9.....	3-63
	Channel 8.....	3-63

Channel 7.....	3-64
Downstream channels <i>k</i> and <i>l</i> .....	3-64
3.7 A history of the latest six ruptures.....	3-65
3.7.1 Constraints from our data.....	3-65
3.7.2 Additional constraints from other data.....	3-67
3.7.2.1 Correlation with the Phelan Creeks site.....	3-67
3.7.2.2 Correlation of cut and fill with climatic variability.....	3-76
3.7.2.3 Revised dates of Wallace Creek events using Phelan Creeks dates..	3-79
3.7.2.4 Further constraints from the Bidart fan record.....	3-81
3.8 Discussion.....	3-82
3.8.1 Slip behavior of the San Andreas fault at the site.....	3-83
3.8.2 Implications for earthquake recurrence models.....	3-86
3.8.3 Slip history of the San Andreas fault at the site.....	3-87
3.8.4 Correlation of earthquakes along the central and southern San Andreas fault.....	3-88
3.8.4.1 The 1857, 1812, and late 17th-century earthquakes .....	3-90
3.8.4.2 Event WC2.....	3-91
3.8.4.3 Event WC3 and WC4.....	3-92
3.8.4.4 Event WC5.....	3-93
3.9 Conclusions.....	3-94
3.10 References.....	3-95
Chapter 4 A Structural Interpretation of the Aftershock "Cloud" of the 1992 Mw7.3 Landers Earthquake.....	4-1
Abstract.....	4-2
4.1 Introduction.....	4-3
4.2 Data.....	4-4
4.2.1 Surface rupture.....	4-4
4.2.2 Aftershocks .....	4-6
4.3 Results.....	4-8

4.3.1	The aftershocks occur in a vertically-dipping cloud.....	4-8
4.3.2	Most aftershocks occur off the mainshock fault planes.....	4-10
4.3.3	Aftershock focal mechanisms further limit which aftershocks can represent re-rupture of the mainshock fault planes.....	4-13
4.3.4	Aftershock b values correlate with mainshock fault complexity.....	4-15
4.4	Discussion.....	4-16
4.5	Conclusions.....	4-23
	Acknowledgements.....	4-23
	References.....	4-23
Appendix A	Field Data (also on the CD attached).....	A-1
A.1	Digital field data (see CD attached).....	A-2
A.2	Folder Description of digital field data.....	A-2
A.3	Procedure for digitizing trench logs in ArcView.....	A-5
Appendix B	Reference Frame for Surveying.....	B-1
Appendix C	Original <sup>14</sup> C dating Reports.....	C-1

## List of Figures

1.1	Simple earthquake recurrence models .....	1-3
1.2	Schematic diagrams of three models of large earthquake repetition along a 2-D.....	1-4
1.3	Location map of the trench site .....	1-6
2.1	Location of the Wallace Creek paleoseismic site.....	2-2
2.2	Geologic map of drainage <u>B</u> and the nearby drainage <u>C</u> at the Wallace Creek paleoseismic site. ....	2-4
2.3	Excavations at the site.....	2-6
2.4	Lithologic and other symbols used in documenting the exposures.....	2-9
2.5	Lateral offset of closely spaced channels can lead to complicated interplay of upstream and downstream channels.....	2-11
2.6	Summary of the results of the excavation of channel <u>a</u> .....	2-15
2.7	Stratigraphic units of channel <u>a</u> illustrated using exposure dn1-ne08.....	2-16
2.8	Map view of three features associated with channel <u>a</u> .....	2-18
2.9	Summary of the results of the excavation of channel <u>b</u> .....	2-22
2.10	Stratigraphic units of channel <u>b</u> illustrated using exposure dn5-ne07.....	2-23
2.11	Summary of the results of the excavation of channel <u>d</u> .....	2-25
2.12	Stratigraphic units of channels <u>d</u> and <u>c1</u> illustrated using exposure dn4-ne08.....	2-26
2.13	Summary of channel <u>c</u> .....	2-27
2.14	Flaring of 4 channels <u>e</u> , <u>f</u> , <u>g</u> and <u>h</u> .....	2-31
2.15	Maps of channels <u>e</u> through <u>h</u> in all 10 exposures.....	2-35
2.16	Longitudinal profile of the thalweg of channel <u>e</u> .....	2-36
2.17	Photographs of exposure dn3-ne02 show the cross-cutting relationships.....	2-37
2.18	Cross-sectional views of channels i, j, k and l.....	2-39
2.19	Selected portions of the logs showing the stratigraphy, cross-sectional morphology...	2-42
2.20	Longitudinal profiles of the thalwegs of channels <u>k</u> and <u>l</u> .....	2-43

2.21	Simplified map of nested channels near the mouth of source channel.....	2-47
2.22	A photograph of the suspended-load lens in channel 1.....	2-48
2.23	Stratigraphic units of channel 1.....	2-50
2.24	Summary of the results of the excavation of channel 1.....	2-53
2.25	Topography of the base of the suspended-load lens in channel 1.....	2-54
2.26	Summary of the results of the excavation of channel 2.....	2-56
2.27	Longitudinal profiles of the main channel 2 and its side channel.....	2-57
2.28	Stratigraphic units of channel 2.....	2-58
2.29	Stratigraphic units of channels 4, 5 and 6.....	2-61
2.30	Maps of channels 3, 4, 5 and 6 in exposures sw01 through sw12.....	2-63
2.31	Map view of the deepest thalwegs of channels 3, 4, 5 and 6.....	2-64
2.32	Stratigraphic units of channels 7, 8 and 9.....	2-67
2.33	Photographs of exposure sw06 show the cross-cutting relationships.....	2-69
2.34	Map of the deepest thalwegs of channels 7, 8, and 9.....	2-71
3.1	Overview of the structure of the fault zone within the excavated volume.....	3-2
3.2	Cross-sectional map of channel thalwegs illustrates the relationship of Faults 1 and 2.....	3-4
3.3	Summary of channels exposed at this site.....	3-6
3.4	The relative ages of upstream and downstream channels.....	3-10
3.5	The correlation of channel 1-a is based on the similarity of stratigraphy and morphology.....	3-12
3.6	The unusual narrowness of channels 2 and b and the similarity of their internal.....	3-14
3.7	Map and cross-sections of channels 4 and d illustrate the basis for correlation of these two channels.....	3-17
3.8	Summary of evidence for the correlation of channels 5 and g.....	3-18
3.9	The similar southward flow directions of channels 6 and h.....	3-21
3.10	Horizontal (a) and vertical (b) offsets of channels on fault strands F1 and F2.....	3-25
3.11	(a) Map view of offset channel 1-a.....	3-27
3.11	(b) Longitudinal profiles of the two piercing lines of channel 1-a.....	3-29

3.12	Five piercing lines constrain the total offset of channel 2-b to 15.1- 15.8 m.....	3-32
3.13	The vertical offset of channel 2-b.....	3-33
3.14	(a) Restorations of channels 3-c require a total right-lateral offset of $20.7 \pm 0.25$ m....	3-35
3.14	(b) The average trend of channel 4-d thalweg.....	3-36
3.15	The irregularity of the long-profile of channel 4-d.....	3-37
3.16	(a) The right-lateral offset of the deepest thalweg of channels 5-g.....	3-39
3.16	(b) The thalweg of channel 5-g displays cumulative net vertical offset.....	3-40
3.17	(a) The lateral offset of channel 6-h is $35.4 \pm 0.3$ m.....	3-41
3.17	(b) The longitudinal profile of the deepest thalweg of channel 6-h.....	3-42
3.18	Summary of the cumulative offsets of channel pairs.....	3-44
3.19	The presence of channel e is consistent with interpreting the 8-m increment.....	3-49
3.20	All dated radiocarbon samples from the upstream exposures.....	3-56
3.21	Radiocarbon date ranges of samples from the Wallace Creek site plotted as a function of age and stratigraphic order.....	3-59
3.22	Map of the extent of the reddish burn in the strata of channel 4.....	3-60
3.23	The stratigraphic positions of offsets WC1 through WC6.....	3-66
3.24	Probability distribution of age range of offset event, generated by OxCal program.....	3-67
3.25	Tentative slip history of the Wallace Creek paleoseismic site.....	3-68
3.26	A paleoseismic investigation conducted at the Phelan Creeks site.....	3-70
3.27	Proposed correlation of units east and west of the San Andreas fault at the Phelan Creeks.....	3-71
3.28	A proposed correlation of the alluviation history at the Wallace Creek site with that at the Phelan Creeks.....	3-73
3.29	The similarity of the record of rises and falls in of the Mono Lake with cuts and fills at the Wallace Creek.....	3-75
3.30	Revised dates of offset events using Phelan Creek dates.....	3-77
3.31	A revised slip history at the Wallace Creek site, incorporating the constraints on alluvial events from the Phelan Creeks site.....	3-80
3.32	Additional constraints on event WC5 from the Bidart fan site.....	3-81

3.33	A test of the randomness in the offset series of events at the site.....	3-84
3.34	Speculative correlation of earthquake ruptures between paleoseismic sites along the southern half of the San Andreas fault.....	3-89
4.1	Map of the surficial ruptures of the 1992 Landers earthquake.....	4-5
4.2	Histograms of horizontal and vertical location errors .....	4-6
4.3	Map view of aftershock density distribution.....	4-7
4.4	Cross-sectional views of aftershock locations ( $ML \geq 2$ ) for the 9 sections.....	4-9
4.5	Map view of the surface traces of the mainshock fault planes and aftershock.....	4-10
4.6	Distributions of Landers aftershocks as a function of distance normal to.....	4-12
4.7	The difference in strike of aftershock focal plane.....	4-14
4.8	Schematic model of the gouge layer-damage zone morphology of a natural fault.....	4-16
4.9	Density distributions of mesoscopic fractures and Landers aftershocks.....	4-17
4.10	Schematic diagram illustrates the classification of aftershocks.....	4-20

## List of Tables

3.1	Radiocarbon samples at the Wallace Creek trench site.....	3-53
3.2	Radiocarbon samples at the at the Phelan Creek site.....	3-71
3.3	Age constraints of paleoseismic events near Wallace Creek.....	3-78
4.1	Ratios of near-fault to the total population of aftershocks.....	4-13

# **Chapter 1**

## **Introduction**

## 1.1 Motivation

The way earthquake ruptures repeat through time for a given fault is not well understood. Such knowledge would be, however, of primary interest, as it would improve our general understanding of earthquake mechanics and would be of major use in earthquake hazard analysis. Our understanding of the nature of earthquake repetition is mainly hampered by a lack of relevant high-quality data bearing on the behavior of past large ruptures. Many models have been proposed to describe earthquake recurrence, yet a lack of reliable data makes it difficult to evaluate the theories.

One group of models is based on 1-D idealizations of the stress loading and unloading of the fault through many seismic cycles (Figure 1.1). The first and simplest is the elastic rebound theory by Reid (1910), which hypothesized that the recurrence of large earthquakes might be periodic. This theory has already been phased out, because it is in contradiction with numerous observations of variable recurrence intervals. Later, Shimazaki and Nakata (1980) put forward the time- and the slip-predictable models to allow the recurrence time as well as slip of large earthquakes to vary. However, their evidence of earthquake recurrence is from the far-field and ambiguous, since the earthquakes occurred tens of kilometers away from the places they made their observations, and source regions of the earthquakes were not the same, though overlapping.

Another group of models considers earthquake rupture as a 2-D problem. Typical models of this class are the characteristic slip-patch model (Sieh, 1978, 1996), and the characteristic earthquake model (Schwartz and Coppersmith, 1984) (Figure 1.2 b and c). The characteristic earthquake model states that faults are rupturing repeatedly in events with nearly identical rupture length, location and slip magnitude. Schwartz and Coppersmith (1984) proposed that this model fit data from paleoseismic studies mainly along the Wasatch faults, Utah and the San Andreas fault. The characteristic-earthquake concept, however, had already been dismissed as improbable for the San Andreas fault several years before it was proposed (Sieh, 1978). Instead, Sieh (1978, 1996) argued that the fault consists of several characteristic-slip patches, or segments, which sometimes fail separately and sometimes fail together, but that the slip on each individual

segment is similar from earthquake to earthquake. Unfortunately, the evidence is still inconclusive.

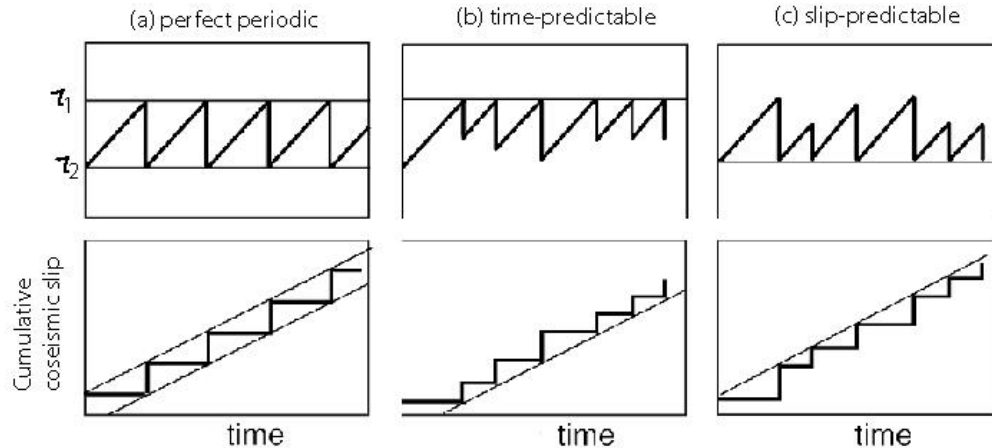


Figure 1.1. Simple earthquake recurrence models, based on the concept of stress loading and unloading through time at a single location along the fault (from Shimazaki and Nakata, 1980).

In contrast, various mechanical and statistical models treat earthquakes as complex or dynamic processes, highly variable both in time and space (e.g., Burridge and Knopoff, 1967; Cao and Aki, 1984; Stuart, 1986; Tse and Rice, 1986; Rundle, 1988, 1989; Bak and Tang, 1989; Carlson and Langer, 1989; Ito and Matsuzaki, 1990; Carlson et al., 1991; Lyzenga et al., 1991; Chen et al., 1991; Huang et al., 1992; Ward and Goes, 1993; Ding and Lu, 1993; Rice, 1993; Pepke et al., 1994; Ben-Zion and Rice 1995, 1997; Morein et al., 1997; Rundle et al., 1997; Shaw, 1994, 1995, 1997; Rice and Ben-Zion, 1996; Ward, 1997, 2000; Cochard and Madariaga, 1996; Ben-Zion et al., 1999; Liu and Heaton, 1999; Klein et al., 1999; Shaw and Rice, 2000; Nielsen et al., 2000; Lyakhovsky et al., 2001; Rundle et al., 2001). This family of models shares the prediction that earthquakes are understandable in a statistical way, but individual earthquakes are non-deterministic, a prediction fundamentally different than that of the previously mentioned models. The presence of so many diverse earthquake recurrence models underscores our shortage of reliable data.

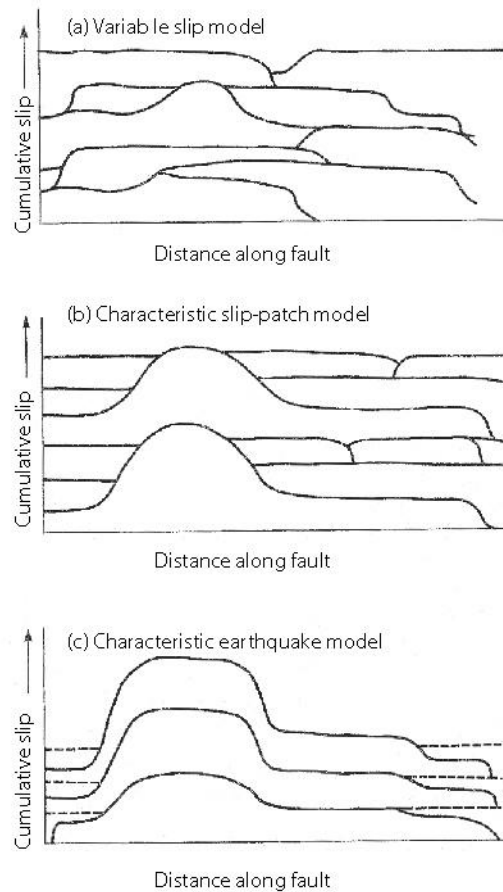


Figure 1.2. Schematic diagrams of three models of large earthquake repetition along a 2-D fault. They also illustrate how slip is accumulated along the fault through individual events (from Schwartz and Coppersmith, 1984).

Our limited understanding of earthquake recurrence is highlighted in the practice of seismic hazard analysis. The characteristic earthquake model was considered such a simple yet reasonable idealization that it was extensively applied in seismic hazard assessment (WGCEP, 1988, 1995). However, one should be aware of our reliance on tenuous concepts of source recurrence in these approaches. For example, we assume that seismicity on a fault can be represented realistically by a repeating characteristic rupture and that slip patterns along large historical ruptures reflect along-strike differences in fault friction (e.g., Stuart, 1986; Rundle,

1988; Ward and Goes, 1993). In reality, we have only very sparse data to support these ideas (Salyards, 1985; Lindvall et al., 1989; Sharp, 1982).

Paleoseismology has contributed to understanding serial fault ruptures. Whereas paleoseismic investigations along faults worldwide represent a large amount of information on the history of earthquakes at specific locations, well-documented examples of successive slip measurements for these earthquakes are still rare. High-quality data rarely span more than three earthquake cycles and the few data available seem to suggest that the slip at a single location is commonly similar through the earthquake series (Sieh, 1996 and references therein). Most measurements are, however, based on indirect evidence; for example, the similar displacement of paleoseismic events on the Wasatch faults was inferred from the heights of colluvial wedges due to these events (e.g., Schwartz and Coppersmith, 1984). The dearth of accurate measurements of serial slip is partly due to the modification or obliteration of offset piercing lines.

## **1.2 The study site**

One of the best places for direct slip measurements is along the Carrizo Plain segment of the San Andreas fault; in particular, a 0.5 km long section just southeast of the Wallace Creek, where displacements for several past earthquakes have been well preserved in a series of beheaded and abandoned ephemeral stream channels (Figure 1.3). These small gullies probably once lined up with their headwater source, but only for a short time. Subsequent faulting removed them from the source and left them abandoned and covered by colluvium.

This is an ideal place to determine whether or not a fault segment experiences similar amounts of slip through many earthquake cycles. First of all, along much of this segment the fault trace is geometrically simple and unusually well expressed. Secondly, previous paleoseismic studies have been done at sites nearby (Grant and Sieh, 1994; Sims et al., unpublished paper, 1994). These provide records of paleo-earthquakes that are independent references we can relate to this study. Thirdly, it has long been speculated that the ubiquitous beheaded channels may

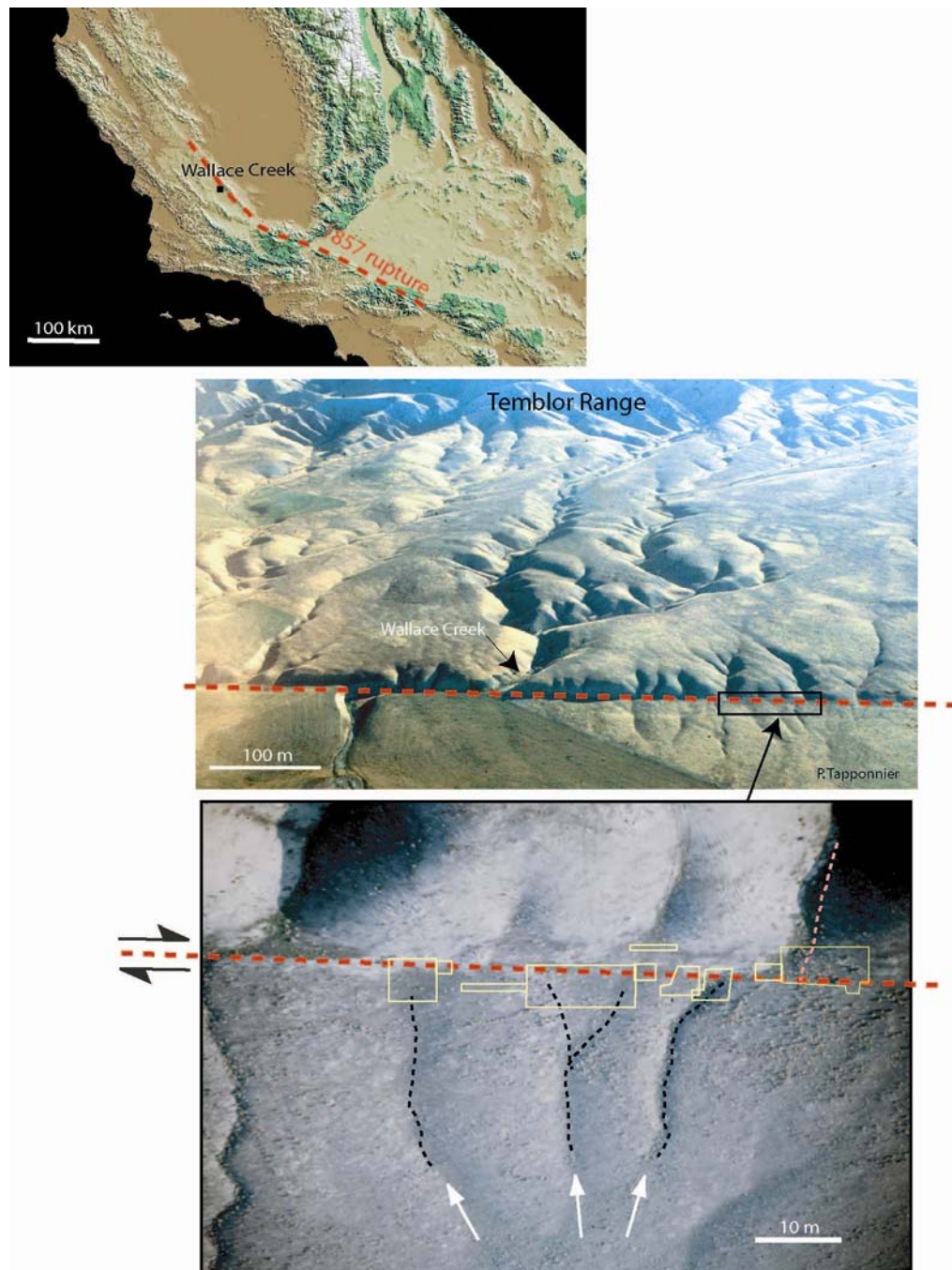


Figure 1.3. Location map of the trench site. The upper panel shows the rupture extent of the great 1857 earthquake, superimposed on the shaded relief map of central and southern California. The middle panel shows that the excavation site is at a small drainage, about 500 m southeast of the Wallace Creek. The lower panel is a close-up photo of the trench site. The yellow boxes indicate the excavation volumes. The arrows and thin dashed lines indicate the geomorphic river channels.

harbor the potential to separate the individual offsets of the past several earthquakes. It was first noted and interpreted by Wallace (1968) that the smallest offsets of streams were the product of the 1857 earthquake, and that the larger offsets in the same area must be the cumulative effects from several earlier earthquakes. Sieh (1978) refined this work, and demonstrated that the 1857 earthquake involved dextral offsets 7 to 9.5 m, from geomorphic expressions alone. Geomorphic evidence of small drainages also suggests 9.5 to 12.3 m of offset during the past three great earthquakes (Sieh, 1978; Sieh and Jahns, 1984). The particular small drainage we choose is the same one studied by Wallace (1968; Figure 8 in his paper), and by Sieh (1978) (site #25) ( $35^{\circ}16'10''$   $119^{\circ}49'05''$ ). The youngest offset gully is the clearest (Figure 1.3). Older offset gullies, farther northwest from the source channel, are more subdued, but nevertheless, still visible downstream of the fault scarp. Sieh (1978) measured the offsets of these beheaded channels to be  $8.7 \pm 1.4$  m,  $24.1 \pm 1.4$  m,  $32.0 \pm 2.0$  m and  $56.4 \pm 2.9$  m from the youngest to the oldest. The large uncertainties in the geomorphic measurements is due to the colluviation at the base of the scarp that has buried these small gullies partially, so their precise geometry near the fault is obscure.

To resolve the uncertainties, we have conducted 3-D excavation on either side of the San Andreas fault and matched channels stratigraphically. Another major objective is to test whether the seemingly regular multiples of 8 m of these offsets represent characteristic slips of individual earthquakes.

### **1.3 Organization of the thesis**

The major part of this thesis, presented in Chapters 2 and 3, is our paleoseismic investigation of the slip behavior of the San Andreas fault through several earthquake cycles. The topic and trench site was initially proposed by my thesis advisor, Dr. Kerry Sieh. My collaborators in collecting the data in the field have been Dr. Yann Klinger, Dr. Kerry Sieh, Dr. Charles Rubin and Clay Stevens. We dug most of the excavations by hand, with the assistance of Brandon Maehr and Jim Nye, Chris Madden and Lingsen Zeng. O. C. Canto and Clay Stevens

helped to digitize the trench logs and to reconstruct channel geometries in 3-D views using ArcView. I was assisted in writing the text of the thesis by the substantial criticism of Yann Klinger and Kerry Sieh.

In Chapter 2, I describe the cross-sectional morphology, stratigraphic characteristics, and the longitudinal sinuosity of all the excavated channels that were exposed in the trenches. This chapter is purely descriptive and summarizes our field data. Field data, including maps of about 100 exposures and over 10,000 surveyed points, as well as digital Arc/View files appear separately in appendices and on the CD attached. In Chapter 3, I summarize the evidence for the matches of channel pairs up- and down-stream across the fault and then measure their offsets. This chapter also contains a tentative time frame for the occurrence of the offsets, based on  $^{14}\text{C}$  dating results. Chapter 3 also includes the slip per event for the last several earthquakes, and the implication of our results for earthquake repetition models.

Part II of this thesis consists of a study of the Landers aftershock sequence, to be published in the *Bull. Seism. Soc. Am.* and coauthored with Dr. Kerry Sieh and Dr. Egill Hauksson. In this paper, we present a structural interpretation of the aftershock cloud of the 1992 Landers earthquake.

## 1.4 References

- Bak, P., and C. Tang, Earthquakes as a self-organized critical phenomenon, *J. Geophys. Res.*, *94*, 15635-15637, 1989.
- Ben-Zion, Y., K. Dahmen, V. Lyakhovskiy, D. Ertas, and A. Agnon, Self-driven mode switching of earthquake activity on a fault system, *Earth and Planetary Science Letters*, *172*, 1-2, 1999.
- Ben-Zion, Y., and J.R. Rice, Slip patterns and earthquake populations along different classes of faults in elastic solids, *J. Geophys. Res.*, *100*, 959-12, 1995.
- Ben-Zion, Y., and J. R. Rice, Dynamic simulations of slip on a smooth fault in an elastic solid, *J. Geophys. Res.*, *102*, 771-17, 1997.
- Burridge, R., and L. Knopoff, Model and theoretical seismicity, *Bull. Seism. Soc. Am.*, *57*, 341-371, 1967.
- Cao, T.Q., and K. Aki, Seismicity simulation with a mass-spring model and a displacement hardening-softening friction law, *Pure and Applied Geophysics*, *122*, 10-24, 1984.
- Carlson, J.M., and J.S. Langer, Properties of Earthquakes Generated by Fault Dynamics, *Physical Review Letters*, *62*, 2632-2635, 1989.
- Carlson, J.M., J.S. Langer, B.E. Shaw, and C. Tang, Intrinsic-properties of a Burridge-Knopoff model of an earthquake fault, *Physical Review A*, *44*, 884-897, 1991.
- Chen, K., P. Bak, and S.P. Obukhov, Self-organized criticality in a crack-propagation model of earthquakes, *Physical Review A*, *43*, 625-630, 1991.
- Cochard, A., and R. Madariaga, Complexity of seismicity due to high rate-dependent friction, *J. Geophys. Res.*, *101*, 321-25, 1996.
- Grant, L.B., and K. Sieh, Stratigraphic evidence for seven meters of dextral slip on the San Andreas Fault during the 1857 earthquake in the Carrizo Plain, *Bull. Seism. Soc. Am.*, *83*, 619-635, 1993.
- Grant, L.B., and K. Sieh, Paleoseismic evidence of clustered earthquakes on the San Andreas Fault in the Carrizo Plain, California, *J. Geophys. Res.*, *99*, 6819-6841, 1994.
- Huang, J., G. Narkounskaia, and D.L. Turcotte, A cellular-automata, slider-block model for

- earthquakes 2. Demonstration of self-organized criticality for a 2-D system, *Geophys. J. Int.*, *111*, 259-269, 1992.
- Ito, K., and M. Matsuzaki, Earthquakes as self-organized critical phenomena, *J. Geophys. Res.*, *95*, 6853-6860, 1990.
- Lindvall, S.C., T.K. Rockwell, K.W. Hudnut, Anonymous, and S.N. Ward, Slip distribution of prehistorical earthquakes on the Superstition Hills Fault, San Jacinto Fault zone, Southern California, based on offset geomorphic features, *Abstracts with Programs Geological Society of America*, *21*, 973-974, 1989.
- Liu, J., and T.H. Heaton, Effect of fault roughness on the scaling of slip with rupture length for shallow earthquakes, *EOS, Trans., AGU*, *79* (suppl.), F659, 1998.
- Lyakhovsky, V., Y. Ben-Zion, and A. Agnon, Earthquake cycle, fault zones, and seismicity patterns in a rheologically layered lithosphere, *J. Geophys. Res.*, *106*, 4103-4120, 2001.
- Lyzenga, G.A., A. Raefsky, and S.G. Mulligan, Models of recurrent strike-slip earthquake cycles and the state of crustal stress, *J. Geophys. Res.*, *96*, 623-21, 1991.
- Morein, G., D.L. Turcotte, and A. Gabrielov, On the statistical mechanics of distributed seismicity, *Geophys. J. Int.*, *131*, 552-558, 1997.
- Nielsen, S.B., J.M. Carlson, and K.B. Olsen, Influence of friction and fault geometry on earthquake rupture, *J. Geophys. Res.*, *105*, 6069-6088, 2000.
- Pepke, S.L., J.M. Carlson, and B.E. Shaw, Prediction of large events on a dynamical model of a fault, *J. Geophys. Res.*, *99*, 6769-6788, 1994.
- Prentice, C.S., and K. Sieh, A paleoseismic site along the Carrizo segment of the San Andreas fault, central California, *EOS, Trans. Amer. Geophys. Union*, *70*, 1349, 1989.
- Reid, H.F., The mechanics of the earthquakes, *Rept. State Earthquake Inv. Comm., The California Earthquake of April 18, 1906. Wahsington, D. C. Carnegie Inst.*, 1910.
- Rice, J.R., Spatio-temporal complexity of slip on a fault, *J. Geophys. Res.*, *98*, 9885-9907, 1993.
- Rundle, J.B., A physical model for earthquakes. 2. Application to southern California, *J. Geophys. Res.*, *93*, 6255-6274, 1988.
- Rundle, J.B., Derivation of the complete Gutenberg-Richter magnitude-frequency relation using the principle of scale invariance, *J. Geophys. Res.*, *94*, 337-12, 1989.

- Rundle, J.B., S. Gross, W. Klein, C. Ferguson, and D.L. Turcotte, The statistical mechanics of earthquakes, *Tectonophysics*, 277, 147-164, 1997.
- Rundle, P.B., J.B. Rundle, K.F. Tiampo, J.S.S. Martins, S. McGinnis, and W. Klein, Nonlinear network dynamics on earthquake fault systems, *Physical Review Letters*, 8714 (14), art. no. 148501, 2001.
- Salyards, S.L., K.E. Sieh, and J.L. Kirschvink, Paleomagnetic measurement of nonbrittle coseismic deformation across the San Andreas Fault at Pallett Creek, *J. Geophys. Res.*, 97, 457-12, 1992.
- Scholz, C.H., *The mechanics of earthquakes and faulting*, Cambridge University Press, 1990.
- Schwartz, D.P.C., Kevin J, Fault behavior and characteristic earthquakes; examples from the Wasatch and San Andreas fault zones, *J. Geophys. Res.*, 89, 5681-5698, 1984.
- Sharp, R.V., J.J. Lienkaemper, M.G. Bonilla, D.B. Burke, B.F. Fox, D.G. Herd, D.M. Miller, D.M. Morton, D.J. Ponti, M.J. Rymer, J.C. Tinsley, J.C. Yount, J.E. Kahle, E.W. Hart, and K.E. Sieh, Surface faulting in the central Imperial Valley, in *The Imperial Valley, California, earthquake of October 15, 1979*, pp. 119-143, 1982.
- Shaw, B.E., Complexity in a spatially uniform continuum fault model, *Geophys. Res. Lett.*, 21, 1983-1986, 1994.
- Shaw, B.E., Frictional weakening and slip complexity in earthquake faults, *J. Geophys. Res.*, 100, 239-18, 1995.
- Shaw, B.E., Model quakes in the two-dimensional wave equation, *J. Geophys. Res.*, 102, 367-27, 1997.
- Shaw, B.E., and J.R. Rice, Existence of continuum complexity in the elastodynamics of repeated fault ruptures, *J. Geophys. Res.*, 105, 791-23, 2000.
- Shimazaki, K., T. Nakata, Time-predictable recurrence model for large earthquakes, *Geophys. Res. Lett.*, 7, 279-282, 1980.
- Sieh, K., The repetition of large-earthquake ruptures, *Proceedings of the National Academy of Sciences*, 93, 3764-3771, 1996.
- Sieh, K.E., Slip along the San Andreas Fault associated with the great 1857 earthquake, *Bull. Seism. Soc. Am.*, 68, 1421-1448, 1978.

- Sieh, K.E., and R.H. Jahns, Holocene activity of the San Andreas Fault at Wallace Creek, California, *Geol. Soc. Am. Bull.*, 95, 883-896, 1984.
- Sims, J.D., T. Ito, J. Hamilton, A. J. Foss, C. D. Garvin and D. B. Meier, A 200-year average recurrence interval of earthquakes on the San Andreas fault at Phelan Creeks, Carrizo Plain, California: reconstruction from paired offset paleochannels, *unpublished manuscript*, 1994.
- Sims, J.D., Stream channel offset and abandonment and a 200-year average recurrence interval of earthquake on the San Andreas fault at Phelan Creeks, Carrizo Plain, California., *Proceedings of the workshop on paleoseismology, U. S. Geological Survey Open-file Report 94-568, C. S. Prentice, D. P. Schwartz and R. S. Yeats (editors)*, 170-172, 1994.
- Stuart, W.D., Forecast model for large and great earthquakes in southern California, *J. Geophys. Res.*, 91, 13771-13786, 1986.
- Tse, S.T., and J.R. Rice, Crustal earthquake instability in relation to the depth variation of frictional slip properties, *J. Geophys. Res.*, 91, 9452-9472, 1986.
- Wallace, R.E., Notes on stream channels offset by the San Andreas fault, in *Proceedings of conference on geologic problems of the San Andreas fault*, edited by W. R. Dickinson and A. Grantz, Stanford University Publications in the Geological Sciences, 1968.
- Ward, S.N., Dogtails versus rainbows; synthetic earthquake rupture models as an aid in interpreting geological data, *Bull. Seism. Soc. Am.*, 87, 1422-1441, 1997.
- Ward, S.N., San Francisco Bay area earthquake simulations; a step toward a standard physical earthquake model, *Bull. Seism. Soc. Am.*, 90, 370-386, 2000.
- Ward, S.N., and S.D.B. Goes, How regularly do earthquakes recur? A synthetic seismicity model for the San Andreas Fault, *Geophys. Res. Lett.*, 20, 2131-2134, 1993.
- Working Group of California Earthquake Probability (WGCEP), Probabilities of large earthquakes occurring in California along the San Andreas fault, *U.S. Geological Survey Open-file Report Open File Report 88-398*, 1988.
- Working Group of California Earthquake Probability (WGCEP), Seismic hazards in southern California: Probable earthquakes, 1994-2024, *Bull. Seism. Soc. Am.*, 85, 379-439, 1995.

## **Chapter 2**

# **Channel Morphology and Stratigraphy Revealed in 3-D Excavations**

Dirt in my hair,  
dirt in my shirt,  
dirt in my shoes,  
....

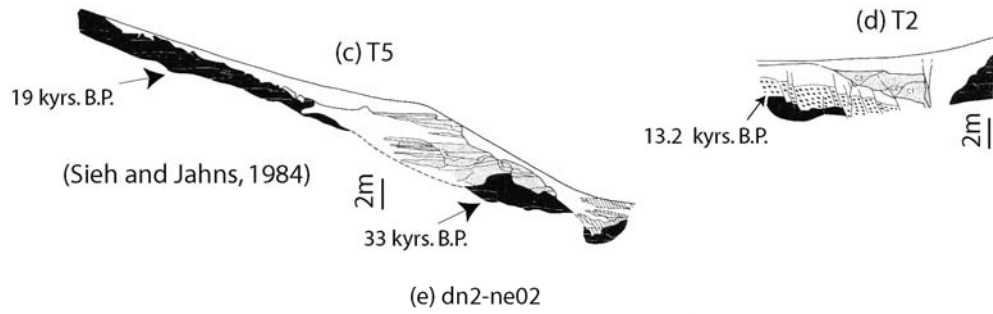
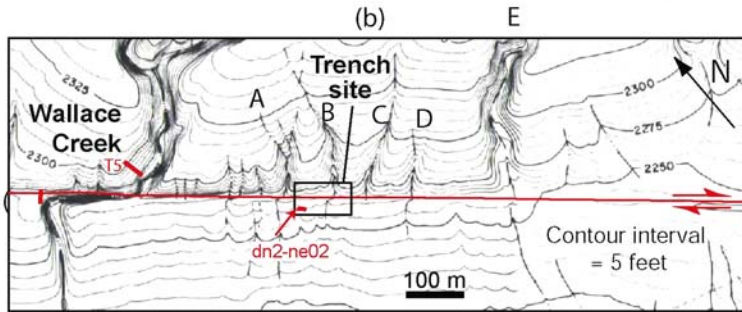
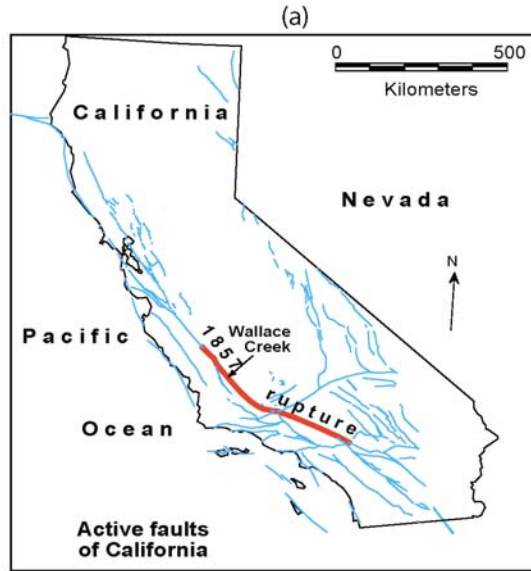
-Brandon Maehr  
Our field assistant  
and a major digger

## 2.1 Site description

The Carrizo Plain is an arid to semi-arid intermontane closed basin about 80 km northeast of the California coastline, with an arid to semi-arid climate. Average rainfall during 1960 – 1990 has been less than 30 cm per year. Ephemeral streams, dry except during local cloudbursts in the dry season or during large Pacific storms during the wetter winter months, flank the Temblor Range on the northeast. In the vicinity of Wallace Creek (Figure 2.1), the main surface is an apron of late Pleistocene alluvial fans derived principally from Miocene marine deposits of the Temblor Range (Dibblee, 1973). The fans were aggrading through the period from 33 Ka to at least 19 Ka (Figure 2.1c). This surface seems to have become inactive before about 13,250 yr B.P. (Figure 2.1d), Sieh and Jahns, 1984), just before the end of the last major global glaciation. Entrenchment of the late Pleistocene surface by active streams has continued throughout the Holocene epoch. At Wallace Creek the vertical component of motion on the San Andreas fault has been northeast side up, resulting in the present south-facing 8 – 9 m high scarp (Figure 2.1b). This section of the San Andreas fault experienced several meters of right lateral offset during the latest large earthquake in 1857 (Agnew and Sieh, 1978; Sieh, 1977, 1978).

We refer to our excavation site as the “Wallace Creek paleoseismic site,” because it is located just a few hundred meters southeast of Wallace Creek (Figure 2.1b). This important

Figure 2.1. (next page) Location of the Wallace Creek paleoseismic site. (a) Active faults in California, with 1857 earthquake rupture on the San Andreas fault highlighted. (b) The excavations, about 500 m southeast of Wallace Creek, are near one of the small drainages that drain the fault scarp (channel B). Here, San Andreas fault cuts through a late Pleistocene alluvial fan, with a several meter-high south-facing scarp. (c) Charcoal fragments within the fan deposits show that aggradation was occurring through the period 33 ka through 19 ka on the upthrown side (d) Charcoal from an alluvial gravel on the downstream side shows that channels had already begun to form at the fault by 13 ka (Sieh and Jahns, 1984). (e) Charcoal within a channel deposit at the trench site shows that incision of the downstream block had begun by 15.8 ka.



neotectonic landform was named informally by Sieh and Jahns (1984), in honor of Robert Wallace, the first geologist to explain the origin of its right-lateral jog (Wallace, 1968). Sieh and Jahns (1984) used Wallace Creek to make the first determination of the slip rate of the San Andreas fault. The site is at the outlet of a small drainage about 500 m southeast of Wallace Creek (labeled “b” in Figure 2.1b). This is one of four small gullies that cuts the late Pleistocene alluvial fan but extend only a hundred meters or so upstream.

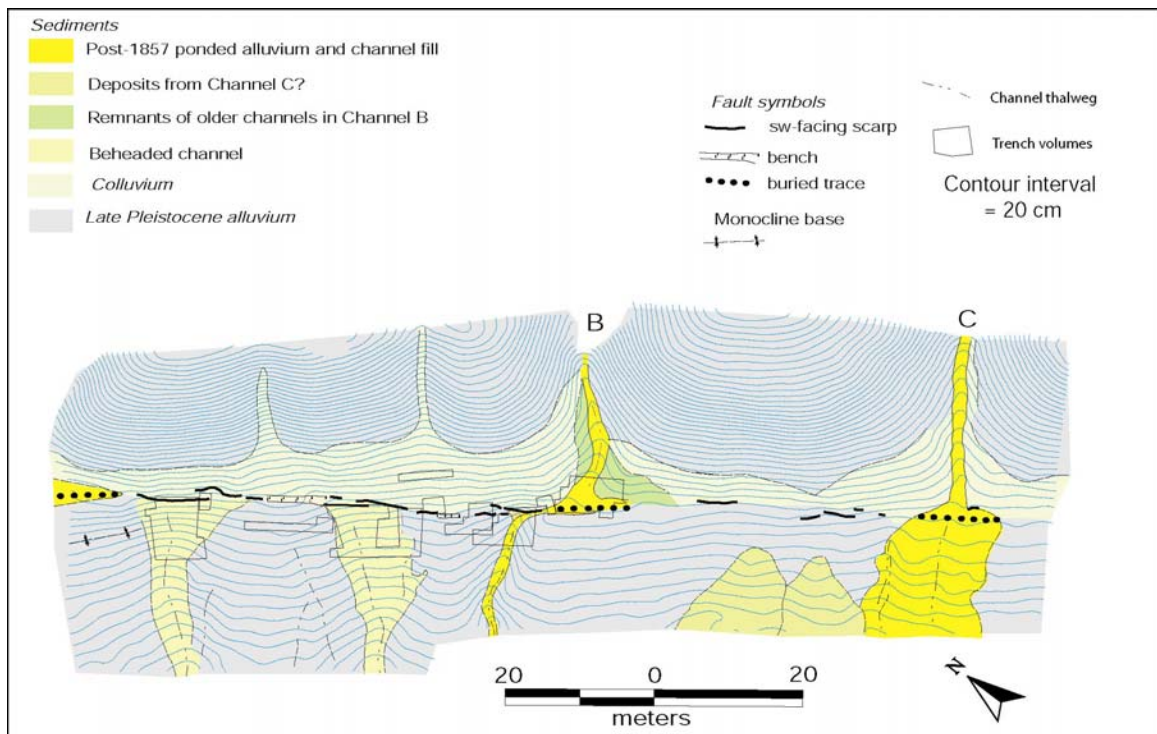


Figure 2.2. Geologic map of drainage B and the nearby drainage C at the Wallace Creek paleoseismic site. Note the presence of a colluvial apron and ponded alluvium on the northeastern side of the fault. Also, note the presence of three principal channels northwest of channel B, downstream from the fault. Contour interval is 20cm. Compiled from 1,418 measurements of elevation by Total Station.

Unlike Wallace Creek, the upstream channel segment here cannot be matched by one of similar size on the downstream side of the fault. Instead, a series of smaller and more subdued

gullies appear downstream from the fault. These appear to be offset dextrally from a common upstream source channel (Wallace, 1968; Sieh, 1977, 1978) (Figure 2.1c). These small gullies probably once lined up with their headwater sources, but only for a short time. Subsequent faulting removed them from the source and they are left abandoned and covered by colluvium, or recaptured if they are moved in front of another source channel. A detailed topographic survey of the site shows that three groups of channels appear to be associated with the upstream channel B (Figure 2.2). The farthest group is located 45 – 60 m NW of channel B. Asymmetric on the southeast side, the topographic contours alone suggest that it comprises at least two channels: a straight channel perpendicular to the fault, and a deflected channel that splays from the straight channel and runs diagonally into the fault. Lying 36 – 22 m northwest of channel B, is a broad, subdued depression, which narrows down-slope. From the broadness of the depression, we reasoned that it consists of multiple half-buried forked channels. Finally, the closest downstream channel to drainage B is a narrow, 0.5 m deep gully just 9 m or so from drainage B. This and numerous gullies with similar offsets appear to record the dislocation associated with just the 1857 earthquake (Sieh, 1978).

Colluviation at the base of the scarp has buried these small downstream gullies partially, and so their precise geometry near the fault is obscure. Thus, geomorphic measurements of offsets are imprecise and sometimes controversial (Sieh, 1978; Lienkaemper and Sturm, 1989; Lienkaemper, 2001).

Another source of ambiguity in the interpretation of geomorphic measurements is the possibility of channel piracy. Strike-slip motion along a fault can bring a downstream channel, whose source is far away, into alignment with a different upstream channel (Wallace, 1968; Gaudemer et al., 1989; Huang et al., 1993; Schumm et al., 2000). It sometimes even causes the channel pairs to have apparent offsets that are opposite in sense to the known sense of lateral slip on the fault.

At our site, we suspected early on that we might have this aliasing problem. To the southeast, within 500 m of drainage B are three more drainages, labeled C, D and E in Figure 2.1b. Of these drainages, channel C, which lies only 50 m southeast of channel B, might well have incised downstream channels of similar size to those near channel B in Figure 2. A little

more than 50 m of right-lateral motion on the San Andreas fault would move them into positions that make them appear to be offset from B. The other two source candidates, channel D and E, are less likely to cause interference, because they are farther to the southeast. Also, channel D has only a small fraction of the drainage area of B. Thus, it is probably too small to incise comparable downstream channel segments. Channel E, almost the same size as Wallace Creek, has enough stream power to incise larger channels than could be incised by B. However, it is about 280 – 340 m from our excavations, so 7,600 – 11,000 years would be required to juxtapose its downstream segments to channel B, at a slip rate of 34 mm/yr, the rate determined by Sieh and Jahns (1984) at Wallace Creek.

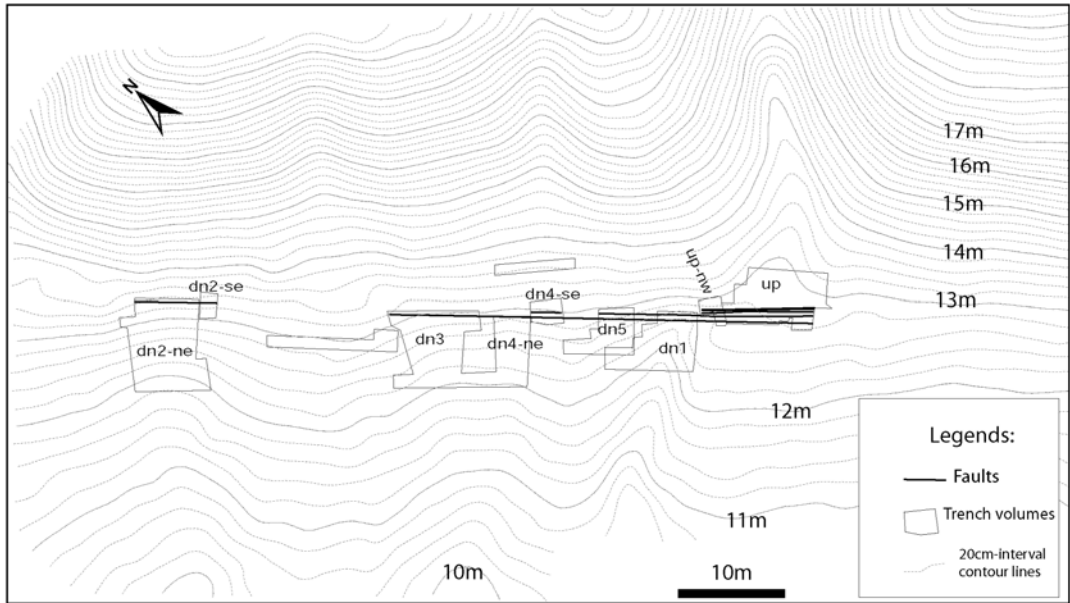
The best way to solve the aliasing problem, as well as other ambiguities, is to study the channel stratigraphy on both sides of the fault and to date the channels. Geomorphic investigation alone is inadequate to uncover the history of channels.

## 2.2 Methods

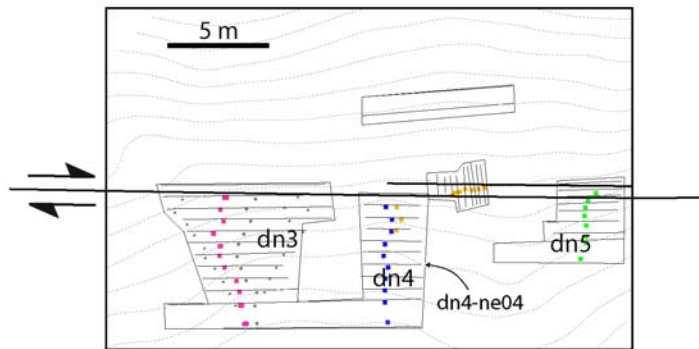
In order to minimize the uncertainties in geomorphic observations, we made a series of excavations to expose the stratigraphy associated with the channels. Basically, we explored 11 volumes to depths that ranged from 1.5 to 3.5 m (Figure 2.3a). Two of these excavated volumes are upstream from the fault, and six are on the downstream side. The excavated volumes downstream from the fault exposed relationships along a 50 – 60 m length parallel to the fault and northwest of source channel B (Figure 2.3a). They were laid out adjacent to each other to reveal all downstream channel segments within this reach from the channel B.

Figure 2.3. (next page) Excavations at the site. (a) Map of the eleven separate volumes that were excavated. The nine that exposed channels are labeled dn or up, depending on their location upstream or downstream from the fault. The suffixes "ne" and "se" indicate the direction of serial cuts within the excavation. (b) An example of the arrangement of mapped exposures within the excavated volumes. Symbols indicate the thalwegs of channels exposed in each cut. (c) Example of a notch cut between exposures. This exploratory cut parallel to the direction of serial excavation, allowed us to explore for a fault or other important features before removal of the volume between mapped exposures.

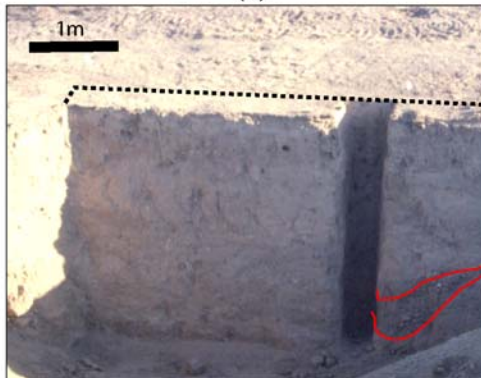
(a)



(b)



(c)



Most of the volumes were excavated progressively. In most cases, we began by excavating a narrow trench by hand, 4 to 5 m from and parallel to the fault, astride the gullies. After mapping both walls of these initial trenches, we cut into the wall closest to the fault, creating another nearly vertical exposure closer to the fault. After mapping this new face, we once again cut a new exposure, still closer to the fault. Subsequent faces were cut by increments of 50 to 60 cm, or as small as 20 cm in the close vicinity of the fault zone. In places where channels flowed nearly parallel to the fault zone, trench cuts would be oriented fault-normal. In this manner, we carefully followed each potential piercing line as presented in channel stratigraphy into the fault zone. Figure 2.3b provides an illustration of the nature of these serial cuts within four of the excavated volumes. As illustrated in Figure 2.3c, between parallel cuts, we would cut a notch and use channel stratigraphy to check if we would cross a fault between the current face and the next.

We named each exposure, in order to keep track of all our data. Each exposure name reflects the name of the volume it belongs to, the sequence in which it was cut, and the direction of cutting. For example, exposure dn4-ne04 is the 4<sup>th</sup> cut within downstream volume 4 and that it was on the northeast wall of the volume.

Exposures were cleaned by scraping and brushing, surveyed in detail with a Total Station (up to 300 control points for the large walls), and mapped at 1:15 scale (except 1:20 scale for trench dn1). Symbols used in mapping appear in Figure 2.4. All surveying used the same reference frame as that for the 20 cm contour topographic map shown in Figure 2.3a. We later reconstructed the three-dimensional geometry of channels and faults by utilizing the coordinates of control points on the densely surveyed excavation walls. Strata within the channels were correlated from one exposure to another based on lithologic similarity, stratigraphic position and elevation of the upper and lower contacts. High-precision channel geometry and location thus gave greatly refined slip measurements.

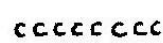
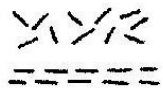
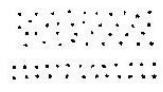
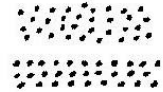
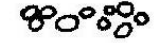
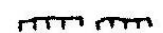
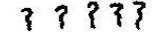
	Clay	
	Silt to very fine sand:	massive laminated
	Fine to medium sand:	massive laminated
	Very coarse to coarse sand:	massive laminated
	Granules	
	Pebbles	
	Cobbles and boulders (to scale)	
	Soil Horizons	
	Roots	
	Burrows	
	Carbonate precipitate	
	Contact (dashed when inferred)	
	Fault (dashed when inferred)	
	Charcoal	
	Fire scar	

Figure 2.4. Lithologic and other symbols used in documenting the exposures.

## **2.3 Channel stratigraphy and morphology**

### ***2.3.1 Underlying Late Pleistocene alluvium***

The substrate underlying all the downstream channels is a massive deposit of indurated and matrix-supported pebbly sand and silt, interbedded with sorted gravelly and sandy lenses (e.g., Figure 2.1e). A more than 1m -thick pedogenic carbonate horizon ( $B_k$ ) has developed within this unit and has penetrated into the matrix, suggesting the relative old age of the deposit. Consistently, the top 1 – 1.5 m of the deposit has been severely bioturbated and homogenized except in some isolated chunks. Such concentrations of soil carbonates have been found in early Holocene or older deposits in this region (Sieh and Jahns, 1984). A piece of charcoal that was extracted 1.3 m below the surface yielded  $^{14}\text{C}$  age of 15,800 yr B.P. (Figure 2.1e, cross-section dn2-ne02). This age suggests that the downstream surface is slightly older than the 13,250-years-old alluvial fan straddling the current downstream segment of the Wallace Creek (Figure 2.1d, cross-section T2), but is probably nearly contemporaneous with the “older alluvial fan” at Wallace Creek (Sieh and Jahns, 1984).

### ***2.3.2 Downstream channels***

The distinction between the late Pleistocene fan and recent channel deposits manifests itself in three ways: 1) the colors of the two units differ. The older is light reddish brown to pink or pinkish white (5YR 8/2 to 5YR 6/4; Munsell soil color charts); the younger is mostly light gray to greenish gray (GLEY1 6/1 to GLEY1 7/1; Munsell soil color charts), darker than the older underlying unit; 2) the edges of the younger channels are generally clear; and 3) lenses of well-sorted sand and gravel within the younger channels are traceable from cut to cut. These beds are usually coarser than the adjacent late Pleistocene deposits. .

These well-sorted sand and gravel layers within the channels, when they can be traced over several meters in the channels, provide good markers for stratigraphic correlation from cut to cut in each trench. However, finding the channel walls is sometimes tricky, especially in the

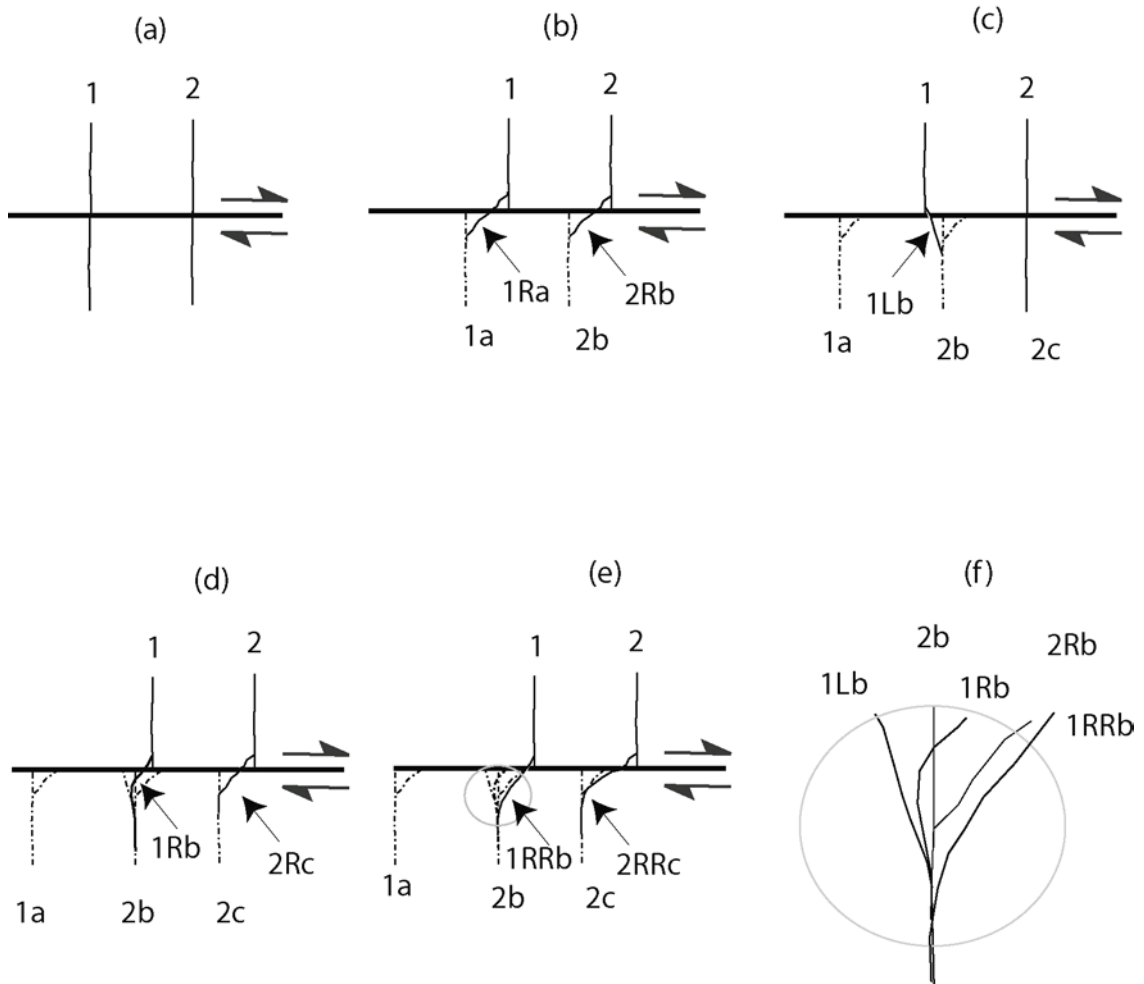


Figure 2.5. Lateral offset of closely spaced channels can lead to complicated interplay of upstream and downstream channels. (a) Initial configuration of two hypothetical channels (1 and 2) traversed by a right lateral fault. (b) After initial offset, right-deflected channels (1Ra and 2Rb) may reconnect the offset pairs. (c) Additional slip on the fault may bring the downstream channel "2b" close to channel 1, resulting in the creation a left-deflected connection "1Lb" between the two channel segments. (d) Another right-lateral rupture moves "2b" to the other side of channel 1, and a right-deflected channel "1Rb" forms as a new connector between the two channels. (e) If "1Rb" is abandoned after yet another rupture, another right-deflected channel "1RRb" might also form, as water from channel 1 continues to seek channel "2b". (f) The resulting configuration of downstream channels would, indeed, be quite complex.

upper part of the channel, where deposits filling the channel are commonly colluvium, derived from collapse of the upper channel wall and thus compositionally similar to the late Pleistocene material. Bioturbation commonly further obscures the upper channel boundaries, also.

We assigned the downstream channels letter names (from a to L), where a is closest to the mouth of channel B, and L is farthest.

### **2.3.2.1 General channel configurations**

Before we delve into the details of individual channels, let us first look at the different scenarios of channel deflections due to right-lateral motion on a fault. Figure 2.5 illustrates the possible complexity in channel arrangement when several drainage systems are involved. Because the upstream channels along this stretch of the San Andreas fault meet the fault at a high angle, we only show the case where two adjacent straight channels cut perpendicularly across a right-lateral fault (Figure 2.5a).

In the illustration, slip on the fault offsets the two channels. Subsequently, the disarticulated upstream and downstream channels are reconnected by diagonal channels “1Ra” and “2Rb” (Figure 2.5b). We will call “1Ra” and “2Rb” right-deflected channels, since they join the straight channels from the right in map view.

If the right-deflected channel is maintained by the stream through many fault ruptures, as the modern Wallace Creek has done through the past 3,700 years, the two channels will maintain these right deflections and the length of the deflection will grows with each rupture.

Additional motion on the fault moves the downstream channel “2b” closer to the upstream channel 1. When channel “2b” is still to the right of, but close to channel 1, the topographic low associated with channel “2b” encourages a left-deflected channel “1Lb” to form between channel 1 and channel “2b” (Figure 2.5c).

As ruptures continue to occur, channel “2b” moves to the left of channel 1. When the channels are in this configuration, a right-deflected channel “1Rb” connects them (Figure 2.5d). Of course, if channel “2b” happened to be moved immediately downstream from channel 1, the new connecting channel segment would not exhibit a deflection.

In panel e of Figure 2.5, yet another offset has occurred, but the offset too small to remove the downstream channel from influence by upstream channel 1. In this case, then another right-deflected channel (1RRb) forms (Figure 2.5e).

From this sequence of events, one can easily imagine that the stratigraphic relationships in both the upstream and downstream channels can be complex. Figure 2.5f illustrates the complexity in the geometry of sequential downstream channels that would have developed in the scenario just described. The channels represent multiple incisions, aggradations and abandonments, resulting from the interplay of fluvial processes and tectonics.

### **2.3.2.2 Channel *a***

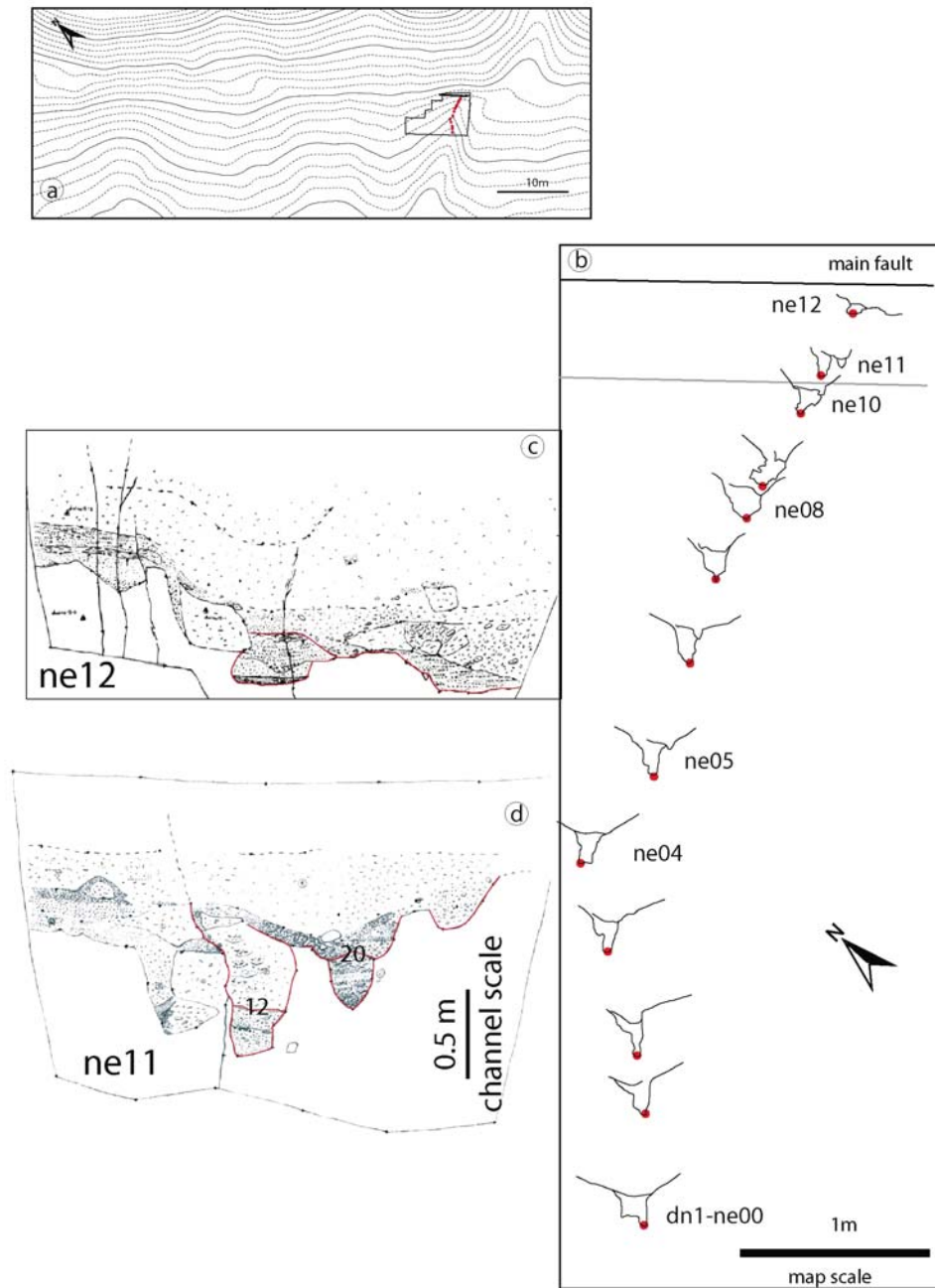
Channel *a* is the southernmost channel on the downstream side of the fault and the youngest channel visible in the topography. It appears to have been offset about 9 m from source channel *B* (Figure 2.6a). Although channel *a* cuts into the landscape only about 0.5 m, the excavations reveal that its deepest thalweg (the deepest part of a channel at any instant of time) is 1.5 m or so deeper. Thus, sediment fills about 75% of channel *a*.

Figure 2.6b shows the simplified cross-sectional profiles of channel *a* derived from our mapping of sequential channel walls. The cross-sections appear on the plan-view map to illustrate the changes in channel shape that occur along the stream profile. The viewing direction in each cross-section is upstream, and the deepest thalweg of the channel in each exposure appears as a dot in its correct geographic location. Six of these simplified cross-sections appear in more detail to the left as panels c through h. In these detailed panels, correlative beds appear with identifying numbers.

Channel *a* is deep and narrow far from the fault (dn1-ne01 to ne06) but is much broader nearer the fault (ne07 to ne09). Near the fault (from ne04 to ne11), the younger, upper part of channel *a* has a thalweg that deviates to the right from the trend of the deepest thalweg. The shape of the channel in cut ne12 appears to indicate shearing near the main fault zone.

These exposures show clearly that the geometry of a channel can change in a short distance. For example, the side branch about 50 cm outside the main channel in exposure ne11 merges with the main channel in exposure ne10, just 20 cm downstream. We keep this feature in

mind, below, in our correlations of downstream channel segments to upstream counterparts. Even so, other features, like channel depth, cross-sectional area, and channel width/depth ratio, are in general reliable in making correlations. Stratigraphy and sedimentary structures within the channels provide additional information that assists in distinguishing individual channels.



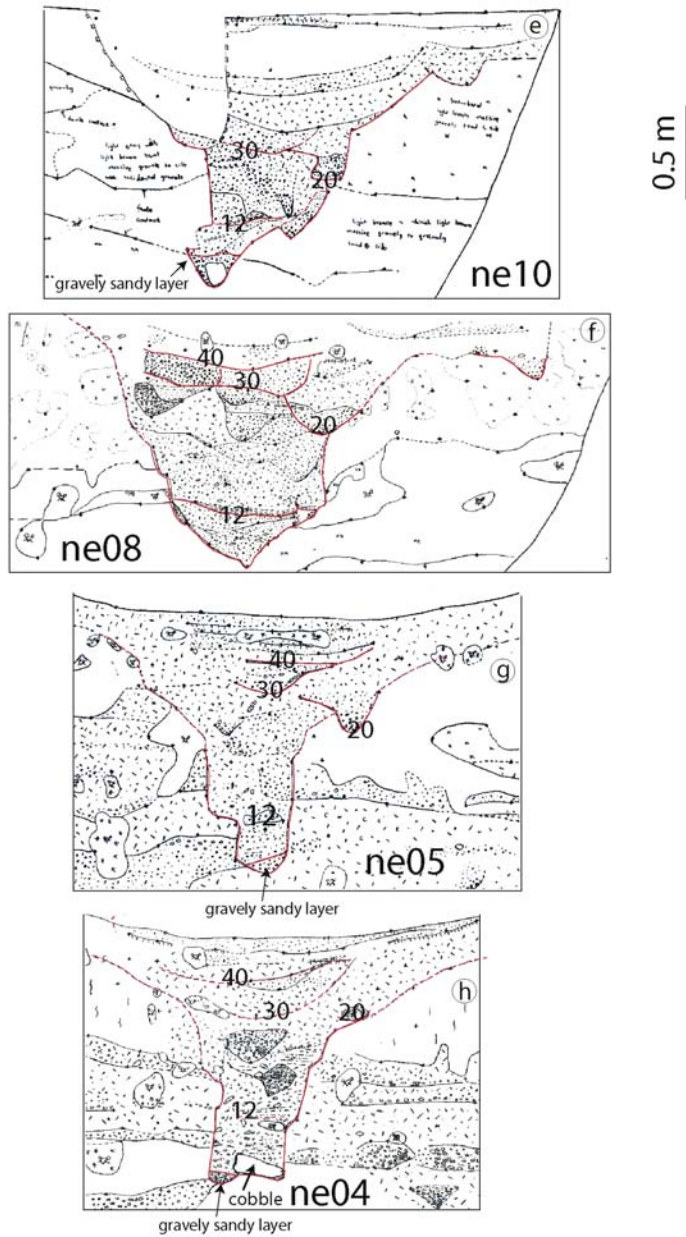


Figure 2.6. Summary of the results of the excavation of channel a. (a) Excavated volume dn1 and deepest thalweg of the channel. (b) Detailed map of the deepest thalweg of channel a. Dots indicate the map position of the thalweg in each mapped exposure. Simplified cross-sections of the channel in each mapped exposure show the variability in channel shape and stratigraphy. Panels (c) through (h) are maps of the channel in selected exposures. The name of each exposure indicates the sequence and direction in which it

was cut and mapped. Only those portions of a mapped exposure that contain the main body of channel a are shown. Major units described in the text are numbered at their lower contacts. The top lines in ne11, ne10, ne05 and ne04 represent the present ground surface.

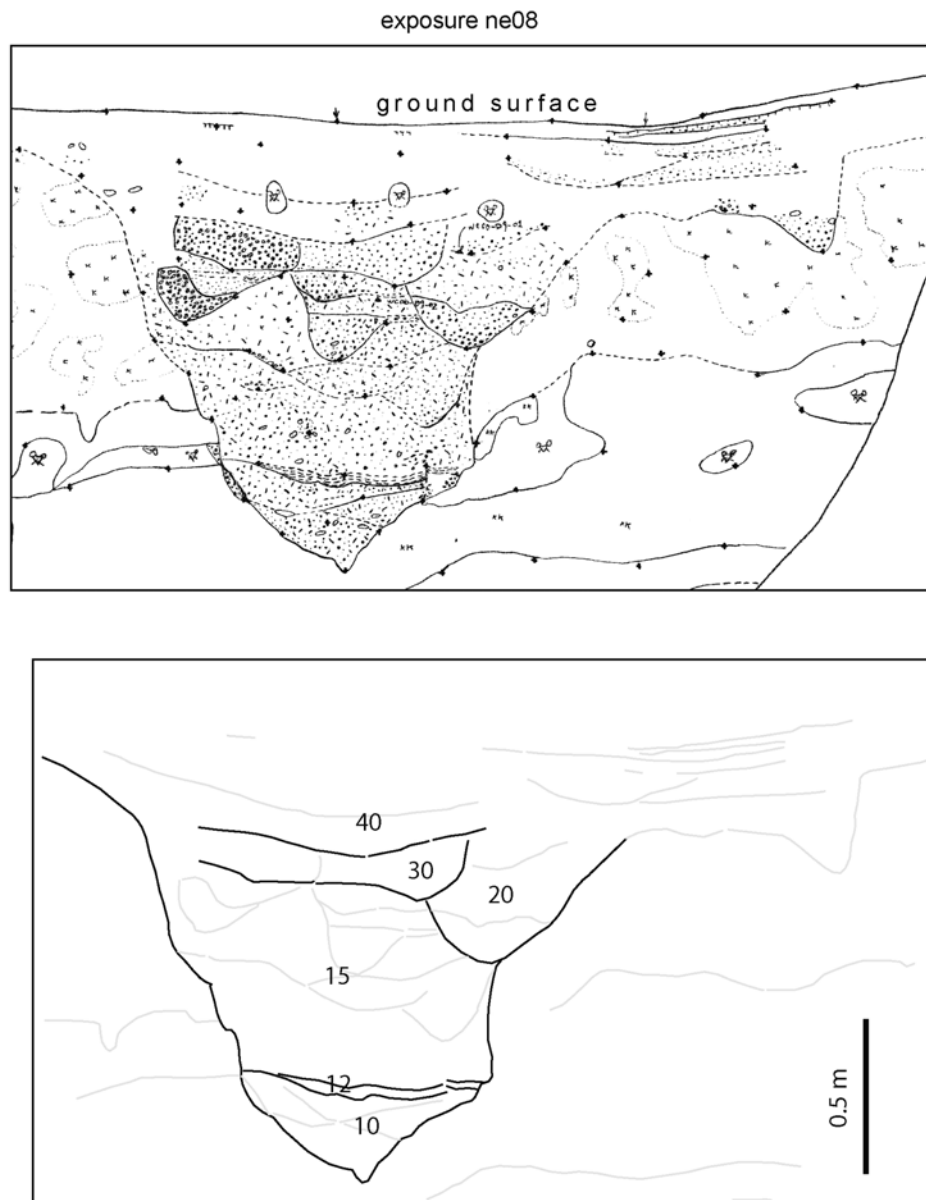


Figure 2.7. Stratigraphic units of channel a illustrated using exposure dn1-ne08. The upper panel is the map of channel stratigraphy; the lower panel shows the general groupings within the channel.

The stratigraphic sequence in channel a, as represented by exposure dn1-ne08, reveals a complex history of cuts and fills (Figure 2.7). We divided the deposits in channel a into 6 units, each of which contains multiple subunits. These units, designated numerically, are defined by their textures and the prominence of their lower contacts, which are generally major erosion surfaces.

Unit 10 consists of massive poorly sorted matrix-supported colluvium, with grain sizes ranging from gravelly sand to silt (Figure 2.7). However, in exposures ne04, ne05 and ne10 (Figure 2.6), a sandy, gravelly layer as thick as 15 cm appears at the very base of the channel. Since these clast-supported sediments are not present in some exposures, they probably exist as isolated piles of sand and gravels above the channel floor. This may be due to a wavelike translation of bed material through a reach, described as migrating sand waves (e.g., Meade, 1985; Gomez et al., 1989; Reid and Frostick, 1994).

Covering unit 10 is unit 12, a 5 cm or thinner layer of laminated fine sand to silt. The lamination in this unit typically drapes the shape of the top of unit 10 (Figure 2.7). Unit 12 is a distinctive bed that appears in almost every exposure of channel a, and is a good candidate for aiding in correlation with the upstream channel from which channel a has been offset.

Unit 15 overlies 12 (Figure 2.7). It is a thick stack of nearly featureless colluvium. We include in unit 15 two channels that overlie the colluvium in exposures downstream from ne08 (Figure 2.6h).

Unit 20 represents a major incision. It is cradled within a distinct channel scour and has distinctive clast-supported sand and fine gravel in its lower portions. The cross-sectional area of unit 20 and its grain sizes diminish downstream. Near the fault, in exposure ne11, unit 20 is an 80-cm-wide lens of cobbles and pebbles (Figure 2.6d). In the exposure farthest from the fault (ne04), 3 m downstream from ne11, it is merely 15 cm wide and 7 cm thick and consists of granules and coarse sand, with no distinct basal scour mark. The upper part of unit 20 is massive, poorly sorted colluvial debris, derived from the channel wall.

This colluvial unit is cut by unit 30, which comprises mainly two channels. Best exposed in ne08, the channel on the left cuts into the one on the right and thus is younger (Figure 2.7); the

younger channel contains better-sorted and coarser-grained size deposits, yet in most exposures the two channels are barely separable.

Unit 30 and all lower units run abruptly into the fault zone and show no indication of bending. The sharp truncation demonstrates that these units are offset by the fault.

In sharp contrast to the clast-supported channel sand and gravels of unit 30, the overlying unit 40 is mostly fine-grained matrix-supported organic silty loam. In exposures near the fault, i.e., exposures ne10, ne11 and ne12, unit 40 is represented by a stack of massive poorly sorted silty sand with gravels. The massive and homogeneous nature of the deposit suggests it is probably fault-scarp derived colluvium.

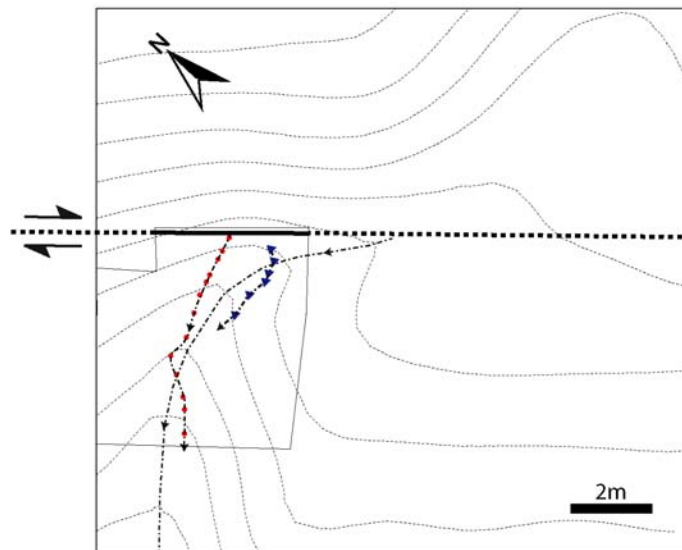


Figure 2.8. Map view of three features associated with channel a. Red dots show the path of the deepest (pre-rupture) thalweg. Triangles trace the path of a post-offset channel. Dashed line indicates the thalweg of the present channel, visible in the current topography.

In map view (Figure 2.6b), the deepest thalweg of channel a curves right as one views it looking toward the fault. It has a prominent right step in the middle of its course, between

exposure ne04 and ne05. This step is demonstrably not an offset across a minor fault. We know from the exposures that the step resulted from diversion of the thalweg by triangular plate large cobble. This large clast, 25 cm long and 3 – 10 cm thick blocked the channel on the right in exposure ne04 (Figure 2.6h). The thalweg skirted to the cobble on the left to pass the blockage.

However, this impediment cannot be the cause of the broader bend in the thalweg between ne04 and the fault zone. Neither can we attribute the deflection to secondary faults. Although several secondary fault traces disrupt the bedrock between ne07 and ne12, they do not break the strata within channel a. One might hypothesize that the curvature is due to non-brittle warping in the meters closest to the main fault. The data we have collected along this channel does not provide a test of this possibility. But this hypothesis is testable. If warping is the cause of the bend, older channels that lie to the northwest of channel a might also display evidence of warping. An alternative hypothesis is that the curvature of the deep channel a thalweg has been inherited. For example, of the thalweg might have been cut into an older channel that formed in the manner shown for right-deflected channels “1Ra” or “2Rb” in Figure 2.5.

Although deflection prior to the most recent offset of channel a is ambiguous, right deflection or rounding after the most recent offset is obvious in the stratigraphy and topography of channel a. The thalweg of the present channel on the surface, shown in Figure 2.8 as a thin dashed line, diverges to the southeast of the deepest thalweg of channel a and partially connects to the upstream channel across the fault. Note also in exposure ne08 (Figure 2.7), a small shallow channel and its deposits lie well to the right of the main channel. In fact, this shallow side channel occurs in exposures that are within 2 m of the fault zone (Figure 2.6). The thalweg of this shallow channel forms a line that lies southeast of the deep thalweg of channel a, but merges with the trace of the deep thalweg farther down-slope (blue triangles in Figure 2.8). These two younger thalwegs indicate the response of a channel to right-lateral slip on the fault.

### **2.3.2.3 Channel b**

Channel b appears in volume dn5, 5 – 6 m northwest of the channel a (Figure 3a). Any geomorphic evidence for this channel was obliterated by incision of channel a. Its presence is only hinted at by the asymmetry of the banks of channel a near the fault, and the slight bending of

a couple of topographic contour lines near the fault (Figure 2.9a). Earlier measurements of sequential offsets (Sieh, 1978) did not include this obscured channel.

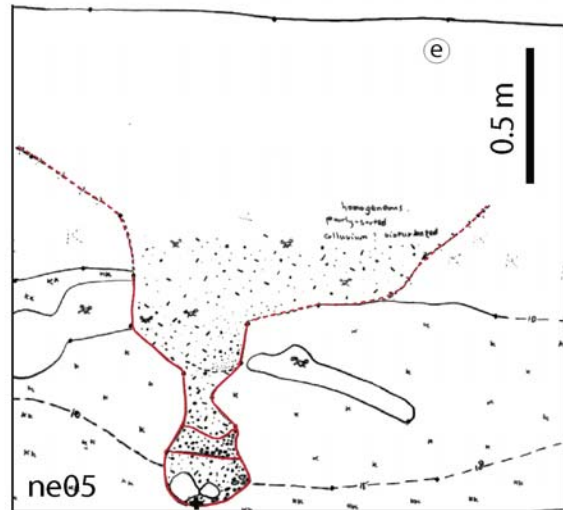
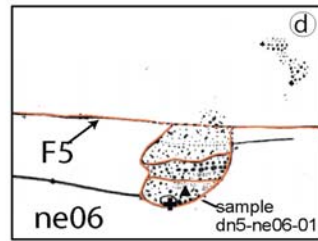
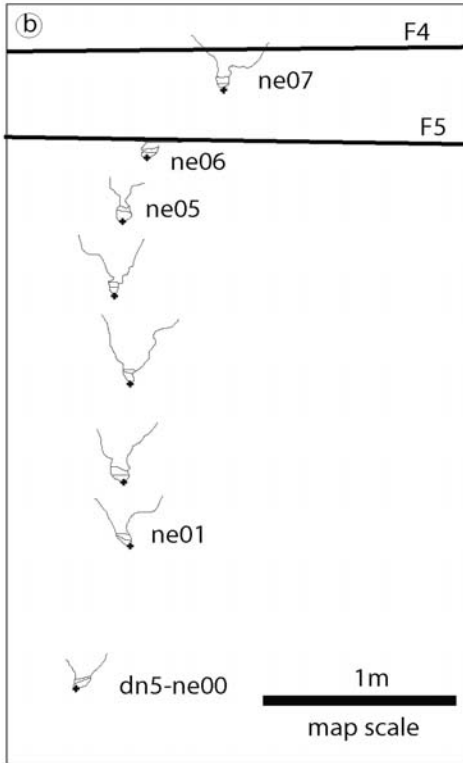
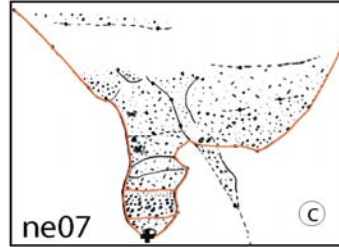
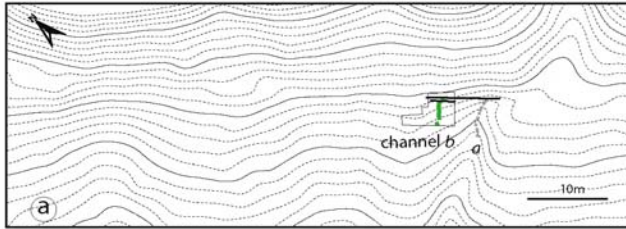
The outline of channel b is commonly well defined by virtue of the distinct differences between channel deposits and surrounding late Pleistocene materials. Furthermore, the narrowness of the channel sets it apart from all other channels downstream from the fault.

The stratigraphy of channel b is less variable from cut to cut than that in channel a, and is therefore easier to trace. Characteristically, 3 fluvial layers at the bottom of the channel are overlain by predominantly colluvial fill.

The basal fluvial layers (units 10, 20 and 30) commonly fill the lowest 30 to 40 cm of the channel (Figure 2.10). Unit 10 is a 10 – 15 cm thick bed, comprised of matrix-supported and poorly sorted pebbly to granule-rich sand with silt. The overlying unit 20 is very distinctive and continuous from cut to cut. It is a 15 cm-thick horizontally bedded and upward-fining sequence, the grain size decreases upward from pebbles to granule sand, then to fine sand, but each individual layer is very well sorted.

In exposure ne07, unit 30 consists of two beds (Figure 2. 10). The lower bed is massive matrix-supported and poorly sorted granule sand and silt. The upper one is relatively well-sorted coarse to medium sand. Although the upper bed is as thick as the lower one in exposure ne07, this layer thins out quickly down-slope, only 2 cm in ne06 and absent from the rest exposures (Figure 2.9).

Units 40 and 50 constitute the bulk of the channel deposits. These are mostly composed of non-descript, loose and homogeneous colluvium (Figure 2.10). The contact between unit 40 and 50 is marked by massive granule and sand, which we interpret as fluvial deposits. These lenses vary in thickness, tending toward lesser cross-sectional and clast size downstream. In the exposures farthest from the fault, they are only faintly recognizable as a higher concentration of granules and coarse sand than in the surrounding colluvium.



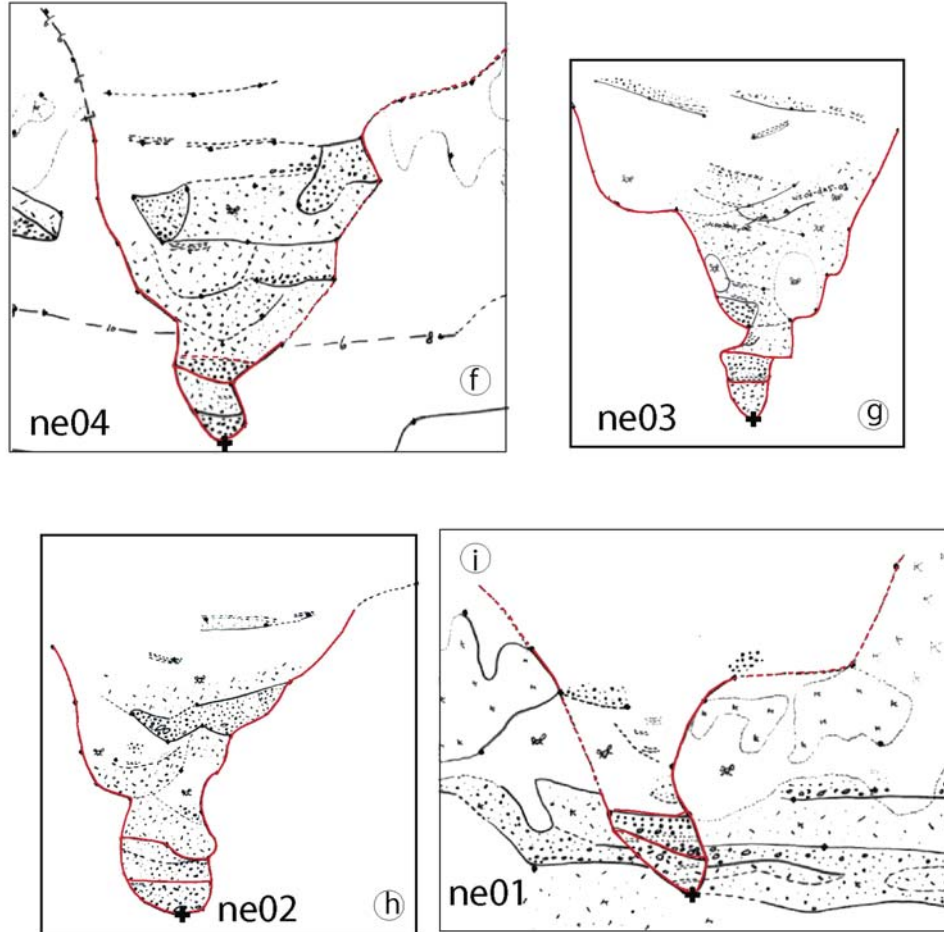


Figure 2.9. Summary of the results of the excavation of channel b. (a) Excavated volume dn5 and deepest thalweg of channel b in map view. (b) Detailed map of the deepest thalweg of channel b. Cross symbols indicate the map view position of the thalweg in each exposure. Simplified cross-sections of the channel show the variability in channel shape. Panels (c) through (i) are the maps of the channel in selected exposures. The name of each exposure indicates the sequence and direction in which it was cut. Only those portions of a mapped exposure that contain the main body of channel b are shown. The top line in ne05 represents the present ground surface.

Channel b is distinctly different than channel a. First, it is morphologically simpler; in all exposures, it is narrow and deep, with a bottleneck in the channel walls some centimeters up from

the thalweg. Unlike channel a, channel b does not have prominent post-offset right-deflected channels. This may indicate that channel b is too narrow to favor a close connection to the upstream channel after its being offset, especially if channel b was initially offset by a large amount. Both factors encourage the isolation of the offset channel segments, so water flows down the upstream segment is less likely to “feel” the topographic influence of the downstream segment.

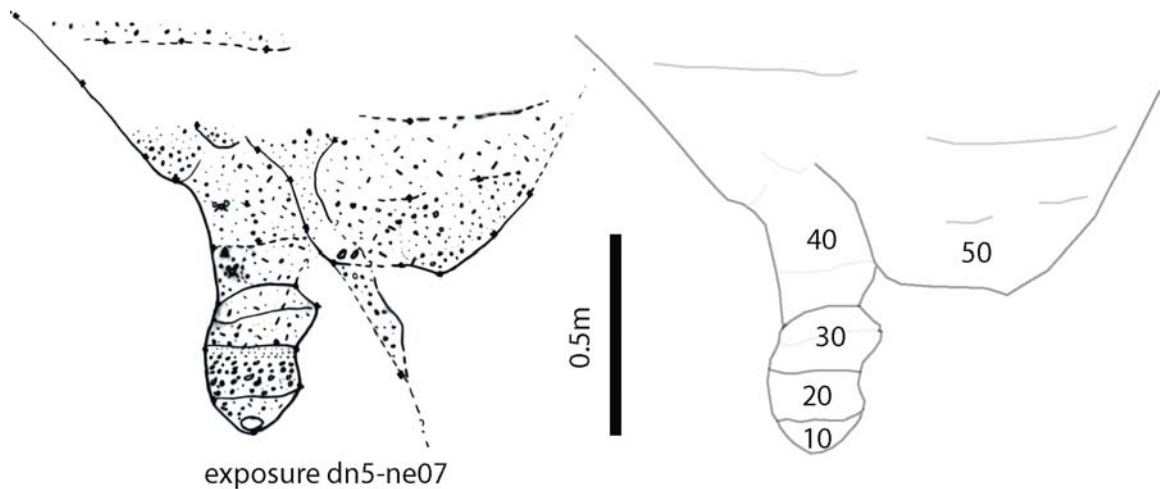
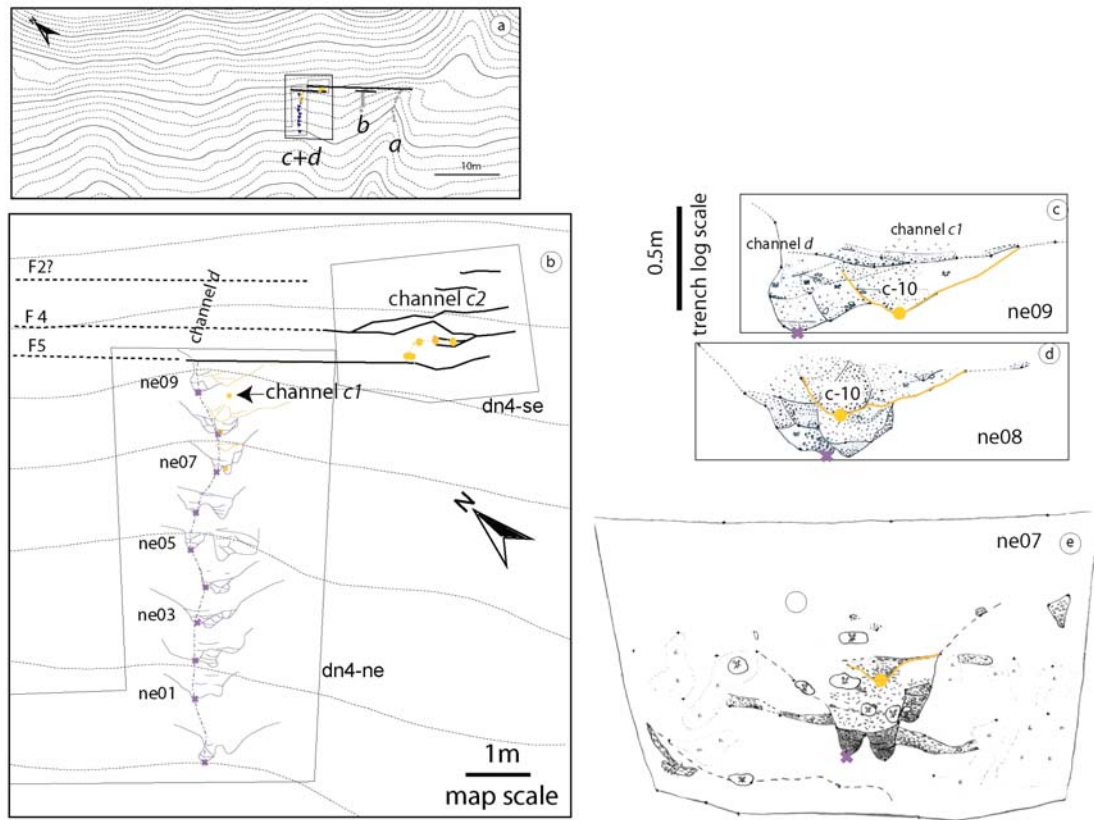


Figure 2.10. Stratigraphic units of channel b illustrated using exposure dn5-ne07. The left panel is the map of the channel stratigraphy; the right panel shows the general groupings within the channel.

The thalweg of channel b runs straight into the fault, without bending (Figure 2.9b). Hence, the bending of channel a within 2.5 m of the fault is not due to tectonic warping. The fact that channels a and b appear to merge about 20 m downstream from the fault suggests that the presence of b led to a diversion of a into channel b after b had been offset along the fault. This suggestion is a bit tenuous, however, since channels a and b are both parallel to the fault and not coincident at intermediate distances from the fault.

Secondary faults (Fault 5) cut through exposure ne06. In this exposure, the faults dip into the exposure and appear as nearly horizontal contacts both above and below a fragment of

channel b (Figure 2.9). The channel is missing above the upper fault. The apparent right-lateral deflection in the channel b thalweg between exposure ne07 and its neighbors probably reflects right-lateral offset on these two faults. The lateral offset on the fault between exposures ne06 and ne07 would be about 0.35 – 0.4 m. This secondary fault does not disrupt younger channel a and thus was active only between filling of channel b and cutting of channel a.



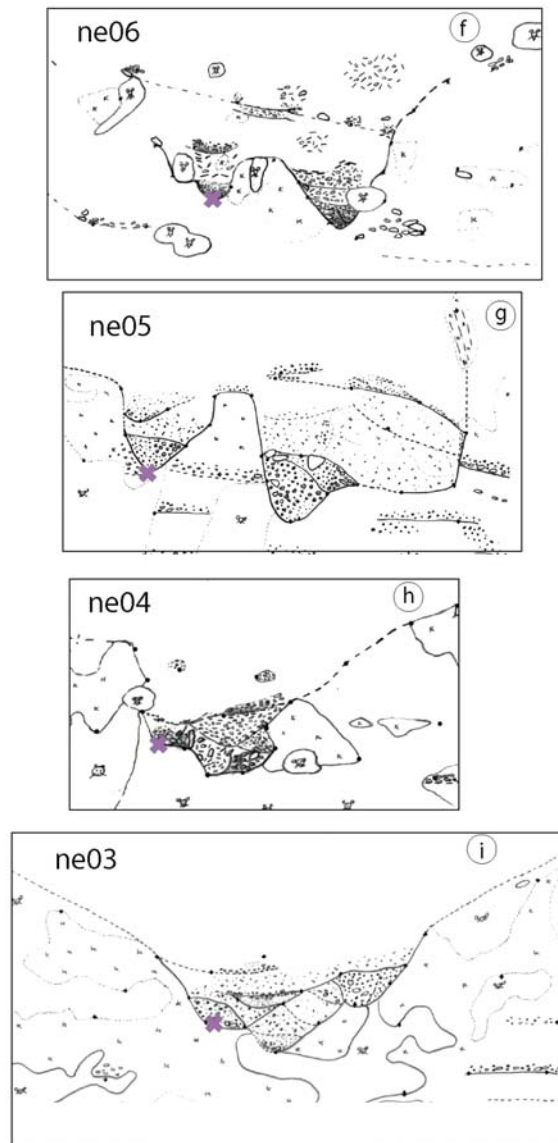


Figure 2.11. Summary of the results of the excavation of channel d. (a) Location of channel d in a map view. (b) Detailed map of the deepest thalweg of channel d. Cross symbols indicate the map view position of the thalweg in each exposure. Two related channels, c1 and c2, are shown in orange. Cross-sections of the channel show the variability in channel shape and stratigraphy. Panels (c) through (i) are the maps of the channel in selected exposures. The name of each exposure indicates the sequence and direction in which it was cut. Only those portions of a mapped exposure that contain the main body of channel d are shown. The top line in ne07 represents the present ground surface.

### **2.3.2.4 Channels *c* and *d***

We excavated two volumes adjacent to each other and 5 to 11 m northwest of channel *B* (Figures 2.3 and 2.11a). In these excavated volumes, dn4ne and dn4se, we found a set of two channels, *c* and *d*. The deeper channel, *d*, is nearly perpendicular to and runs straight into Fault 5 (Figure 2.11b). The shallower one, channel *c*, is more complicated. It consists of two segments, on either side of Fault 5. In plan view, channel *c1* nearly coincides with underlying channel *d*. Channel *c2*, is a 1.5-m-long channel segment within in the fault zone and to the southeast of *c1*.

Cross-sectional views of channel *d* show that it is 1.0 to 1.2 m deep and generally W-shaped. The stratigraphy suggests that this shape is the result of two major phases of scour and fill, the first of which created unit d-10 and the latter of which formed d-20 (Figure 2.12). The resultant geometry is two adjacent, nearly parallel channels that intersect the fault zone at nearly right angles (Figure 2.11b).

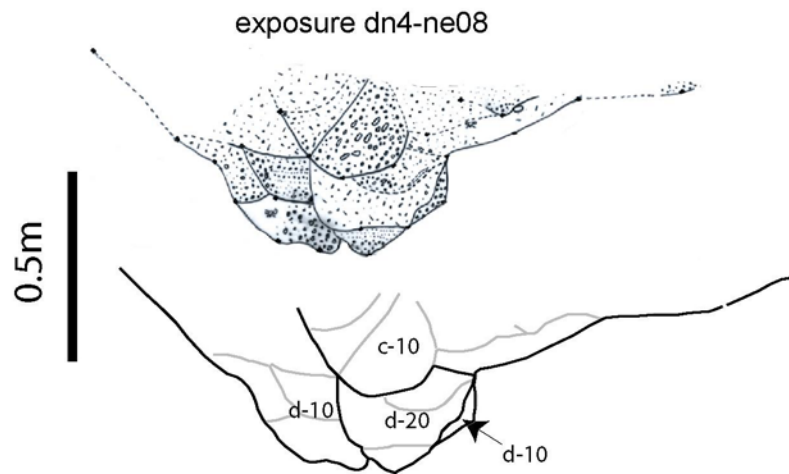


Figure 2.12. Stratigraphic units of channels *d* and *c1* illustrated using exposure dn4-ne08. The upper panel is the map of the channel stratigraphy; the lower panel shows the general groupings within the channels. c-10 designates the unit of channel *c*; d-10 and d-20 are the units of channel *d*.

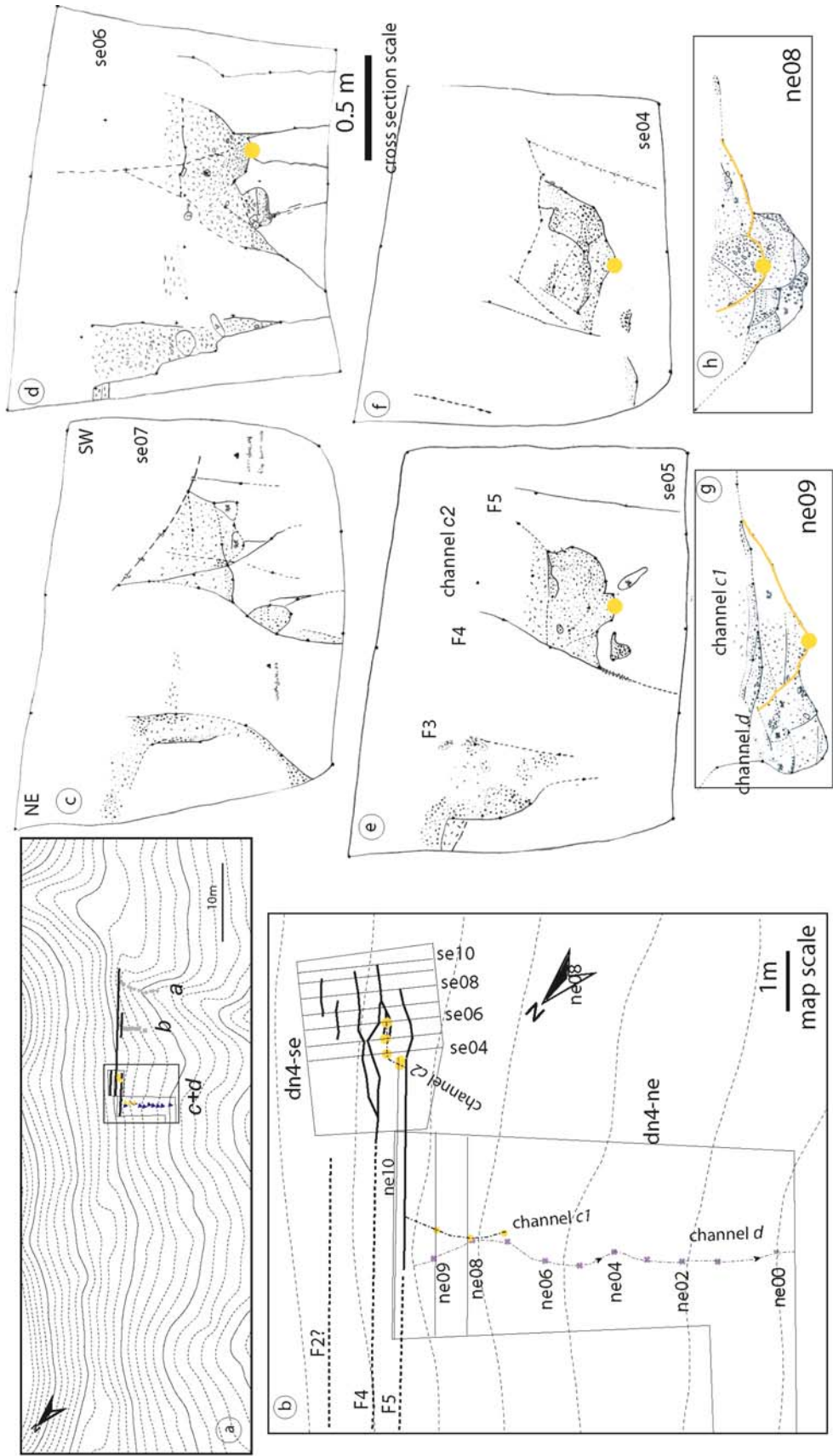
The first phase of down-cutting, recorded by unit d-10, left a thin (<15 cm) fluvial layer of massive pebbly granule-rich sand at the base of the channel. This layer was covered later by

homogeneous colluvium. Secondary cut and fill sequences in this cycle are preserved most clearly in ne08, and moderately well in a ne05 and ne06. The second major down-cutting event widened channel d, mostly by scouring the southern bank. This cutting extended as deep as the first incision, thus forming a second thalweg less than a meter southeast of the first (Figure 2.12). The deposits within this second channel, unit d-20 are like those in the first channel. They consist of a thin, massive basal granule, pebble and coarse sand and an overlying thick non-descript colluvial bed.

Above these two pieces of channel d in a couple of near-fault exposures, is another channel, c1. Best exposed in ne08, it consists of a semi-circular erosion surface filled with gravel and sand. These beds are labeled “10” in Figure 2.12. The erosion surface cuts the upper colluvium of channel d. The deposits within the channel are thickest near the fault (30 cm in exposures ne08 and ne09) and diminish quickly downstream (to 15 cm in ne07) and to zero farther downstream.

Channel c1 diverges from the path of channel d in a right-lateral sense within a meter of the fault (Figure 2.13 g and h). This channel is very similar to channel c2 a few meters to the southeast, within the fault zone.

Figure 2.13. (Next page) Summary of channel c. (a) Location of channel c. Map view of the thalweg of channel c (dots) in (b) indicates that the channel was offset into two segments. One segment is trapped in the fault zone and flows sub-parallel to the fault; the other flows perpendicular to the fault zone and re-occupies channel d, whose thalweg is indicated by crosses. Panels (c) through (f) are the logs of selected exposures showing the cross-sections of channel c in the fault zone. View towards SE. (g) and (h) are two fault-parallel exposures showing that channel c cuts into the upper colluvium of channel d. View towards NE. In the logs presented here, the thalweg of channel c is highlighted by dots in corresponding exposures.



Channel c2 has a cylindrical shape and is about 40 – 50 cm wide in cross-sections perpendicular to the fault zone (dn4-se04, se05 and se06; Figure 2.13 d, e and f). The bottom 30 cm of the channel is covered with loose, massive clast-supported pebbly sand and granules. Above these deposits, a nearly horizontal contact, marked sometimes with a thin layer of well-sorted granules to medium sand (Figure 2.11e), suggests that the horizon of channel abandonment, because the deposits above the horizon consist of massive colluvium, devoid of any signs of running water.

Exposures of channel c2 also reveal the fault zone structure. This is one of the few places in our excavation where both trench orientation and channel stratigraphy are optimal for us to observe faults in cross-section. Three major faults 0.5 m apart appear in exposures se04 and se05 (Figure 2.11 e and f). Between fault strands Fault 4 and Fault 5, a couple of minor faults cut the bottom of channel c2, but with very little offset. They merge with Fault 4 at a position between cuts se07 and se08 (Figure 2.11b).

We cannot trace channel c2 southeast beyond exposure se08. It is very likely that the channel has been cut off by multiple fault strands there. On the northwest end of channel segment c2, its piercing point with Fault 5 was unfortunately destroyed when we knocked down the slice from ne09 and ne10, because the location of Fault 5 is between the two parallel cuts. However, Fault 5 is probably close to the position of ne10, judging from the field observations in the notch cut that slices along the thalweg of channel d between exposures ne09 and ne10. The strata in channel d were observed to be continuous yet diminished against wall ne10.

We consider that c1 correlates with channel c2. Together, they constitute a single right-deflecting channel that postdates channel d. Our correlation is based on their lithologic similarity, their stratigraphic position and the similar elevations of their upper and lower contacts. Other evidence includes: 1) the similar thicknesses of the deposits; 2) the arrangement of and imbrications in the pebbly gravels in c1 are consistent with a right-curving channel course (Figure 2. 11h), as indicated by its thalweg (Figure 2.11b); and 3) it is consistent with the asymmetric widening of channel d on the right.

Could the fault-bounded segment c2 be a piece much older than c1, and lag behind due to differential motion along multiple fault strands? In other words, are we correlating pieces of

different ages? We think this possibility is very remote. First of all, the shape of channel and deposits within c2 are still coherent, which suggests a relatively young age. Secondly, as will be shown later, the older channels lying to the northwest do not appear to be better candidates than c1 to be the downstream correlative of c2.

In support of this correlation, it is worth reiterating that channel c merges with d right after it departs the fault zone. This proximity of the right deflection of channel c to the fault zone suggests that when channel c was incised, channel d was nearly connected with its former upstream segment. Perhaps, the rupture that immediately post-dated formation of channel d offset the channel only a small amount, enabling a new channel-c connection to form between the upstream and downstream channels. If, for example, the offset were merely half the width of the channel, it would be relatively easy for water in the upstream channel find its way into the slightly offset downstream channel and to erode that portion of the fault zone between the channels. However, if the offset of channel d were much larger than the width of the channel, the connection would be more difficult to re-establish.

### **2.3.2.5 Channels e, f, g and h**

The excavation of volume dn3 revealed four channels that fan out upstream toward the fault zone, about 30 to 36 m northwest of the mouth of Channel B (Figure 2.3 and 2.14a). We have designated these channels e, f, g, and h. Channels f and g trend roughly at right angles to the fault, whereas channels e and h display left-lateral and right-lateral bends, respectively (Figure 2.14). All four channels merge into a single channel 6 to 7 m downstream from the fault.

#### **Channel morphology and stratigraphy**

The largest of the channels in the excavated volume dn3 is channel f. It is the deepest and widest of the four channels (Figure 2.14c). Its thalweg is about 1.1 m beneath the ground surface in exposure dn3-ne10, which is barely 20 cm downstream from Fault 5, and 0.95 m below the ground surface in the most distal exposure, ne00 (Figure 2.15). Its cross-sectional shape deviates only moderately from a flat-bottomed, U-shaped profile. Locally, it has a secondary thalweg to the southeast, most likely the remnant of an earlier phase of down-cutting. Within the channel, three well-sorted clast-supported sand and gravel beds continue from one exposure to

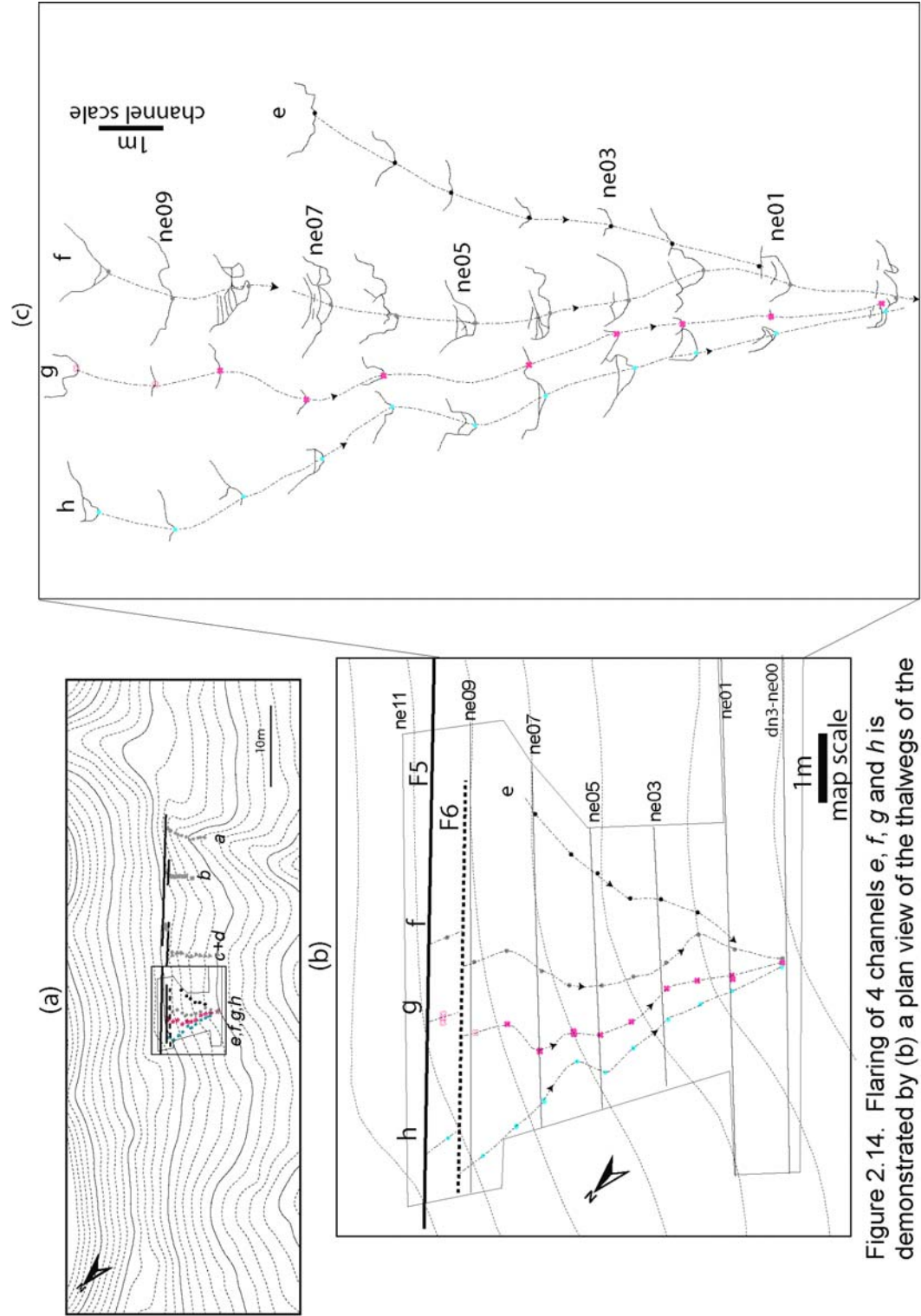
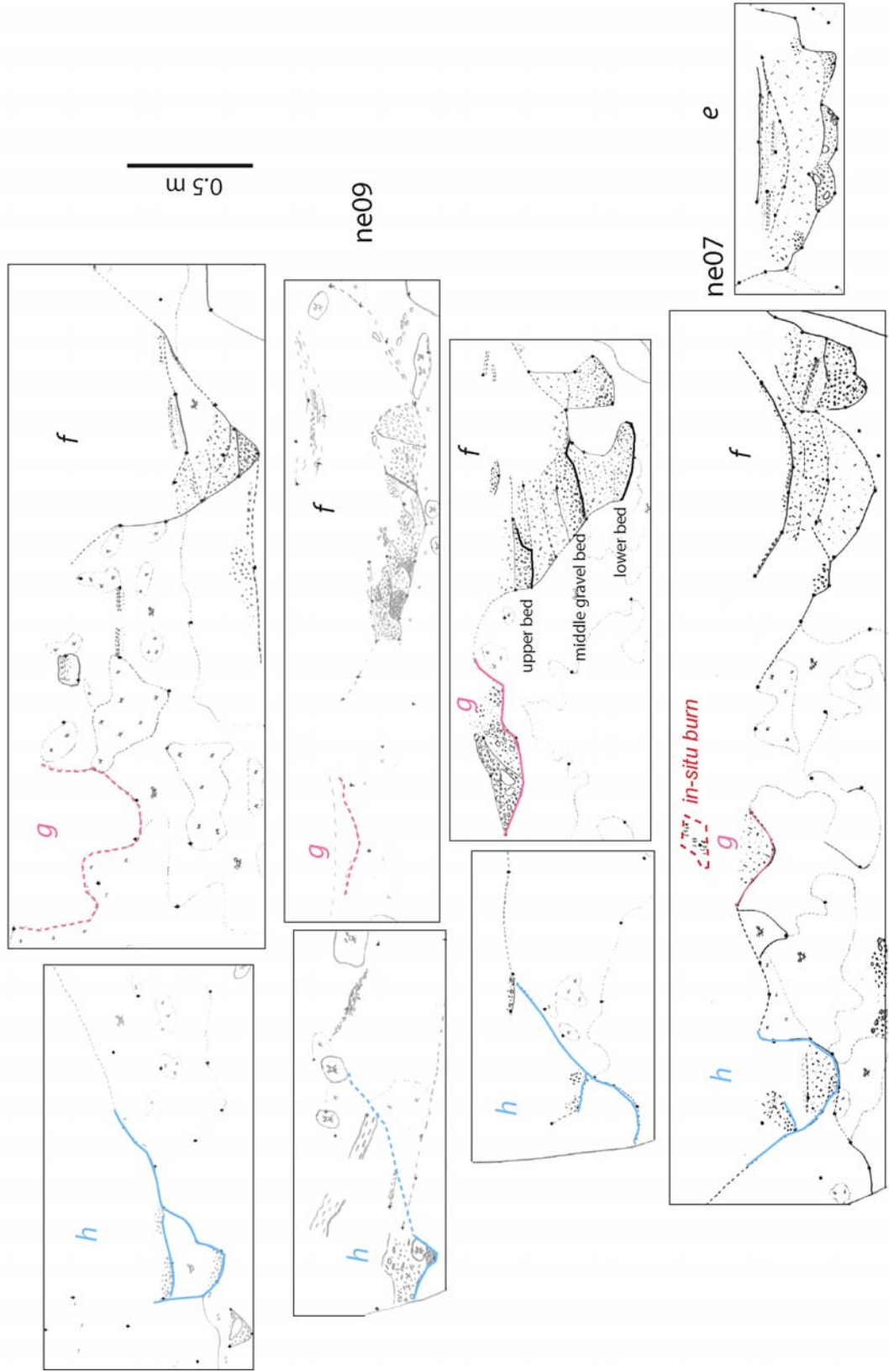


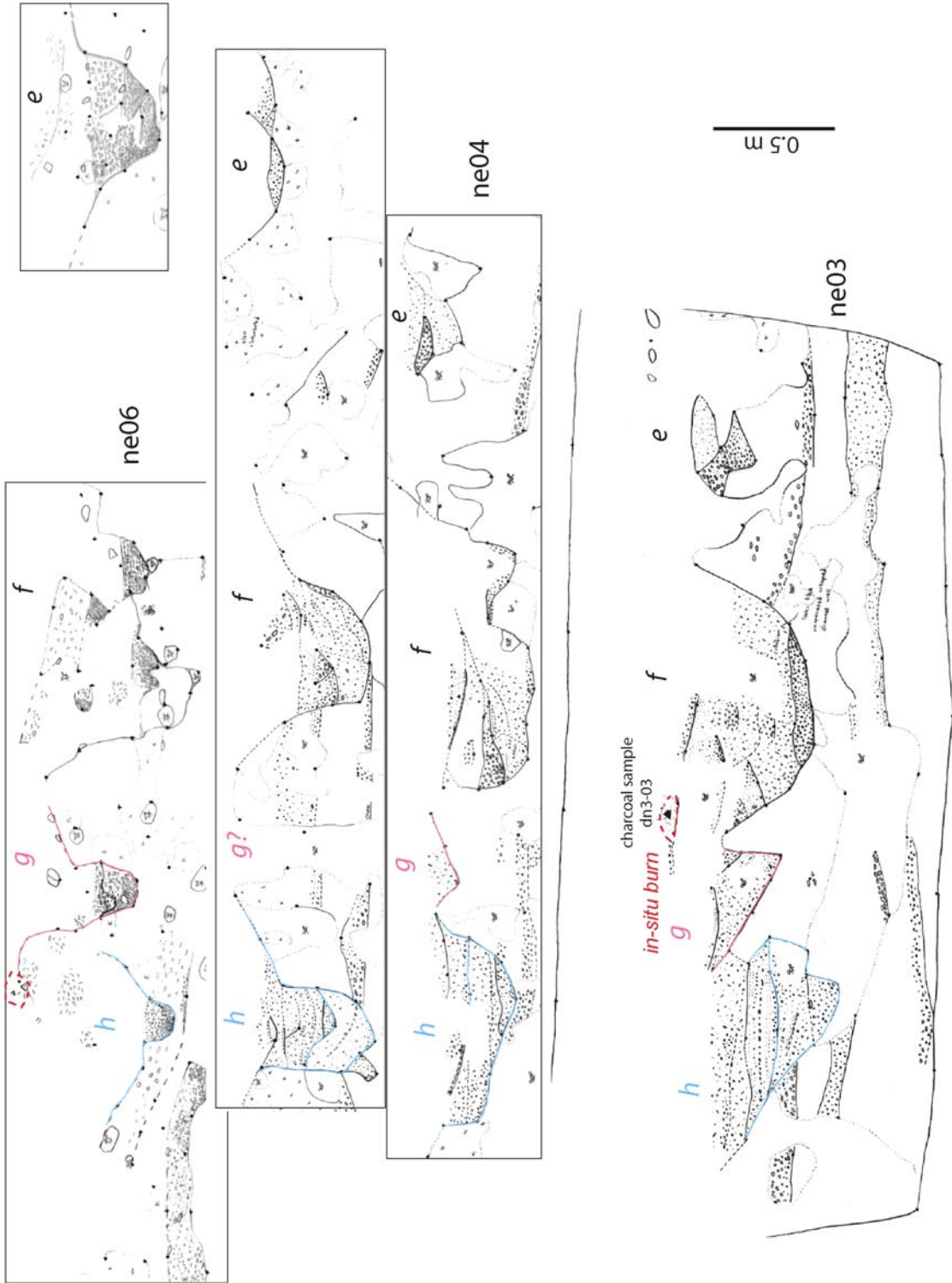
Figure 2.14. Flaring of 4 channels e, f, g and h is demonstrated by (b) a plan view of the thalwegs of the channels and (c) cross-sectional views. Locations of the four channels are shown in (a).

another (i.e., marked in exposure ne08). The well-sorted fluvial sediments at the bottom of channel  $\underline{f}$  are prominent and continuous; the middle bed is best exposed in ne02, where it splits into two small bowl-shaped channels side by side. Here these two small channels are almost outside channel  $\underline{f}$ , and appear to go straight downstream as the lower portion of channel  $\underline{f}$  curves to the southeast (Figure 2.14c). The upper lens of fluvial sediments is the least recognizable of the three. It is best expressed in exposure ne08, where it is 8 cm thick and 50 cm above the channel thalweg.

Channel  $\underline{h}$ , another deep channel, has variable cross-sectional shape and stratigraphy. The strata within the channel are very well defined in exposures ne01 through ne05 (Figure 2.15), characterized by two clast-supported sand and gravel layers in the lowest 40 cm of the channel. The bottom layer comprises massive coarse-grained and moderately sorted sediments, with cobbles up to 10 cm in diameter in ne01. The upper layer is finer-grained; best exposed in ne03. It is 12 cm-thick, well-bedded and consisted of well-sorted gravels and sand, separated by 25-cm-thick colluvium above the bottom layer. In other exposures, especially those close to the fault zone, channel  $\underline{h}$  is nearly devoid of well-sorted sand and gravel deposits, and is, instead, completely filled with poorly sorted, massive colluvium derived from the channel walls. The highly irregular thickness of these sorted and coarse-grained sediments is good indication of migrating sand waves. The two sand and gravel layers that are so well defined in downstream exposures are instead barely indicated by locally higher content of coarse sand than the surrounding colluvium. Nonetheless, even in these exposures the two layers have the consistent 25 cm separation in elevation.

The cross-sectional shape of channel  $\underline{h}$  changes dramatically from cut to cut. For instance, it is 35 cm wide in ne05, but its width is twice this value in ne04, just 65 cm farther downstream. Note that in exposures ne08 through ne10, which are immediately proximal to the fault zone, channel  $\underline{h}$  has a steep northern bank and reclining southern bank. The asymmetry in channel shape suggests that channel  $\underline{h}$  makes a sharp turn to the southwest as it departs the fault zone. Such a turn would be consistent with the trace of its thalweg indicated by the plot of thalwegs in map view. This geometry downstream from the fault suggests that the upstream correlative of channel  $\underline{h}$  should bend to the right as it approaches the fault zone from upstream.





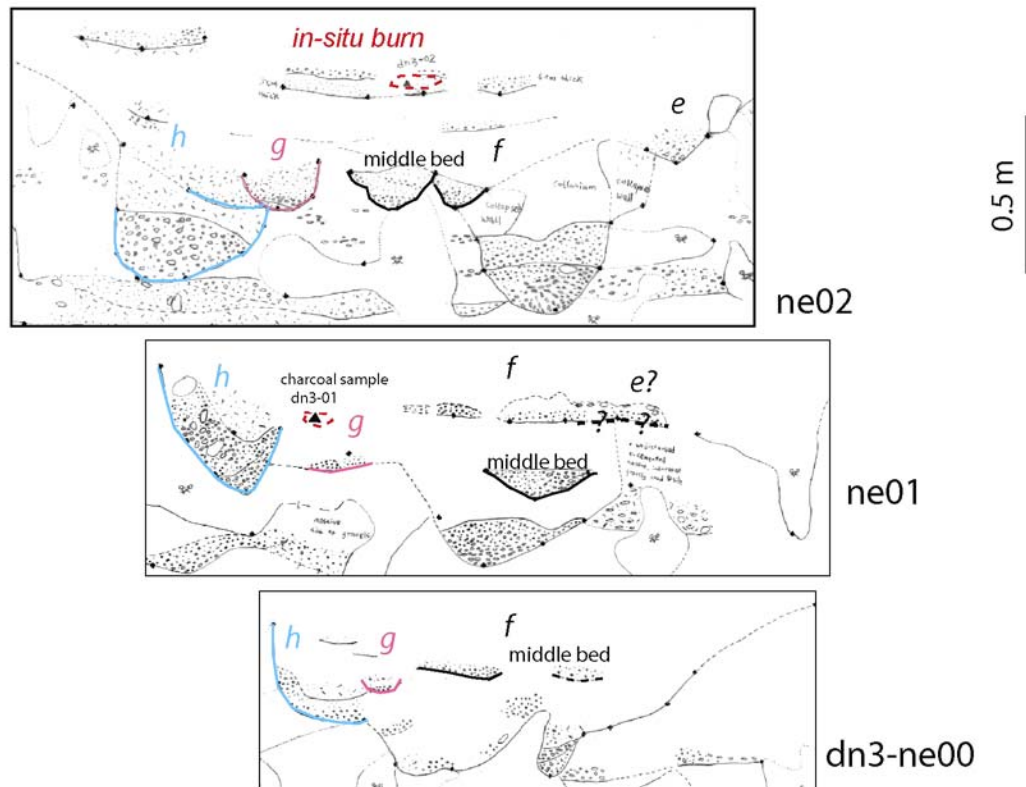


Figure 2.15. Maps of channels *e* through *h* in all 10 exposures. The name of each exposure indicates the sequence and direction in which it was cut. Only those portions of a mapped exposure that contain the main body of channels are shown.

Channel *g* is a shallow, less conspicuous channel between channels *f* and *h*. In cross-sections, its thalweg is 75 to 90 cm below the ground surface. Channel *g* is narrow and contains channel sand and gravels of varying thickness at near its base. It does not have any distinctive well-sorted coarse-grained layers in exposures ne09 and ne10, and is barely recognizable by slight color contrast between channel-filling colluvium and bioturbated alluvium. Hence, the positions of channel *g* in these two exposures are conjectural. However, channel *g* has one common and distinctive feature where well exposed. We found an in-situ burn and disseminated charcoal grains at depths of 35 – 60 cm below surface, throughout the excavation of trench dn3. They are all in the vicinity of channel *g*; either in the colluvium directly above the channel (ne07,

ne01, Figure 2.15), or at the upper left or right corners (ne06, ne03, ne02 in Figure 2.15). The burn is in-situ and very likely occurred shortly after channel *g* was abandoned. A dated sample from this burn horizon provides a minimum age for channel *g*.

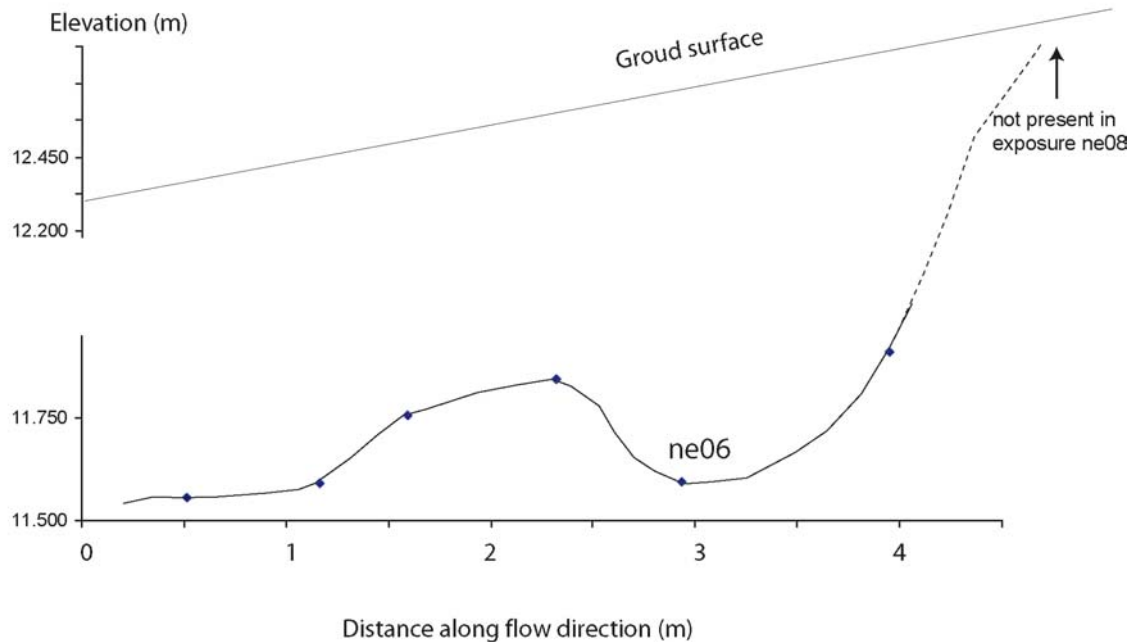


Figure 2.16. Longitudinal profile of the thalweg of channel *e*. The hollow in the profile near exposure ne06 suggests that channel *e* was eroding a plunge pool at this location and may not have eroded headward across the fault. If it is true, this channel can not be used as an offset piercing line.

Channel *e* lies southeast of channel *f* and is also shallow. Its thalweg is 65 – 75 cm beneath the ground surface. The width and grain sizes of channel *e* diminish downstream between exposures ne07 and ne02 (Figure 2.15) Channel *e* also converges downstream toward channel *f*. Whereas channel *e* is still recognizable in exposure ne02 as a 10 cm-thick lens lying about 40 cm to the right of *f*, it seems to disappear downstream in ne01 and ne00 (Figure 2.15). Channel *e* cannot be traced with confidence either upstream beyond ne07, closer than 2 to 3 m of the fault zone. One possibility is that bioturbation has obliterated the trace of channel *e* near the fault. Although we cannot rule out this possibility, it seems unlikely as no other channels, including

much older ones, have been completely erased by bioturbation. Another possibility is that the headward limit of channel  $e$  is near exposure ne07 and that the channel was formed by headward erosion and that the channel did not reach or cross the fault zone. The longitudinal profile of channel  $e$  supports this hypothesis. From exposure ne07 to ne06, the profile exhibits a sharp drop in elevation (Figure 2.16) and the width of the channel narrows, (Figure 2.15). Thus, ne07 may be within the knick-point of channel  $e$ .

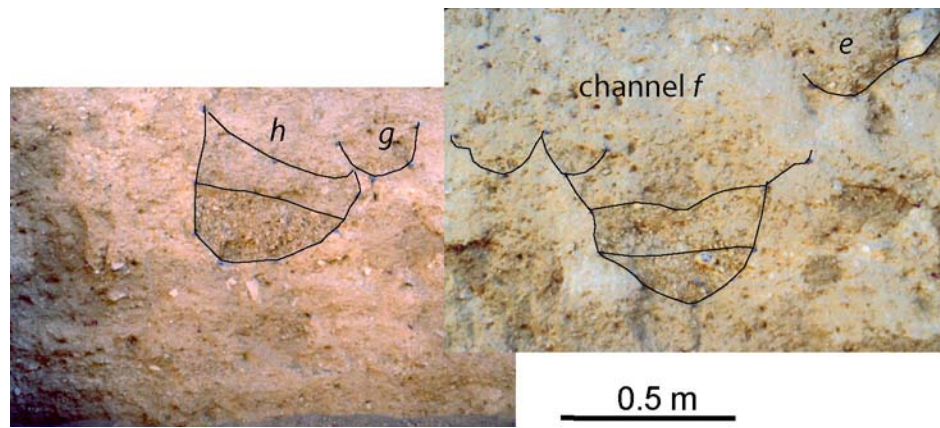


Figure 2.17. Photographs of exposure dn3-ne02 show the cross-cutting relationships between channels  $e$  and  $f$ , and channels  $g$  and  $h$ .

### Relative ages of channels

The history of channels  $e$ ,  $f$ ,  $g$  and  $h$  present a challenge to unravel. Of the four channels, channel  $f$  occurs in the middle and perpendicular to the fault, flanked by channels  $h$  and  $e$  from left and right, respectively (Figure 2.14c). Channel  $g$ , also straight from the fault, is shallower, and as will be demonstrated below is stratigraphically younger than  $h$ . To us, traces of thalwegs alone suggest a scenario that channel  $f$  is the oldest of the four channels. Channels  $g$  and  $h$  are younger than  $f$  even though they appear to be offset more than  $f$  from source  $B$ . If this is true, then channel  $f$  must have come from a source southeast of  $B$ . The rationale behind the above speculation is that the upstream channels in this stretch of the San Andreas fault meet the fault almost orthogonally. This implies that downstream channels should also depart the fault perpendicularly, unless the microtopography near the fault, for example, an older downstream

channel in close vicinity, favors a deflected channel course, e.g., channel h. Such a scenario of channel f from far southeast of h is quite possible, since a couple of upstream channels southeast of h are capable of incising moderately deep channels (Figure 2.1b), whose downstream segments could move in juxtaposition to h due to continuous dextral slip along the fault.

The stratigraphic cutting relationship provides independent and more reliable information on the relative ages of channels. Figure 2.14c shows an array of simplified cross-sectional views of the channels that converge downstream. Of all the exposures, dn3-ne02 and ne00 are the two most important ones. Exposed in dn3-ne02, channel g cuts the upper right corner of h, thus is younger (Figure 2.17). Likewise, channel e is younger than f. In ne02, the relative age of channels f and h is unclear, as they are still meters apart shoulder to shoulder. However, channels f and h come into contact in ne00. At this point, channels become smaller and stratigraphically less recognizable; channel e cannot even be identified. In exposure ne00, channel f occupies the major portion of the composite channel, while channel h perches on the northern side. Their relative positions suggest that channel h cuts channel f, thus is younger. Although it could be argued the other way as the stratigraphy is slightly ambiguous, this interpretation is favored. Besides, this interpretation would be consistent with the above inferences based on the pattern of the thalweg configuration. The correlation of channels f and h from one exposure to the next is based on the continuity in stratigraphic sequence (the comparison of trench logs of ne02, ne01 and ne00 in Figure 2.15). Under the correlation, the small channel that cuts h at the upper right corner is probably channel g, and it is also younger than f as it overlies f. In summary, we argue that the stratigraphic relationships favor the interpretation that channel f is older than channel h, which is in turn older than channel g.

One important conclusion that follows from this interpretation of the stratigraphic relationships is that channel f does not share the same source with h. If channel f is indeed older than channel h, it would have already existed southeast of h when h was cut straight across the fault from its upstream equivalent. A similar argument applies to channel g. When g was cut immediately downstream from its upstream correlative, channel f would already have existed meters or so to the southeast. Thus it appears that at least two upstream drainages are involved in the creation of this cluster of channels.

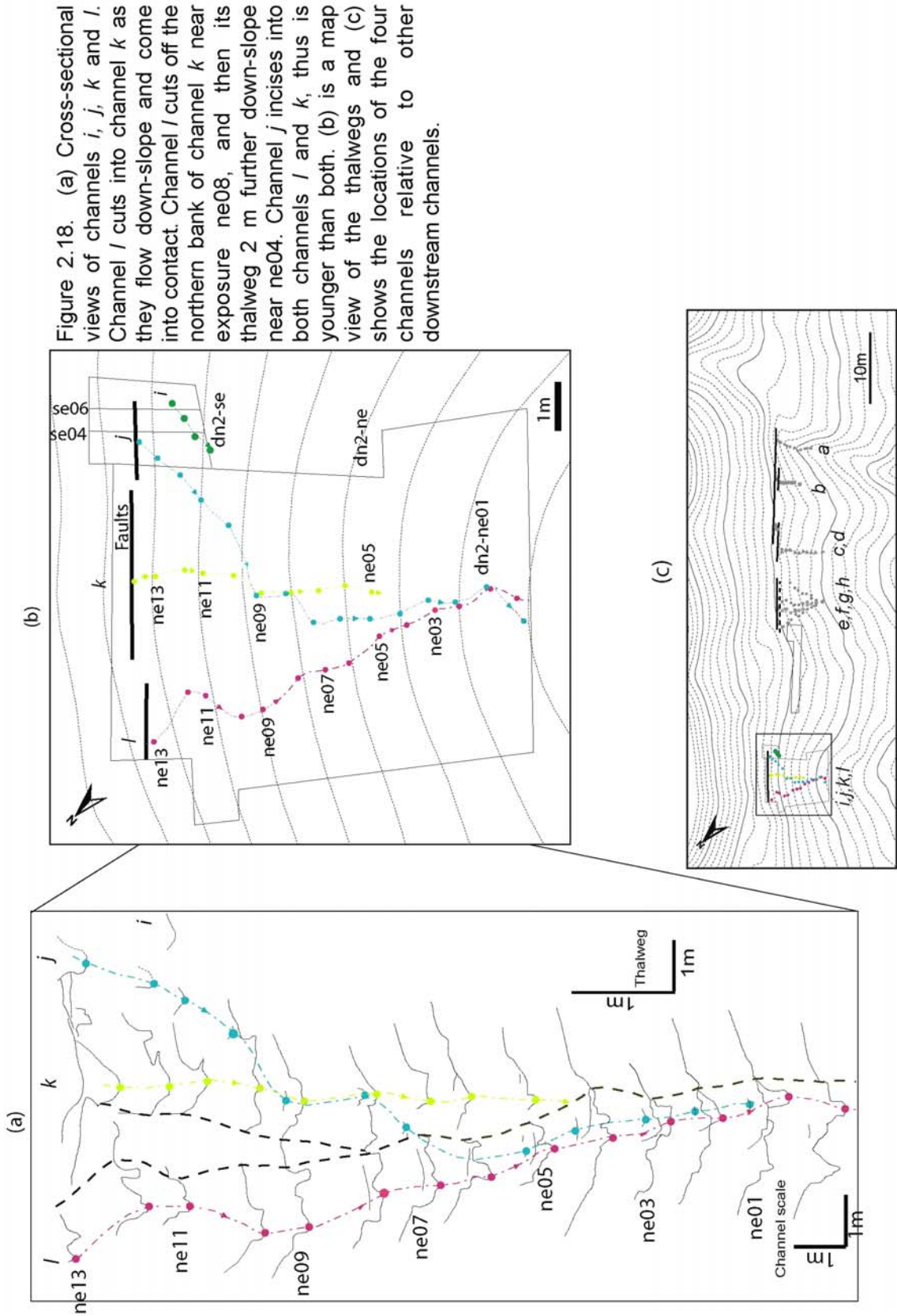
The age of channel e relative to the ages of channels f and g is indeterminate. Stratigraphic relationships show only that e is younger than f. We will see in the next chapter that this creates an ambiguity in reconstruction of the fault's slip history.

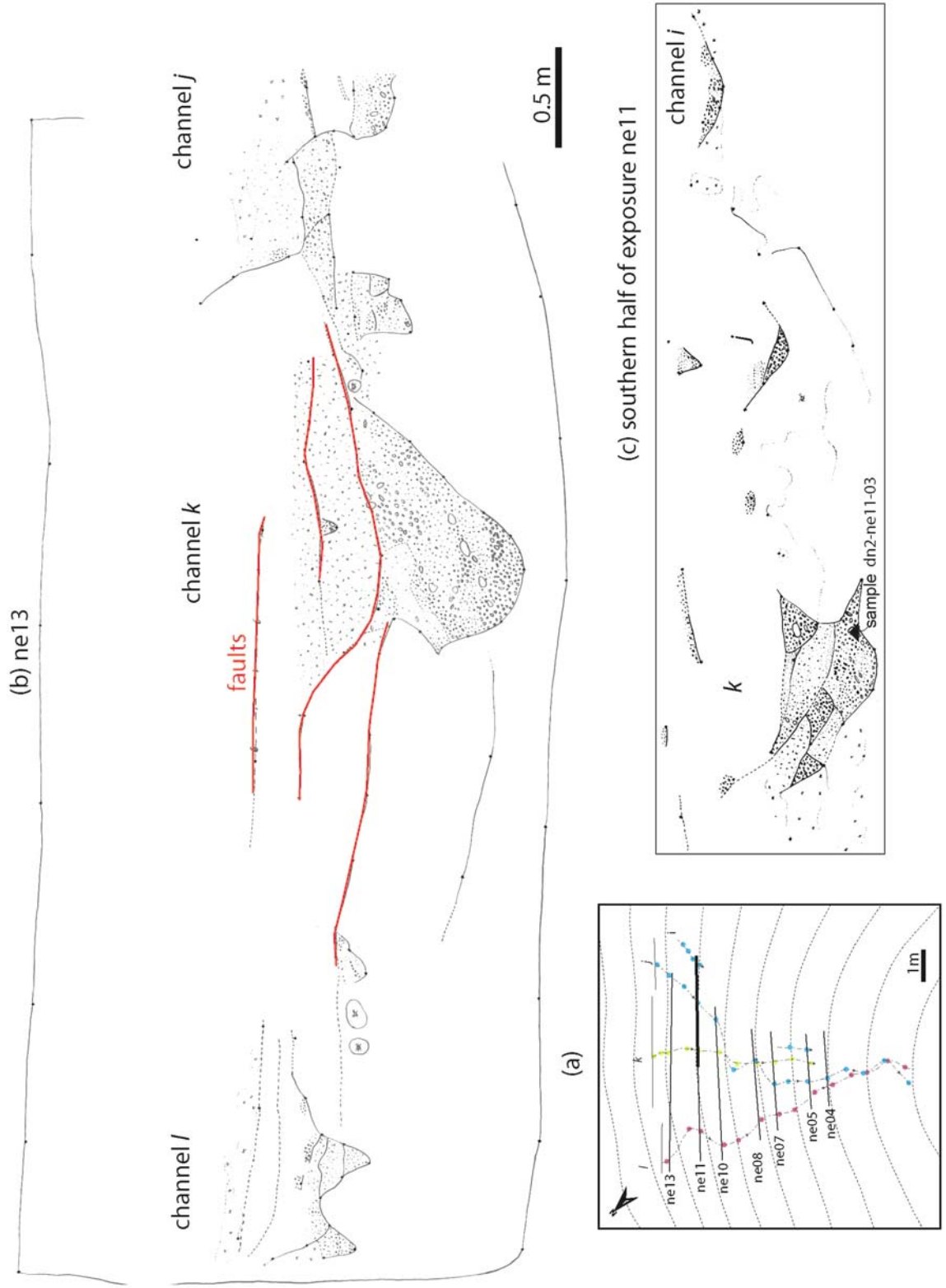
The strata in channels f, g and h are truncated at roughly the same position from the center of the fault zone. Since this fault lines up in strike with Fault 5 in the excavation volumes to the southeast, we consider them the same fault. We suspect there is a secondary Fault 6 lying south of Fault 5, although we did not recognize during the excavation process.

Fault 5 was observed in the fault-normal notch cut during the excavation from exposure ne10 to ne11; channel f is truncated by Fault 5 nearly half way between ne10 and ne11. Fault 6 was not directly observed in the field. But we noticed that the strata were not continuous from exposure ne09 to ne10. We suspected a fault between ne09 to ne10, however, we could not rule out the possibility that the stratigraphy was simply poor. Later mapping seems to support faulting hypothesis: the shapes of channel f, g and h in exposure ne09 are distorted probably due to shearing (Figure 2.15). In particular, the strata in channel f in ne09 are laid out horizontally, possibly due to near-fault collapse. The thalwegs of channel f, g, and h further suggest the existence of Fault 6, because the thalwegs of all three channels in exposure ne10 shift systematically to the right from those in exposure ne09.

#### **2.3.2.6 Channels i, j, k, and l**

Another group of 4 channels exists still farther northwest of the mouth of source channel b (Figure 2.18c). The excavation of volume dn2 revealed the geometry and stratigraphy of these channels (Figure 2.3a). Channel k is the largest and deepest channel in the volume and intersects the fault at nearly a right angle, near the center of the topographically expressed channel swale (Figure 2.18 b and c). Channels i and j flank this central channel on the southeast and intersect or approach the fault at acute angles. Channel l flanks central channel k on the northwest. It also intersects the fault at an acute angle. All of these flanking channels converge on channel k several meters downstream from the fault. An unnamed trench cut parallel to the fault confirms that no channels exist downstream from the fault between this group of four channels and channel h to the southeast (Figure 2.3a).





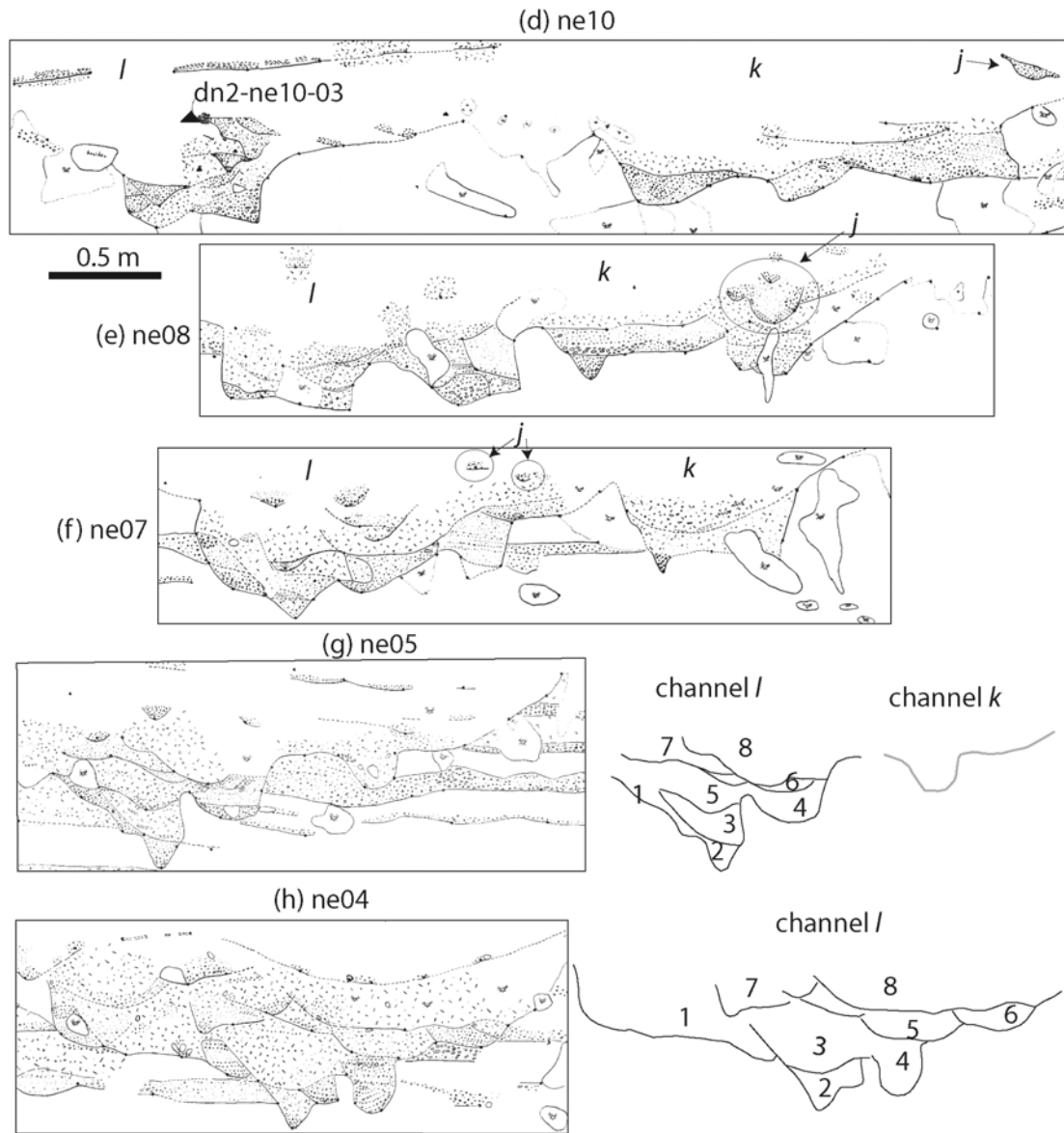


Figure 2.19. Selected portions of the logs showing the stratigraphy, cross-sectional morphology and the cutting relationships of channels i, j, k and l in various exposures in trench dn2. (a) indicates the locations of exposures in a map view. The top line in (b) exposure ne13 represent the present ground surface. Panels g and h show the maps (left) and interpretations (right) of the channel stratigraphy. Channel k and channel l are both present in exposure ne05, but only channel l is in ne04, probably because channel k was eroded away by channel l. Numbers in the interpretations denote individual beds in channel l to indicate the continuation of stratigraphy.

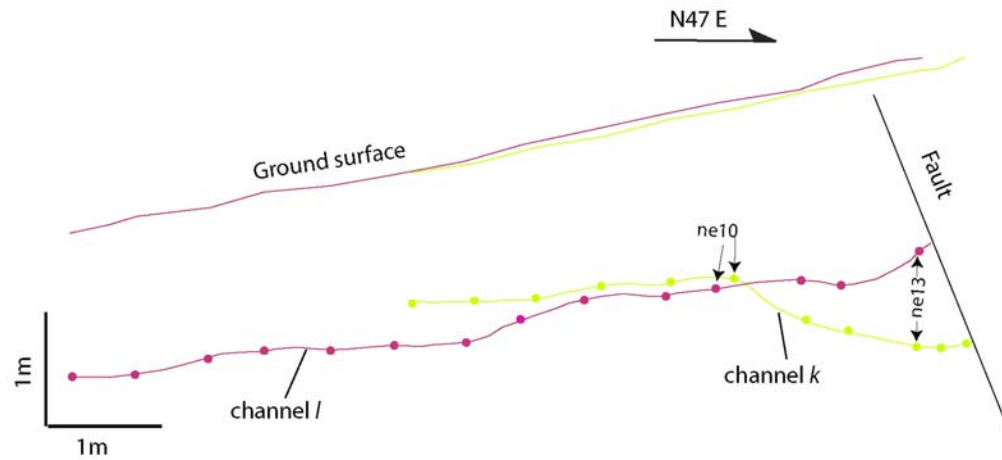
**Channel  $k$** 

Figure 2.20. Longitudinal profiles of the thalwegs of channels  $k$  and  $l$ .

The thalweg of channel  $k$  is nearly straight and diverges almost orthogonally from the fault zone. It is one of the deepest downstream thalwegs at the site -- about 2.45 m beneath ground surface at its intersection with the fault (Figure 2.19b). The thalweg at the fault appears to be in a scour pool, since it rises downstream about a meter as it diverges from the fault (Figure 2.20). The scour pool is filled by a 75-cm-thick bed of loose cobbly, pebbly gravel. The high degree of sorting of this bed indicates that it is fluvial, and its structure suggests it was deposited as bedload rather than as debris flow. The channel shallows and widens appreciably downstream (Cf. Cuts ne10 and ne08; Figure 2.19 d and e), then narrows again (Cf. Cut ne07; Figure 2.19f). Despite large variations in the details of channel shape and fill, channel  $k$  is still easily correlated from ne13 to ne08, because another deep channel  $l$  is still meters away on the left (Figure 2.18a), and because the fills of channel  $k$  are characteristic. The deposit mainly consists of a multi-layered basal gravel bed and overlying thick massive, poorly sorted finer sediment, which appears to be colluvial infill from the channel walls (Figure 2.19 b and c). The variations in channel infill occur in a systematic way, i.e., the thickness and grain size of the basal gravel deposit decrease

downstream as the channel fill is increasingly dominated by colluvium. Channel “k” disappears between cuts ne05 it is cut off by channel l (Figure 2.18a)

### **Channel l**

The thalweg of channel l exits the fault zone at an acute angle and snakes a path downstream (Figure 2.18a). The gradient of its longitudinal profile is about 8.8° (Figure 2.19). Excavation reveals that channel l has an irregular channel floor, with multiple thalwegs, separated by lateral ridges (Figures 2.18a and 2.19 e, g, and h). Its fill consists of at least 8 cut-and-fill sequences. However, these gravelly lenses are rarely continuous enough for us to trace them from cut to cut.

### **Relative age of channels k and l**

The configurations of channels k and l suggest that k is older than l. Channel k leaves the fault at nearly a right angle and continues downstream in a nearly straight path. Furthermore, the channel thalweg runs immediately below the lowest point in the topographically visible channel (Figure 2.18c). This suggests that it is related to the cutting of the channel that is still visible topographically and was not diverted into a pre-existing channel. Channel l, by contrast, flows in the center of the topographic channel only in its lower reaches and enters the topographic channel from a position well up on the northwestern flank of the topographic channel. This suggests that it was diverted left-laterally into the channel. Thus, an analysis of channel geometries, alone, suggests that channel k antedates channel l.

Our exposures of stratigraphic relationships in volume dn2 confirm this relationship. Figure 2.18a shows their cross-cutting relationship. Channel l truncates the northern bank of channel k in exposure ne08 and its thalweg a few meters farther downstream, between ne05 and ne04. Downstream from ne04, channel k is completely absent, having been completely obliterated by channel l. Figure 2.19g shows that channels k and l are both present in exposure ne05. But only one of the two channels appears in ne04 (Figure 2.19h). The continuation of sedimentary structures from ne05 to ne04 suggests that the channel in ne04 is l. Thus, channel k was re-occupied and erased by the younger channel l at this juncture.

### **Channel *j***

Channel *j* intersects the fault zone at a 45 degree angle (Figure 2.18b). It flows westward, away from the fault zone and merges with channel *l* about 7 m downstream. The channel is particularly deep and well-expressed within a few tens of centimeters from the fault (Figure 2.19b), but is typically marked solely by a thin lens of fine sandy gravel. In exposure ne11, this gravel lens is a 50-cm-wide, less than 30-cm-thick lens of sand and fine gravel, with a prominent basal contact (Figure 2.19c). Farther downstream, channel *j* cuts into the upper colluvial fill of channel *k* (exposures ne10 and ne08 in Figure 2.19 d and e).

Two lines of evidence indicate that channel *j* continues northwestward over channel *k* and then merges with channel *l*. First there is no continuation of the prominent channel *j* above channel *k* farther downstream. Instead, two small channels, separated by 30 cm, show up for the first time at the upper right corner of channel *l* in ne07 (labeled *j* in Figure 2.19f). These occur at the same stratigraphic position in cuts farther downstream. These small channels overlying channel *l* appear to be the downstream continuation of channel *j*.

This correlation implies that channel *j* is younger than both channels *k* and *l*. Furthermore, the time between formation of channels *l* and *j* may be relatively short. This is suggested by the fact that the colluvium between the channel deposits is relatively thin. In exposure ne07 it is a mere 10 cm thick, whereas the colluvial mantle over both channels elsewhere is about 80 cm thick. If the thinness of colluvium between the two channels is indicative of the time that elapsed between their formations, then channel *j* was incised shortly after the abandonment of channel *l*, when *l* was still fresh enough to control the topography.

### **Channel *i***

Channel *i* lies just a meter or so south of and runs almost parallel to channel *j*. The course of the channel is well-defined by 4 cuts, but its long-profile is a mere long. In the southernmost exposure of *i* (ne11) channel *i* is a 60 cm-wide lens of sand and fine gravel (Figure 2.19c). Further downstream, channel *i* is not visible, probably due to a lack of coarse fluvial channel fill. In its furthest exposure upstream (se06), channel *i* is barely visible as a 8-cm-thick

lens of fine gravel and coarse sand. At this point, it is still about 50 cm downstream from the fault zone (Figure 2.18b). The projection of the trend of channel  $\underline{i}$  intersects the fault zone 0.8 m southeast of the limit of the excavated volume.

The relative age of channels  $\underline{i}$  and  $\underline{j}$  is indeterminate, because no direct cross-cutting relationship was exposed.

### **2.3.3 Upstream channels**

#### **2.3.3.1 General**

The subsurface stratigraphy of the outlet of drainage  $\underline{B}$ , just upstream from the San Andreas fault, differs greatly from the subsurface stratigraphy we have just described downstream. We have shown that downstream from the fault are 12 separate channels, a through  $\underline{L}$ , strung out along a 55-m length of the fault. In contrast, the excavated volume just upstream from the fault contains 9 nested channels, which represent repeated cutting and filling in roughly the same place, the outlet of drainage  $\underline{B}$ . In this section we describe in some detail the stratigraphy of these channels and their relationships to one another.

Figure 2.21 illustrates the basic nature of the nested upstream channels. It is a map of exposure up-sw06, the sixth in the sequence of cuts into the southwest side of the volume labeled “up” in Figure 2.3a. This exposure is 1.4 – 1.6 m upstream of the main fault zone and the view is from the fault looking upstream. Eight of the 9 upstream channels are visible in this cut.

The base of the deposit containing these young channel deposits is easy to recognize, because the underlying late Pleistocene deposits are massive and featureless fine-grained sand and silt with sparse gravel lenses. Bioturbation has homogenized the late Pleistocene substrate, and pedogenic carbonate precipitation has given it a pale hue and induration that contrasts sharply with the richer shades and looser consolidation of the recent channel deposits. In general, the boundaries of individual channels are also easy to recognize. Commonly, the lower parts of the

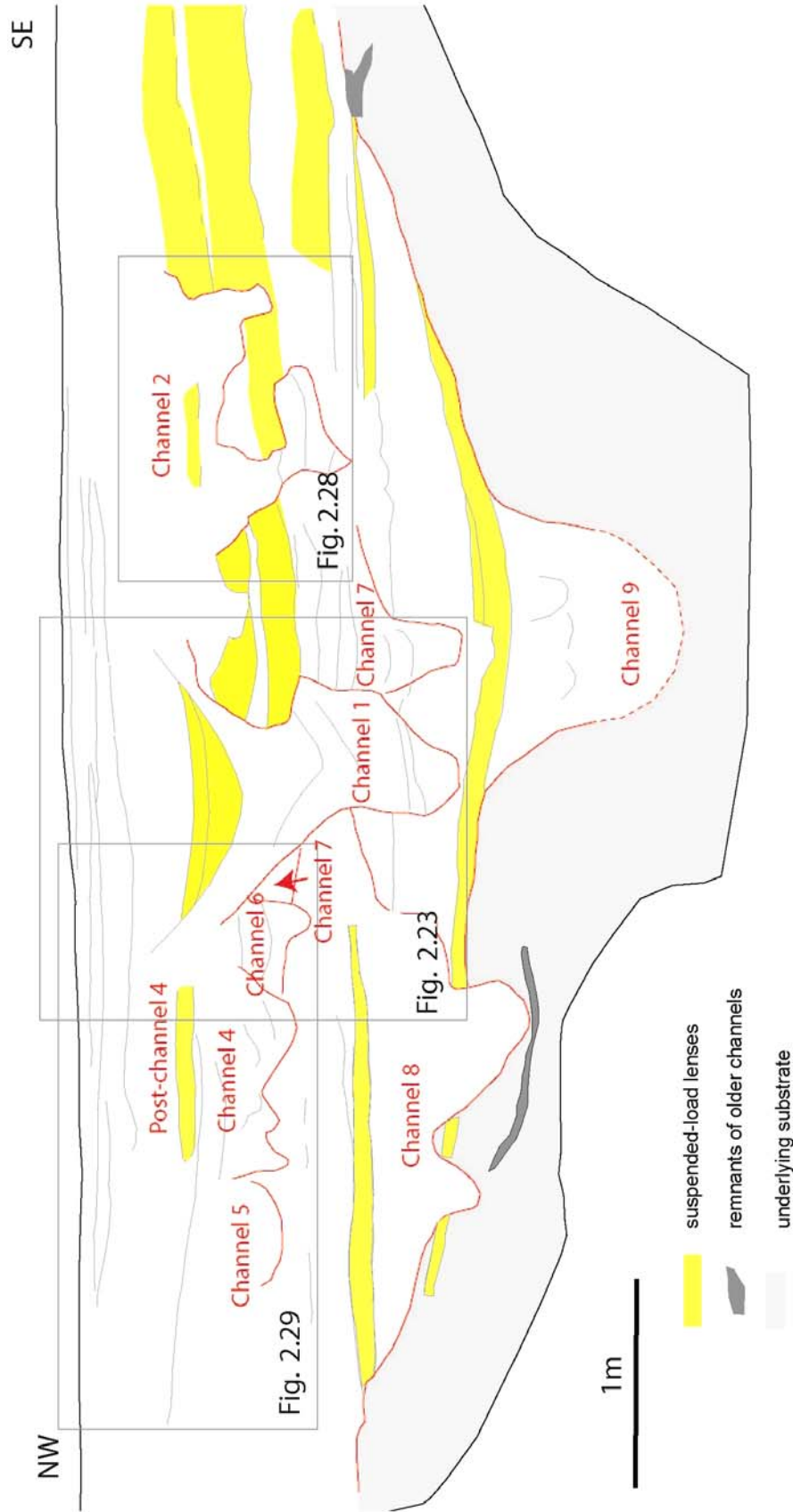


Figure 2.21. Simplified map of nested channels near the mouth of source channel upstream from the fault. Suspended-load lenses, which have been deposited behind shutter ridges, are highlighted in yellow.

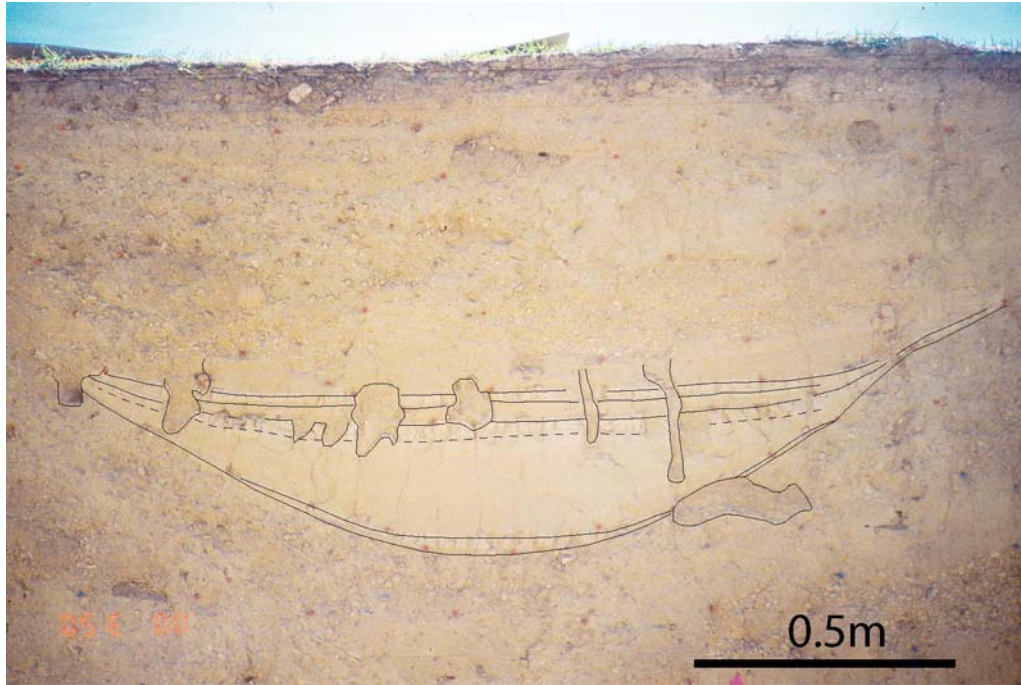


Figure 2.22. A photograph of the suspended-load lens in channel 1. Note that the lens has a gently curved top and deeply curved base and consists of 5 individual lenses. Each of the lenses is thickest in the middle and thin to feather edges toward their margins. The lenses consist of fines deposited out of suspension in a muddy puddle just upstream from the fault and straddling the middle of the channel. Look direction is upstream.

channels are filled with well-sorted, well-bedded fluvial sand and gravels. Thus, the lower portions of the channel walls are clearly visible, because the fluvial channel fill contrasts sharply with fluvial channel fill of adjacent channels or massive, poorly sorted colluvial fill on the other side of the channel wall. The upper portion of individual channel fill typically is poorly sorted massive sand, silt and gravel -- colluvial debris derived from erosion of adjacent channel walls.

A prominent feature of many of the channels is a distinctive lens of well-sorted fine sand to silt. These beds are highlighted in yellow in Figure 2.21. Such beds are absent from any of the downstream channels. Figure 2.22 is a photograph of one of the lenses. The lenses consist of fines deposited out of suspension in a muddy puddle just upstream from the fault and straddling the middle of the channel. They appear to be the result of blockage of the channel by a shutter ridge,

emplaced by large dextral offset along the fault. If this is correct, the silty lenses are direct evidence of occasional large ruptures of the fault.

Cross-cutting relationships among the channels reveal the sequence of their formation. We indicate the sequence by numbering the channels from 1 to 9, from the youngest to oldest. We know that channel 1 is the youngest, because its walls cut channels 4, 6, 7 and 8 on the northwest and channels 7 and 2 on the southeast (Figure 2.21). Some of these relationships are ambiguous in Figure 2.21, but are more clear in other exposures.

We know the relative age of channel 4, because its walls cut those of its neighbors, channels 5 and 6. Likewise, channel 6 cuts the upper left of channel 7. We know this patch is part of channel 7, because its stratigraphy matches that of channel 7 on the other side of channel 1. It is clear in Figure 2.21 that channel 9 is older than both channel 8 and channel 7. Channel 8 is older than channel 7 because it is overlain by a patch of channel 7 on the upper right.

The relationship between channels 2 and 4 is ambiguous in Figure 2.21, because the two channels have no direct contact. Likewise, the relationship between channels 5 and 6 is obscured by channel 4. In these cases, we use other evidence to determine relative ages. We develop this evidence in the following sections.

### **2.3.3.2 Channel 1**

Channel 1 sits in the middle of the exposures (Figure 2.21). About 1.8 m deep, it is deeper than channels 2, 3, 4, 5 and 6 in the upper level of the exposures.

The stratigraphy is well preserved. Figure 2.23 illustrates the stratigraphy of channel 1, with the log of exposure sw06 on the right and its interpretation on the left

Basal unit 10 is an indurated, matrix-supported deposit, composed of gray to dark gray poorly sorted gravelly sand and silt. But locally, it has sub-horizontal laminae of well-sorted silt, and well-sorted granule sand. The degree of sorting and form of this unit indicates that it is a fluvial deposit.

Overlying unit 12 consists of discontinuous laminae of well-sorted fine sand to silt. The degree of sorting and the fine grain size indicates that unit 12 is also fluvial origin, but represents a reduced speed of water current. Perhaps, unit 12 and underlying 10 represent deposits of a

single storm, in that unit 10 were deposited at the high peak of the storm, and unit 20 at the waning period of the same storm.

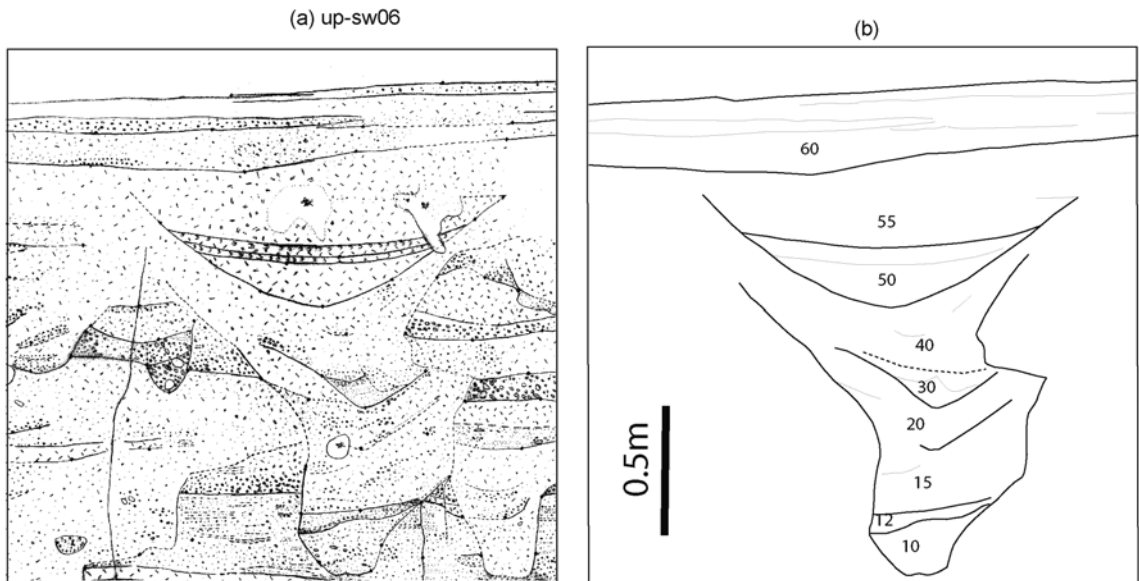


Figure 2.23. Stratigraphic units of channel 1, illustrated using exposure up-sw06. The left panel is the map of the channel stratigraphy; the right panel shows the general groupings within the channel.

Unit 15, which is a 20- to 30-cm-thick massive, heterogeneous, silty pebbly sand. Such characteristics are typical of channel deposits derived from adjacent channel walls, that is, colluvium. The sloping upper surface of unit 15 and sloping internal boundaries support this interpretation. Mud-coated and mud-cemented sloping gravel trains also indicate a colluvial origin.

Unit 20 looks similar to 15, except that it has higher content of pebble and granule clasts. The transition from unit 15 to 20 is not obvious in the exposure shown in Figure 2.23, because the composition of unit 20 resembles that of 15.

The contact between unit 30 and 20 is a sharp erosion surface, which is overlain by lens-shaped unit 30 (Figure 2.23). Unit 30 consists of two well-sorted sandy beds which form an inversely graded sequence. The lower bed, composed of laminated fine sand and silt, is finer

grain-sized and better sorted; the upper one is mainly composed of massive to faintly bedded granule-rich coarse and medium sand, interbedded with laminae of fine sand and silt.

Unit 40 is a massive matrix-supported deposit of poorly sorted gravelly sand and silt. The sloping internal boundaries and sloping mud-coated small gravel trains suggest that unit 40 is mostly colluvium;

Unit 50 is a distinctive lens of well-sorted fine sand to silt. The upper sub-layers are even finer grain sized. It is one of those suspended-load lenses that represent behind-the-shutter ridge

The overlying unit 55 is massive matrix-supported and poorly sorted sandy silt, and locally it contains small gravels 3 mm or less in diameter. The indurations, the poor sorting and the lack of fluvial structures indicate that unit 55 is a fine-grained colluvium. The darker color in the upper colluvium suggests paleosols had developed in unit 55.

Unit 60 is multi-layered, consisting of lenses of light yellowish deposits of pebbles to granules above scoured lower boundaries. The degree of sorting of gravels, as well as the scouring marks, clearly indicate that they are fluvial deposits. These fluvial deposits are covered by gray to dark gray loam, the transition is gradational. The gravels-loam sequence will be scoured and overlain by another fluvial bed. Thus the fine-grained loam represents the hiatuses between depositions of the fluvial materials. Consistently, dark soils mm-thick are commonly seen in the upper part of loam.

The stratigraphy of channel 1 correlates well among exposures, but some down slope variations are also evident. Figure 2.24 shows the stratigraphy of 7 other exposures. Major units are numbered accordingly in each exposure.

Unit 30 is lithologically uniform, and easily correlates among exposures. Because it has a sharp lower boundary with a point-sharp lowest point, this contact can be a good offset piercing line.

Unit 40 shows significant yet systematic variations, which may be due to coseismic shaking. Unit 40 is ~15 cm thick in exposure sw05, increases dramatically to ~40 cm in sw07, and more than 60 cm in sw10. The increase is caused by some extra debris. The added material is in chunks, or blocks with a concave lower boundary (i.e., sw07, sw10 sw11; Figure 2.24 d, f and g), and often internally coherent. In addition, the southern channel bank above the elevation of

unit 30 protrudes visibly into the interior of the channel in exposures sw07 (Figure 2.24c) and sw06 (Figure 2.23), appears to be rotated or smeared. Thus, the chunky debris in unit 40 probably represents collapse due to shaking, and we are observing cross-sectional views of a mole-track along the rupture. The lower boundary of the collapse is sharp and continuous through several exposures (i.e., sw07, sw10 and sw11). This lower contact is probably a north-converging thrust interface, which disappears near exposure sw06.

The distinctive suspended-load lens, unit 50, is continuous. However, it exhibits down-slope variations as well. The lens is 40 cm thick at the center in sw05, decreases to 25 cm thick in sw07. It is not only thinner in exposure sw08, but also less coherent. The well-sorted fines only exist in patches; the majority of the deposit of unit 50 is substituted with homogeneous and poorly sorted silty sand, a colluvium undistinguished from those above and below.

The lower boundary of the lens also exhibits interesting down slope change. The thalweg swings to the left as it approaches the fault zone. The collapse volume originates from the southern bank of channel 1 and resulted in diversion of the thalweg of the suspended-load lens northward (Figure 2.25).

Unit 20 shows perhaps the largest along flow direction variations. Recall that unit 20 is a colluvium, similar to the underlying unit 15. The contact between 20 and 15 is barely recognizable. But in exposure sw07, unit 20 is a 15 cm-thick lens of gravels in sandy matrix, its lower boundary is sharp and erosional. Further downstream in sw13, the unit is made of more than 25-cm-thick massive and loose deposits of sorted pebbly gravels. At this position, unit 20 is well outside the main body of channel 1. This feature may be important for later match of its downstream segment, because exposure sw13 is only about 10 cm northeast of the main fault strand Fault 4 where channel 1 is completely cut off (Figure 2.24a).

Figure 2.24 depicts the geometry of channel 1 in three dimensions. Panel a shows the locations of the deepest channel thalweg (dots) and the locus of the base of unit 30 (crosses) in map view. The cross-sectional shapes of the channel walls and the basal contact of unit 20 in all 13 mapped exposures are also shown. Starting with a V-shape in sw00, channel 1 gradually changes downstream to U-shaped, as the channel floor broadens from point sharp to about 30 cm wide at its intersection with Fault 4 (Figure 2.24h).

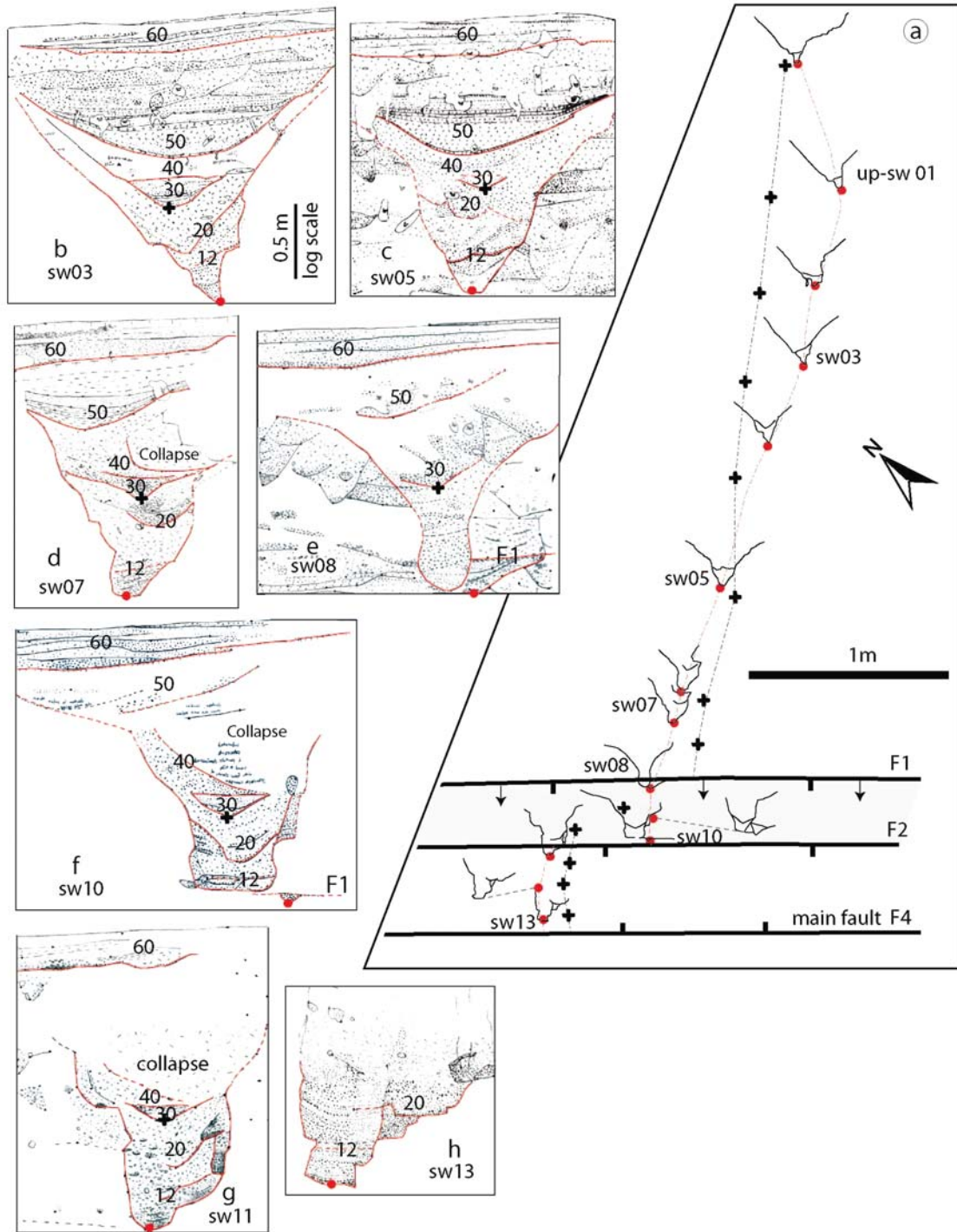


Figure 2.24. Summary of the results of the excavation of channel 1. (a) A map view of the deepest thalweg (dots) and the thalweg of unit 30 (crosses) of channel 1. Simplified cross-sections of the channel in each mapped exposure show the variability in channel shape and stratigraphy. Faults are shown at the location projected on the present ground surface. The barbs are placed on the downthrown side. The

shading between F1 and F2 indicates that F1 is non-vertical. F1 merges with F2 at depth. Panels (b) through (h) are maps of the channel in selected exposures. The name of each exposure indicates the sequence and direction in which it was cut and mapped. Only those portions of a mapped exposure that contain the main body of channel 1 are shown. Major units described in the text are numbered. Except in sw13, the top lines represent the present ground surface.

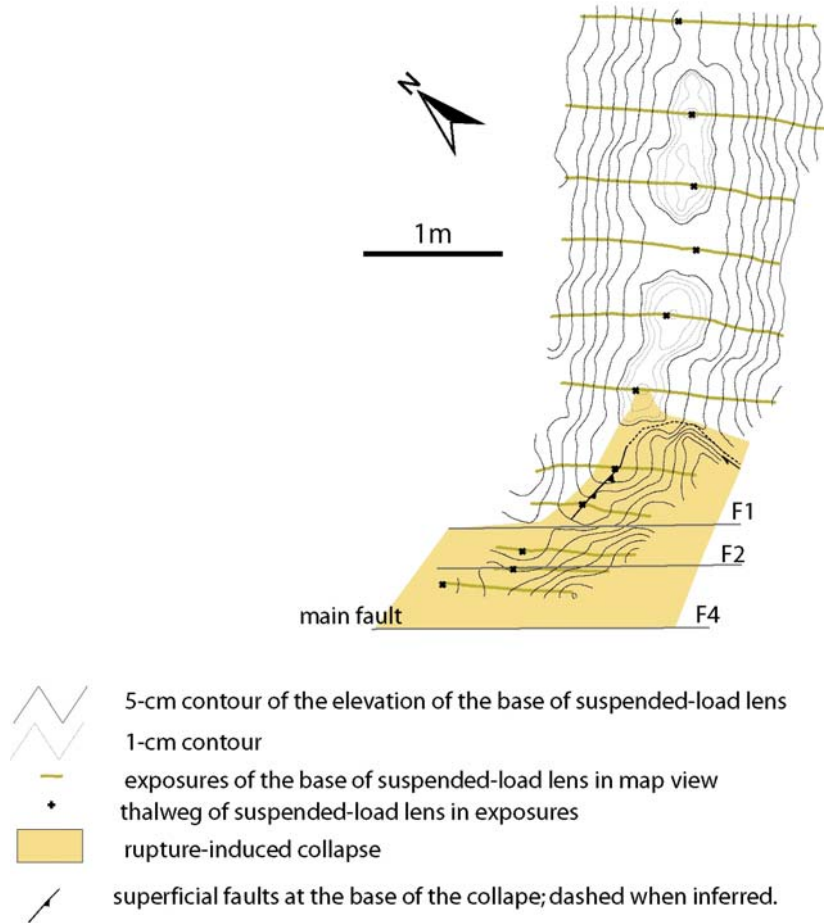


Figure 2.25. Topography of the base of the suspended-load lens in channel 1. Note that the deposit is about 35 cm thick in the center. Variations in the elevation of the edge of the deposit is probably due to bioturbation of the thin margin of the deposit. The shaded polygon indicates the map extent of a block of rubble shoved into the channel by faulting prior to deposition of the lens. This partially blocked the channel, and influenced the shape of the puddle from which the lens formed.

In map view (Figure 2.24a), the thalweg of channel 1, denoted by dot symbols, indicates that the channel floor runs into fault zone at a high angle. The base of fluvial unit 30, denoted by cross symbols, is less sinuous than the channel floor. Both reference lines are offset by minor strands before completely cut off by the main strand Fault 4. The thalweg of unit 30 is offset by Fault 1, and the displacement is distributed within a half meter-wide zone between exposures sw07 and sw09. The deeper thalweg is offset the same amount, but by a strand Fault 2. Our analysis based upon the maps of exposures sw07 through sw11 suggests that Fault 1 is a shallow branch off Fault 2, through a sub-horizontal ramp. This ramp is clearly suggested by a fault at a depth barely above the thalweg in exposures sw08 through sw10 (Cf. “F1” in Figure 2.24 e and f).

### **2.3.3.3 Channel 2**

Channel 2 lies a meter or so southeast of channel 1 (Figure 2.21). It is characteristically narrower than channel 1, which means that it provides a particularly precise piercing line for measuring offset. The channel geometry is complicated by a second, higher side-channel, which disappears prior to intersection with the fault zone. Like channel 1, channel 2 is filled with a combination of well-sorted coarse debris (which we interpret to be of fluvial origin) and poorly sorted materials (which we interpret to be the result of colluviation).

Figure 2.26 depicts the geometry of channel 2 in three dimensions. The summary map (Panel a) shows the location of the main thalweg in map view (dots) and its relationship to a secondary fault and the main fault. The cross-sectional shape of the channel walls and principal bedding contacts in all 13 mapped exposures is also shown. The other panels in the figure show the stratigraphy of the channel in seven representative cross-sections. The principal characteristic of channel 2 is its narrowness. In many of the exposures, it is more than a meter deep but only ten or twenty centimeters wide.

In sw01 through sw08, a higher side-channel appears to the right of the channel in cross-sections. In exposures sw01 and sw02, the side channel is a broad, shallow notch, but it widens and deepens downstream (exposures sw06 and sw07). In exposure sw08, the side channel has

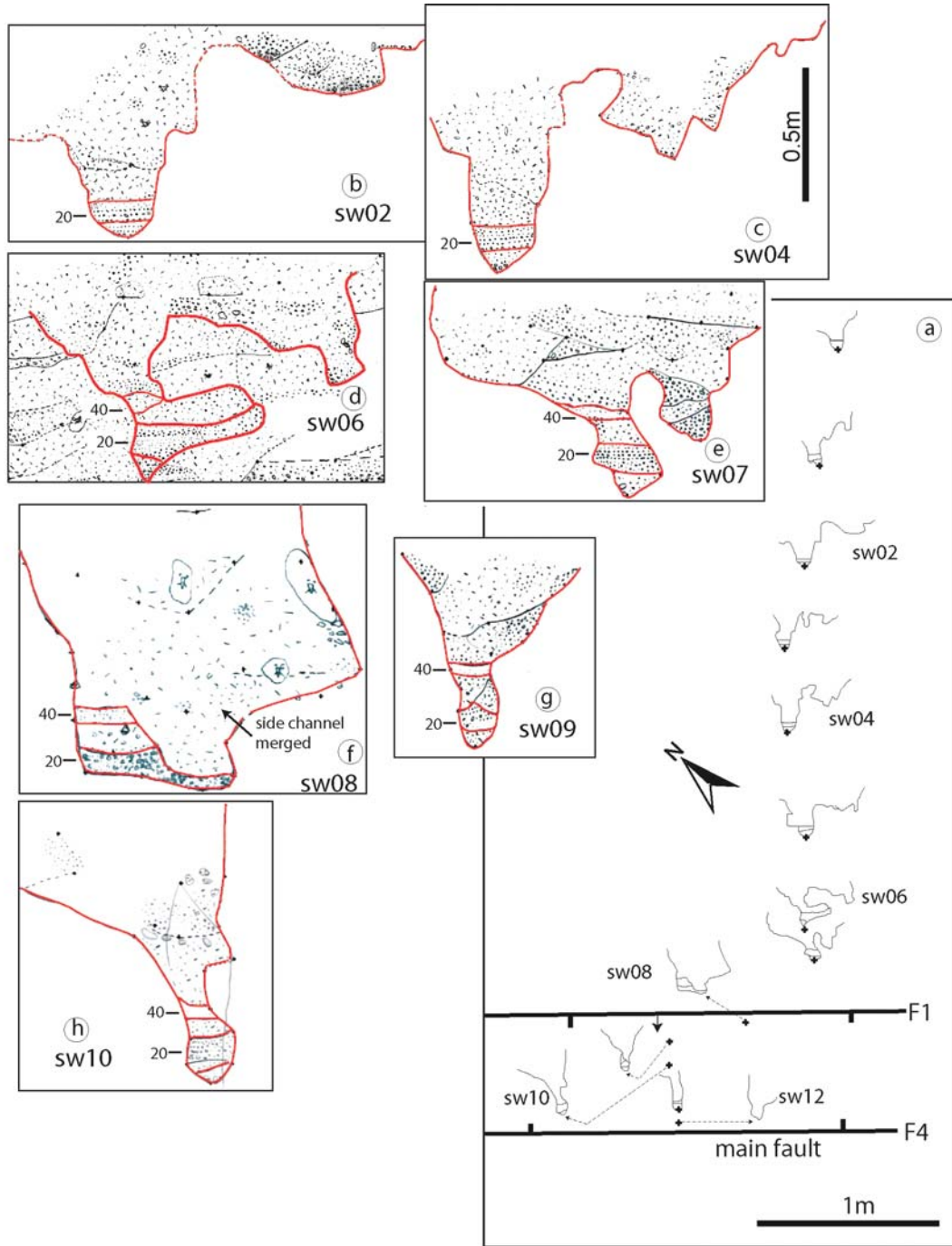


Figure 2.26. Summary of the results of the excavation of channel 2. (a) A map view of the deepest thalweg of channel 2. Simplified cross-sections of channel 2 in each mapped exposure show the variability in channel shape. Faults are shown at locations projected onto the present ground surface. Panels (b) through (h) are maps of the channel in selected exposures. Only those portions of a mapped exposure that contain the main body of channel 2 are shown. Units 20 and 40 are highlighted in selected maps of exposures.

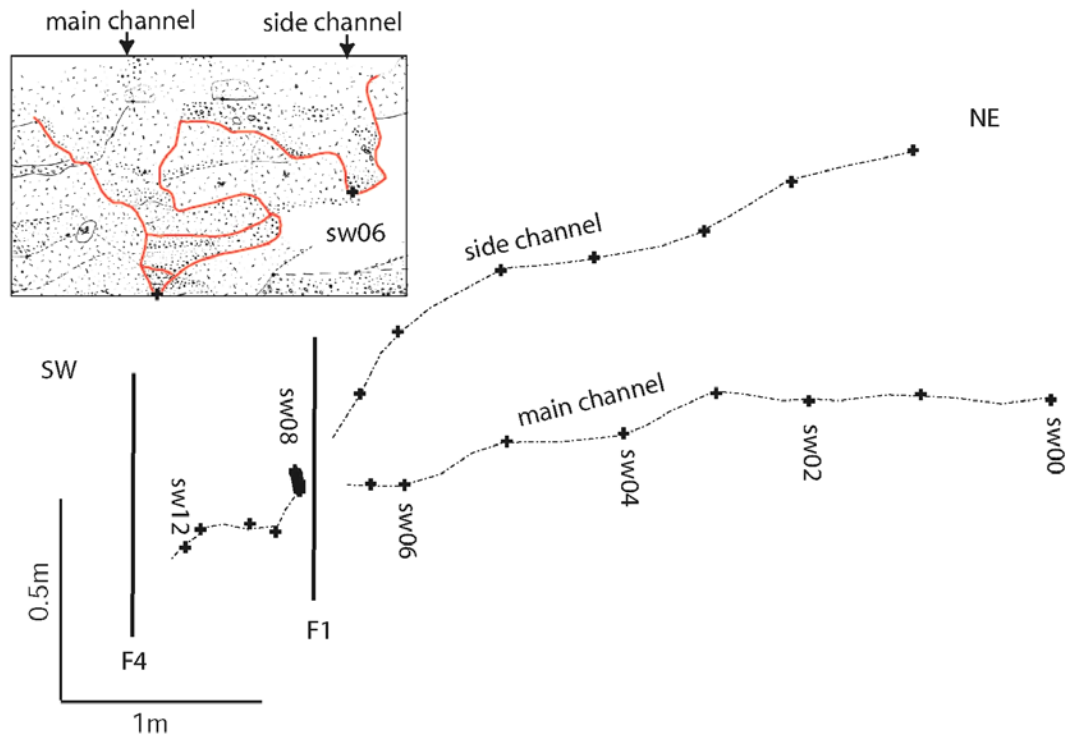


Figure 2.27. Longitudinal profiles of the main channel 2 and its side channel. The side branch, which has steeper gradient, merges into the main channel near the fault zone.

merged with the main channel. The side channel does not exist as a separate channel farther downstream. Longitudinal profiles of the thalwegs of main and side channels differ markedly. The main channel has an undulating and low-gradient floor whereas the side channel has an increasingly steeper slope downstream (Figure 2.27). This indicates that the side channel was abandoned before it could form a concave upward long profile.

The stratigraphy of channel 2 correlates well between exposures (Figure 2.28). Units 10, 20, 30 and 40 are typically about 40 cm thick and do not change their characteristics much from exposure to exposure. Unit 10 is a gray to light gray massive and loose pebbly, granule-rich poorly sorted sand. Tiny charcoal fragments were found in this bed in exposures sw06 and sw07.

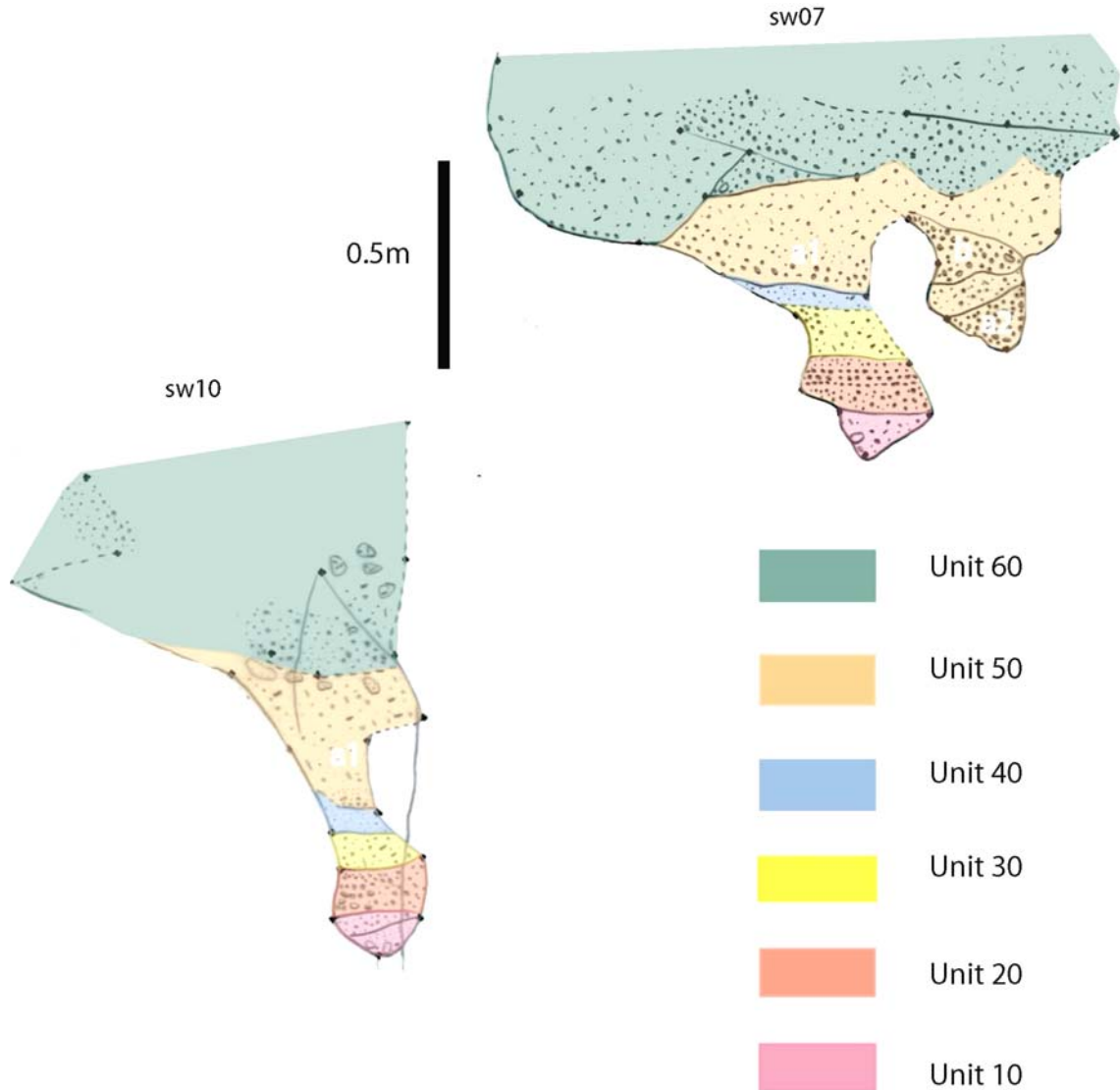


Figure 2.28. Stratigraphic units of channel 2 illustrated using exposures up-sw07 and sw10.

The overlying unit 20 consists of a thin, planar-bedded, well-sorted fining-upward bed, grading from pebbles at the base through granules and coarse sand in the middle to medium to fine sand at the top. Despite the range of grain size, each thin bed in unit 20 is remarkably well-

sorted. The high degree of sorting of this bed and its planar laminae clearly indicated that it was emplaced as bed load in the channel 2 stream.

The contact between unit 20 and overlying 30 is sharp but non-erosional. Unit 30 is a matrix-supported layer of massive small pebbly, sandy silt. Its massive character and poor sorting tell us that it formed as colluvium, derived from exposed channel walls above.

Unit 40 is a thin bed of well-sorted coarse to medium sand. The high degree of sorting indicates that it is fluvial in origin.

Unit 50 consists of both well-sorted and poorly sorted subunits. The basal few centimeters of the unit in the main channel (“a1” in Figure 2.28) consist of small pebbly, granule-rich medium to coarse sand, which fines upward to a poorly sorted silty sand. The basal unit in the side channel also consists of well-sorted granules to coarse sand (“a2” in exposure up-sw07 in Figure 2.28a). These basal, fluvial units in the two channels may be correlative, since the “a2” subunit in the side channel appears to overlie unit 40 in the main channel in exposure sw08 (Figure 2.26). A second reason for believing that these two deposits are contemporaneous is that the deposits of “a2” have both the same texture and faint upward-fining structure as those of “a1” in the main channel. Thus it appears that the side channel was cut after the main channel had been cut and partially filled.

The second phase of fluvial deposition and colluvial cover is represented by a lens of sandy gravel in the side channel (labeled “b” in Figure 2.28). It and “a1” in the main channel are overlain by darker (more organic) massive, poorly sorted silty pebbly sand, indicative of a short-lived period of soil formation that was disrupted by deposition of unit 60.

The contact between unit 50 and 60 is not generally well defined. Although in some places, the contact is marked by a sharp transition to clastic deposits of pebbles in moderate amount of sandy matrix, often it is indicated only by aligned gravels and sand of higher content than in the colluvium underneath.

The basal few centimeter of unit 60 consists of moderately sorted deposits, mostly pebble to granules in sandy matrix. The majority of 60 is, however, massive homogeneous poorly sorted gravelly sand.

### **2.3.3.4 Channels 4, 5 and 6**

Channels 4, 5 and 6 appear in the northwestern part of the excavated upstream volume. All three are shallow channels at a depth of 1 to 1.2 m below the ground surface (Figure 2.21a). Channel 4 is the broadest of the three and has a W- to nearly square-shaped cross-section. It sits in the middle and cuts both channels 5 and 6. Thus it is the youngest of the three.

#### **Channel 4**

We divide the stratigraphic sequence in channel 4 into five units (Figure 2.29).

Unit 10 is a loose, massive and homogeneous mixture of granules and poorly sorted sand; pebbles are rare. The majority of unit 10 is colluvial in nature, with abundant colluvial structures, such as sloping internal boundaries, and sloping gravel trains; however a thin, well-sorted layer of framework-supported pebbles and granules occurs at the base of unit 10 in some of the exposures of channel 4 (sw01, sw02, sw06, Figure 2.30).

Unit 20 is also a mixture of granules and poor-sorted sand. Despite the similarity in composition and texture of units 20 and 10, the contact between them is commonly sharp and erosional (Figure 2.29). As at the base of unit 10, a well-sorted layer of coarser grains is locally present at the base of unit 20 (e.g., in sw08, where they are well-sorted and horizontally bedded granules to very coarse sand, which fine upward to coarse sand, then to fine sand, Figure 2.30). The down-cutting prior to the deposition of unit 20 is as deep as that which preceded deposition of unit 10, in lower reaches of the channel, near the fault zone. This double incision is the origin of the W-shaped bottom of channel 4.

Unit 30 consists of a sequence of two well-sorted fluvial beds of sand and gravels, each topped by massive, poorly sorted clastic debris. The base of the lower fluvial bed is a concentration of aligned granules to very coarse sand in most exposures, but has cobbles and pebbles in sw06 and sw07 (Figure 2.30). It is overlain by loose poorly sorted gravelly sand with silt. The upper part of this first fluvial/colluvial packet is scoured by a fluvial channel in some exposures (e.g., sw05, Figure 2.29). The upper fluvial bed is finer grain-sized than the lower bed; it is mostly composed of sand. A prominent feature within this upper scour-and-fill packet is an

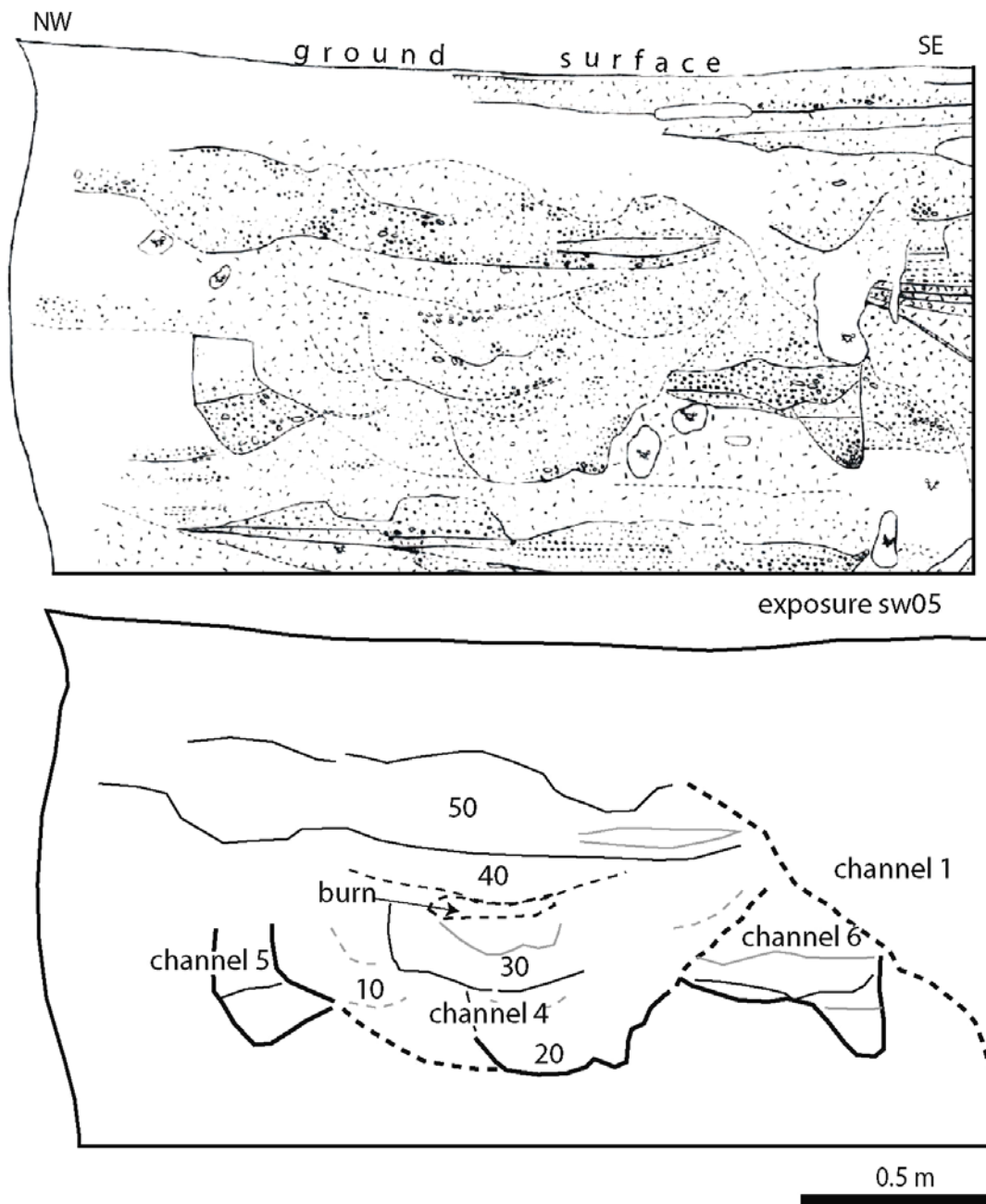
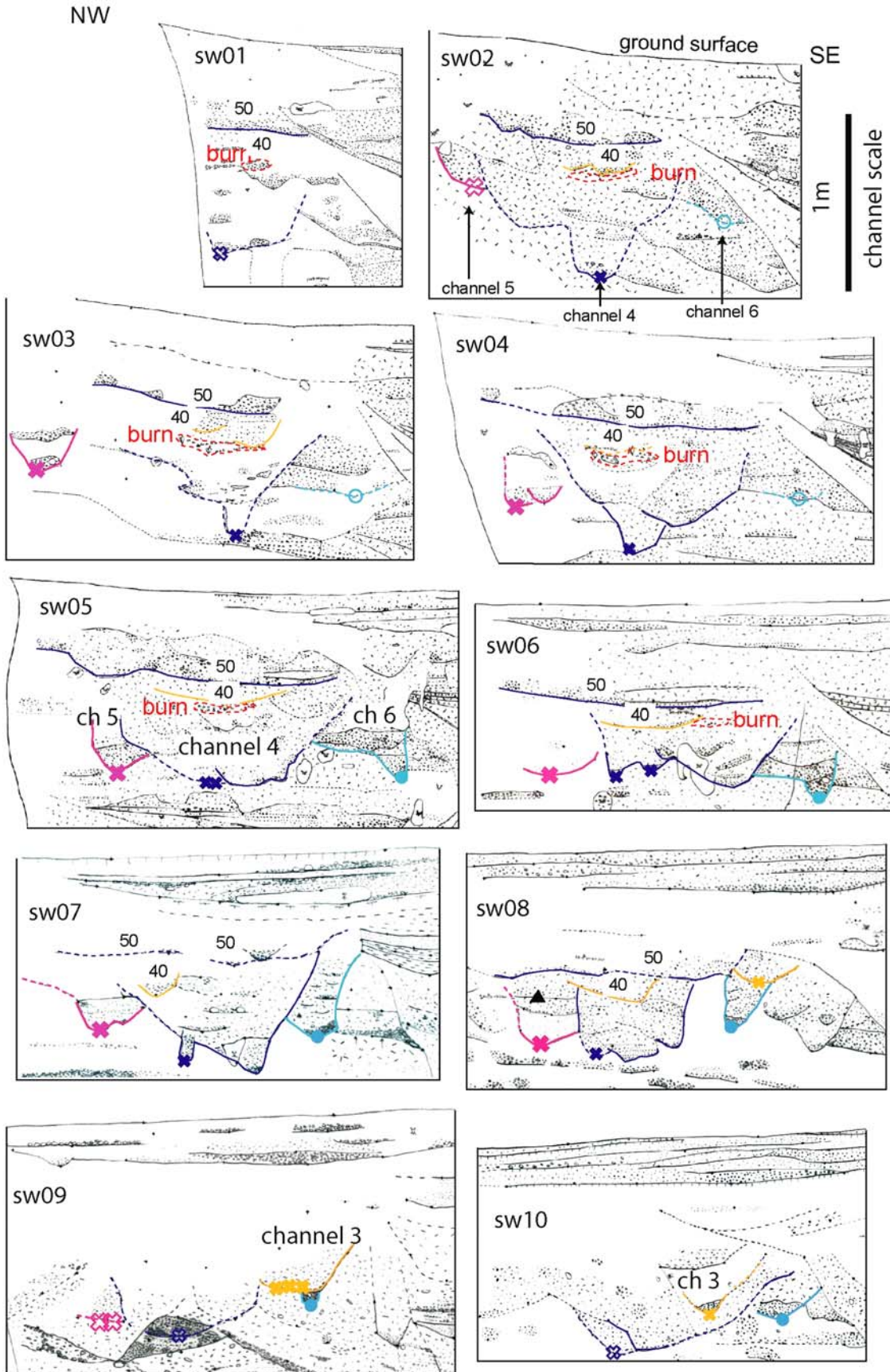


Figure 2.29. Stratigraphic units of channels 4, 5 and 6, illustrated using exposure sw05. The upper panel is the map of the channel stratigraphy; the lower panel shows the general groupings within the channels.



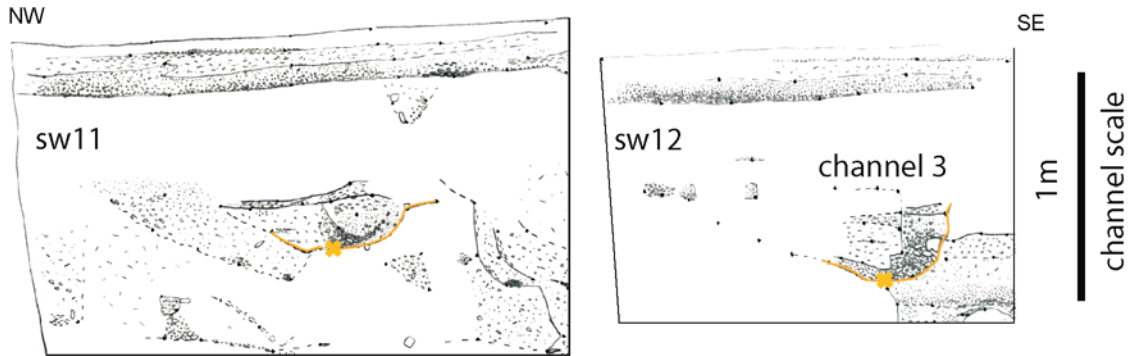


Figure 2.30. Maps of channels 3, 4, 5 and 6 in exposures sw01 through sw12. Only the portion of a mapped exposure that contain the channels are shown. The top line represents present ground surface. The name of each exposure indicates the sequence and direction in which it was cut and mapped. Colored symbols mark the thalwegs of channels in each exposure. Open symbols are used when uncertain. Units 40 and 50 of channel 4 and a burn horizon that are discussed in the text are highlighted. Look direction is upstream.

in-situ burn, marked by black charcoal powder and by a red hue in the surrounding sediments (marked by red dashes in Figure 2.30, exposures sw03 through sw06). This burn is several cm thick,  $\leq 40$  cm wide, but 3 to 4 m long, with its long axis parallel to the channel. Its top was partially removed by erosion prior to the deposition of overlying unit 40.

Unit 40 is best defined in exposures sw04, sw05 and sw06. It is an approximately 0.7-m-wide lens of indurated silt. In exposures far from the fault, the deposits are coarser, and sit above distinctive channel scour (Cf. sw02 and sw03, Figure 2.30). Downstream from sw06, it is identifiable only in exposures sw07 and sw08, where it is correlative to channel deposits of yellowish sand and granules, better sorted than the surrounding colluvium.

Unit 50 is the only bed of coarse-grained fluvial deposits in channel 4. It consists mainly of sandy, framework-supported pebbly gravels, alternating with blobs of sand and silt. Locally, in exposures sw05 and sw06, a lens of well-sorted silty medium to fine sand sits within the coarser sediment. This fine deposit resembles the suspended-load bed in channel 1, which we ascribe to settling of fines from a pond behind a shutter ridge. The deposit in channel 4 is not as extensive,

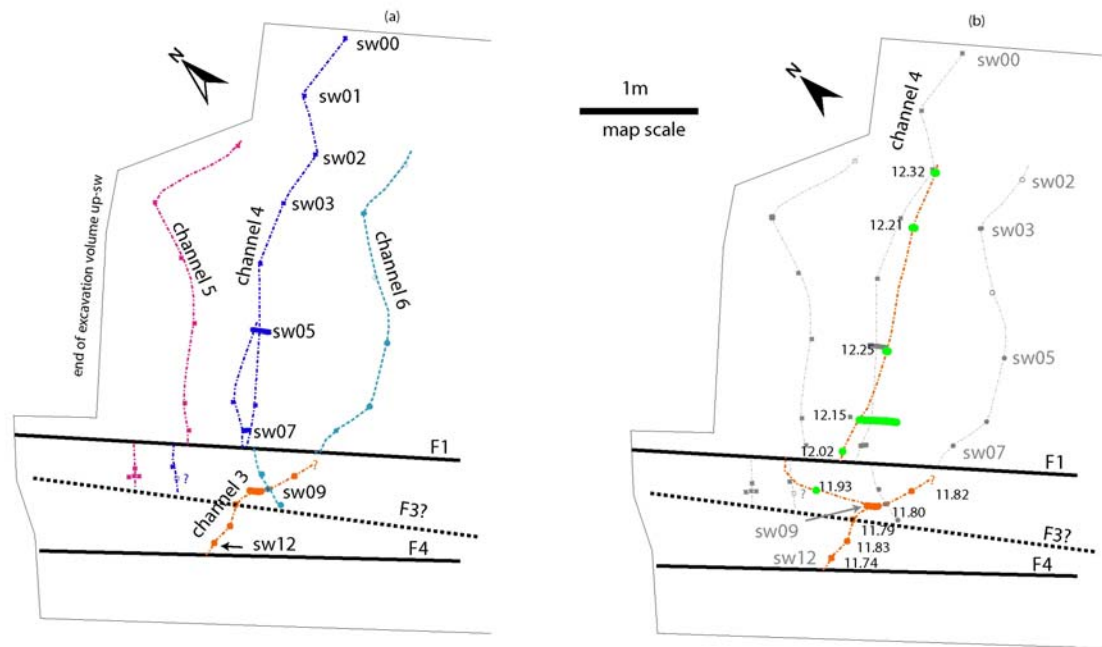


Figure 2.31. Map view of the deepest thalwegs of channels 3, 4, 5 and 6. (a) Channels 4, 5 and 6 are offset by Faults 1 and 3, whereas channel 3 runs across F3 without being offset. This indicates that channel 3 is the youngest of the four. (b) A speculative source of water for the down-cutting of channel 3. The green dots with numbers represent the thalweg of unit 40 of channel 4 and its elevation in each exposure. Prior to the deposition of unit 40, water in channel 4 may have been diverted southward and flew along the base of scarp of Fault 3. It might well have then merged into channel 3 near exposure sw09.

but could have the same origin. The overall shape of the unit 50 fine bed is lenticular, with a concave bottom. It is thickest in sw05, where it reaches a thickness of about 0.3 m. The unit thins both up- and down-stream, but probably for different reasons. The upstream decrease in thickness of this bed is likely the result of the increase in elevation of the channel bottom, which would have resulted in a lapping of the pond onto the channel floor upstream. Downstream, the lens is markedly thinner in exposure sw06. In exposure sw07, the alluvium of unit 50 is absent,

but its stratigraphic position is replaced by thick, massive and homogeneous colluvium. The non-descriptive and indurate nature of the deposit suggests it is probably derived from fault scarp collapse downstream. Thus, unit 50 appears to lap onto a fault-scarp-derived colluvial wedge that pinches out upstream. Hence, we interpret unit 50 to represent a period of aggradation behind a scarp, after an offset event during which a shutter-ridge cut the upstream channel off from its downstream continuation.

### **Channel 5**

Channel 5 is a small channel whose upper section was eroded away by scouring of channel 4 (Figure 2.29). The shape of channel 5 and deposits within it does not vary much from exposure to exposure. Its thalweg is marked by a blue “x” in Figure 2.30. Channel 5 is narrow with a semi-circular floor in most exposures. Locally, (i.e., in sw04 and sw07) it has a double thalweg.

The preserved portion of channel 5 commonly contains two packets of fluvial sediments. In sw05 (Figure 2.29), the lower of the two beds is massive and coarser-grained, composed of pebbles in a matrix of granules to coarse sand. The upper bed is finer-grained, well-sorted coarse to medium sand. The sorting of both of these beds indicates they are fluvial deposits.

Near the fault, in exposures such as sw06, sw07 and sw08, these fluvial layers are not differentiable and consist of massive fine-grained, well-sorted, coarse to medium sand (Figure 2.30).

### **Channel 6**

Channel 6 is truncated by channel 4 on the northwest and by channel 1 on the southeast (Figure 2.29). Only the lowest 40 cm of the channel is preserved. The surviving portion of channel 6 is preserved best in exposure sw05. There it is filled with two well-sorted fluvial beds separated by a thin layer of poorly sorted granule-rich silty sand. The lower fluvial layer consists of loose pebbly granule-rich sand that fine upward slightly. The upper fluvial bed is coarser-grained, and it was deposited when the channel floor was flat and wider.

In plan view, channels 4, 5, and 6 are subparallel and moderately sinuous (Figure 2.31a). They are sharply a similar amount by Fault 1. And they disappear about 0.5 m north of the main strand Fault 4. Because of this disappearance before the main fault strand, we suspect that they are offset by another strand, Fault 3. In the reach between Fault 1 and Fault 3, channels 4 and 5 remain straight, whereas channel 6 flows southward. It is worth noting that channel 6 is the only exposed channel that flows southward. This distinctive feature means that the correlative downstream segment of channel 6 may depart from the fault zone southward. We could further speculate that channel 6 was incised when a channel from another drainage system was moved by the fault close to but to the right of this drainage, a scenario illustrated in Fig. 2.5c).

### **2.3.3.5 Channel 3**

Channel 3 is unlike the other channels upstream from the fault, in that it does not exist upstream from the fault zone. It is only about a meter long, exists only within the fault zone and trends westward, rather than southwestward (Figure 2.31a). If it extended farther upstream, it has been eroded away by the younger channel 1. Channel 3 is demonstrably younger than channels 4, 5 and 6, because it is not offset by Fault 3, and because it cuts channel 6 (exposure sw09 in Figure 2.30).

Channel 3 is 35 cm thick in exposure sw12 (Figure 2.30), where it consists mainly of loose pebbly gravel. Both thickness and clast size decrease upstream. In exposure sw11 it is 25 cm thick and consists of pebbles and blobs of granule sand. In exposure sw10 it is merely a 7-cm-thick lens of granules and coarse sand. Still farther upstream, in exposure sw09, it is barely recognizable as an arcuate scour filled with poorly sorted debris atop a wisp of coarse to very coarse sand. The deepening of the channel downstream suggests that perhaps a downstream-facing fault scarp had existed before the down-cutting of channel 3, or that water from multiple paths merged downstream and thus had more erosion power.

In exposures sw10, 11 and 12, the fluvial deposits are capped by a thin layer of fine-grained silty fine to medium sand. This deposit, particularly clear in exposure sw11, has the texture and grain size consistent with deposition in a puddle.

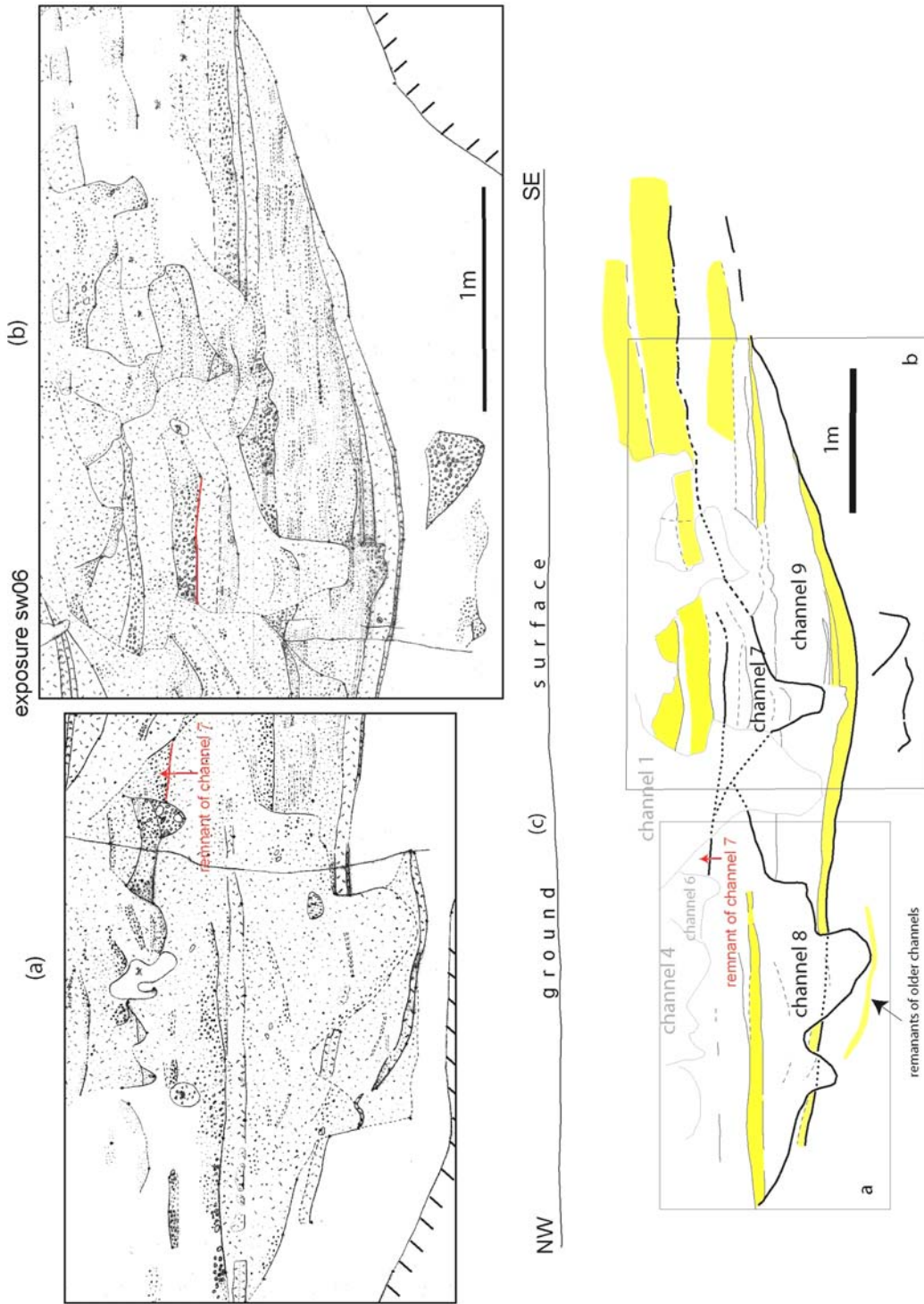


Figure 2.32. Stratigraphic units of channels 7, 8 and 9 illustrated using exposure up-sw06. (a) and (b) are clipped maps of the channel stratigraphy. (c) shows the channel outlines and the general groupings within the channels. The triangular patch between channels 1 and 6 appears to be a remnant of channel 7.

Based upon its stratigraphic position and elevation, channel 3 deposit is probably contemporaneous with unit 40 of channel 4 (Figure 2.29). Recall that unit 40 is yellowish sand and granules on top of channel scours and better sorted than the surrounding colluvium, in exposures sw07 and sw08. The trace of the deepest part of unit 40 appears as a red dashed line in Figure 2.31b. The geometry of the trace of unit 40 suggests that water in channel 4 may have been diverted southward at the fault and flowed along the base of scarp of Fault 3. If so, it might well have then merged with channel 3 near the exposure sw09. Consistent with this interpretation, the breadth of the floor of channel 3 is the flattest and broadest in exposure sw09 (Figure 2.30).

### **2.3.3.6 Channels 7, 8, and 9**

In a typical upstream cut, channels 7, 8, and 9 occupy the lower two-thirds of the exposure (Figures 2.21 and 2.32c). Channel 9 is the deepest and oldest upstream channel whose stratigraphy is still largely preserved. In its deepest portions, up to 3 m below the ground surface, it cuts directly into bioturbated late Pleistocene alluvium. Channels 7 and 8 cut into channel 9 from above its center and northwestern flanks, respectively.

#### **Channel 7**

The overall shape of channel 7 is T-shaped, with a less than 0.5 m – wide narrow lower part which widens dramatically in the upper part. The walls of channel 7 are distinct in most exposures, due to the great contrast between fluvial and colluvial beds within the channel and those into which it is cut.

Along much of its length, however, channel 1 has removed portions of the northwestern wall of the channel. This creates significant ambiguities in many exposures. Particularly important is the relationship of channel 7 to younger channels 4, 5 and 6. This ambiguity is resolvable Figure 2.32c shows that between channel 6 and channel 1, there is a triangular-shaped remnant. It consists of well-sorted small pebbles and granules overlying a well-defined scour mark (Figure 2.33). The texture and grain size of this deposit resemble that of a middle bed within channel 7, on the opposite side of channel 1. The elevation and the sloping of the lower

contact also suggest that they are the same bed. If this interpretation is correct, then channel 6 cuts into channel 7, is thus younger.

Channel 7 clearly incised about 80 centimeters into older deposits of channels 8 and 9 (Figure 2.32). The incision is roughly V-shaped and nearly 2 m wide at the top, where it cuts massive colluvial slope wash that rests atop beds of channels 8 and 9. The fill within the narrow part of the channel is predominantly massive, poorly sorted pebbly, silty granule-rich sand, which we interpret as slope-derived colluvium and bioturbated materials. The channel contains a few wisps of well-sorted debris that appear to be the unbioturbated remnants of fluvial beds.

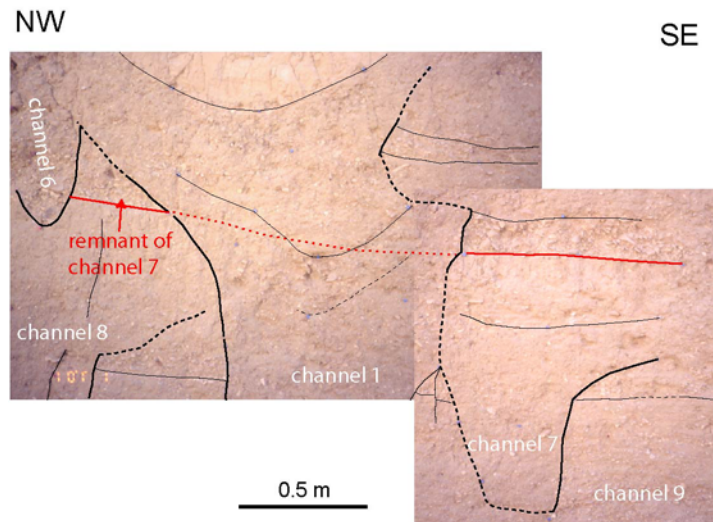


Figure 2.33. Photographs of exposure sw06 show the cross-cutting relationships between channels 6, 7, 8 and 9. The triangular patch of material between channels 1 and 6 is likely the continuation of a middle gravel bed of channel 7.

Channel 7 is topped by two distinctive beds of silty fine sand (highlighted in yellow in Figure 2.32c). These beds overlie the central channel and extend over pre-channel 7 colluvial apron up to 5 m farther southeast. They might have also extended to the northwest, but if so, they have been removed by erosion during the creation of younger channels. In the exposures near the fault, these beds are severely bioturbated, which indicates a long time has passed since their

deposition and that sediment that accumulated above them accumulated too slowly to significantly retard bioturbation. In exposures far from the fault, they are composed of multiple upward-fining sequences of coarse sand to fine sand and silt. These are clearly suspended-load deposits that fell out of an ephemeral pond upstream from the fault. A short hiatus between the deposition of the two lenses is apparent in well-preserved patches, where the coherent upper lens with its original sedimentary structure directly overlies the partially bioturbated lower lens at a sharp, uneroded contact. In upslope exposures and at places of best preservation, the lenses are composed of multiple sub-layers of upward-fining sequences from coarse sand to fine sand and then to silt.

Underlying each suspended-load lens is a thin layer of coarser-grained fluvial deposits, which represent the deposition prior to ponding. These coarser deposits display a lateral facies change: They are predominantly pebbly gravel in the center of the channel, but fine toward the southeast to granules and then to coarse sand.

### **Channel 8**

Channel 8 cuts into the northwest flank of channel 9 (Figure 2.32). In the plane of exposure sw06, a fraction of a meter upstream from the fault zone, the channel appears as an asymmetric channel about 1.8-m-wide channel with twin thalwegs (Figure 2.32a and c). In actuality, the channel is much narrower, because the exposure is oblique to the long axis of the channel.

The deposits of channel 8 are readily separated into those that antedate a large offset on the San Andreas fault and those that post-date that offset. Pre-offset beds fill most of the channel and are massive, loose poorly sorted sand and pebbly gravel, coarser and less indurated than the sediments in the other upstream channels. The period of post-offset deposition began with laying down of a 15-cm-thick bed of laminated coarsening-upward silty fine sand, which represents the formation of a closed basin just upstream from the fault. As in previously described cases, we interpret this to indicate the movement of a long shutter ridge in front of the stream by slip on the fault. These suspended load deposits are, in turn, overlain by highly bioturbated, interbedded fluvial and colluvial sandy gravels and granule-rich sand and silt.

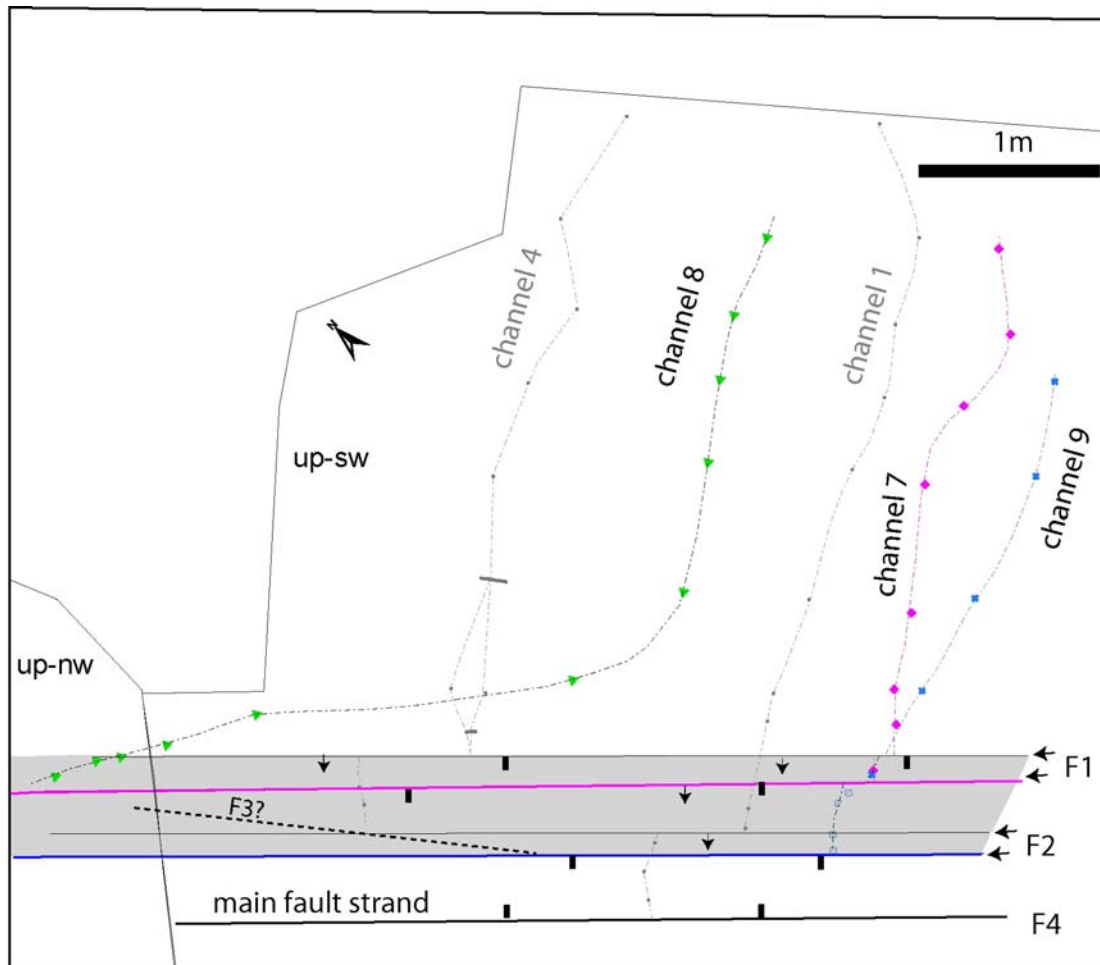


Figure 2.34. Map of the deepest thalwegs of channels 7, 8, and 9. Channel 8 curves to the north and intersects F2 at a small angle, whereas channel 7 and 9 run into the fault zone at a high angle. The thalwegs of channel 1 and 4 provide a reference. The shaded region indicates the non-vertical nature of Faults 1 and 2. Faults are placed where they offset features.

### Channel 9

Channel 9 is the deepest and broadest upstream channel. It sits almost directly over the whitish late Pleistocene deposit, massive and homogeneous poorly sorted gravelly sand and silt (unmapped area near the bottom of trench exposure; Figure 2.32).

The channel infill consists of two sets of strata that are distinctively different. The upper set is a suite of laminated beds that pinch out laterally and outline a broad swale of channel wall. The lower set is represented by patches of well sorted framework-supported gravel lenses beneath the center of the broad swale.

The thalweg of channel 9 is not clear in exposure sw06 (Figure 2.32), because most of lower channel infill is collapse from channel wall, thus indistinguishable from the late Pleistocene deposit into which channel 9 cuts. However, patches of gravel lenses indicate that channel 9 may be more than 0.8 m deeper than the broad swale outlined by the upper suite of strata. Although only two gravel lenses appear in the exposure in Figure 2.32, in some exposures, they can be as many as 5 – 6, and reach about 1 m below the broad swale.

The upper set of strata starts with a distinctive bed of silty fine. It is a concave lens about 15 cm thick at the center, the sorting and grain size suggests it is one of the behind-the-shutter-ridge suspended-load beds. Two more beds of well sorted fine deposit were found at higher level in channel 9. They are near the channel edge, and clearly interfinger with beds of well-sorted pebbly gravel, which we believe are fluvial deposits, near the center of the channel. Therefore, these two beds of fine deposit, even though they look similar to the suspended-load fines, may represent reduced speed of water current away from the center when the coarse debris deposited. Between the middle and lower fine deposit beds, is a thick stack of layered or laminated deposits. The deposits exhibit fluvial sedimentary structures such as horizontal bedding as well as cross-bedding. The grain size spans from cobbly pebbles to silt; nonetheless, each layer or lamination is very well-sorted. This stack of deposit was probably accumulated in quick succession because the fine structures of bedding and lamination are still preserved. Depositional hiatus, indicated in some places by soil development of mm thick, should be relatively short.

The description above suggests that channel 7 is younger than channel 8, which is younger than channel 9. It is obvious that channels 7 and 8 both cut into channel 9. The relationship between channels 7 and 8 is not as straightforward, but the best interpretation is that channel 8 is older than 7, because channel 8 is overlain by a patch of remnant of channel 7 on the upper right (Figures 2.32c and 2.33).

In plan view, the trends of channels 7, 8 and 9 are interesting. Figure 2.34 shows that channel 7 approaches the fault zone at nearly a right angle. Its course is cut off by Fault 1 and does not appear in the excavated volume on the opposite side of the fault. The path of channel 8 differs markedly from all other upstream channels: It approaches the fault at nearly a right angle, but veers sharply to the northwest less than a meter upstream of the fault. It then flows parallel to the fault before being truncated by Fault 1 at the northwestern edge of the excavated volume. Thus, both channel 7 and channel 8 have been offset far more than younger channels 1 and 4, which have experienced only about a half meter of dextral slip across Fault 1.

The thalweg of the oldest one, channel 9, is not cut off by Fault 1, but by Fault 2. Channel 9 approaches the fault zone at an angle of about 60°. Its course across Faults 1 and 2 is uncertain, but possibly as shown by the open circles within the fault zone. The uncertainty is because the infill at the base of channel 9 is mostly collapse of channel wall, which is not distinguishable from the surrounding deposits and thus obscures the thalweg. However, as mentioned before, the gravel lenses at the bottom of channel 9 still indicate the rough position, if not the elevation of the thalweg.

## 2.4 Summary

In this chapter, we have presented the basic stratigraphic and geomorphic data from our 3-D excavation at the Wallace Creek site.

We have mapped many exposures within a volume excavated across a stream channel just upstream from the fault. And we have mapped numerous exposures in 6 volumes excavated across beheaded channels downstream from the fault. This work will be the basis determining the sequential rupture history of the fault.

The upstream volume contains 9 distinct nested channels, within a broad, 3-m-deep V-shaped channel scoured into late Pleistocene substrate. Cross-cutting relationships of these channels have allowed us to determine the relative ages of the channels. Several of the channels contain distinctive beds of well-sorted fine sand to silt. These fine deposits document the ponding

water upstream from the fault following large offset events that emplaced shutter ridges in front of the channels.

Downstream exposures tend to reveal singular filled channels 1 – 3 m deep cut into bioturbated late Pleistocene alluvium. Twelve separate channels exist within a span of 50 – 60 m along the fault. Several of these were not geomorphically obvious. For example, nine of the twelve channels are within two geomorphically obvious channels. This observation indicates that using geomorphology alone may possibly result in misinterpretation of offsets. In addition, the sequence of downstream channels can be complex. As we show in some cases (i.e., channels *f* and *k*), the sequence includes pre-existing channels that are probably from sources tens of meters southeast of our excavation site.

Most channels run into the fault zone at a high angle. Some channels, however, flow subparallel to the fault zone, in deflections under the topographic influence of older pre-existing channels.

The stratigraphy and cross-sectional morphology of the channels are distinctive enough to enable us to match channels across the fault and to calculate vertical and horizontal offset of individual channels. That is our task in the following chapter, Chapter 3.

## 2.5 References

- Arrowsmith, R. J., D. D. Pollard, and D. D. Rhodes, Hillslope development in areas of active tectonics, *J. Geophys. Res.*, *101*, 6255-6275, 1996.
- Buwalda, J. P., Shutterridges, characteristic physiographic features of active faults, *Proceedings of the Geological Society of America*, pp, 307, 1937.
- Dibblee, T. W., Regional geologic map of the San Andreas and related faults in Carrizo Plain, Temblor, Caliente, and La Panza ranges and vicinity, California, *U. S. Geological Survey Miscellaneous Geologic Investigations Map, I-757*, 1973.
- Gaudemer, Y., P. Tapponnier, and D. L. Turcotte, River offsets across active strike-slip faults, *Annales Tectonicae*, *3*, 55-76, 1989.
- Gomez, B., R. L. Naff, and D. W. Hubbell, Temporary variations in bedload transport rates associated with the migration of bedforms, *Earth Surface Processes and Landforms*, *14*, 135-136, 1989.
- Huang, W., Morphologic patterns of stream channels on the active Yishu fault, southern Shandong Province, Eastern China: implications for repeated great earthquakes in the Holocene, *Tectonophysics*, *219*, 283-304, 1993.
- Lienkaemper, J. J., 1857 slip on the San Andreas fault southeast of Cholame, California, *Bull. Seism. Soc. Am.*, *91*, 1659-1672, 2001.
- Lienkaemper, J. J., and T. A. Sturm, Reconstruction of a channel offset in 1857(?) by the San Andreas fault near Cholame, California, *Bull. Seism. Soc. Am.*, *79*, 901-909, 1989.
- Meade, R. H., Wave-like movement of bedload sediment, East Fork River, Wyoming, *Environmental Geology and Water Sciences*, *7*, 215-225, 1985.
- Reid, I., and L. E. Frostick, Fluvial sediment transport and deposition, in *Sediment transport and depositional processes*, edited by K. Pye, pp. 89-155, Blackwell Scientific Publications, 1994.
- Schumm, S. A., J. F. Dumont, and J. M. Holbrook, *Active tectonics and alluvial rivers*, Cambridge University Press, 2000.
- Sieh, K., M. Stuiver, and D. Brillinger, A more precise chronology of earthquakes produced by

- the San Andreas fault in southern California, *J. Geophys. Res.*, *94*, 603-623, 1989.
- Sieh, K. E., A study of Holocene displacement history along the south-central reach of the San Andreas fault [Ph.D. thesis] Stanford University 243p, 1977.
- Sieh, K. E., Prehistoric large earthquakes produced by slip on the San Andreas fault at Pallett Creek, California, *J. Geophys. Res.*, *83*, 3907-3939, 1978.
- Sieh, K. E., Slip along the San Andreas fault associated with the great 1857 earthquake, *Bulletin of Seismological Society of America*, *68*, 1421-1448, 1978.
- Sieh, K. E., Lateral offsets and revised dates of large prehistoric earthquakes at Pallett Creek, Southern California, *J. Geophys. Res.*, *89*, 7641-7670, 1984.
- Sieh, K. E., and R. H. Jahns, Holocene activity of the San Andreas fault at Wallace Creek, California, *Geol. Soc. Am. Bull.*, *95*, 883-896, 1984.
- Sieh, K. E., and R. E. Wallace, The San Andreas fault at Wallace Creek, San Luis Obispo County, California, *Cordilleran Section of the Geological Society of America, Centennial field guide* 233-238, 1987.
- Stuart, W. D., Forecast model for large and great earthquakes in southern California, *J. Geophys. Res.*, *91*, 13771-13786, 1986.
- Wallace, R. E., Notes on stream channels offset by the San Andreas fault, in *Proceedings of conference on geologic problems of the San Andreas fault*, edited by W. R. Dickinson and A. Grantz, Stanford University Publications in the Geological Sciences, 1968.

## **Chapter 3    A Slip History for the Past Several Earthquakes**

Nature uses only the longest threads to weave her patterns,  
so each small piece of her fabric reveals the organization of the entire tapestry

--Richard Feynman

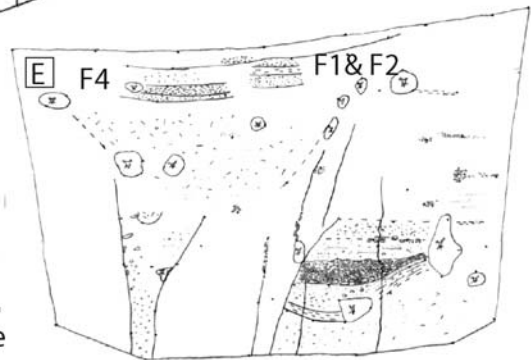
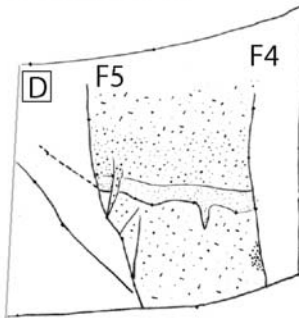
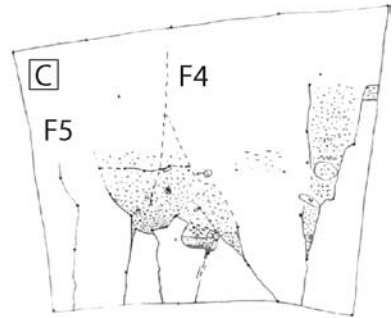
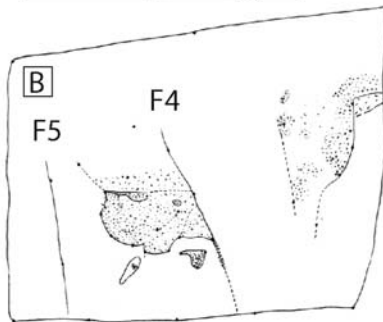
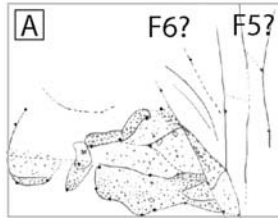
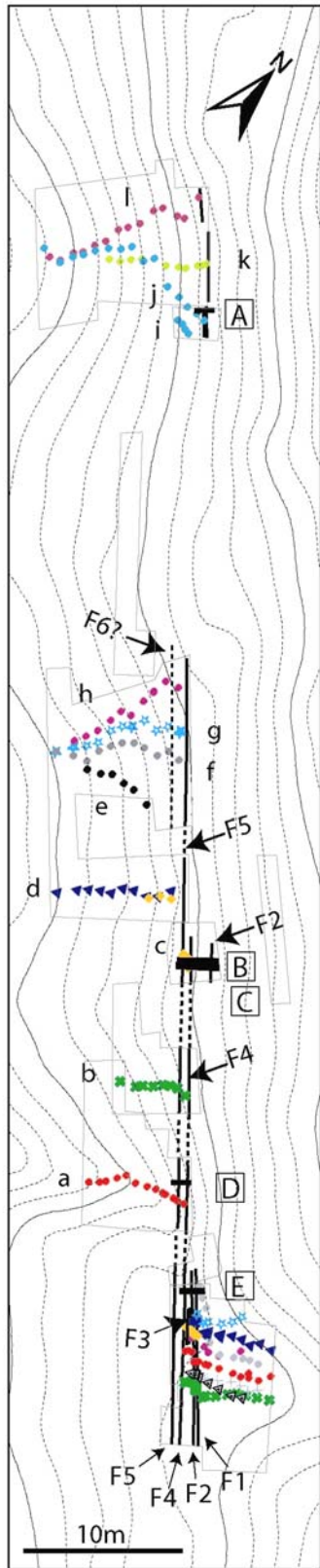
### 3.1 Overview

In Chapter 2, I described the morphologic and stratigraphic characteristics of the channels that we exposed at the Wallace Creek paleoseismic site. In this chapter, I use these characteristics to match upstream and downstream channel segments and to measure their offsets across the fault. I also present the results of our  $^{14}\text{C}$  analyses on materials from the channels and use these data to constrain the ages of the channels and the dates of the numerous fault ruptures. I refine these rupture dates further by incorporating published and unpublished data from two nearby paleoseismic sites (Grant and Sieh, 1994; Sims et al., 1994b). Finally, I incorporate the data from the Wallace Creek paleoseismic site into a speculative rupture history for the entire southern half of the San Andreas fault and discuss the general implications of our results for understanding earthquake repetition.

### 3.2 Fault zone structure

Figure 3.1 summarizes the geometry of the traces of the San Andreas fault zone and offset stream channels at the Wallace Creek paleoseismic site. In many cases, we can trace major fault strands from exposure to exposure, based on the projection of strikes, relative position, and the spacing between traces. Correlations are tenuous, however, in some cases. For example, correlation of the fault traces exposed at location A in Figure 3.1 with Fault 5 or Fault 6, nearly 20 m to the southeast, is uncertain.

Figure 3.1. (Next page) Overview of the structure of the fault zone within the excavated volume. Panels A through E are maps of the walls of excavation faces cut across the fault. They show that traces on the edges of the fault zone typically dip toward the fault zone. Panel F is a map of the fault zone and shows the locations of the exposures. It also shows the offset channel thalwegs and excavation limits.



1 m  
trench log scale

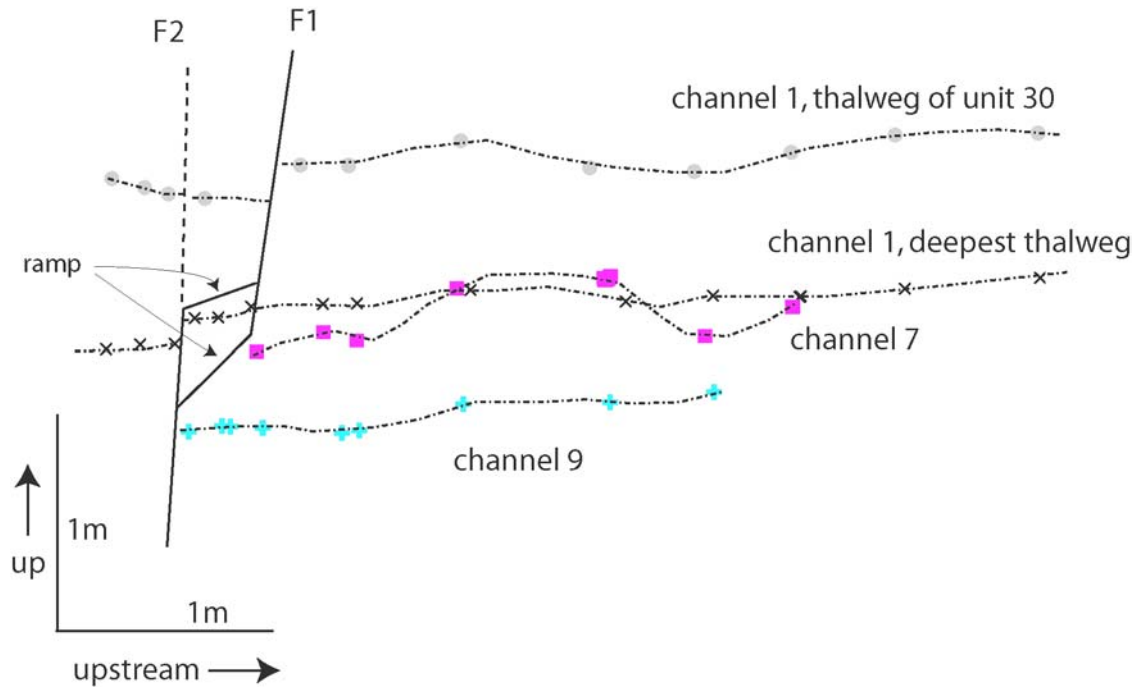


Figure 3.2. Cross-sectional map of channel thalwegs illustrates the relationship of Faults 1 and 2. During the most recent event, Fault 1 connected with Fault 2 by way of a sub-horizontal ramp between the deepest thalweg and the thalweg of unit 30 of channel 1. Older and deeper channels 7 and 9 terminate against the faults at different places, indicating that Fault 1 must have connected to Fault 2 through a deeper ramp during earlier ruptures.

Recent faulting activity has been concentrated in a zone just 1.5 to 2 m wide. This narrower zone comprises six principal fault planes, Fault 1 through F6 (Figure 3.1F). We did not find secondary traces outside this narrow zone offsetting the channels, within the 10-m aperture of our excavations. However, the total width of the fault zone is larger than that is indicated by channels. The main fault zone in the late Pleistocene substrate, not depicted in Figure 3.1, is at

least 4 to 5 m wide, judging from the extent of shear fabric within the substrate exposed in the excavations.

The width of the fault zone is the cumulative result of fault rupture during several earthquakes; the distribution of slip on these fault traces varies along strike and probably from earthquake to earthquake. For instance, Fault 5 accommodates most of the offset of channels d, f, g and h, but only 40 cm of the offset of channel b and none of the offset of channel a (Figure 3.1F); instead, Fault 4 is the major strand for channel a and b. Likewise, Fault 2 is the principal strand that offsets channel 9 but is a secondary trace at the crossing of channel 1 (Figure 3.2).

Exposures of the fault zone reveal that dips of individual fault planes vary from nearly vertical to 40 degrees (Figure 3.1A-E). The shallower dips are commonly on auxiliary structures, not the principal fault plane. Faults on the southwestern side of the fault zone commonly dip northeastward, whereas fault planes on the northeastern side of the fault zone often dip to southwestward. This pattern is typical of moletracks along strike-slip faults and results in a fault zone that is narrower at depth than at the surface. Moreover, the dip angle of an individual fault sometimes varies considerably within a distance of few centimeters (e.g. F4 in Figure 3.1B and C). Thus, in the map view (Figure 3.1F), the faults are shown in a simplistic way, and are generally shown where they intersect the ground surface.

Interplay between adjacent fault traces can be complex. Figure 3.2 provides an example, from our excavations of the volume upstream from the fault. The figure has been composed of a series of cuts made nearly parallel to the faults and shows four reference features offset by the fault. Note that the base of unit 30 in channel 1 is offset across Fault 1 but not across Fault 2, whereas the thalweg of channel 1 is cut by Fault 2 rather than Fault 1. This indicates that during the offset of channel 1 and its fill, rupture occurred on Fault 2 at depth but shunted onto Fault 2 via a sub-horizontal ramp that resides just above the floor of channel 1. During an earlier rupture Fault 1 and Fault 2 connected via another ramp at slightly greater depth. This indicated by the fact that channel 7 is cut off by Fault 1, but older and deeper channel 9 is by Fault 2, instead.

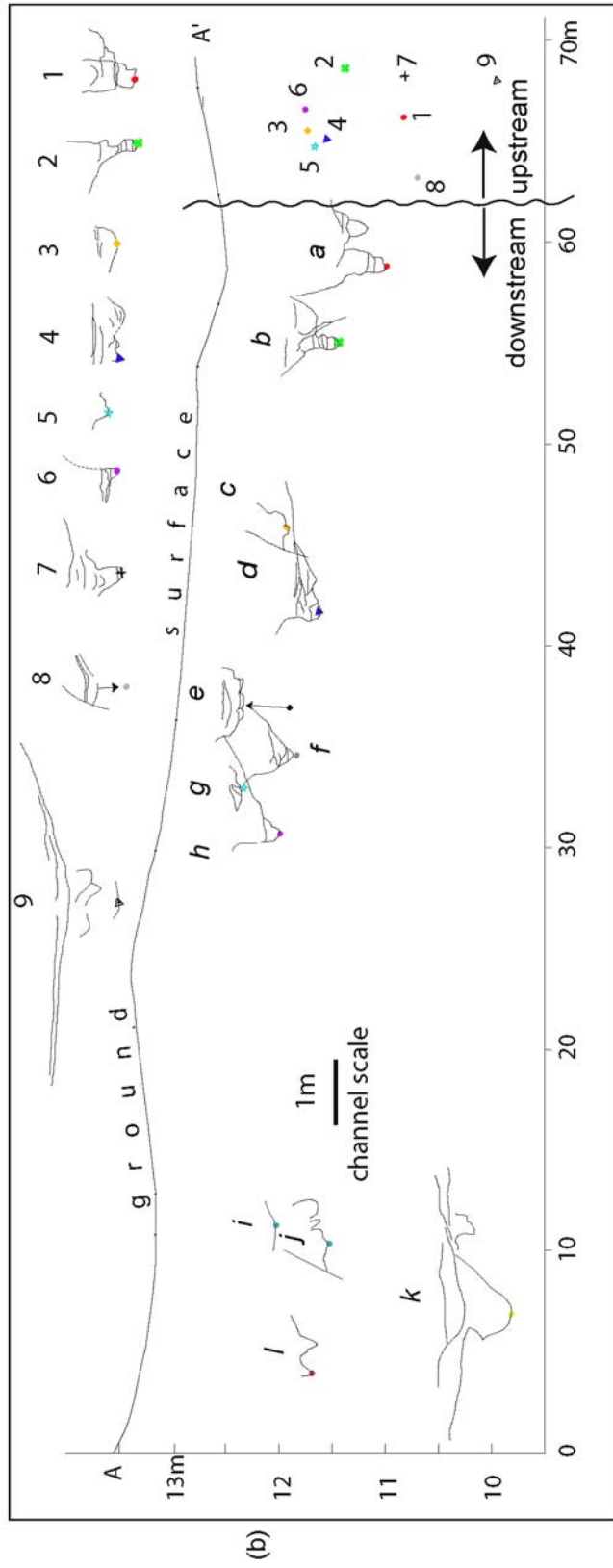
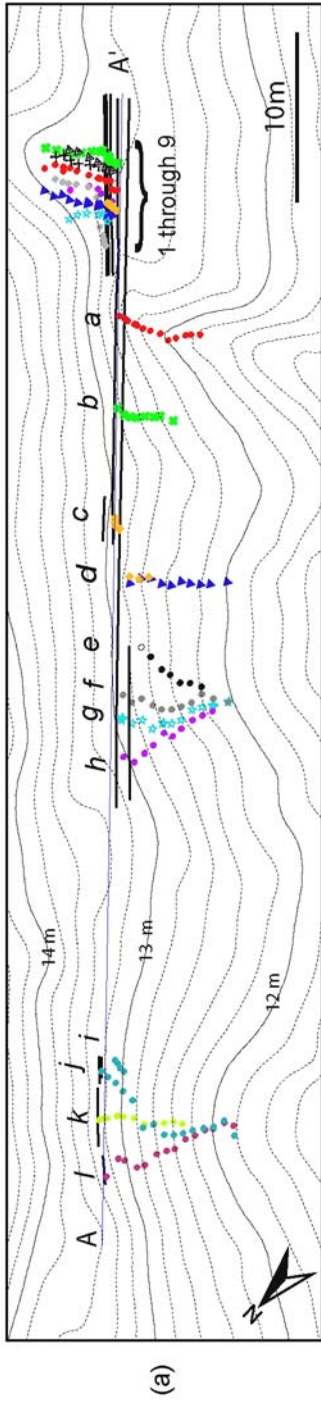
### 3.3 Channel correlation

#### 3.3.1 Recapitulation of basic channel geometries

Our excavations exposed 12 nested channels on the downstream side of the San Andreas fault and revealed 9 channels on the upstream side. Figure 3.3a shows the geometry of these channels in map view. Each color represents a different channel and each symbol represents one measured location of a channel thalweg. Figure 3.3b is a vertical plane along the fault, which depicts the cross-sectional shapes and simplified stratigraphy of these channels. In this figure, the colored symbols indicate the vertical and horizontal positions of downstream channels *a* through *l* and upstream channels 1 through 9, where they intersect the fault. The symbols correspond to those in Figure 3.4a. The shapes of the downstream channels appear above the symbols, without any vertical exaggeration. The channel geometries for the upstream channels appear in a line above the ground surface, separate from the locations of their thalwegs, since these channels are nested so close together. Figure 3.3 helps us summarize several primary observations about the channels that were made in Chapter 2. First, the four channels farthest from the upstream channel (*i* through *l*) intersect the fault at different points, but merge downstream in a broad topographically obvious channel. Among these four, the one that traverses the center of the topographic swale, channel *k*, is the oldest and deepest. Channels *l*, *i* and *j* feed into the channel from the north and south. Thus, these three appear to have fed into the older channel from positions not quite aligned with the downstream channel.

The second general observation made clear by Figure 3.4a is that no channels or young alluvial fan beds appear in the 15 to 20 m southeast of channel *i*. A third important observation is that six channels occupy the broad topographic swale in the middle

Figure 3.3. (Next page) Summary of channels exposed at this site in map view (a) and cross-sections (b). The map view shows the locations of all channel thalwegs, superimposed on a 20-cm-contour topographic map; the cross-sections show the depths and shapes of the channels along the fault.



of Figure 3.3. Four of these, e, f, g and h cluster near the northwestern edge of the swale. Among these, the oldest one is f, the one that trends at the highest angle away from the fault. The other three channels in this fan-shaped cluster fed into this older channel from upstream positions slightly misaligned with the older downstream channel.

The two channels, d and c lie beneath the other edge of the middle topographic swale. Channel c re-occupied d after d was first offset.

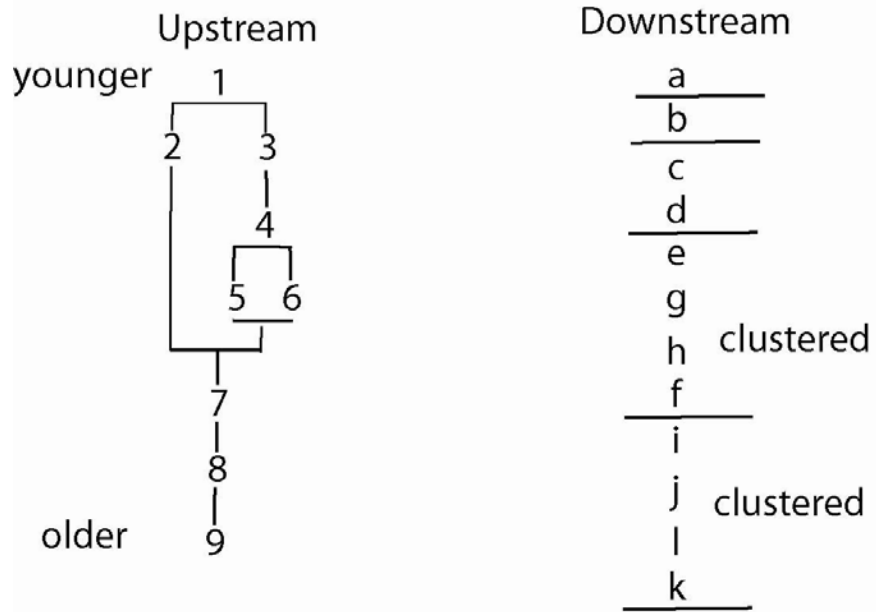
A fourth important observation is that channel b is the only channel without an associated topographically visible channel. It exits the fault at nearly a right angle. A fifth important observation is that channel a is a solitary channel and occupies the downstream swale closest to the upstream channel. This channel and channel b probably merge about 15 m downstream from the fault, judging from the topography. The sixth and final primary observation is that the 9 upstream channels cluster just upstream from the fault zone, but intersect the fault at different places along a distance of about 8 m. Channel 9 is the deepest and oldest upstream channel; channel 1 is the youngest.

### **3.3.2 General criteria for channel correlation**

Figure 3.3b also provides a first hint of possible correlations of channels across the fault. Based upon their cross-sectional shapes, alone, for example, we could propose that channels 1, 2, 3 and 4 correlate with channels a, b, c, and d, respectively. These hypothetical correlations would be consistent with the relative ages of these channels: From stratigraphic relationships, 1 is older than 2, which is older than 3, which is older than 4. And, based upon their position along the fault, channel a is older than b, which is older than c, which is older than d. By the same two criteria, relative age and channel shape, we might hypothesize that channels 9 and k are also correlative. Such correlations are internally consistent, but not compelling. That is, they are a necessary but not a sufficient basis for making the correct correlations.

Fortunately, more than just these two criteria are available for assessing correlations. In

(a)



(b)

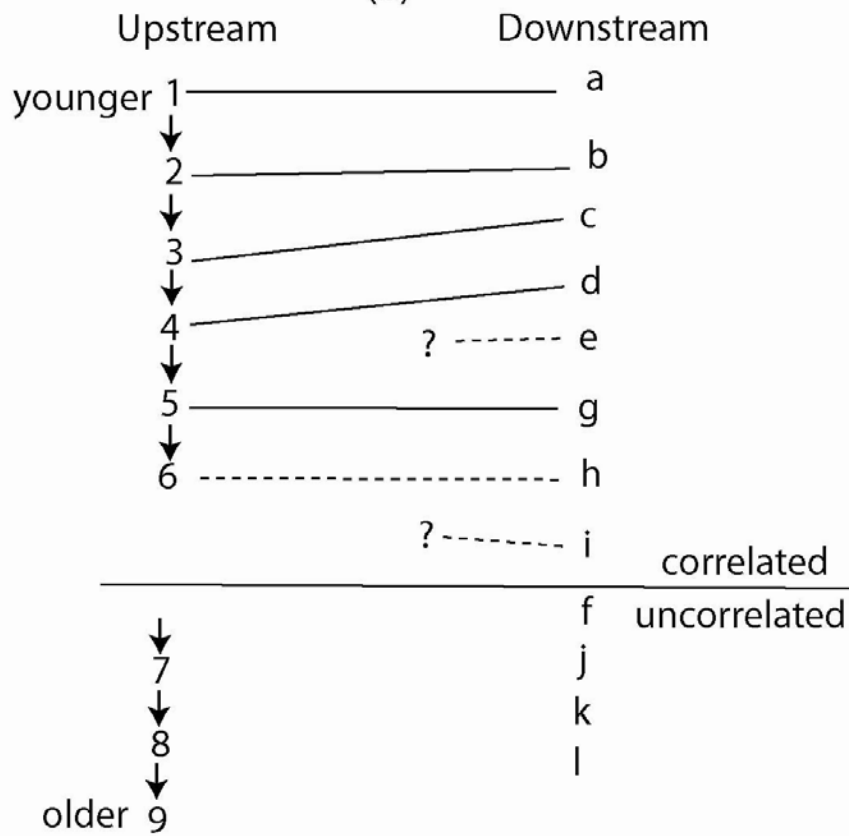


Figure 3.4. (Previous page) (a) The relative ages of upstream and downstream channels. The upstream sequence is based on cross-cutting relationships. Ambiguities in the sequencing of channels 2 and 3 and 5 and 6 result from erosion, which destroyed direct contacts between these channels. On the downstream side, age is assumed to increase with the distance from the upstream trench, with a couple of exceptions that are constrained by stratigraphic relationships. Channels f and k are much older channels that came from drainages southeast of the excavated volumes. Ambiguities appears as bifurcations. (b) Correlation of upstream and downstream channels, based on their temporal ordering and the matching of stratigraphy within channels. Solid lines designate confident correlations. Dashed lines indicate uncertainty.

addition to channel shape and position, three other considerations are important in making *bona fide* correlations. These are 1) the similarity of stratigraphy within the channels 2) the similarity of the angles at which channels enter and exit the fault and 3) age constraints from  $^{14}\text{C}$  dates on charcoal extracted from channel strata. We use all five criteria in proposing correlations, below.

First, we begin by ordering the relative ages of the channels on each side of the fault. Figure 3.4a summarizes the upstream and downstream sequences, based on the information presented in Chapter 2. On the upstream side of the fault, the relative ages of many of the channels are clear from their cross-cutting relationships. The figures and text of Chapter 2 demonstrate that channel 1 is clearly younger than channels 2 and 3. Channel 3 is clearly younger than 4. And channel 4 is younger than both 5 and 6. Channels 5 and 6 cut channel 7 and, hence, are surely younger. By virtue of its cross-cutting relationship, channel 7 post-dates channel 8, which clearly post-dates channel 9. Two uncertainties exist because erosion has removed critical relationships: The stratigraphic position of channel 2 in relation channels 3, 4, 5 and 6 is uncertain, because channel 2 was isolated from these channels by the incision of younger channel 1. Likewise, an uncertainty in the relative ages of channels 5 and 6 exists because they are separated by channel 4.

On the downstream side of the fault, the order of formation of the channels may be inferred from their distance from the nearest upstream channel and, where available, their cross-cutting relationships (Figure 3.4a). By this criterion, channel a would be the youngest, by virtue of its close proximity to the upstream channel. And channel l would be the oldest, because it sits farthest from its hypothetical upstream source. This criterion would, of course, be inappropriate

for any channel that originated from upstream channels farther to the southeast, but it is a useful starting point.

Figure 3.4a illustrates a problem that arises immediately upon showing this hypothetical ordering of upstream and downstream channels -- the downstream side has three more channels than the upstream side. There are two plausible explanations for this mismatch: 1) upstream channels have been obliterated by the incision of younger channels or 2) the downstream sequence contains channels that do not originate from the upstream channel. We consider both possibilities below.

In matching of upstream and downstream channels, it is a necessary but not a sufficient condition that these relative ages be obeyed. In the discussions that follow, we also investigate internal stratigraphy, entry and exit angles, and radiocarbon ages to propose correlations of the channels. The correlations that we will propose appear in Figure 3.4b. Notice that the older channels, both upstream and downstream, do not correlate with other channels within the excavation.

### **3.3.3 Channel pairs**

#### **3.3.3.1 Channel 1-a**

We begin with the hypothesis that the youngest channel pair, channels 1 and a are correlative. Three lines of evidence support this. First, channel 1 is the youngest channel on the upstream side, and channel a is the closest of all the downstream channels to the upstream channel. Thus the proposed correlation meets our relative-age criterion.

Second, the shapes of the channels are similar. But, in considering the match of channel shapes across the fault, we must first evaluate just how similar channel shapes need to be in order to be plausibly correlated across the fault. Perhaps the best way to determine this is to examine the natural variations in channel shape along profile. These variations are large. Consider, for example, the variations in the profile of channel 1, depicted in Figure 3.5. Generally, only the principal characteristics of the channel continue from one exposure to the next. These are the

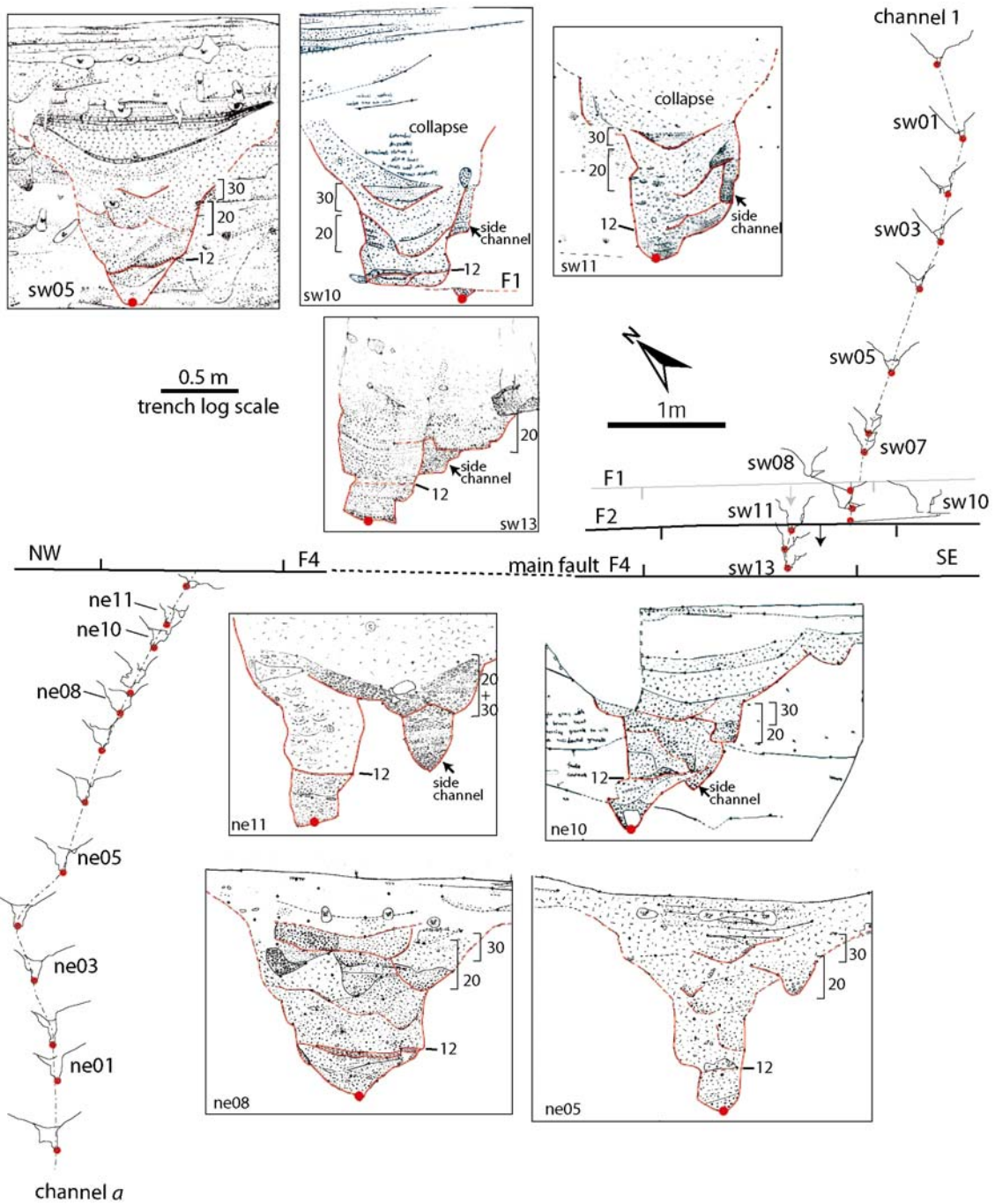


Figure 3.5. The correlation of channel 1-a is based on the similarity of stratigraphy and morphology in channels 1 and a. The 8 vertical exposures show examples of the stratigraphic details within the channels. In map view, the red dots indicate the geographic position of the deepest channel thalweg. Outlines of the channel shape and key internal contacts allow viewing the changes in the features along the channel. Note that the scale of the detailed maps of stratigraphy is larger than that of the map.

basic V-shape geometry of the channel and its depth. Second-order features, such as overhangs and other details of the channel walls, commonly are not continuous from exposure to exposure. Thus, we should require only that the first-order characteristics correlate across the fault.

The shapes of channels 1 and a are quite similar immediately upstream and downstream from the fault. In downstream exposure ne11, channel a is about 2 m deep and consists of a deeper and a shallower channel, separated by an uneroded septum (Figure 3.5). The deeper channel has a nearly flat base, about 40 cm across. In upstream exposure sw13, channel 1 consists of only one channel. But, like channel a it is about 2 m deep. Channel 1 is also asymmetric, with a steep and a shallow wall. This asymmetry would be very similar to the shape of channel a in exposure ne11, if one removed the septum between the principal and auxiliary channels in channel a. Without this septum channel a would have the same asymmetry as channel 1 – steep on the northwest and shallow on the southeast.

A close inspection of the internal stratigraphy of the upstream and downstream channels supports this interpretation, because it shows that the smaller channel has longitudinal continuity. Close to the fault (in exposures sw10 through sw13), this “side channel” cuts to the southeast and is plastered onto the southeast wall of the older main channel (Figure 3.5). Downstream from the fault, the channel remains on the southeast side of the main channel from exposures ne11 through ne09, and merges into the main channel in the rest downstream exposures. The correlation of channels 1 and a is supported by other details of the stratigraphy within the channels, as well. In particular, units 12, 20 and 30 are comparable. Unit 12 is a diagnostic thin bed of laminated fine sand to silt that mantles the underlying basal, coarse-grained deposits of both channels (Cf. exposures sw05 and ne08; Figure 3.5 ). It occurs in most upstream and downstream exposures.

Unit 20 constitutes the fill of the side channel. It is similar on both sides of the fault, in near-fault exposures. Typically, unit 20 is a 25-cm-thick group of massive, loose, well-sorted pebbly gravels and sands. Unit 30 is the bed immediately pre-dated the offset event. It consists of two well-sorted fluvial layers, which form an inverse graded sequence; the lower bed is finer grain-sized than the upper one (Cf. exposures sw10 and ne08; Figure 3.5). It is continuously correlative among most exposures. However, it is unrecognizable in exposures nearest to the

fault, probably due to the near fault disturbance, as this bed was probably at the ground surface during rupturing.

In summary, channel-wall geometry, internal stratigraphy and relative age all support the hypothesis that upstream channel 1 and downstream channel a are correlative. Later, we will investigate how this correlation constrains post-channel offset. But first, we will assemble correlations for other, older channels.

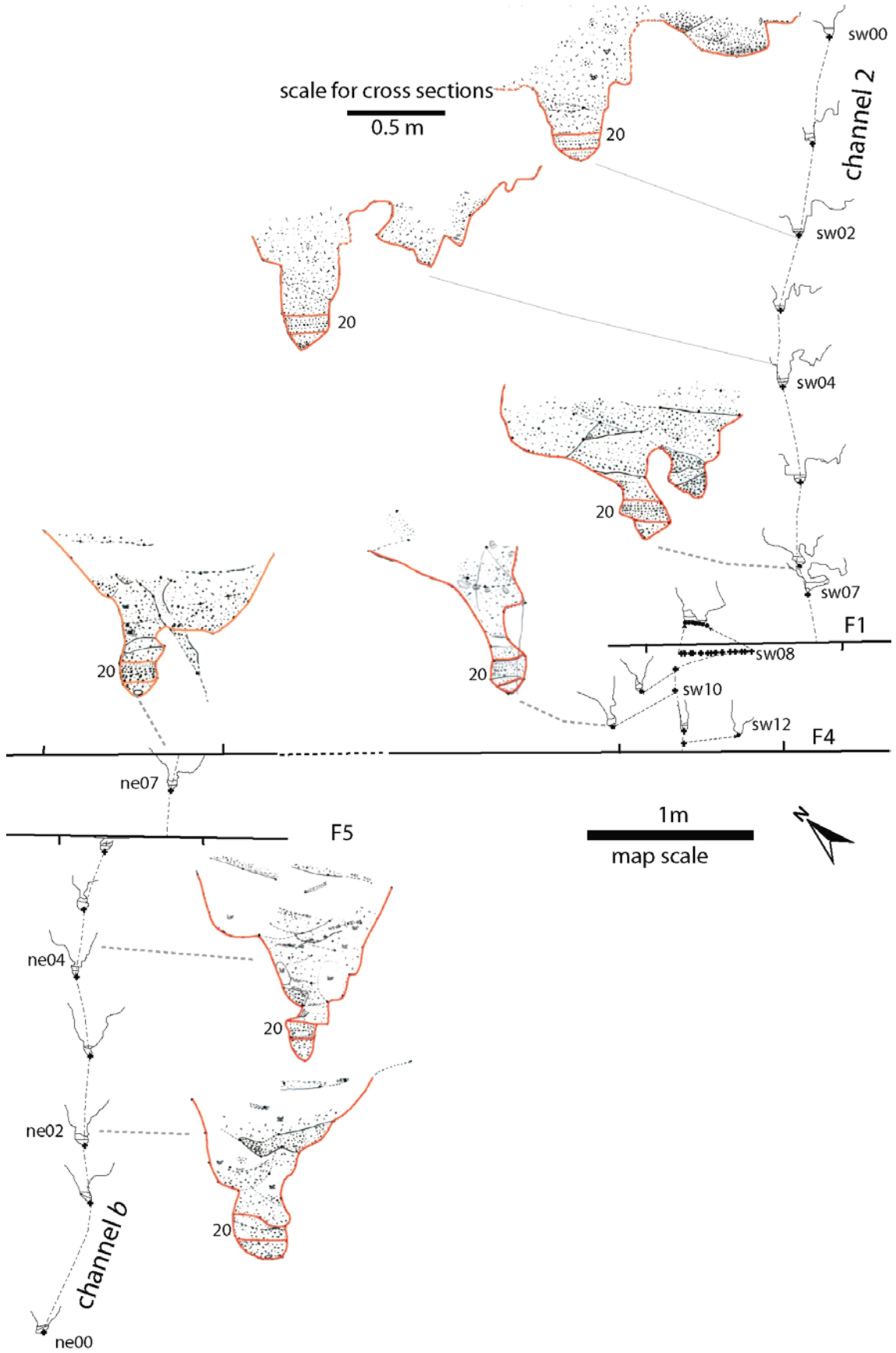
### **3.3.3.2 Channel 2-b**

Of all our proposed correlations, the match of channels 2 and b is the strongest. The strength of the correlation lies in the similarity of their channel shapes and internal stratigraphy. Recall that from the cross-cutting relationships in the upstream exposures, one can not determine whether channel 2 is older or younger than channel 3 (Figure 3.4a). The strong similarity between downstream channel b and channel 2 indicates that, in fact, channel 2 is younger than channel 3.

Figure 3.6 displays the outlines of the two channels. As in the previous figure, the deepest thalwegs of each channel appear in their correct geographic positions relative to one another, except that some meters have been removed along Fault 4 to allow all data to appear on the same page.

The shapes of both channels b and 2 are about 1.5 m deep and very narrow. These two channels have, in fact, the lowest width-to-depth ratio of all the channels at the site. The bottom of the channels is either circular or pointed. A side channel in the upper reach of the channel 2 merges with the main channel just upstream from the fault zone. Thus, the shape of channel 2 in its lower reach is as simple as that of channel b.

Figure 3.6. (Next page) The unusual narrowness of channels 2 and b and the similarity of their internal stratigraphy provide definitive evidence for their correlation. The dotted portion of the fault indicates much of the fault length between the upstream and downstream segments was removed to enable presentation of the comparison on a single page. Note the different scales for different features.



The strata within channels 2 and b also correlate exceptionally well. Both channels have four characteristic units, 10, 20, 30 and 40. Chapter 2 contains detailed descriptions of these units (Figure 2.10 and 2.27). Among these, unit 20 is the most diagnostic. This upward-fining sequence comprises horizontal-bedded thin layers of framework-supported, pebbles and sand. Within each layer, the sediments are remarkably well-sorted.

### **3.3.3.3 Channel 3-c and channel 4-d**

Based upon cross-cutting relationships, channels 3 and 4 are the 3<sup>rd</sup>- and 4<sup>th</sup>-oldest channels upstream from the fault. Similarly, channels c and d are the 3<sup>rd</sup>- and 4<sup>th</sup>-oldest channels downstream from the fault (Figure 3.4a). Let us begin by testing the hypothesis that channels 3 and c and 4 and d are correlative. We consider the match of channels 3 and c and the match of channels 4 and d together because the stratigraphy of channel c is superposed upon channel d downstream from the fault.

The similarity of channels 4 and d strongly suggests that they are correlative. The morphologic features common to both channels include their “W”-shaped channel profile, their large width/depth ratio, their 1.2-m depth beneath the surface near the fault zone, and the fact that they both approach the fault at nearly right angles (Figure 3.7). Furthermore, both upstream and downstream channels experienced two cut-and-fill sequences. On both sides of the fault, the second down-cutting reached as deep as the first phase and widened the channels by scouring the southeastern bank.

The deposits within channels 4 and d are also similar. Sediment within both channels is predominately massive, poorly sorted sandy, pebbly debris. The only fluvial units within this colluvial debris are thin basal wisps of granule- and pebble- dominated fluvial deposits above each of the basal channel scours.

Having established a likely correlation between channels 4 and d we can now consider plausible upstream correlations of channel c. Recall from Chapter 2 that channel c consists of two parts. Channel c1 is superimposed on channel d downstream from the fault zone but diverges eastward away from channel d near the fault (Figure. 2.11). Channel c2 is within and parallel to downstream segments and the similarity of their stratigraphic sequences. This match is also consistent with

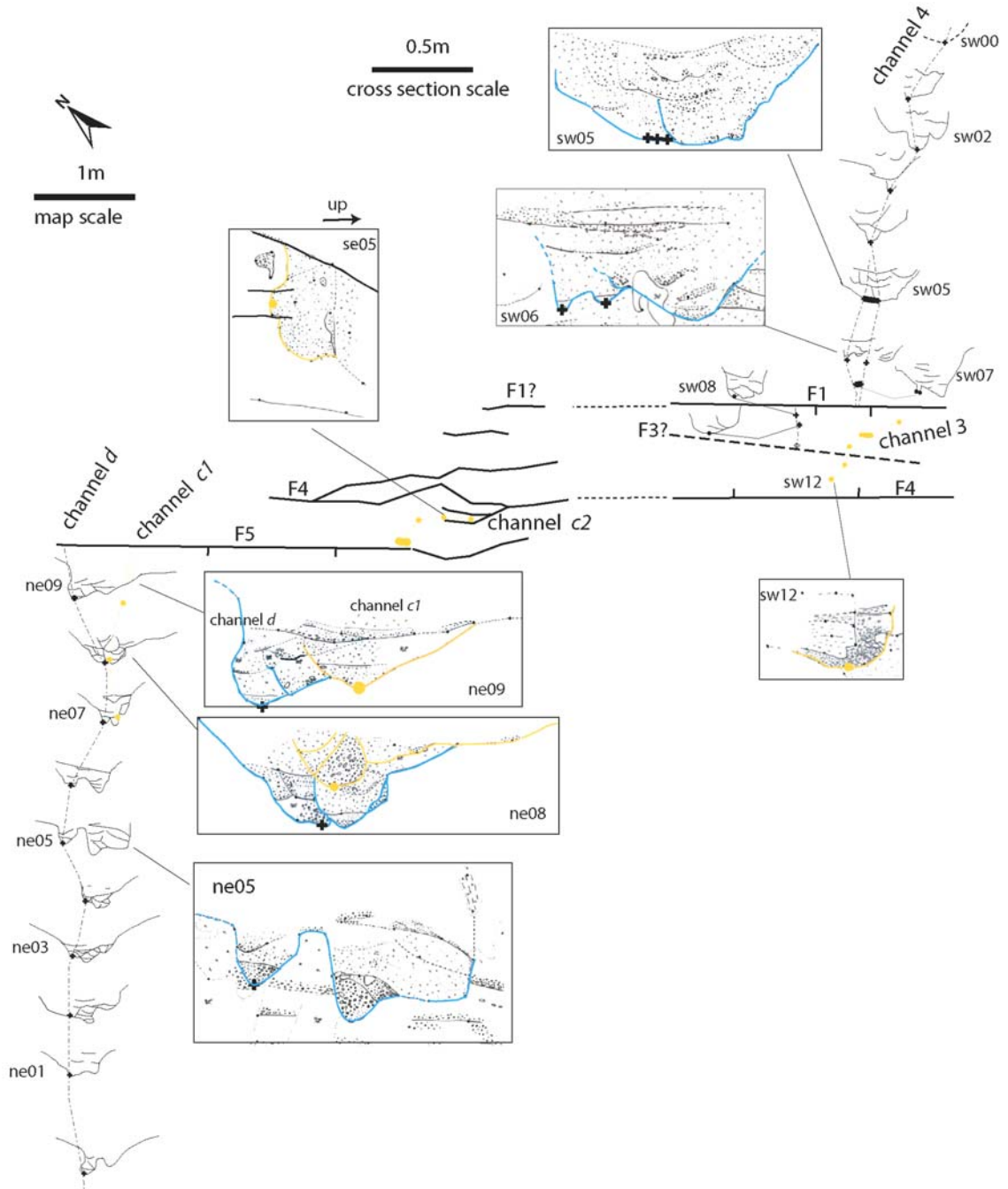


Figure 3.7. Map and cross-sections of channels 4 and d illustrate the basis for correlation of these two channels. The correlation is strongly suggested by the W-shaped channel profiles of both up- and the match of the deflected channels 3 and c.

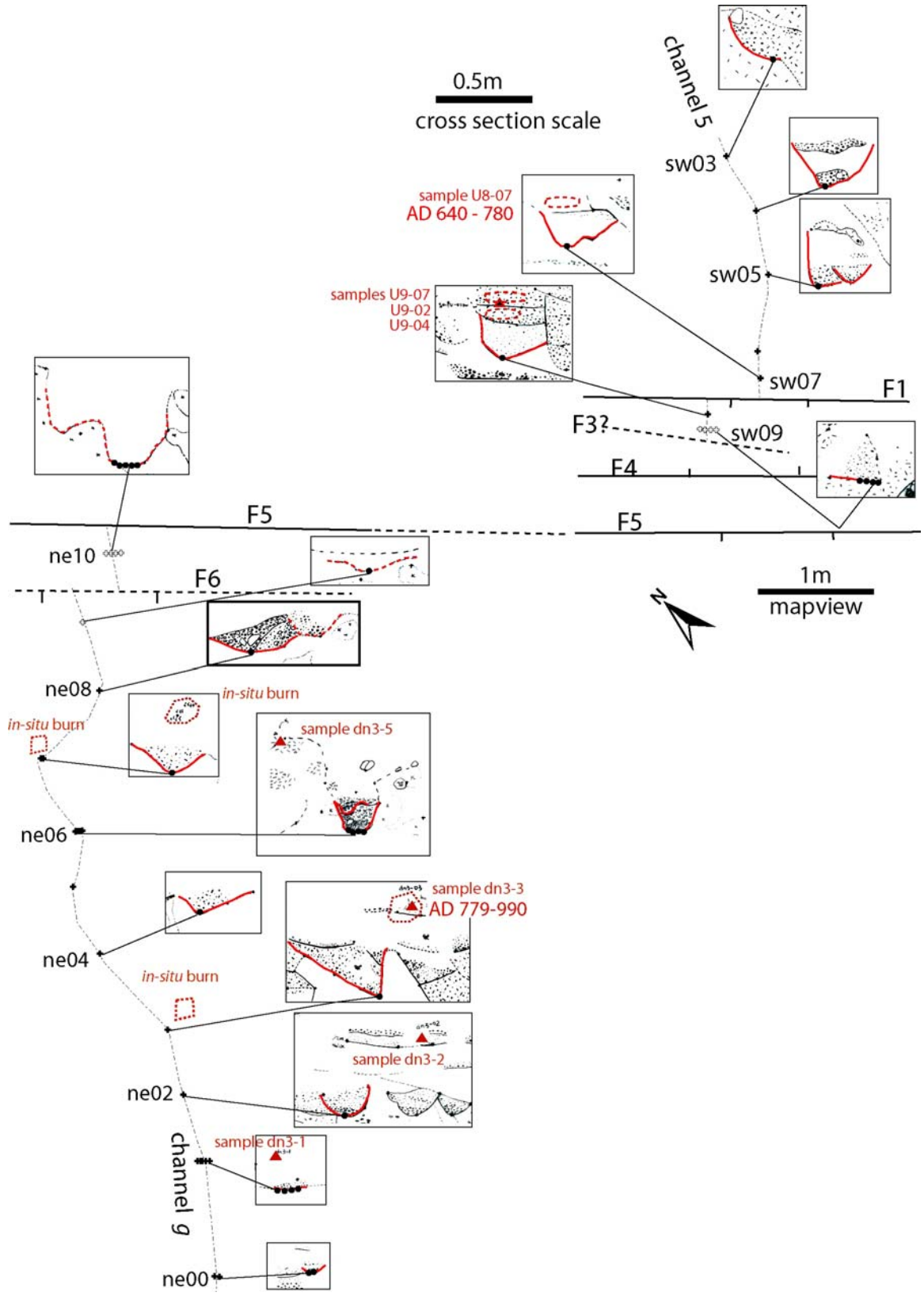
the fault zone just a few meters to the southeast. The similarities of channels c1 and c2 suggest that they are correlative, but were offset a couple meters by dextral slip along Fault 5.

The salient question, now, is whether channel c2 is correlative with upstream channel 3. The stratigraphic position of channel 3 is proper for such a correlation, since it is demonstrably younger than channel 4 (Chapter 2, section 3.3.5). The fact that both channel c2 and channel 3 run nearly parallel to the fault and within the fault zone also supports the correlation. The similar shapes of channels 3 and c2 provides further support for correlation. Both have a clear, circular channel profile. Strata within both channels vary greatly along profile, so we can not marshal this as strong evidence for correlation. However, in both channels the thickness of the strata is about 30cm in exposures near the fault.

#### **3.3.3.4 Channel 5-g**

The next correlation of upstream and downstream channels is more difficult to make, because of ambiguities in the relative ages of channels both upstream and downstream from the fault. Upstream channels 5 and 6 antedate channel 4, but there are no cross-cutting relationships to tell which is the younger of the two (Chapter 2, section 2.3.3.4 and Figure 2.29). Downstream channels e, f, g, and h are nested together, but not so closely that all the requisite cross-cutting relationships are available for knowing their relative ages (Chapter 2, section 2.3.2.5 and Figures 2.14 and 2.15). Cross-cutting relationships do show, however, that channel f is the oldest of the four, and that channel h is older than channel g, and that channel e is younger than channel f. Additionally, we have reason to suspect that channel f is older than h. This leaves us with this temporal ordering:  $f > h > g$  and  $f > e$ . Channel e does not reach the fault, so we would not expect to be able to find a match for it across the fault. This leaves downstream channel g as the channel to match with either channel 5 or 6, upstream.

Figure 3.8. (Next page) Summary of evidence for the correlation of channels 5 and g. Their size and stratigraphy are similar. The similar ages of two radiocarbon samples from the two channels support the correlation.



The best match is between channel *g* and channel 5 (Figure 3.8). The basis for this proposed match is channel geometry, stratigraphy and datable carbon in both channel segments. Both channels are narrow and shallow in mappable channel stratigraphy ( $\leq 40$  cm wide and  $\leq 40$  cm deep). Unlike channel 6, both are roughly as wide as they are deep and are relatively flat-bottomed. Their stratigraphy is similar --predominantly well-sorted fluvial sands with sparse pebbles, overlain by poorly sorted sandy colluvium (Figure 3.8). In neither channel is there a consistent record of multiple incisions and aggradations.

Further support for the correlation of channels 5 and *g* is the presence of charcoal in both channels. We will discuss the radiocarbon ages of these samples in much more detail later in this chapter, along with ages determined for other samples at the site. For now, let it suffice to say that samples from both channels yielded similar  $^{14}\text{C}$  ages. The slight difference in age may result from the fact that the younger age comes from a sample (dn3-03) that was higher above the fluvial channel fill than the sample that yielded the older age (u8-07).

### **3.3.3.5 Tentative correlation of channel 6-h**

The next upstream channel to match with a downstream segment is channel 6. Erosion of much of channel 6 by younger upstream channels makes matching of this channel a special challenge and less certain. Nonetheless, the correlation we suggest is the most plausible one. The bases for correlation are the channel size, fill and its orientation.

The angle of intersection of channel 6 with the fault is the strongest basis for correlation (Figure 3.9). In Chapter 2 we showed that the channel approaches the fault zone at a distinctly acute angle. It is, in fact, the only upstream channel to trend southward as it approaches the fault. We might expect, then, that its downstream equivalent would also trend southward away from the fault. Of all the downstream channels, only channels *h* and *l* have flow directions near the fault that are compatible with the deflection of channel 6. But channel *l* is unlikely a match, because it is much larger than channel 6. It also has a more complex sequence of cut-and-fills and a more complex cross-sectional profile (Figure 2.18). Channel *h* is the most likely match, even though

its thalweg appears to bend eastward at the fault. This apparent bend is most probably not a bend at all, but rather the result of offset along Fault 6, between the mapped exposures.

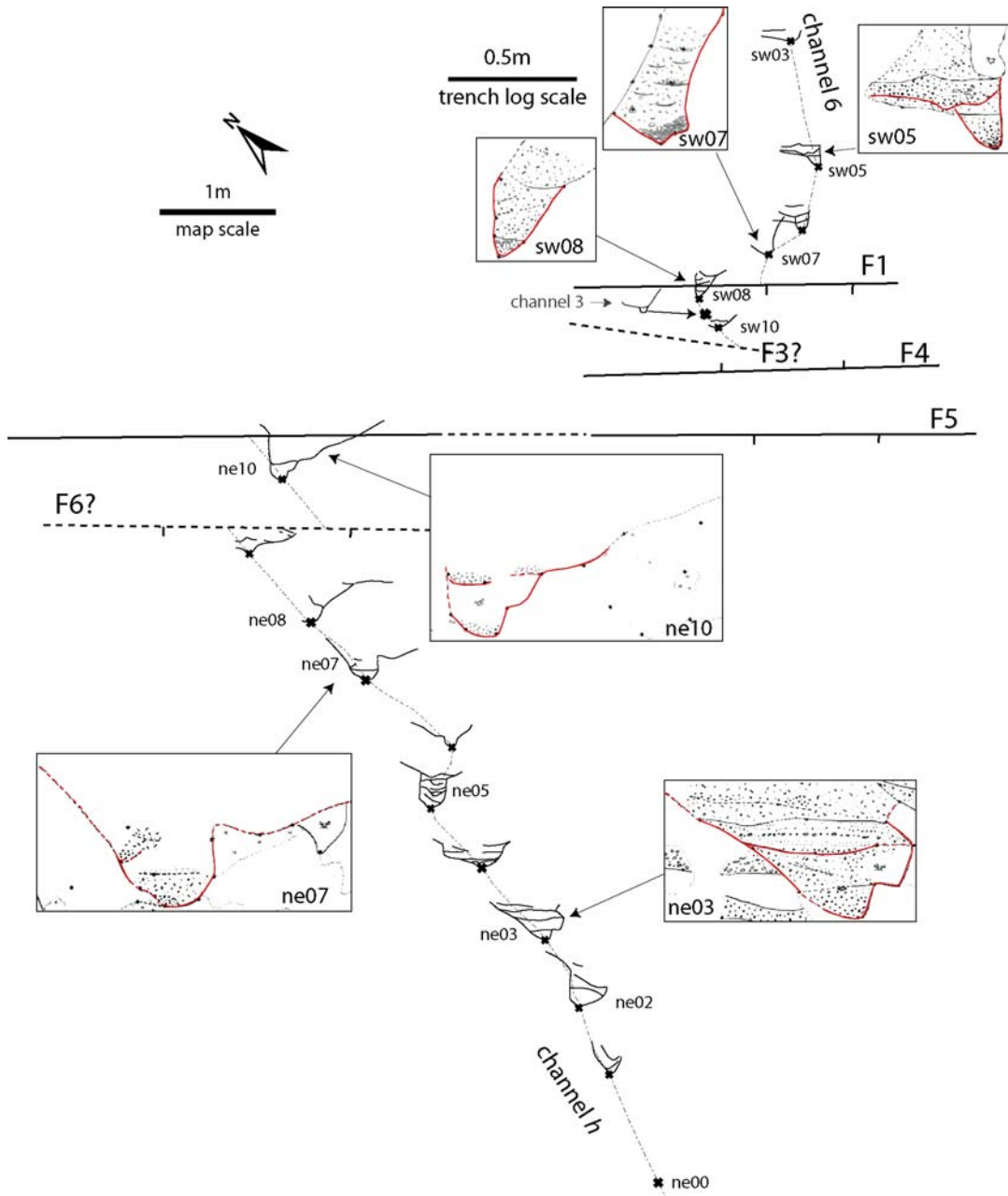


Figure 3.9. The similar southward flow directions of channels 6 and h suggest that these channels match. Their internal stratigraphy is also similar.

The general resemblance of the stratigraphy within the channels also favors correlation of channels 6 and h. Both channels have two well-sorted gravely to sandy fluvial beds near their base, separated by a poorly sorted 25-cm-thick colluvial deposit (Cf. exposures sw05, ne10 and ne03; Figure 3.9).

### **3.3.3.6 Correlations between older channels**

#### **Possible correlations with channel 7**

Up to this point, we have made plausible correlations between 5 sets of upstream and downstream channels. Three upstream channels remain to be matched with downstream channels. From youngest to oldest, these are channels 7, 8 and 9 (Figure 2.21). Five downstream channels remain unmatched – f, i, j, k and l (Figure 2.14 and 2.18). None of these channels appear to match across the fault.

We begin with a consideration of the possible downstream matches to upstream channel 7, the youngest of the remaining three unmatched channels. Candidate matches should exit the fault at about the same angle that channel 7 approaches the fault, that is, at nearly a right angle (Figure 2.33). Like channel 7, they should also have a depth of a half meter or more and a width at its shoulder of about a half meter (Figures 2.21 and 2.32). Furthermore, their fill near the fault should be sparsely pebbly fluvial sand. Only one of the five remaining downstream channels within the excavation fits all of these requirements. Only channels f and k exit the fault at nearly a right angle. Channel k, however, is an implausible match, because it is about 1.5 m wide at the fault and is filled with coarse sands and pebbly, cobbly gravel there. Channel f is a plausible match. Its width and depth of fluvial fill at the fault are comparable with those of channel 7, and its fluvial fill sparsely pebbly sand.

Despite the plausibility of a geometric and stratigraphic match between channels 7 and f, one relationship nixes the match. The match of channel 7 and downstream channel f requires six younger upstream channels (1 through 6) to rematch with only five downstream candidates (channels a through e). The number of candidates is already insufficient, let alone other constraints. If our correlations of channels 6 and h and channels 5 and g are correct, we cannot

match channel 7 with the closest unmatched downstream channel *f* either. Channel *f* is about 2.5 m closer to channel 7 than channel *g* is to channel 6. Correlation of channels 7 and *f* would, therefore, require us to propose an episode of about 2.5 m of left-lateral slip. This is a possibility we are unwilling to entertain, and so we are unable to underwrite any match with channel 7.

### **Possible correlations with channel 8**

Channel 8 is unique among the nine upstream channels in that it bends sharply northwestward just upstream from the fault and intersects the fault at a very low angle (Figure 2.33). This geometry implies diversion around a shutter ridge at least 3.5 m long. No other unmatched downstream channel exits the fault zone toward the northwest at such an acute angle. But channel *j* comes close and is thus the only candidate match. It diverges westward from the fault zone at an angle of about 45°. One could well argue that within the fault zone, these two channels could meet at the same angle. Channel *j* is also comparable in dimensions to channel 8 in the nearest cut to the fault (Figure 2.19), even though along most of its exposed length, channel *j* is an order of magnitude narrower, shallower than channel 8. The difference in internal stratigraphy however, argues against the match. Channel 8 is filled with massive poorly-sorted gravely sand whereas channel *j* is filled with well-sorted sand and fine gravel.

### **Possible correlations with channel 9**

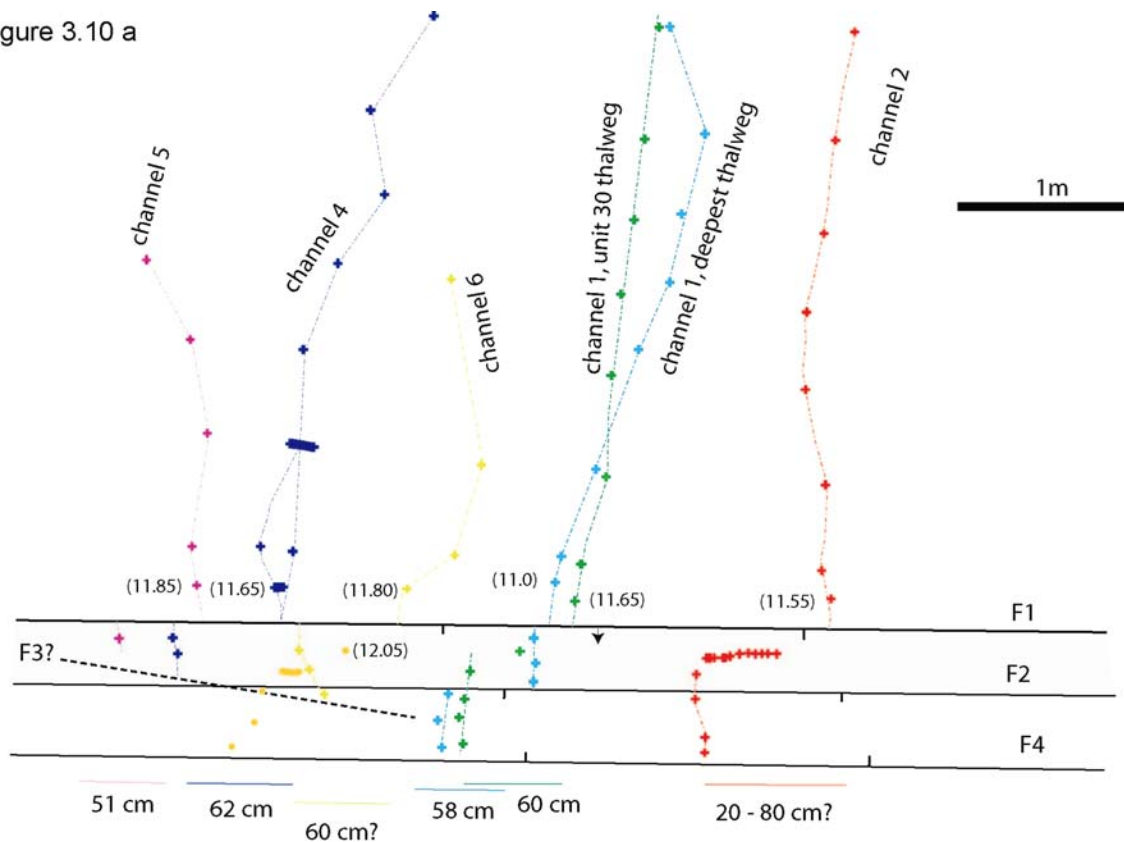
The oldest upstream channel is channel 9. Figure 2.21 and 2.32 show that near the fault it is about 1m wide and has a shoulder about 1 m wide. Much of the channel fill is poorly sorted colluvium, but there are fluvial deposits nestled within the colluvium. Furthermore, Figure 2.33 shows that channel 9 approaches the fault at a high angle. Any plausible match downstream should have similar geometric and stratigraphic characteristics.

The most plausible downstream match is channel *k*. It is the oldest of the most distant channels, and its width is a bit larger, but similar. At the plunge pool near the fault, its depth is similar. But, its fill is exclusively coarse, fluvial sand and gravel. To claim that the channel correlates with channel 9, one would have to explain this difference. Thus, there does not appear to be a plausible match for channel 9 on the downstream side.

### 3.4 Measurement of offsets

Since we have matched 6 pairs of channels across the fault, we can proceed to measure their offsets. The offset of each pair represents the cumulative displacement since the abandonment of the channel. We will mainly use the deepest thalwegs of channels as offset piercing lines, but will also use other stratigraphic positions when they provide tight constraints. We are able to measure both horizontal and vertical offsets, because 3-D excavations and Total Station surveying enable us to reconstruct the channel geometries in three dimensions. The precision of the measurements is on the order of ten centimeters in horizontal, and is about what can be achieved measuring the offsets of a natural feature immediately after a rupture.

Figure 3.10 a



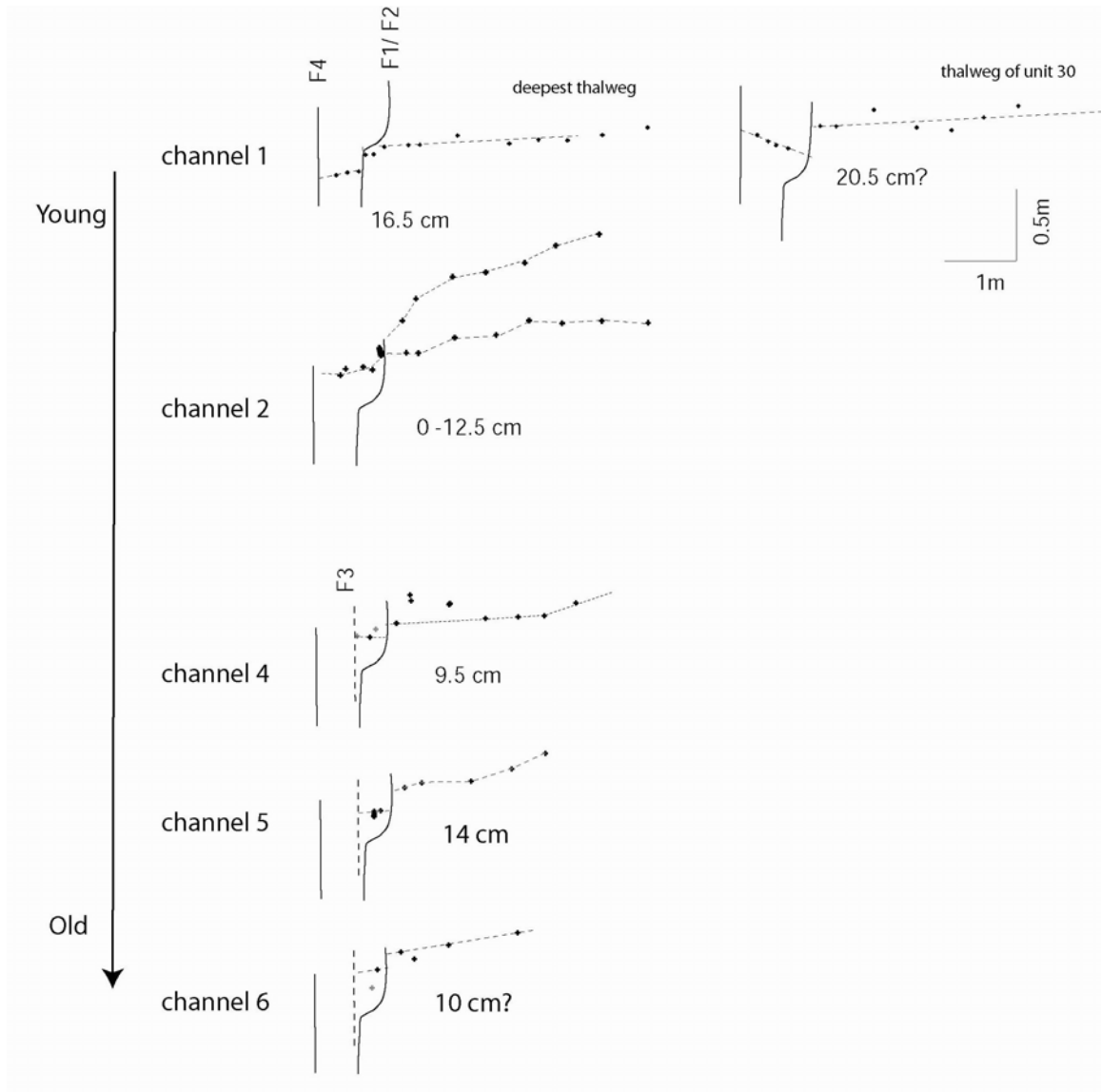


Figure 3.10. Horizontal (a) and vertical (b) offsets of channels of various ages on fault strands F1 and F2. (a) The youngest channel 1 is horizontally offset about 60 cm, the same amount as older channels 4, 5 and 6. The numbers in brackets indicate elevations of the channel thalwegs near Fault 1. (b) The vertical components of offset of channels 1 to 6 are also similar (10-16 cm). This suggests that these amounts of offset on Faults 1 and 2 occurred in a single event that post-dated channel 1.

### **3.4.1 Minor offset on Fault 1 and Fault 2**

We will first discuss the offsets of channels on secondary faults Fault 1 and Fault 2, because these secondary faults appear to offset channels 1 through 6 nearly identical amount. This discussion will avoid redundancy later when we measure the total offset of each channel pair.

Figure 3.10a is a map view of the thalwegs of channels 1 to 6 and their offset across Faults 1 and 2. Recall that Fault 2 is a shallow branch off Fault 1. To indicate the vertical slip transfer from Fault 1 to Fault 2 in a map view, we also show the elevation of each offset feature in the exposure nearest to Fault 1. Channel 1, both the thalweg of unit 30 and the deepest thalweg, is dextrally offset about 58 cm. The offsets of channels 4, 5, and 6 are almost identical, in the range of 51cm to 62cm. The difference in these numbers is more likely to represent the uncertainty in measurements, rather than to indicate multiple offset events. Faults 1 and 2 appear to have slipped only once after the down-cutting of channel 6, probably during the post-channel 1 event.

The vertical offsets of channels 1 to 6 across Fault 1/Fault 2 are similar, and in the range of 8 to 21 cm with southwest side going down (Figure 3.10b). The relatively larger range in vertical offset is probably because measurements of vertical offsets can be less accurate due to factors such as the rotation of the block within the fault zone. The undulation in channel floor also contributes considerably to the uncertainty.

We have not mentioned the offset of channel 2 across Fault 1/Fault 2 because the offset of this channel can be ambiguous. Channel 2 is broad and has relatively ill-defined thalweg near Fault 1 (In exposure sw08; cf. Figures 2.26f and 3.6). Because of this ambiguity, the dextral offset of channel 2 across Fault 1 has a relatively large range of 80 - 30 cm (Figure 3.10a). However, if channels both older and younger than channel 2 are offset nearly identical 60 cm, then channel 2 must also have offset this amount. The abnormal channel meander immediately downstream of Fault 1 could indicate a pre-existing fault scarp near Fault 1.

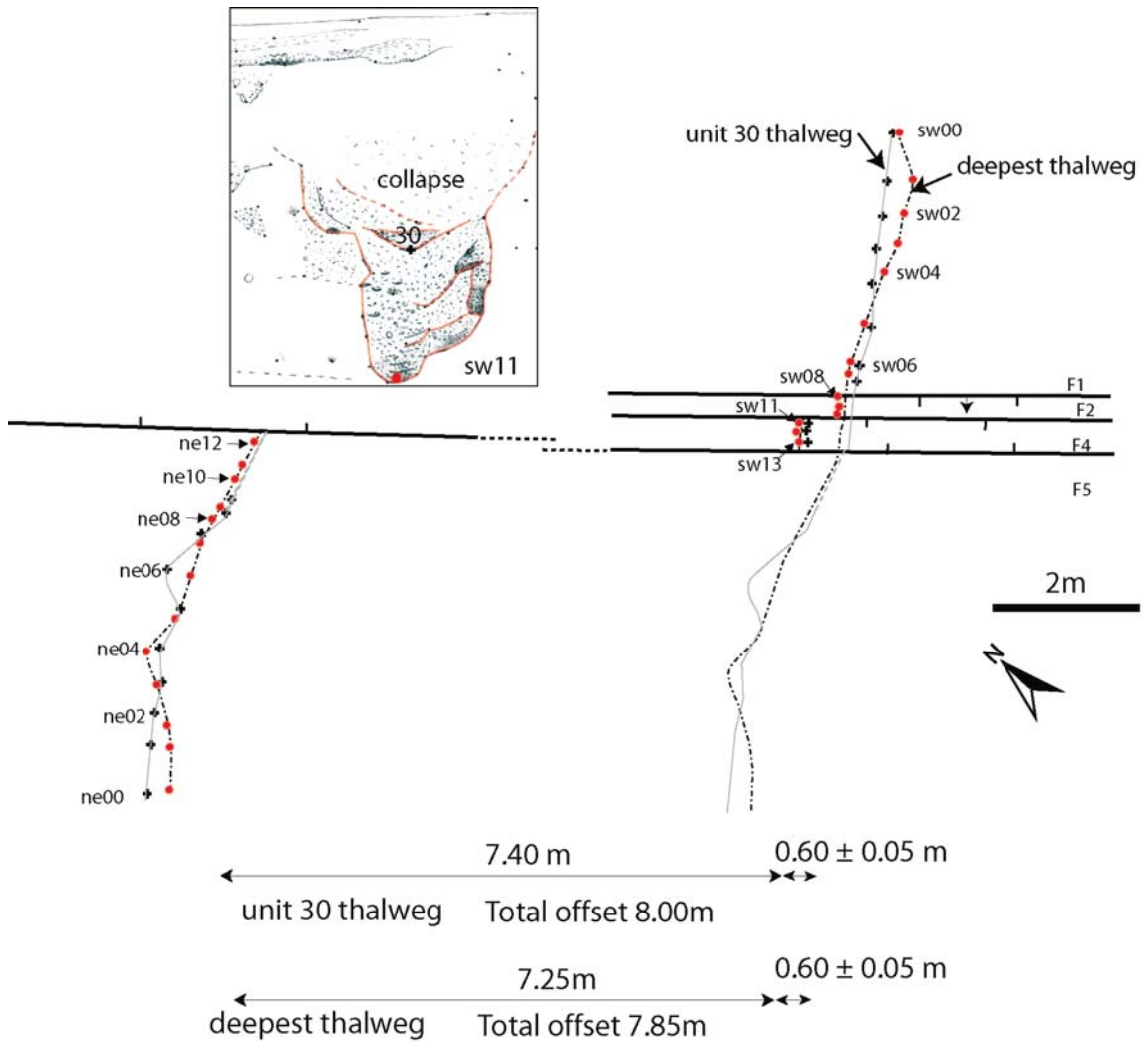


Figure 3.11a. Map view of offset channel 1-a. The thalweg and the base of unit 30 provide two piercing lines that show right-lateral slip is 7.8 - 8.0 m. Most of this (7.25- 7.40 m) is across the major strand, Fault 4.

Based on the measurements of offsets of channels of different ages, we conclude that Fault 1/Fault 2 offset channels 1 through 6 uniformly,  $60 \pm 5$  cm in horizontal and  $15 \pm 5$  cm in vertical.

### **3.4.2 Channel 1-a: 8m-offset**

Two piercing lines constrain the offset of channel 1-a. In addition to the deepest thalweg, the basal contact of unit 30 also provides a constraint (Figure 3.11a). These are the best-defined and most continuous pre-offset stratigraphic contacts within channel 1-a.

These two piercing lines constrain the right-lateral offset of channel 1-a to between 7.8 and 8.0 m. The deepest thalweg is offset across three strands a total of 7.85 m. This includes 7.25 m across the main strand, Fault 4 and 0.60 m across the Faults 1 and 2. The offset on the secondary faults is based on the best estimation of  $0.60 \pm 0.05$  m offset of multiple channels of various ages (Figure 3.3a). Our measurements of offset across all three strands have little uncertainty, since our mapping constrains the piercing lines close to the faults. In the case of the 7.25-m offset across the principal strand, Fault 4, for example, we have mapped the piercing lines to within just 10 to 20 cm of the fault. Hence, the extrapolation of piercing lines to the fault yields a trivial uncertainty of only a few cm, at most.

Figure 3.11a shows the piercing lines in their relative positions both before and after the latest offset. Note that after the restoration of the 7.85 m offset, the thalwegs of channel 1-a are aligned well. The offset of the thalweg of unit 30 is about 8.0 m. This measurement is about 20 cm larger than that for the basal thalweg, perhaps because it is less precise. Extrapolation to the principal fault from the downstream segment is greater for unit 30 because its location is not clear within 1 m of the fault.

Figure 3.11b displays the vertical offsets of channel 1-a across the entire fault zone. At the level of both piercing lines, the fault zone forms a shallow graben. Visual inspection suggests that the uncertainties in the measurements are a few centimeters. Offset of the deepest thalweg across the principal fault F4 is about 22 cm, down on the upstream side. Offset across the secondary fault is about 17 cm, down on the downstream side. Hence, net vertical offset across the graben is about 5 cm, downstream side up. This vertical offset is a mere 0.5% of the horizontal value.

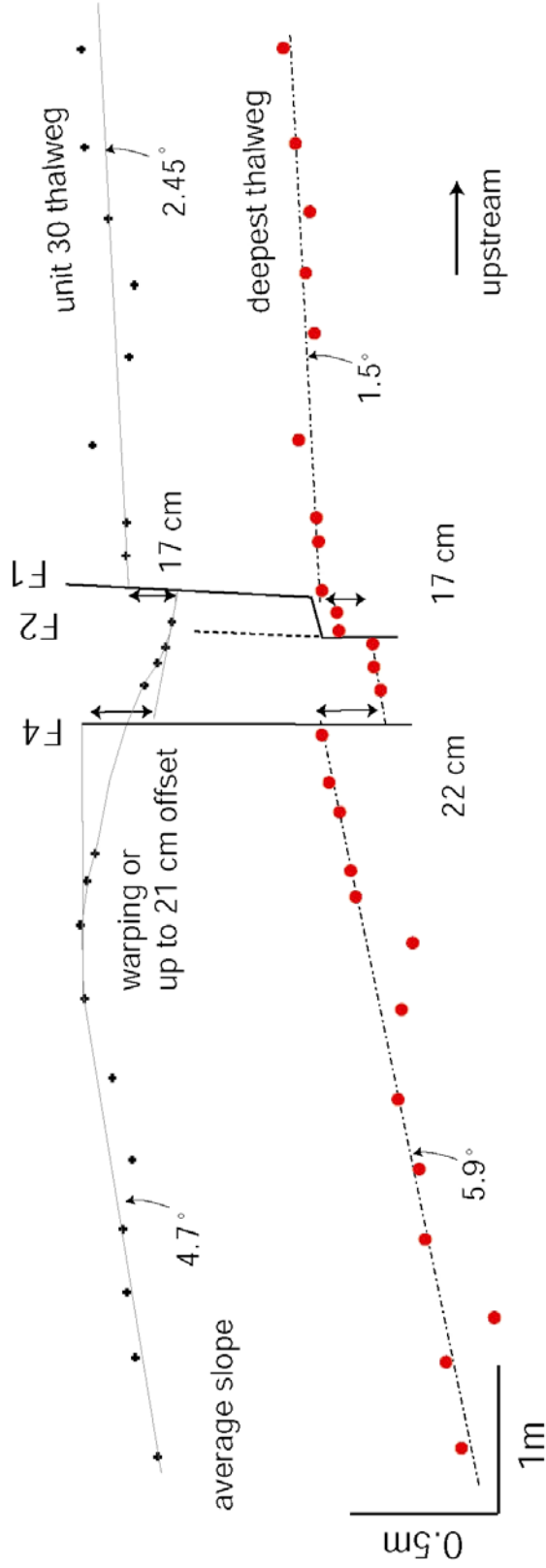


Figure 3.11b. Longitudinal profiles of the two piercing lines delineate a graben within the fault zone, but the overall vertical offset across the entire fault zone is 5 cm, downstream side up.

It is interesting to note also that the gradient of channel floor along the downstream reach is markedly steeper than that along the upstream reach. This may indicate that warping is associated with brittle faulting. The best evidence of warping is perhaps indicated by the trend of the thalweg of unit 30 across Fault 4 (Figure 3.11b). However, it is possible that the difference in slope of channel floor is a non-tectonic erosion feature. In the downstream reach, the channel cuts into indurated late Pleistocene alluvium whereas the upstream channel is imbedded in less cemented late Holocene channel deposits. Perhaps, higher gradient of channel floor in the downstream reach is due to the greater resistance of the underlying strata.

### **3.4.3 Channel 2-b: 15.5 m-offset**

Five superb piercing lines delimit the offset of channel 2-b. These are the deepest thalweg of the channel and the two upper and two lower contacts of unit 20 against the channel wall (Figure 3.12). We know the location of each piercing line to within about 20 cm of each fault, so the imprecision of offset measurements is only a few centimeters.

The five piercing lines yield horizontal offsets of between 15.1 and 15.80 m across three strands. The uncertainty is largely due to about 0.5 m suspected near-fault warping across F5, which normally shows up when extrapolating channel traces from far field.

Figure 2.13a shows two interpretations of the offsets of channel banks, at the elevation of the upper contact of unit 20. The northern bank is offset 15.25 m, if we extrapolate using the trends of the nearest data points. This amount includes, 0.3 m on F5, 14.40 m on F4 and 0.6 m on Fault 1. But in the close vicinity of F5, the downstream segment of channel 2-b seems to arch with a bending suggestive of warping. If the bending is due to warping instead of river meandering, we would have to add 0.3 m to the offset of simple juxtaposition. Thus, the total offset would be 15.7 m, if we include the possible warping. Similarly, the southern channel bank of unit 20 is offset nearly identical amount of 15.2 m with no warping, and 15.7 m with warping.

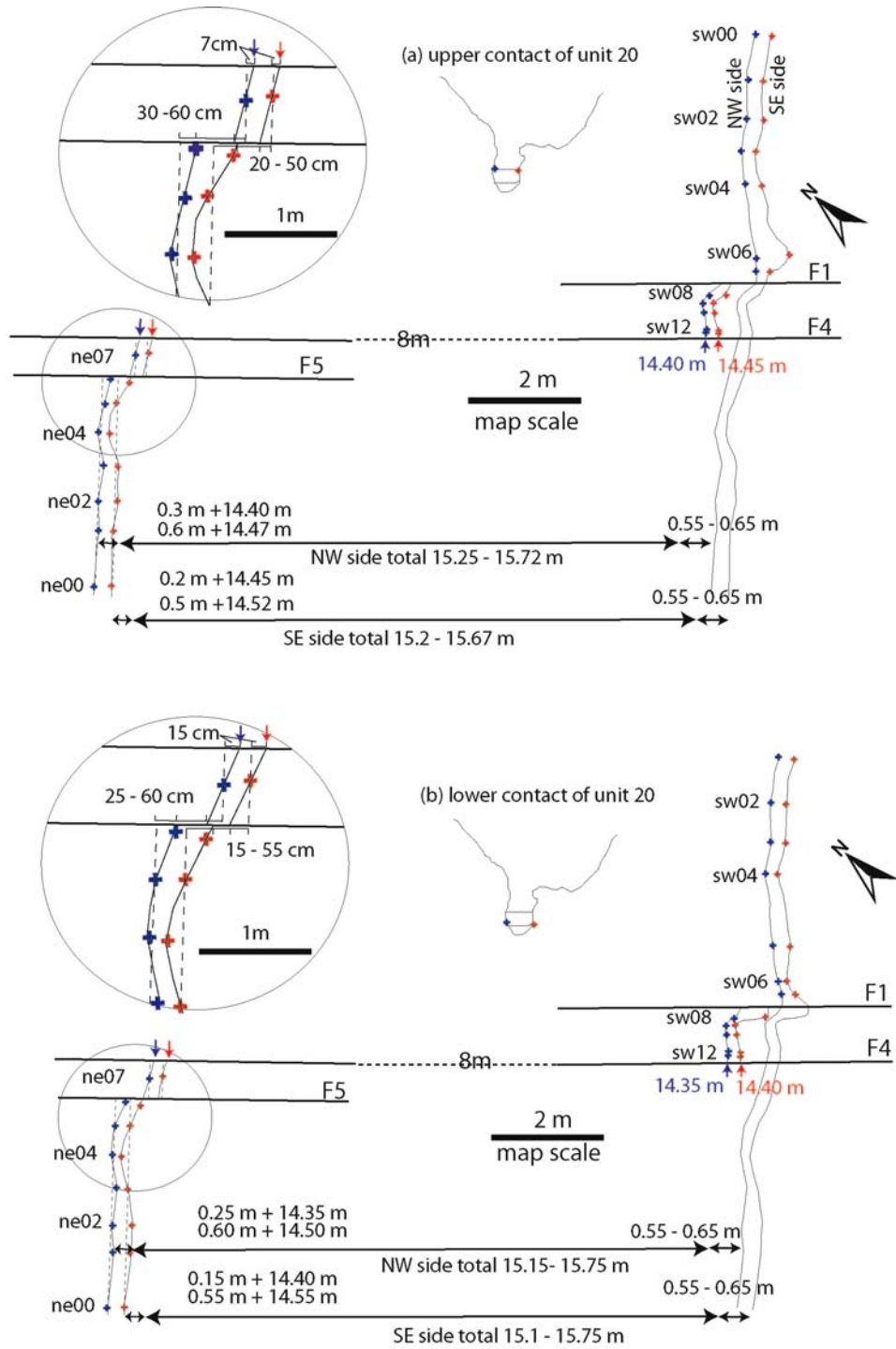


Figure 3.12 a and b

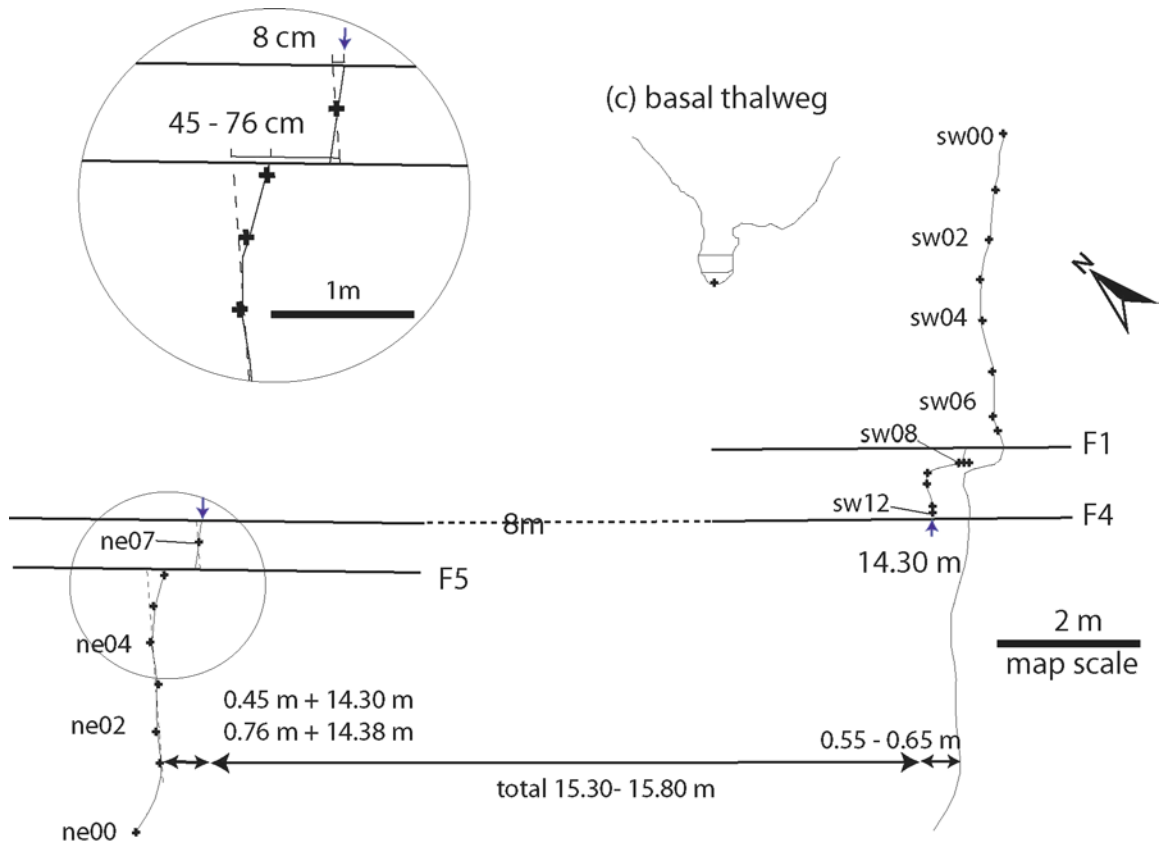


Figure 3.12. Five piercing lines constrain the total offset of channel 2-b to 15.1- 15.8 m and show that warping is confined to the reach immediately downstream from fault F5 and is about 0.5 m. The five piercing lines are the intersection of two stratal contacts with channel banks (a and b) and the deepest channel thalweg (c).

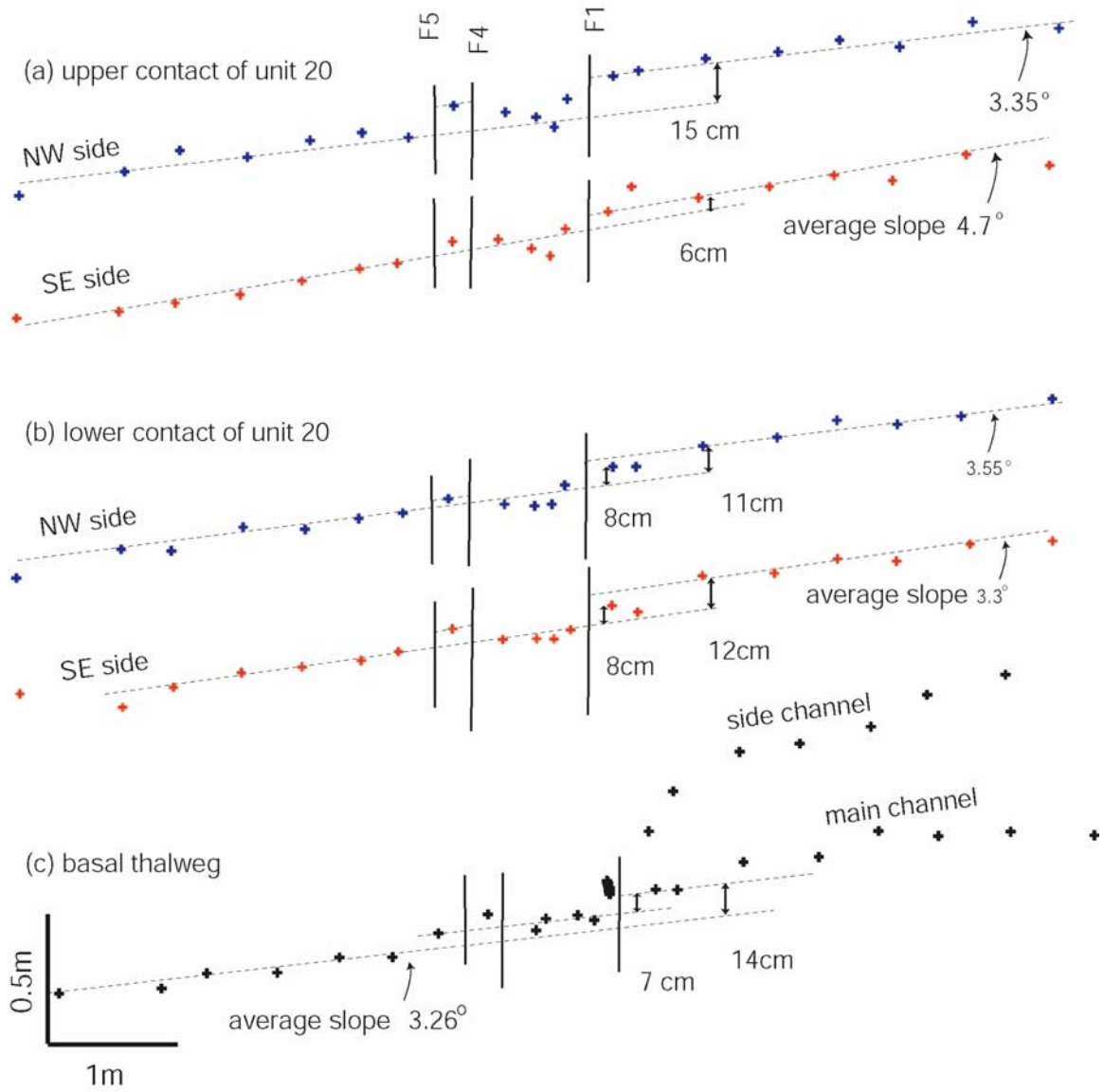


Figure 3.13. The vertical offset of channel 2-b is well-constrained by the elevations of the same piercing lines, unit 2-30 (a) and unit 2-20 (b), and the channel thalweg (c). The total vertical motion across the fault is 6-15 cm, downstream side down. Vertical exaggeration is 2x.

The offset across Fault 1 is assumed to be  $0.60 \pm 0.05$  m, as we have discussed above in section 3.4.1. The sharp bend in the piercing lines in the vicinity of Fault 1 is very likely the channel meanders, perhaps due to a pre-existing fault scarp near Fault 1.

Three other piercing lines yield similar results. The lower contact of unit 20 suggests offsets of 15.15 m -15.75 m across the fault zone (Figure 3.12b). This range includes 0.5 m suspected warping near Fault 5. The basal thalweg is offset 15.3 – 15.80 m, including 0.5 m warping.

Net vertical offset of channel 2-b ranges from about 6 to about 15cm, depending on which of the five piercing lines one measures (Figure 3.13). The block upstream from the fault is up relative to the block downstream. This sense is opposite that across channel 1-a. Each of the five lines shows that the thin block between Faults 5 and 4 has moved up and that the block between Faults 4 and 1 has dropped.

#### **3.4.4 Channel 3-c: 20.7 m-offset**

Figure 3.14a illustrates our interpretation of the horizontal offset of channel 3-c, which involves the restoration of three channel segments along Faults 5 and 4. The total offset is  $20.7 \pm 0.25$  m, the sum of 0.6 m across Fault 1,  $17.5 \pm 0.15$  m across Fault 4 and  $2.6 \pm 0.1$  m across Fault 5. Measurement of offset across F4 produces most of the uncertainty for this channel, because channel c2 trends nearly parallel to the fault zone. If channel c2 turns abruptly into Fault 4 at its southeasternmost exposure (exposure se06 in Figure 3.14a), then the offset of channel c2 from channel 3 is 17.65 m. This would certainly be a maximum bound on the offset across Fault 4. If however, the channel c2 thalweg continued toward the southeast before intersecting Fault 4, the offset would be less. A cut 25 cm southeast of the southeasternmost exposure of channel c2 constrains the southeasternmost possible extent of the channel. Thus, the minimum offset of c2 and 3 across Fault 4 is 17.35 m. To derive the total offset across the fault zone since creation of

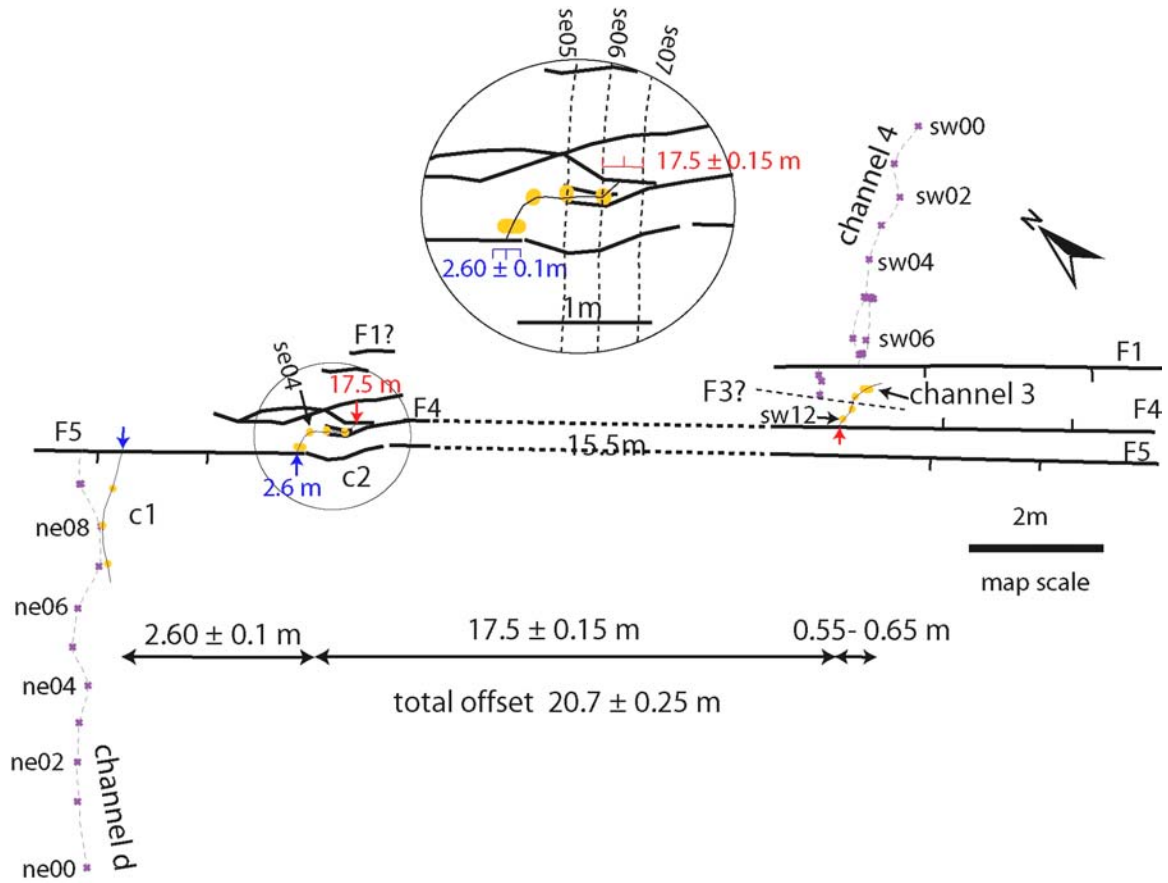


Figure 3.14a Restorations of channels 3-c require a total right-lateral offset of  $20.7 \pm 0.25 \text{ m}$ . The 0.6 m offset on Fault 1 is included, since Fault 1 has moved this amount during the most recent event.

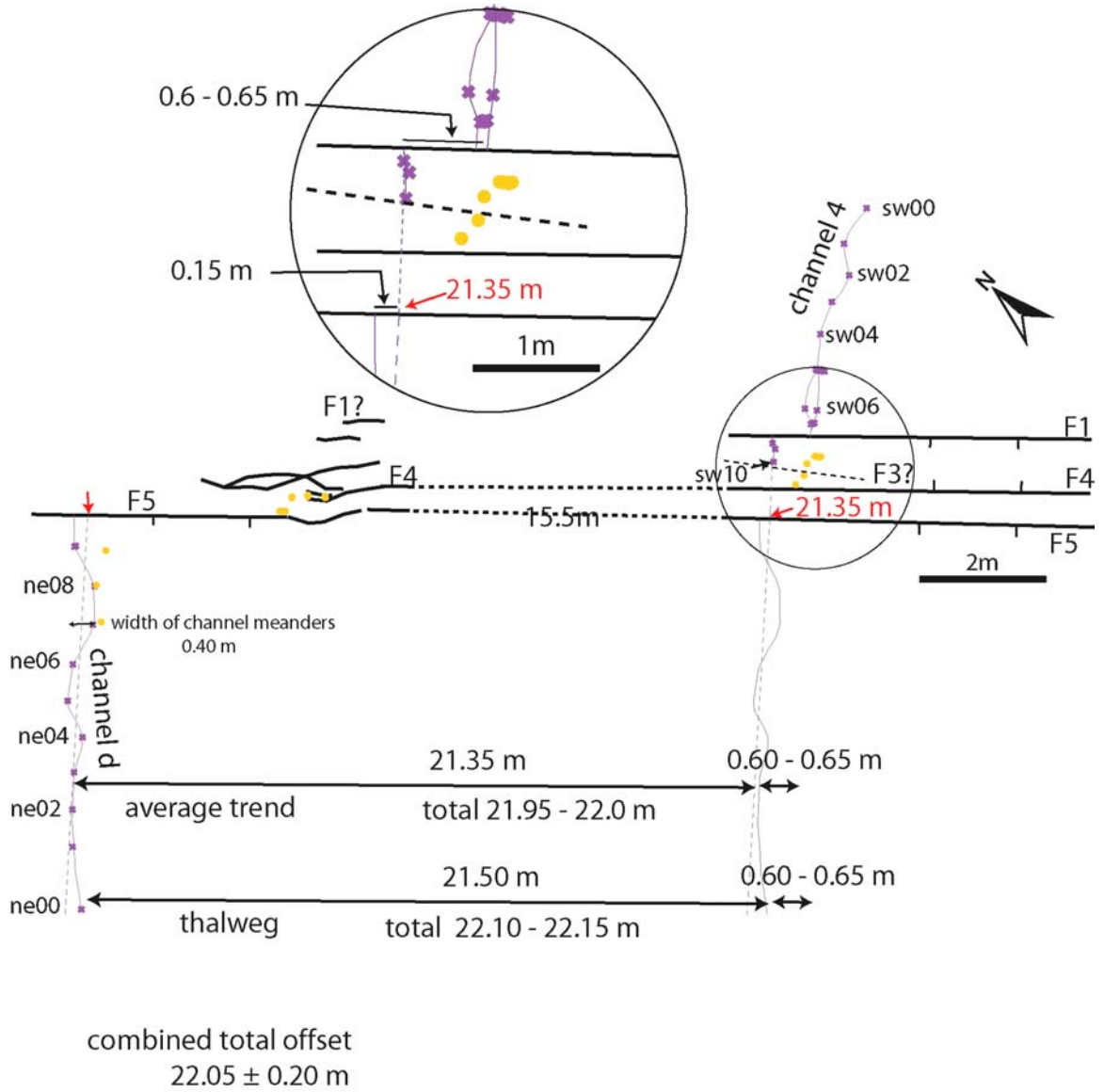


Figure 3.14b. The average trend (dashed lines) of channel 4-d thalweg indicates that channel 4-d has been offset  $22.0 \pm 0.2$  m. The uncertainty is half the amplitude of channel meanders. Direct connection of channel thalweg suggests a slightly larger offset, but within the uncertainty bound of that of the average trend. The majority of the offset is accommodated in the 0.8 m-wide zone between Faults 3 and 5.

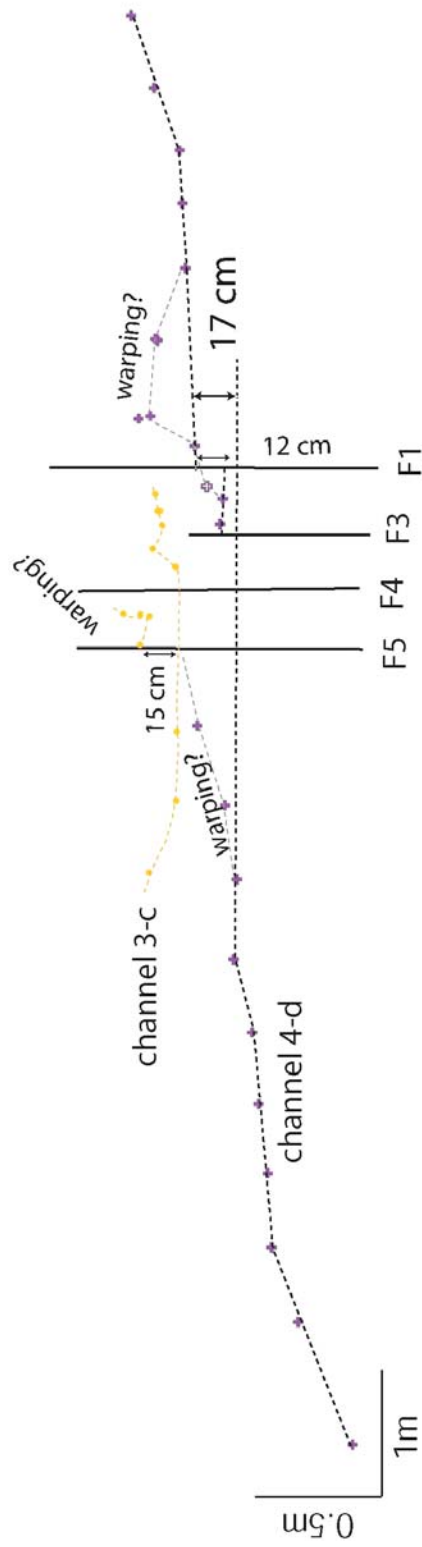


Figure 3.15. The irregularity of the long-profile of channel 4-d near the fault zone suggests warping. The vertical offset of channel 4-d across the entire fault zone is about 17 cm. The long-profile of channel 3-c shows that the block between Faults 4 and 5 is a small horst, and there is little if any vertical offset across the horst.

channel 3-c, one must include not just offset across Faults 5 and 4, but also the 0.6-m offset of younger channels across Fault 1. The sum of these measurements is  $20.7 \pm 0.15$  m.

Figure 3.15 shows that net vertical offset of the thalweg of channel 3-c is almost nil cross Faults 4 and 5. As with channel 2-b, the sliver of ground between Faults 5 and 4 is a horst. Its height is about 15 cm. Offset across Fault 1, even though it is not shown by channel 3, is implied to be  $10 \pm 5$  cm, the amount occurred during the post-channel 1 event. Therefore, the total net vertical offset should be  $10 \pm 5$  cm, downstream side down.

### **3.4.5 Channel 4-d: 22 m-offset**

The best estimation of the lateral offset of channel 4-d pair is  $22.05 \pm 0.2$  m. This is the combination of measurements using two piercing lines: the thalweg and the average trend. The thalweg suggests a total offset of about 22.10 m. This includes 0.6 m on Fault 1 and 21.50 m on Faults 3, 4 and 5, combined (Figure 3.14b). The measurement across Faults 3, 4 and 5 assumes a 0.8-m-long extrapolation of channel 4 downstream to Fault 5 and a 0.45-m-long extrapolation of channel d upstream to Fault 5. The trend of each extrapolated line is the overall trend of the thalweg with the fault zone. If instead, we were to use the overall trend of the upstream and the downstream channel segments to extrapolate to the fault zone, the total offset would be slightly smaller -- 22.0 m. Thus, we take the average of two measurements to get the best value of total offset, 22.05 m. The 0.2-m uncertainty that we assign to the total offset is half the amplitude of the largest channel meanders exposed in the trenches.

Vertical offset of channel 4-d is about 17 cm, down on the downstream side (Figure 3.15). The thalweg in the vicinity of the fault zone is irregular, probably an indication of warping associated with brittle faulting.

### 3.4.6 Channel 5-g: 30 m-offset

Channel 5-g has accumulated about  $30.0 \pm 0.3$  m of right-lateral offset since its creation. The general trend of channel thalweg suggests that the offset is accommodated by three strands, 0.5 m on Fault 1, 29.3 m on Fault 5, and 0.2 m on Fault 6 (Figure 3.16a). We estimate the error of this measurement to be 0.3 m, half the largest amplitude of channel meanders observed in the excavations of channel g.

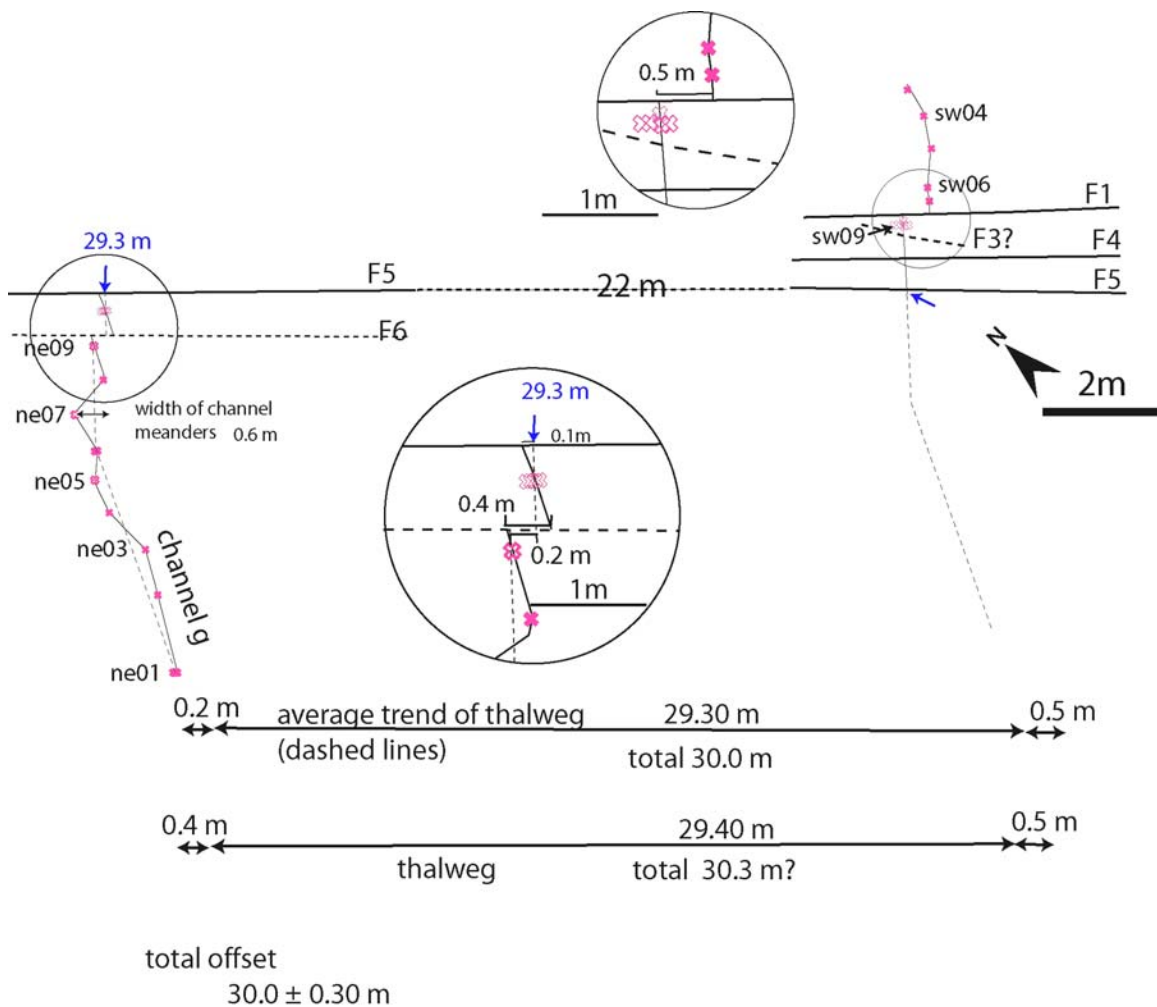


Figure 3.16a. The right-lateral offset of the deepest thalweg of channels 5-g is  $30.0 \pm 0.3$  m. Direction connection of data points suggests an offset larger than, but within the uncertainty bound of, that of the average trend.

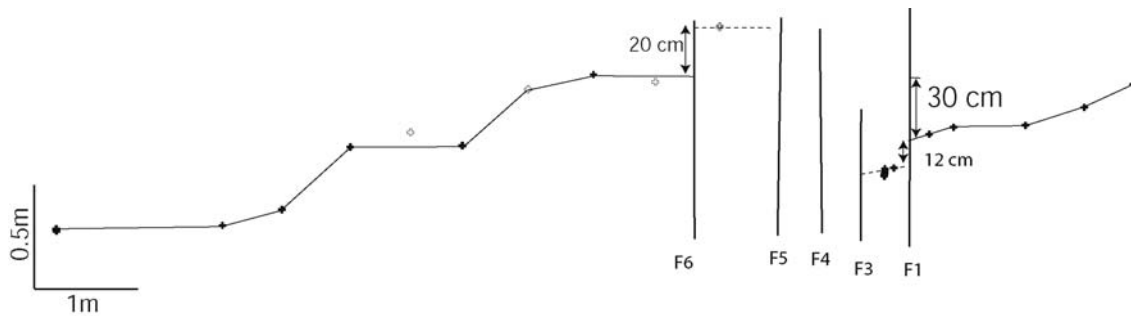


Figure 3.16b. The thalweg of channel 5-g displays cumulative net vertical offset of at least 30 cm across the fault, with downstream side up. Irregularity of the longitudinal profile on the downstream block complicates measurement of the actual value of the net offset. The sliver between Faults 5 and 6 is a horst about 20 cm high. Open symbols for data points represent uncertain positions of the thalweg.

A slightly larger total offset, 30.3m, is estimated if extrapolating the thalweg using data points at the nearest positions. Figure 3.16a shows that only one mapped exposure of channel g is between Faults 5 and 6. If we estimate the position of the thalweg based upon the trend between the nearby exposures ne09 and ne08, then we would have add 0.2 m on F6, and maybe 0.1 m on F4 to the offset of general trend. This interpretation implies an offset 0.3 m larger than, but still within the uncertainty of, the previous measurement. We favor the previous  $30.0 \pm 0.3$  m measurement, because the general trend of thalweg provides a longer reference line, and thus more robust estimation of the offset.

Vertical offset of channel 5-g appears to be about 30 cm, downstream side up. Undulations in the long-profile of the thalweg give this measurement an uncertainty of several centimeters. Immediately downstream from the fault zone, the thalweg gradient is anomalously low. If we assume that this reflects tectonic warping, the actual vertical displacement across the faulted and warped zone would be closer to 50 cm. The thin block between Faults 5 and 6 has moved up about 15 cm, compared to the block downstream of Fault 6.

### 3.4.7 Channel 6-h: 35.5 m offset

Channel 6-h records a cumulative right-lateral offset of about  $35.4 \pm 0.3$  m (Figure 3.17a). The 35.4 m offset is measured using straight-line extrapolation of the local channel trends. The 0.3 m uncertainty is half of the maximum amplitude of channel meanders observed in the excavations of channels 6 and g.

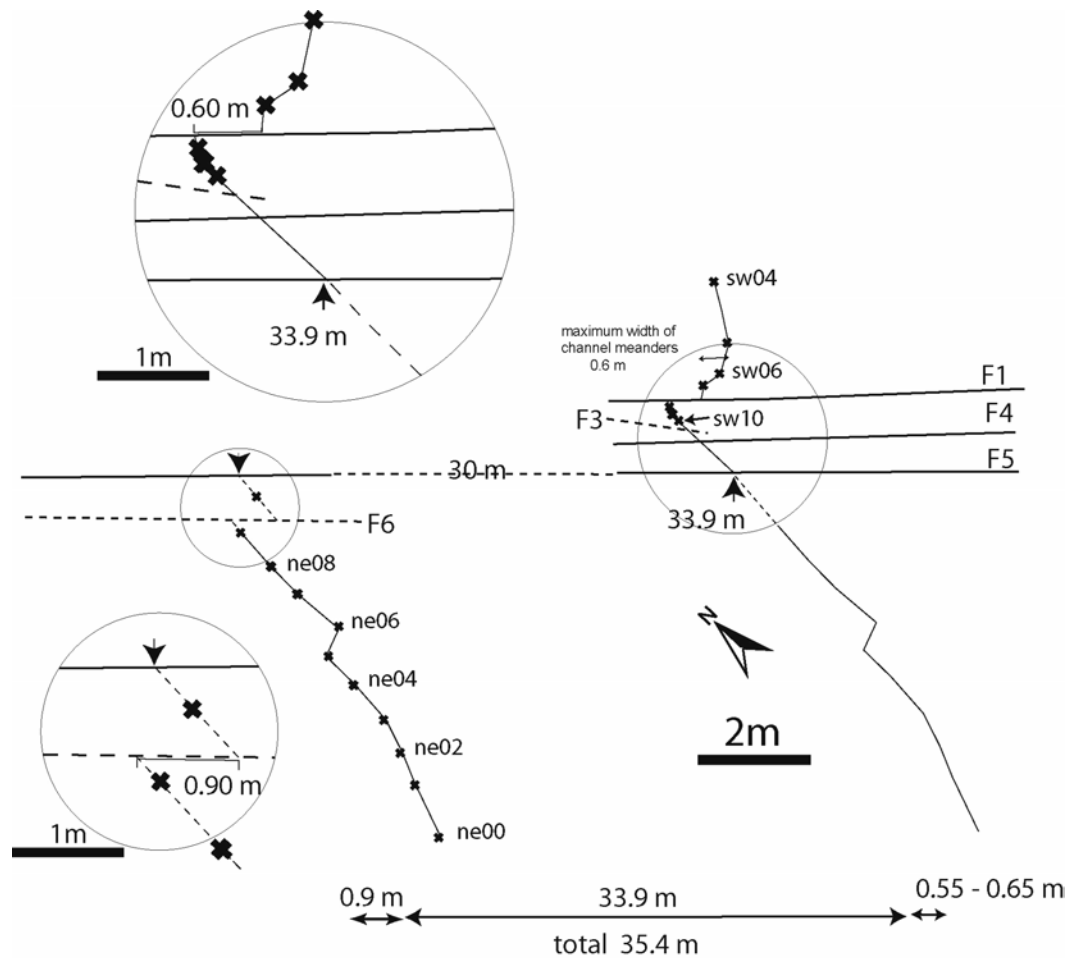


Figure 3.17a. The lateral offset of channel 6-h is  $35.4 \pm 0.3$  m, using straight-line extrapolation. The obliquity with which this channel intersects the fault zone creates ambiguities that are greater than for other channels. A simple interpolation of downstream and upstream channels yields a best estimate of 35.4 m. The 0.3 m uncertainty is half the maximum amplitude of channel meanders.

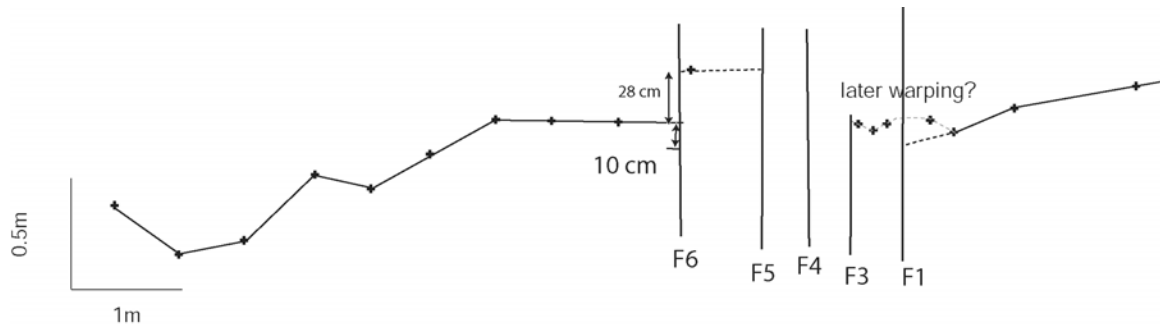


Figure 3.17b. The longitudinal profile of the deepest thalweg of channel 6-h suggests that vertical offset across the fault is about 10 cm, downstream side up. The shape of the profile immediately south of the fault zone suggests warping, which makes measurement of the vertical offset across the fault zone difficult. The amplitude of the horst between Faults 5 and 6 is about 28 cm.

Channel 6 is offset about 0.60 m across Fault 1, similar to the younger channels. This measurement is based upon interpretation that the curvature in channel 6 thalweg immediate upstream from Fault 1 is due to channel meanders. If the curvature indicates tectonic warping of a straight channel, then the offset across F1 could be as large as 1.2 m. We favor the meandering hypothesis because the next older channel 7 runs straight into Fault 1 and displays no deflection in the same reach. On the other hand, the strong asymmetry in the shape of channel 6, the southern wall steeper than the northern one (Figure 3.9), is consistent with the curving direction in channel meanders.

The total offset of this channel is subject to greater ambiguity than that of other pairs, because channel 6 has fault-subparallel deflection in the reach where the channel stratigraphy is missing and the measurement of offset is more sensitive to the assumption of initial channel configuration in this case. A larger deflection of the channel through the fault zone will yield a larger value. We cannot completely rule out the possibility that the 35.4-m measurement may represent a lower bound of the total offset. However, we are more inclined to believe that channel 6-h does not have much fault subparallel deflection, because most channels at the site cut straight across the fault. The only exception is channel 3-c, which has about a meter-long fault-parallel segment. This 90° deflection is probably a special case in that channel 3-c was incised shortly

after channel 4-d was offset only 1 – 2 m. However, such a condition was absent when channel 5-g was formed.

Since this maximum width of channel meanders occurs in channel 6 one could argue that the curvature indicates tectonic warping given its closeness to the fault zone.

Figure 3.17b shows that of the net vertical offset of channel 6-h is probably about 10 cm, down on the downstream side. The anomalous thalweg gradient in the vicinity of Fault 1 is distorted by later rupturing, perhaps by warping, as the nearby channel 4 shows warping of similar amplitude. The oddly flat section of the long-profile immediately downstream from the fault may also reflect tectonic warping. Since nearby channel g also shows this flattening (Figure 3.16b), we interpret it as tectonic warping. If one includes this in determining vertical deformation across the fault zone, the downstream block has risen about 40 cm relative to the upstream block. Another feature of the long profile is the elevation of the one data point between Faults 5 and 6. It indicates that this narrow block is a horst within the fault zone, with about 28 cm of uplift. Nearby channels g (Figure 3.16b) and channel f display the same feature. This confirms the existence of and vertical motion on Fault 6.

### ***3.4.8 Non-brittle warping***

Within the aperture of our excavations, we found no significant warping in horizontal offsets, except a possible 0.5 m for channel 2-b (Fig. 3. 12). In all other channels, there are not noticeable systematic deviations in the alignments of channel thalwegs that we can attribute to non-brittle warping.

However, if warping is widely distributed away from the main fault zone, our narrow excavation aperture, about 5 m on each side of the fault, do not allow us to observe it. Moreover, channel thalwegs are not ideal for the recovery of the warping component because of the meandering nature of channels. Thus, the offsets we measured in the trenches should be considered only as the brittle component and could be smaller than the total offsets. Nonetheless,

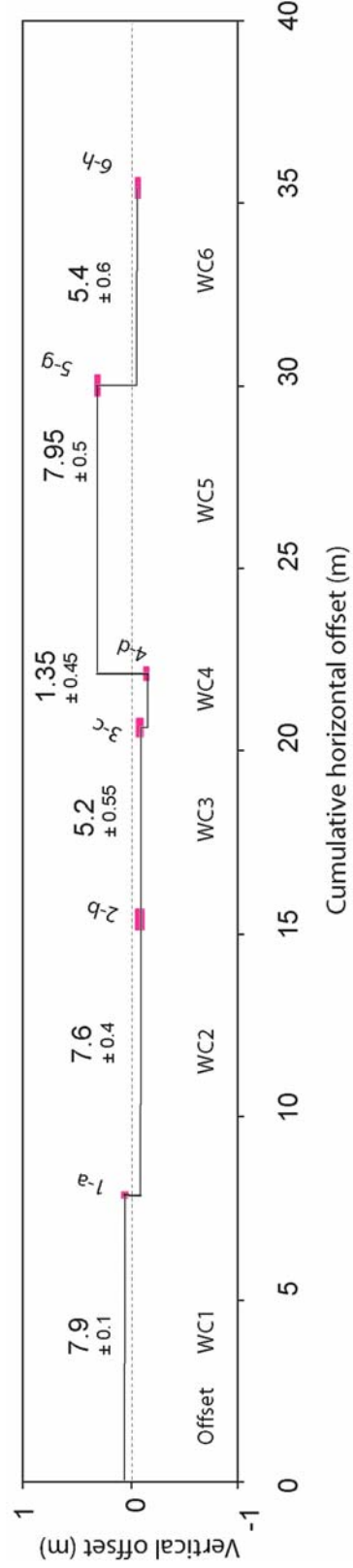


Figure 3.18. Summary of the cumulative offsets of channel pairs. These channels have recorded right-lateral slip of 7.9, 15.5, 20.7, 22.1, 30.0, and 35.4 m. The increments of difference in offsets are mostly about 7 to 8 m. The vertical component of slip in each increment is only a small fraction of the horizontal offset. Positive for downstream side up. Vertical exaggeration is 3x.

we can conclude that warping is probably less than half the amplitude of channel meanders. Thus the warping components, if they exist, should be included in the uncertainties of offset measurements.

On the other hand, warping is more prominent in a vertical plane than in horizontal. Warping in a vertical plane is commonly indicated by the anomalous gradient in long profiles of the channels, particularly channels 3, 4, 5 and 6, within or in close vicinity of the fault zone. This is consistent with the appearance of a large *moletrack*, i.e. welts, mounds and troughs along the surface rupture of an earthquake.

### 3.5 Derivation of a rupture sequence at the site

Now that we have measurements of the latest six individual offsets, we can construct an offset sequence. Figure 3.18 illustrates that sequence by plotting the cumulative horizontal and vertical offsets for the channel pairs and their associated horizontal errors. Note that the vertical axis is exaggerated 3-fold, so that the vertical offsets are legible. For ease of reference, each increment of offset bears a designation, where WC1 is the youngest and WC6 is the oldest increment.

The total dextral offset of about 36 m accumulated in at least six increments, since offset increases distinctly from youngest to oldest. The uncertainties in these measurements are small, just tens of centimeters. The differences between these values yield the magnitude of the six incremental offsets. In sequence from oldest to youngest these are  $5.4 \pm 0.6$ ,  $8.0 \pm 0.5$ ,  $1.4 \pm 0.5$ ,  $5.2 \pm 0.6$ ,  $7.6 \pm 0.4$  and  $7.9 \pm 0.1$  m. Note that four of the six increments are within about a 10% of 7.5 m, but two consecutive offsets, WC3 and WC4, are about 5.5 and 1.5 m. Cumulative vertical offset is nil. Vertical offsets for individual offsets are always less than 50 cm, but range from northeast-side-up to southwest-side-up.

### ***3.5.1 Is each offset a single rupture event?***

The goal of this thesis is to determine a rupture history for this one site along the San Andreas fault. To reach that goal, we must consider how many rupture events this sequence of incremental offsets represents. Although a one-for-one correlation may exist, it must be supported by the details of the stratigraphy and geomorphology. Could it be, for example, that two separate ruptures occurred within a 200-year period during which no new channels were incised? Is it possible that one of the offsets represent two ruptures, one of which was only a few centimeters or a few tens of centimeters? In this section we address these questions, first generally and then offset-by-offset.

The completeness of the Wallace Creek paleoseismic record is a function of the number and duration of hiatuses in the record of alluviation and channelization. Hiatuses in either deposition or erosion that occur between rupture events would result in the events not being recorded in the excavated volume. If earthquake ruptures have occurred more frequently than alluviation or erosion, then some of these would not be differentiable in the geologic record. For example, between 35 and 50 m northwest of the upstream channels there are no downstream correlatives to the upstream channels. There probably have been a hiatus in deposition and erosion at the site when that 15-m section was in front of the channel. This is an example of the influence of sedimentary activity on the completeness of the seismic record. Below, we consider the less-obvious possibilities for significant hiatuses within our six-offset sequence.

The completeness of the record is also a function of the size of ruptures relative to the size of the depositional and erosional features in the excavated volume and the spacing of our serial excavations. The width of a channel may set the limit of the offset that can be detected at the site. For example, we probably would not recognize a 10 - cm offset event, if the channel is 1 m wide. But, if the offset is more than half the width of channel, and if alluviation is frequent enough, the offset event should be recognizable.

We turn now to specific discussions of each of the offset channel pairs. There is strong evidence that at least the youngest two offset increments are associated with single paleoseismic events.

### **3.5.1.1 Offset WC1 and the 1857 earthquake.**

The 1857 earthquake is known to have involved rupture of this portion of the San Andreas fault. The shaking pattern, alone, implies rupture of this section of the fault (Wood, 1955; Agnew and Sieh, 1978). But there is more compelling evidence, as well. An account states that a circular sheep pen was offset into a rough “S” shape by the fault somewhere in the Carrizo plain (Wood, 1955, p63). This suggests at least a couple of meters of dextral slip during the earthquake. The offsets of youngest stream channels yield values of 8 to 10 m, which have been ascribed to the 1857 earthquake (Wallace, 1968, Sieh, 1978). Three-dimensional excavations a few km to the southeast yielded a sharp offset of about 7 m, which has also been ascribed to the 1857 rupture (Grant and Sieh, 1993). Furthermore, Grant and Donnellan (1994) showed, by comparison of an 1855 survey of section corners with a modern GPS reoccupation that the broad-aperture offset across the fault at Wallace Creek was  $11 \pm 2$  m. None of these geodetic, geomorphic or stratigraphic offsets can include more than a few centimeters of creep in the past century, since fences constructed in 1908 a few kilometers to the northwest show no misalignments (Brown and Wallace, 1968).

Thus it appears that all or at least most of offset WC1 is attributable to slip in 1857. The geodetic measurement of  $11 \pm 2$  m is slightly greater than the 7.9-m offset of WC1, but this discrepancy may well be due to off-fault warping that would be recorded in the geodetic, large-aperture measurement but not in the narrow-aperture paleoseismic offset.

The geometry and stratigraphy of channel 1-a indicate that all but a few tens of centimeters of the 7.9-m offset must be associated with the 1857 event. Channel 1-a is offset very abruptly across the fault zone. On both sides, we have traced the channel to within 20 cm of the main fault strands. The width of channel 1, which is about 50 cm wide near the fault, also argues that events of more than 50 cm offset could not have occurred during the initial stage of the down-cutting of channel 1.

### **3.5.1.2 Offset WC2 and the penultimate rupture**

The 7.5-m WC2 offset also appears to represent a solitary, sudden event. There is no historical record of an event prior to the 1857 earthquake in the region, so this must be a prehistoric rupture. Several observations suggest all or nearly all of WC2 accrued in one event. First, similar to channel 1-a, channel 2-b is offset sharply across the fault. We have traced the channel to within a couple of ten centimeters of the main fault strand. If there had been an offset of the channel greater than a 20 cm or so after initial incision and before filling of the narrow lower portion, the stratigraphy of units 10 through 40 would not have been continuous up to and across the fault zone. Near the fault zone, we would have expected to see collapse debris from the scarp within the unit 10-40 sequence. Furthermore, an event in the early stages of channel filling would have led to development of a channel meander at the fault. Such a meander would be apparent in the map of the channel thalweg and walls (Figure 3.6). There is also no evidence for a second large event in the shape of the upper units of the channel fill.

### **3.5.1.3 Offsets WC3 and WC4**

The channels that define offsets WC3 and WC4 provide a good example of how multiple offsets of a channel can be discriminated if the stratigraphic and geomorphic record is adequate. The upstream channels (3 and 4) sit adjacent to each other and the downstream channels (c and d) occupy the same channel, except near the fault (Figure 3.7). Whereas the older channel (d) flows straight across the fault in a deep channel, the upper channel (c) leaves the fault at an angle, and merges with the straight channel 1 m or so downstream.

Channel 4-d has been offset 1 - 2 m when channel 3-c was incised. This small offset, WC4, is indicated by the difference in the offsets of channel 4-d and channel 3-c. More interestingly, we see channel c cuts the upper right of channel d, and causes the asymmetrical cross-section of d, as one would expect for a corner-cutting deflection after a channel was offset a small amount.

We do not see any evidence suggesting that the 1 - 2 m offset was accumulated through multiple events. There is no asymmetric widening of the channel wall of 4-d that we can attribute

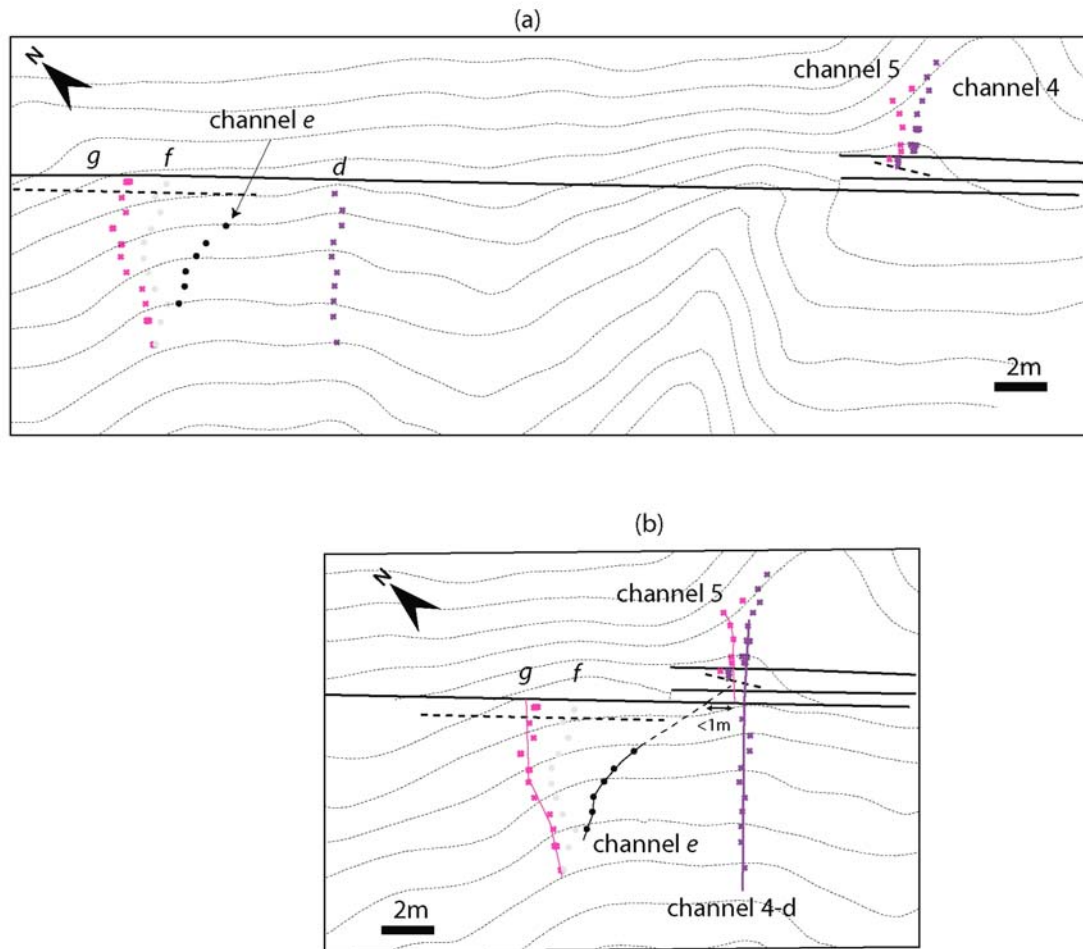


Figure 3.19. The presence of channel e is consistent with interpreting the 8-m increment between the offsets of channel 4-d and channel 5-g as a single event. Panel A shows the present channel configuration of downstream channels g through d and upstream channels 4 and 5. Channel f is older than both channels e and g. In Panel B, the 22-m offset of channel 4-d has been restored to illustrate the relationship of e and g to the upstream channels just after offset of channels 5 and g. The trajectory of channel e toward the upstream channels is consistent with channels 5 and g being offset 7 to 8 meters in a single event.

to faulting, except in the case of channel c. The double thalwegs of channel 4 and channel d appear to indicate an asymmetric widening. But since that they are in the same direction on both

sides of the fault, the widening is clearly not a response of offset. One would expect that after an offset, the upstream channel will widen in a direction opposite to that of the downstream segment.

It is possible, but there is no evidence, that the 5 - 6 m offset of WC3 represents multiple events. There is only one cut-and-fill sequence within channel 3-c, evidence of multiple offset events could be hidden in the colluvium that overlies the channel.

#### **3.5.1.4 Offset WC5**

There is more uncertainty whether the 8-m offset of WC5 represents a single event. The shallow depth and a simple cut-and-fill sequence of channel 5-g may indicate that channel 5-g was incised in a period with more infrequent storms. If it is the case, then the possibility of hiatus in alluviation is higher for channel 5-g than other channels, thus the chance of missing event is higher.

Although there is more uncertainty than in the cases of WC1 and WC2, WC5 appears to be due to a single event. Channel 5-g runs into the fault zone at a high angle. The next younger channel, channel 4-d also crosses the fault zone at nearly a right angle. Both upstream and downstream segments are less than 1m wide near the fault.

The existence of downstream channel e (Figure 3.19a), supports the contention that most, if not all, of offset WC5 is from a singular event. Channel e does not merge downstream with channel g, and thus it is unclear whether channel e is younger than g or older. Channel e does not extend upstream as far as the fault, so it has no match across the fault, either. But if channel e was incised after channel 5-g was offset, it likely originated from an overflow of the stream that cut the channel pair, 4-d. Figure 3.19b illustrates this. It shows a restoration of the two sides of the fault with channels 4 and d aligned. Notice that channel e trends upstream toward channels 4 and 5. It is possible that channel e is roughly coeval with channel 4-d, though headward erosion did not reach as far upstream as the fault zone. This relationship suggests that the initial offset of channel 5-g would be large. Channel e comes to within about 1 m from channel 5. Channel 5-g would have been offset at least 7m before such an alignment would be likely. The remaining 1 m does not necessarily represent the slip of an additional event, because the stream of water that fed

into channel e might have curved as it crossed the fault zone. This geometry of channel e does not preclude all of offset WC5 being due to a single, 8-m event.

### **3.5.1.5 Offset WC6**

WC6 is perhaps the most uncertain case, because of the poor stratigraphy and asymmetric shape of channel 6-h. The downstream channel h is about 1m wide in the immediate vicinity of the fault zone; the cross-section of channel h is asymmetric towards the south (Figure 3.9). This geometry would be consistent with that of widening of a downstream channel after being right-laterally offset. However, the less preserved channel stratigraphy in the upstream reach prevents us from more rigorous assessment of this possibility.

## **3.5.2 Summary**

In summary, most of the channels run straight into the fault zone. The abrupt termination of channel walls and channel stratigraphy at the fault strongly suggest that they are offset in sudden events. The steep channel walls and the lack of corner-cutting deflection in channel stratigraphy also suggest that most, if not all of the 6 six offsets represent single event, rather than the accumulation of multiple smaller events. The possibility of multiple events has been discussed individually in each of the six offsets.

Channels are narrow, about 1m or less. This indicates that events with more than 1 m can be discriminated if the stratigraphic and geomorphic record is adequate.

We cannot argue, however, that hiatuses in either deposition or erosion that occur between rupture events would result in the events not being recorded in the excavated volume. But the large depth, 0.7 m or more, and multiple sets of cut-and-fill sequences within channels indicate that alluviation is often frequent. At least, the quiescent period between rupturing events are long enough to allow these channels to stabilize. A quantitative assessment of the frequency of significant storms vs. rupture events would certainly help to resolve the issue of completeness of offset record. This depends on the abundance and quality of dateable materials.

### 3.6 Radiocarbon constraints

Radiocarbon dating of samples from excavations yields estimates of dates of serial offset events. The results of radiocarbon analysis of all dated samples are summarized in Table 3.1.

Numerous tiny fragments of detrital charcoal were embedded in strata of channels, particularly in poorly-sorted debris or well-sorted fine-grained suspended-load sediments, and rarely in well-sorted coarse-grained channel sand and gravel beds. Charcoal grains are mostly small and flaky in appearance at the site; only a small percentage of the samples are large enough to be dated by accelerator mass spectrometry (AMS).

Since few of charcoal grains are large enough to be dated individually, we also extracted and consolidated charcoal fragments from the bulk dirt samples of dirt that were collected at locations where tiny charcoal grains were seen. We first soaked the sample, and since charcoal grains normally floated on top of the water, we then poured the liquid residual that contained charcoal through a set of two sieves, one 0.5 mm-diameter and the other 0.5 mm - 0.25 mm. Charcoal grains that are larger than the holes of the sieves were retained. After washing and drying, we handpicked the charcoal grains and removed remaining dirt, root etc.

We also found several burn horizons in the excavations. Unlike detrital charcoal, a burn horizon generally contains a pocket of tiny charcoal fragments, and the surrounding sediment displays a baked reddish color. Dates of samples from a burn horizon are generally considered to be better approximation than detrital charcoal, of the age of deposition of sediments that contain them.

We selected 27 carbon samples from a total of over 70 and sent them to the Accelerator Mass Spectrometry Laboratory at Lawrence Livermore National Laboratory for radiogenic  $^{14}\text{C}$  analysis (Table 3.1). Among dated samples, some belong to regular type of single grain detrital charcoal; some are composite samples of fine grain detrital charcoal extracted from bulk samples as described above. Three dated burn horizons were dated: one within downstream channel *l*, one in the colluvium above downstream channel *g*, one within the upstream channel 4.

Table 3.1 Radiocarbon samples at the Wallace Creek trench site

Sample ID	Sample Location		Conventional $^{14}\text{C}$ ages years BP $\pm$ 1 $\sigma$ <sup>(1)</sup>	$\delta^{13}\text{C}$ <sup>(2)</sup>	Calendar years <sup>(3)</sup> 2 $\sigma$	Sample descriptions and significance <sup>(4)</sup>
	Channel resided	From fault				
U5-03	70750	Channel 1 up	170 $\pm$ 40	-25	A.D. 1650 - 1960	Pieces broken from single consolidated charcoal grain; post-event
U7-24	77913	Channel 1 up	490 $\pm$ 40	-21.4	A.D. 1320 - 1480	~6mg bulk fine grain charcoals <sup>(5)</sup> ; pre-event
U9-08	81174	Channel 1 up	530 $\pm$ 40	-25	A.D. 1300 - 1450	8-10mg bulk fine grain charcoals; pre-event
U10-01	78165	Channel 1 up	560 $\pm$ 40	-25	A.D. 1300 - 1440	~10mg bulk fine grain charcoals; pre-event
U9-03	77914	Channel 2 up	780 $\pm$ 40	-25.6	A.D. 1180 - 1300	~15mg 3-4 pieces of 2-5mm detrital charcoals; pre-event?
U3-02	70751	Channel 2 up	610 $\pm$ 80	-25	A.D. 1260 - 1450	A large piece of charcoal; pre-event?
U8-03	77915	Channel 2 up	760 $\pm$ 40	-25.5	A.D. 1190 - 1300	~15mg bulk fine grain charcoals pre-event
dn5-ne06-01	77922	Channel <u>2</u> down	330 $\pm$ 40	-25.4	A.D. 1460 - 1650	~20mg bulk fine grain charcoals; pre-event
No carbon samples found in channels 3 and <u>4</u>						
U5-04	81173	Channel 4 up	1855 $\pm$ 45	-25	A.D. 60 - 320	Charcoal powder from a burn horizon; pre-event
U9-09	78160	Channel 4 up	1780 $\pm$ 40	-25	A.D. 130 - 390	~3mg bulk fine grain charcoal; pre-event
U7-31	78161	Channel 4 up	1760 $\pm$ 50	-25	A.D. 130 - 400	~5mg bulk fine grain charcoal; pre-event
U8-07	78162	Channel 5 up	1310 $\pm$ 40	-25	A.D. 640 - 780	~11mg bulk fine grain charcoal; post-event to approximate age of the event
dn3-03	7817 2	Channel <u>3</u> down	1140 $\pm$ 40	-25	A.D. 770 - 1000	In-situ burn in colluvium; post-event
U8-01	78164	Channel 6 up	270 $\pm$ 40	-25	modern	~1.5cm in diameter, rounded single grain charcoal, suspected to be re-worked??
U7-09	78613	Channel 6 up	200 $\pm$ 50	-25	modern	~1mg bulk fine grain charcoals.
U4-01	77917	Channel 7 up	2760 $\pm$ 40	-24.4	B.C. 1000-820	14mg broken pieces of detrital charcoals; post-event
U5-01	81175	Channel 7 up	2690 $\pm$ 40	-25	B.C. 920-790	Large pieces of consolidated charcoals; post-event

U7-19	81176	Channel 7	up	2830 ± 45	-25	B.C. 1130-840	2-4mg bulk fine grain charcoals; pre-event
U7-20(1)	77918	Channel 8	up	2490 ± 30	-22.3	B.C. 790 - 410	~0.1g bulk fine grain charcoals; in the suspended load layer immediately post-event
U7-20(2)	78166	Channel 8	up	3010 ± 50	-25	B.C. 1410 - 1080	~0.15g bulk fine grain charcoals; in the same layer as U7-20(1); post-event
U7-22	77919	Channel 8	up	3380 ± 40	-23.7	B.C. 1770 - 1520	7mg bulk fine grain charcoals; pre-event
U8 - 04	77920	Channel 9	up	2520 ± 50	-23.1	B.C. 800 - 410	~8mg bulk fine grain charcoals; in a thin organic rich layer of alluvial fills, post-event
U7-01	78167	Channel 9	up	3380 ± 40	-25	B.C. 1770 - 1520	2-4mg bulk fine grain charcoals; post-event
U8-05	78168	Channel 9	up	3380 ± 40	-25	B.C. 1770 - 1520	4mg bulk fine grain charcoals; in the suspended load layer immediately post-event
U7-10(1)	78169	Channel 9	up	3600 ± 40	-25	B.C. 2130 - 1770	~20mg bulk fine grain charcoals; in the same layer as U8-05
U4-03	77921	Channel 9	up	2580 ± 50	-10.6	B.C. 840 - 520	~6mg 5mm single grain detrital charcoal; pre-event?
dn2-ne10-03	70752	Channel I	down	2980 ± 50	-25	B.C. 1380 - 1040	Charcoal powder, in situ burn; pre-event
dn2-ne11-03	78170	Channel k	down	15620 ± 190	-25	B.C. 17500 - 16000	1-2mg 1 mm detrital charcoals; pre-event
dn2-ne02-01	78171	Basement	down	15840 ± 120	-25	B.C. 17700 - 16300	1-2 mg 1mm single grain detrital charcoal
dn1-ne03-01	78173	Basement	down	16920 ± 140	-25	B.C. 19000 - 17500	2-3mg detrital charcoal

- (1) The quoted age is in radiocarbon years using the Libby half life of 5568 years and following the conventions of Stuiver and Polach (Radiocarbon, v. 19, p.355, 1977).
- (2) <sup>13</sup>C values are the assumed values according to Stuiver and Polach (ibid.) when given without decimal places. Values measured for the material itself are given with a single decimal place.
- (3) Dendro-calibrated calendar ages are calculated by using Oxcal v3.5 Bronk Ramsey (2000), atmospheric data from Stuiver et al. (1998).
- (4) The material dated was acid-base-acid treated charcoal, except the samples marked by \*, in which case the material dated was reprecipitated base-soluble humic extracts. The large uncertainties for some of these samples are due to the very small sample sizes.
- (5) Bulk fine grain charcoals refer to generally 0.5-1mm charcoals extracted from bulk dirt sample. Dirt samples were collected on exposures at locations where tiny charcoals were visible yet too small to be dated individually. Sample pre-treatment includes only physical handling: washing, sieving through 0.5mm sieve, drying and removing remaining dirt, root etc.

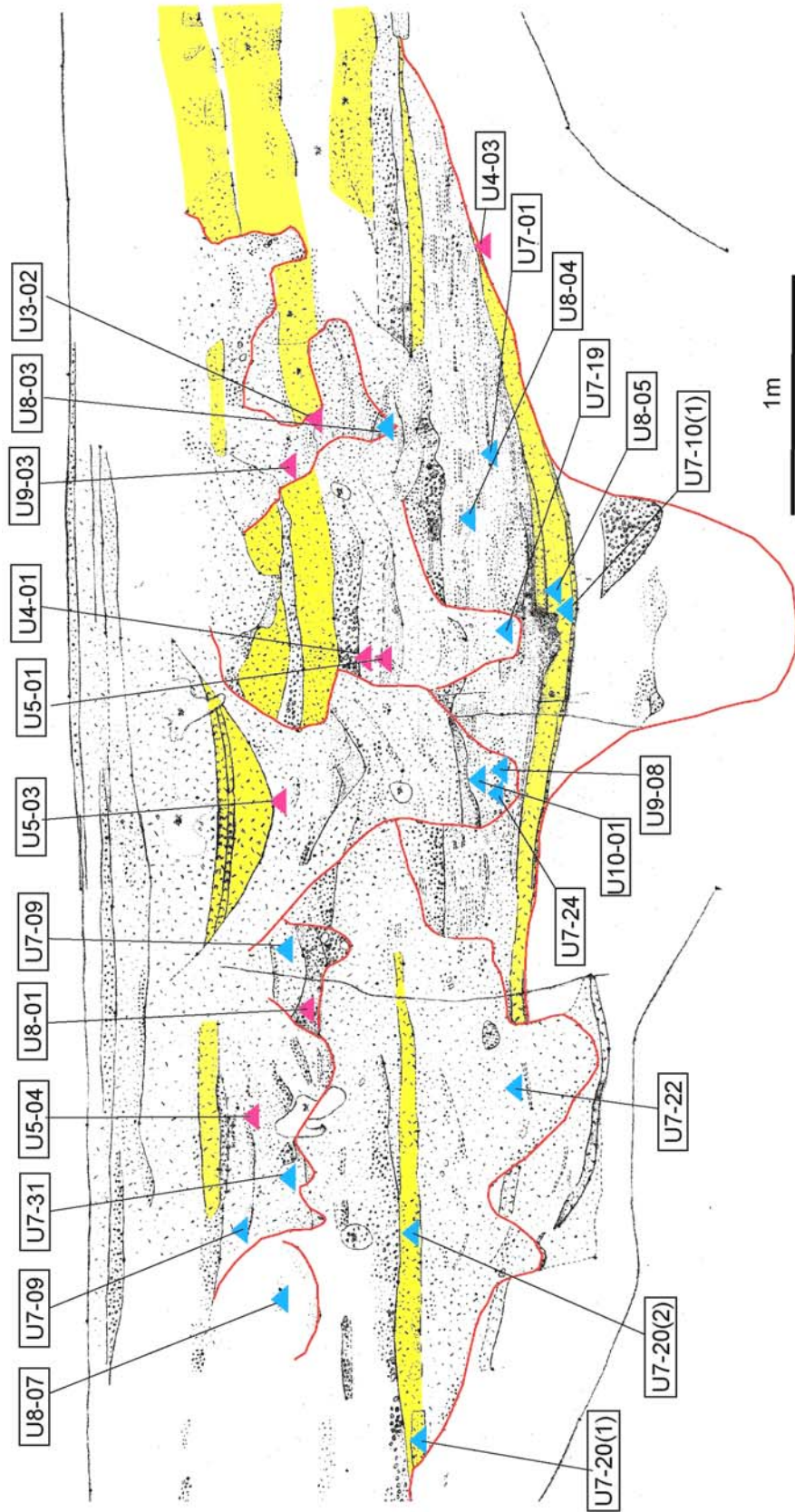


Figure 3.20. (Previous page) All dated radiocarbon samples from the upstream exposures appear as colored triangles on the log of trench cut up-sw06 (U7), to show their stratigraphic positions. The red triangles represent single-grain charcoal samples, and the blue triangles show the location of those extracted from bulk dirt samples.

Only 6 samples were from the downstream side, including two embedded in the underlying bedrock of late Pleistocene alluvium; the majority of samples were from the upstream trench. Shown in Figure 3.20, the locations of the upstream samples are superimposed on the map of exposure up-sw06 (U7) in order to show most simply their stratigraphic positions and the channels they represent.

### **3.6.1 Inheritance problem**

A serious problem is the detrital nature of most of our samples. The radiocarbon age of detrital wood could be considerably greater than the depositional age of a bed which contains it, because it represents the age of the death of woody material, and charcoal may reside in a system for an extended period of time, especially in the arid regions. Long residence time can be caused by the lifespan of long-lived plant species, the protracted transportation time between the death of plant and deposition, and charcoal re-working. At the Wallace Creek site, the depositional environment makes the chance of charcoal reworking high because the upstream stretch was repeatedly incised, filled and re-incised; thus charcoal fragments that were originally deposited in older channels can be removed and re-deposited in younger generation of channels.

Inheritance is clearly demonstrated in several cases at the site. For example, U7-20(1) and U7-20(2), which are in the same suspended-load layer in channel 8 and only 85cm apart on the same trench exposure (Figure 3.18), are 500-600 years different with calibrated ages of  $2550 \pm 190$  ( $2 \sigma$ ) yrs. BP and  $3195 \pm 165$  yrs BP respectively (Table 3.1 and Figure 3.20). Similarly,

two samples from the same suspended-load layer in channel 9, U8-05 and U7-10(1) are 400 years different, with calibrated ages of  $3595 \pm 125$  yrs. BP and  $3900 \pm 180$  yrs BP respectively.

The inheritance problem is not unique to this site, since other sites locally and far have encountered same problem. Disconcordant or stratigraphic inverse ages of detrital charcoal are common (e.g. Rockwell et al., 2001; Vaughan et al., 1999; Rubin et al., 1997; Grant and Sieh, 1993, 1994; Nelson, 1992; Blong and Gillespie, 1978). At Phelan fan site, 5 - 6 km southeast of the Wallace Creek site, Grant and Sieh (1993) reported that radiocarbon dates on samples from the same stratum can differ by more than five hundred years. At Bidart fan site, a 2m-thick section that were probably deposited in two to three centuries, contain charcoal samples of identical even stratigraphic inverse ages (Grant and Sieh, 1994).

### **3.6.2 Ages of the channels**

Despite the inheritance problems, ages of the channels and the intervening offset events, can still be bracketed roughly, if the radiocarbon ages of samples are evaluated in the context of other information. Figure 3.21 displays the date ranges of radiocarbon samples from channels. Unless stated otherwise, we will discuss dendro-calibrated calendar ages (Stuiver et al., 1998; Ramsey, 2000) in  $2\sigma$  ranges rather than  $1\sigma$  in order to reduce the likelihood of erroneous interpretation, given the detrital nature of most carbon samples.

Figure 3.21. Radiocarbon date ranges of samples from the Wallace Creek site plotted as a function of age and stratigraphic order. The age ranges that are the most reliable and are used to calculate event dates appear in black, whereas other ages appear in gray. Bars under the age ranges are 1- and 2-sigma ranges. OxCal program Ver. 3.5 (Ramsey, 2000) uses atmospheric data from Stuiver et al. (1998).

#### **Channel 1-a**

Four samples from the upstream segment of this channel yielded dates. Three dates are from the basal deposits and thus constrain the age of pre-event strata, and one date is from the post-event sediments (Figure 3.20). Three pre-event samples yielded an age of AD 1300 - 1480,

and their ages are consistent with their stratigraphic order (Figure 3.21). The sample from the post-event stratum yielded an age range of A.D. 1650 - 1960.

### **Channel 2-b**

The age of channel 2-b is constrained by several charcoal samples in channels 2 and *b*. Three charcoal samples U8-03, U3-02 and U9-03 in upstream channel 2, with the first being stratigraphically the lowest and the last being the highest, yielded  $2\sigma$  calendar age ranges of A.D. 1190 - 1300, A.D. 1260-1450 and A.D. 1180-1300, respectively. Within their 2-sigma errors, these dates are consistent with their stratigraphic order.

The age of a sample from the same, basal stratum 10 as U8-03 but in the downstream channel (dn5-ne06-01) (Figure 2.9) yielded an age range of A.D. 1460 - 1650. This is significantly younger than the age of sample U8-03. The downstream stratum that contains the sample is not bioturbated, so we have no reason to suspect the sample was introduced after deposition of the basal unit. The deposits are within well-defined channel walls; above this bed is the characteristic layer of horizontally bedded and well-sorted gravels to sand. Neither the channel scouring nor the characteristic layer above shows evidence of bioturbation. Thus, we interpret the date from the upstream basal unit 10 to be inherited and the date from the downstream channel (A.D. 1460 – 1650) to more closely reflect the age of the basal unit. The greater age of stratigraphically higher samples U3-02 and U9-03 probably indicate that these samples are also reworked charcoal.

The radiocarbon age of sample dn5-ne06-01 implies that dates from samples in the basal units of channel 1, which formed later, indicate an incision of the channel sometime within the range A.D. 1300 – 1480 suggests that these dates are greater than the actual age of the stratum.

### **Channel 3-c**

There is no constraint of the absolute age of the incision of channel 3-c and the faulting event that followed, because no charcoal grains were found within this channel, or in the colluvium immediately above.

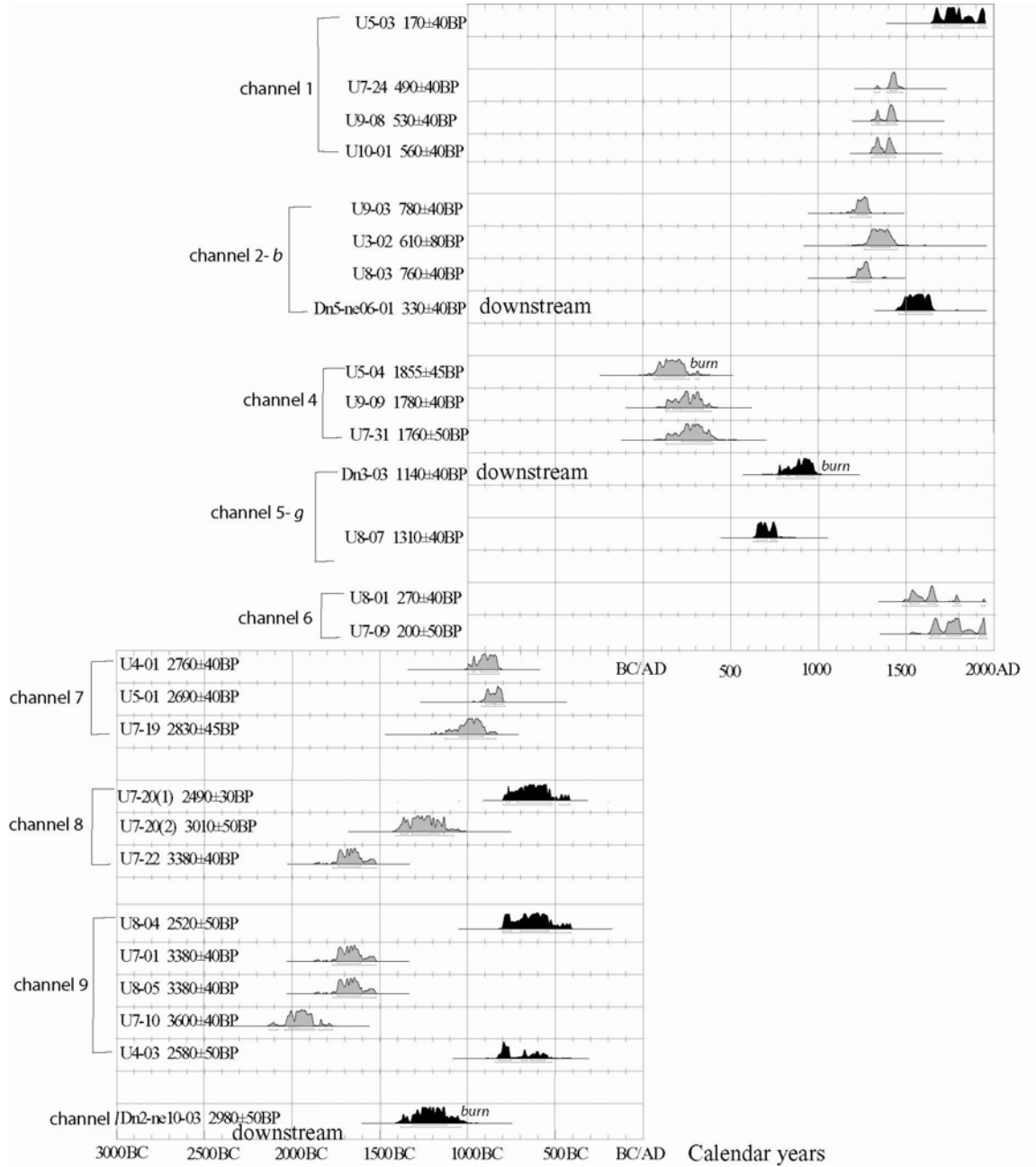


Figure 3.21. Radiocarbon date ranges of samples from the Wallace Creek site plotted as a function of age and stratigraphic order. The age ranges that are the most reliable and are used to calculate event dates appear in black, whereas other ages appear in gray. Bars under the age ranges are 1- and 2-sigma ranges. OxCal program Version 3.5 (Ramsey, 2000) uses atmospheric data from Stuiver et al. (1998).

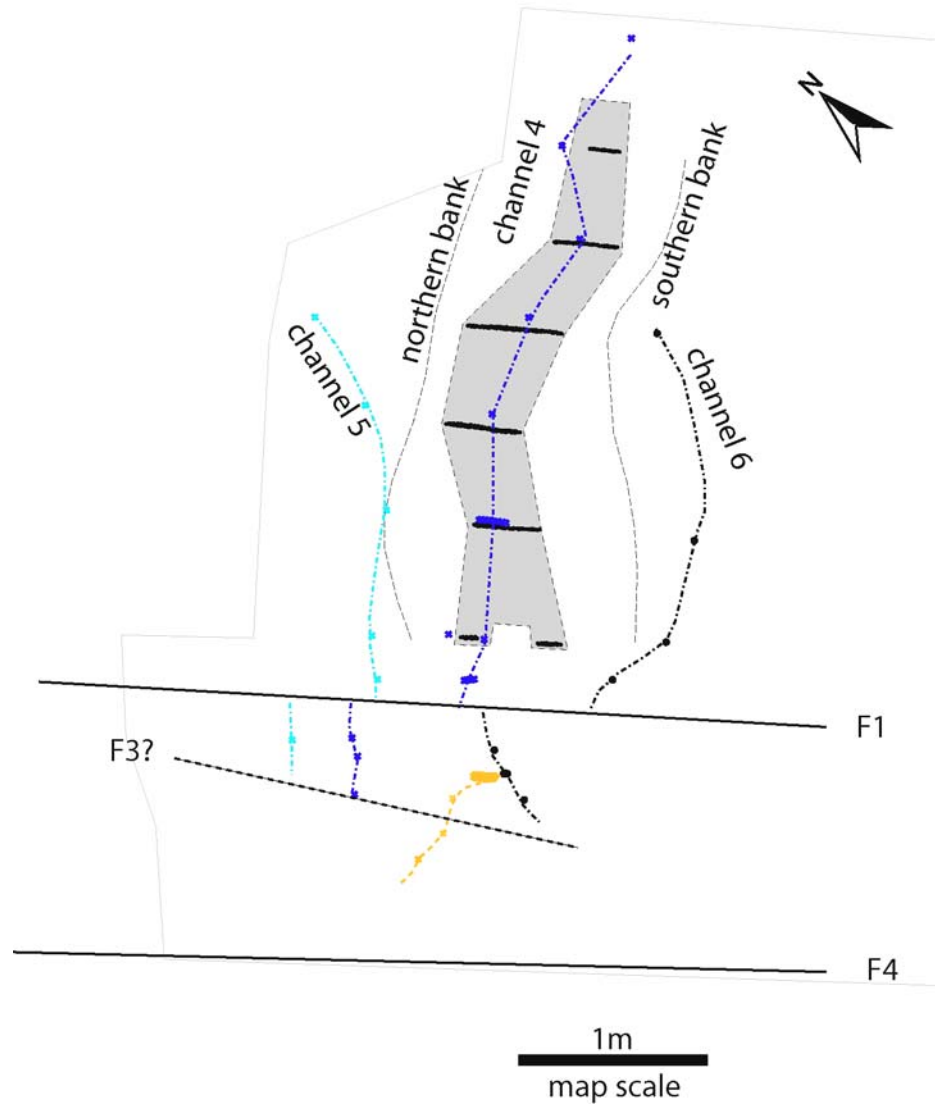


Figure 3.22. Map of the extent of the reddish burn in the strata of channel 4. The burn is a 3 to 4-m-long patch that winds along the center of channel 4. The sinuous nature of the burn and the fine grain size of the charcoal contained within it suggests that it is not likely to represent a woody log that was transported to the channel and then burned in-situ. Still the material appears to be older than the stratum that contains it (see text).

### **Channels 4-d and 5-g**

A burn horizon in channel 4 yielded sample U5-04 and beds below the burn yielded two additional samples, U9-09 and U7-31. The reddish horizon of the burn forms a 3- to 4-m-long, 0.2- to 0.4-m-wide and 3- to 8-cm-thick body in the center of channel 4 (Figure 3.22). We are not sure the implications of the continuation and extensiveness of this burn horizon, at least none of other burn horizons at the site are as continuous.

The calendar age range of the sample from the burn horizon is A.D. 60 - 320, roughly in the same range as that of the overlying and underlying samples -- A.D. 130 - 390 and A.D. 130 - 400 (Figure 3.21). Such harmony in ages of charcoal samples from adjacent strata is unusual in a desert environment and is a cause for joy – at least initially! The similarity of the three date ranges could imply that channel 4 filled in a few hundred years or less. More importantly, it could imply that the charcoal samples do indeed represent the date of deposition of the strata.

However the ages of samples from underlying channel 5-g raises suspicions. Two carbon samples help date channel 5-g, U8-07 on the upstream side and Dn3-03 on the downstream side of the fault. U8-07 and Dn3-03 yielded slightly overlapping calendar age ranges of A.D. 640 - 780 and A.D. 770 - 990, respectively. These ages are much younger than those of samples in channel 4-d.

Sample U8-07 came from a bed 20 cm above the channel floor (Figure 3.20). The sample is composite fine-grained detrital charcoal extracted from a bulk sample.

In contrast, dn3-03 was a single grain of charcoal sample from a reddish-orange burn horizon in the colluvium that overlies channel g (Figures 3.8 and 2.15). The fire scar and the sample Dn3-03 are all located in the vicinity of channel g, either above the edges of channel g or in the colluvium directly on top of the channel (Figure 3.8). We have no reason to believe that the date of this sample would not provide a good constraint on the timing of its burial.

The spatial distribution of the fire scar led us to conclude that it occurred shortly before or after channel g was abandoned, as a result of beheading by strike-slip motion along the fault. It is uncertain, however, whether the burn horizon is in strata that pre-date the abandonment of channel g. The burn is in the poorly sorted fine-grained colluvium, 15 - 20 cm above the evident coarser-grained fluvial channel fills and about 50 cm below the present ground surface. If the

transition from fluvial to colluvial fills indicates the abandonment of the channel, then the fire would postdate the offset event that caused the abandonment of channel g. The 20 cm or less vertical separation between fluvial channel fills and burn might indicate the fire only shortly postdated the abandonment of channel g. But if the transition simply reflects the onset of a hiatus in deposition, the burn horizon may either pre-date or post-date the offset event.

The ages of samples from channel 5-g implies that the samples from channel 4-d may be reworked.

Could the burn in channel 4 consists of reworked materials, say, for example, a very old tree branch that washed down a slope into a channel and then was burned *in situ*? This hypothesis is highly speculative, but not impossible. A similar scenario was proposed by Grant and Sieh (1993) in their 3-D excavation study of offset associated with the 1857 earthquake. At a site several km southeast of Wallace Creek, they found a burn horizon in the upper sediments of a channel. A sample from the burn yielded a date that is several centuries older than those of samples from the underlying sediments. In particular, the burn sample had a 2  $\sigma$  calendar age of A.D. 901-1151 whereas a sample from the substrate had a 2  $\sigma$  range of A.D. 1305 – 1623. The woody texture and high  $\delta^{13}\text{C}$  value of the burn sample led them to suspect that the burn was a saltbush transported to the excavation site by flood waters, burned *in situ* as detrital wood by a wildfire, and then buried by sediments. Thus the discordant older age of the burn probably reflects the death of material, centuries older than the deposition of sediments that contain the burn.

### **Channel 6-h**

Samples U8-01 and U7-09 from channel 6 yielded abnormally young and nearly modern ages, obviously inconsistent with the stratigraphic ordering and dates from other channels, e.g. channel 1 and 2, from where we are more confident with the intactness of the stratigraphy that bears the sample. Sample U8-01 was a rounded single charcoal grain about 1.5 cm in diameter and was suspected initially to be re-worked based upon its roundness. U7-09 was extracted from a bulk sample that was collected from the gravelly poorly sorted sand and silt bed. The place we sampled was not obviously bioturbated in the exposure surface, but we surmise that we might

have dug into a burrow when we dug centimeters into the trench wall to collect the bulk dirt sample. This would help us explain the anomalously young age of sample U8-01.

### **Dates of older channels**

Samples collected from older channels do not help to constrain the rupture sequence derived in the study. Nonetheless, they may offer important information for later studies of finding the matches of these channels across the fault, and thus, we will discuss briefly the dates of these samples.

### **Channel 9**

Five samples from the oldest upstream channel, channel 9, were dated (Figure 3.21). Except sample U4-03, other four are in normal stratigraphic sequence, yet span over 1,000 years from B.C. 2130 - 1770 (sample U7-10(1)) to B.C. 800 - 410 (sample U8-04) (Figure 3.21 and Table 3.1). As discussed above, 400 years or more difference between two same-bed samples U8-05 and U7-10(1) presents the evidence for their detrital nature.

Of the samples from channel 9, the youngest age of sample U8-04 may represent the closest approximation to the date of deposition of the alluvium that contains the sample. U8-04 was collected from a 5-cm thick dark charcoal-rich bed; the absence of such high charcoal concentration in beds either above or below suggests the approximation of a range fire in time of the deposition of this charcoal-bearing bed.

One may find the age of sample U4-03 is a violation of this interpretation, since U4-03 yielded an age range similar to U8-04 even though it appears to be stratigraphically lower than the latter. However, sample U4-03 was collected from channel slope and only 5 cm below the post-offset channel fills (Figure 3.20), it is arguable that sample U4-03 may also represent the age of the post-offset filling, given its closeness to the channel edge.

### **Channel 8**

Three samples from channel 8 also gave disparate ages with a maximum difference of one thousand years or so (Figure 3.21). Of the three samples, U7-20(1) yielded the youngest age

range -- B.C. 790 - 410, about 600 years younger than sample U7-20(2), which came from the same layer of post-offset suspended-load fines. Curiously, the youngest date in channel 8 from sample U7-20(1) is indistinguishable from that of U8-04 in channel 9. However, if the real age of U7-20(1) were close to the upper bound and that of U8-04 to the lower bound of the same date of 790-410 B.C., perhaps the incision of channel 8 and the following faulting event both occurred in this 400-year span. Sample U7-22, collected from pre-offset deposits, yielded an age of B.C. 1770 - 1520, significantly older than that of sample U7-20(1) but identical to that of post-offset samples U8-05 and U7-01 in channel 9. Sample U7-20 is likely reworked.

### **Channel 7**

All three dated samples from channel 7 yielded ages that fall into a 300-year range -- B.C. 1130 - 790. Younger than some samples from underlying channels 8 and 9, they are nevertheless older than that of the youngest sample in channels 8 and 9. If the youngest dates in channels 8 and 9 are valid, channel 7 would have started its incision sometime after B.C. 400.

### **Downstream channels k and l**

Dn2-ne11-03 was a single grain of charcoal collected from the sandy matrix of the very coarse bedload deposits of channel k. It has an age range of 17 -18 kyr. B.P., as old as the underlying late Pleistocene alluvium (Table 3.1). Thus, it could very well be a piece of reworked charcoal.

A burn horizon was clearly exposed in the upper alluvium of channel l. The bulk sample dn2-ne10-03 from this burn yielded a calendar age range of B.C. 1380 - 1040. This date suggests that channel l is coeval to upstream channel 9. However, the correlation of channel l with channel 9 is implausible, because channel l leaves the fault zone diagonally whereas channel 9 enters the fault zone at a right angle. Not unlikely though, channel l was incised when connected to drainage C about  $110 \pm 3$  m to the southeast; if it is true, then the slip rate would be around 31 - 37mm/yr, nearly identical to that in Sieh and Jahns (1984).

## 3.7 A history of the latest six ruptures

### 3.7.1 Constraints from our data

Now that we have established a sequence of offsets and our best estimates of the dates of deposition of various beds, we are prepared to create an offset history. Understandably, the magnitude of the offsets in this history will be more tightly constrained than their dates of occurrence.

Figure 3.23 displays the date ranges of all radiocarbon samples and our estimates of the dates of the six events. The radiocarbon ages that we have argued most closely reflect the age of the surrounding strata appear black, whereas the ones that appear to have substantial inheritance or are far too young appear gray. The stratigraphic location of each of the six events appears as a thick horizontal line. The horizontal positioning and length of the line indicates the age range of the event, which we will defend, below.

A quick glance at the relationship of the event horizons and the black constraining date ranges shows that the ages of the events are poorly constrained. Nonetheless, they are loosely bracketed by the dates of samples from immediately older and younger channels.

We do not have the sort of stratigraphy that would allow us to interpolate between the bounding sample ages in the way that Biasi et al. (2002) refined event dates within the peaty, tabular-bedded Wrightwood and Pallett Creek paleoseismic sites. Unfortunately, our highly channelized and bioturbated stratigraphy provides little opportunity to refine the event dates much beyond an averaging of the upper- and lower-bounding dates.

Figure 3.24 shows an example of an event's age range calculated from the weighted average of superjacent and subjacent strata. In this case, the  $2\sigma$  age range for WC2 is A.D. 1470 – 1955, based upon the averaging, alone. But since we know the event occurred before the great earthquake of 1857, we can remove a century from the younger end of this range.

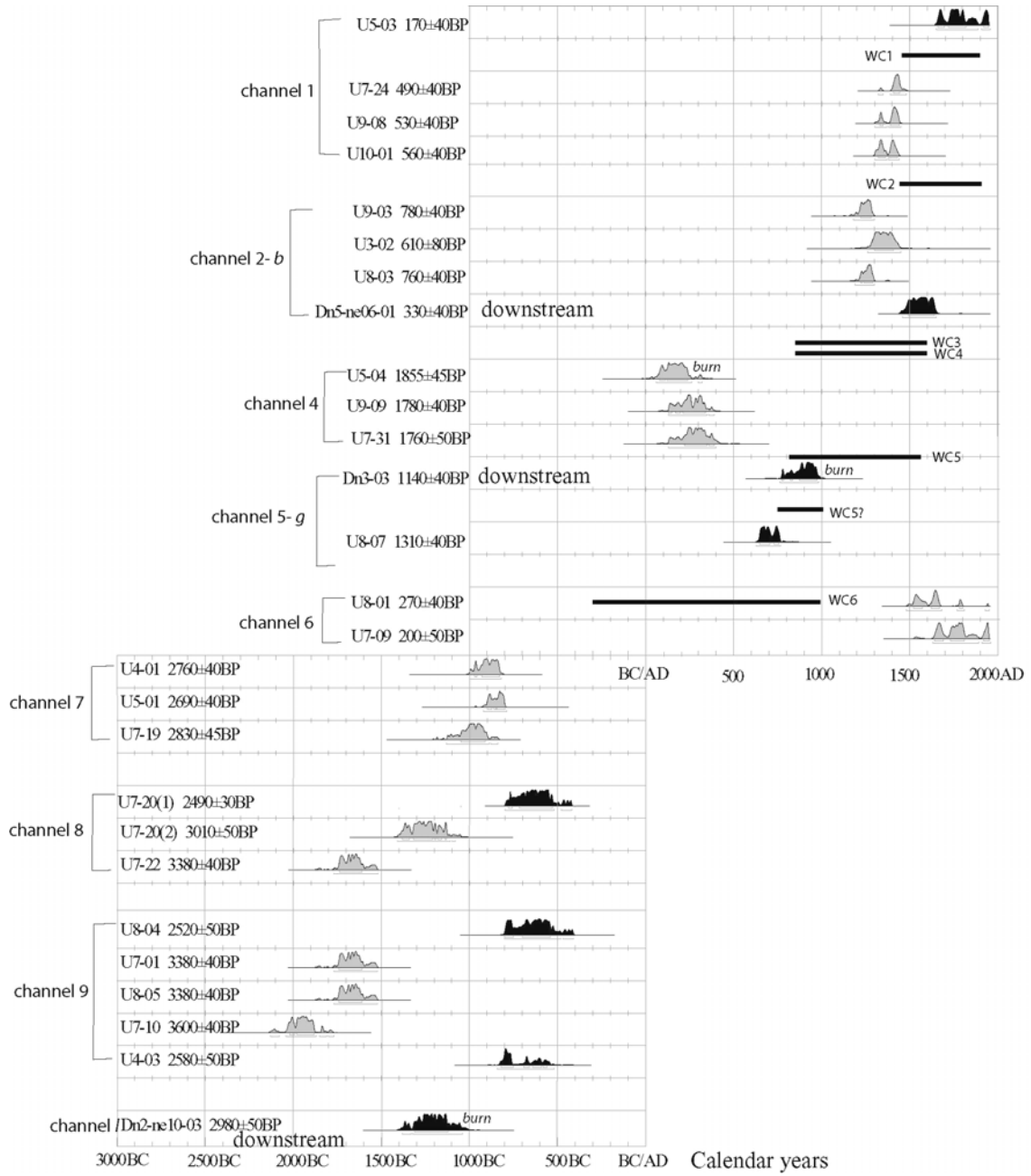


Figure 3.23. The stratigraphic positions of offsets WC1 through WC6. The horizontal bars indicate their date ranges.

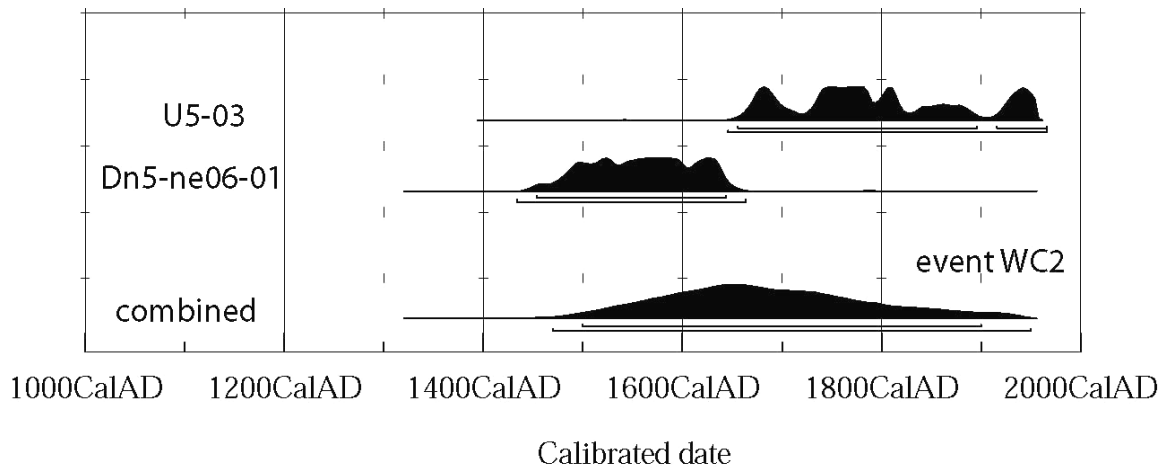


Figure 3.24 Probability distribution of age range of offset event WC2, generated by OxCal program\*.

Events WC3 and WC4, which occurred between the filling of channel 5-f and the cutting of channel 3-c, are more poorly constrained. We have no dates from channel 3-c and unreliable dates from channel 4-d (section 3.6.2). Channel 5-g yielded the tightest older bounding date range-- about A.D. 800 to 1000. And channel 2-b provides the closest younger bounding date range – about A.D. 1450 – 1650. Thus, the best we can do is say that both events occurred sometime within the millennium between the 8<sup>th</sup> and 17<sup>th</sup> centuries.

Event WC5 occurred sometime before a date within the range A.D. 800 – 1000, the age range of the *in situ* burn immediately above channel g (sample dn3-03, Figure 3.8). Event WC6 is also poorly constrained. The bracketing ages, from channels 8 and 5, constrain the date to between dates in the ranges B.C. 500 – 700 and A.D. 800 – 1000.

\* Combinations of probability distribution are simply done by using the Bayesian rules for combinations of probabilities (see Bayes 1763 and Doran and Hodgson 1975). We first calculate the probability of the event before the date of Dn5-ne06-01, which gives us a distribution B(t) and the probability after the date of U5-03, which is A(t). The date range for the event is the combination of the two: A(t) B(t). For the purposes of display the maximum of the resultant distributions is always normalized to 1.

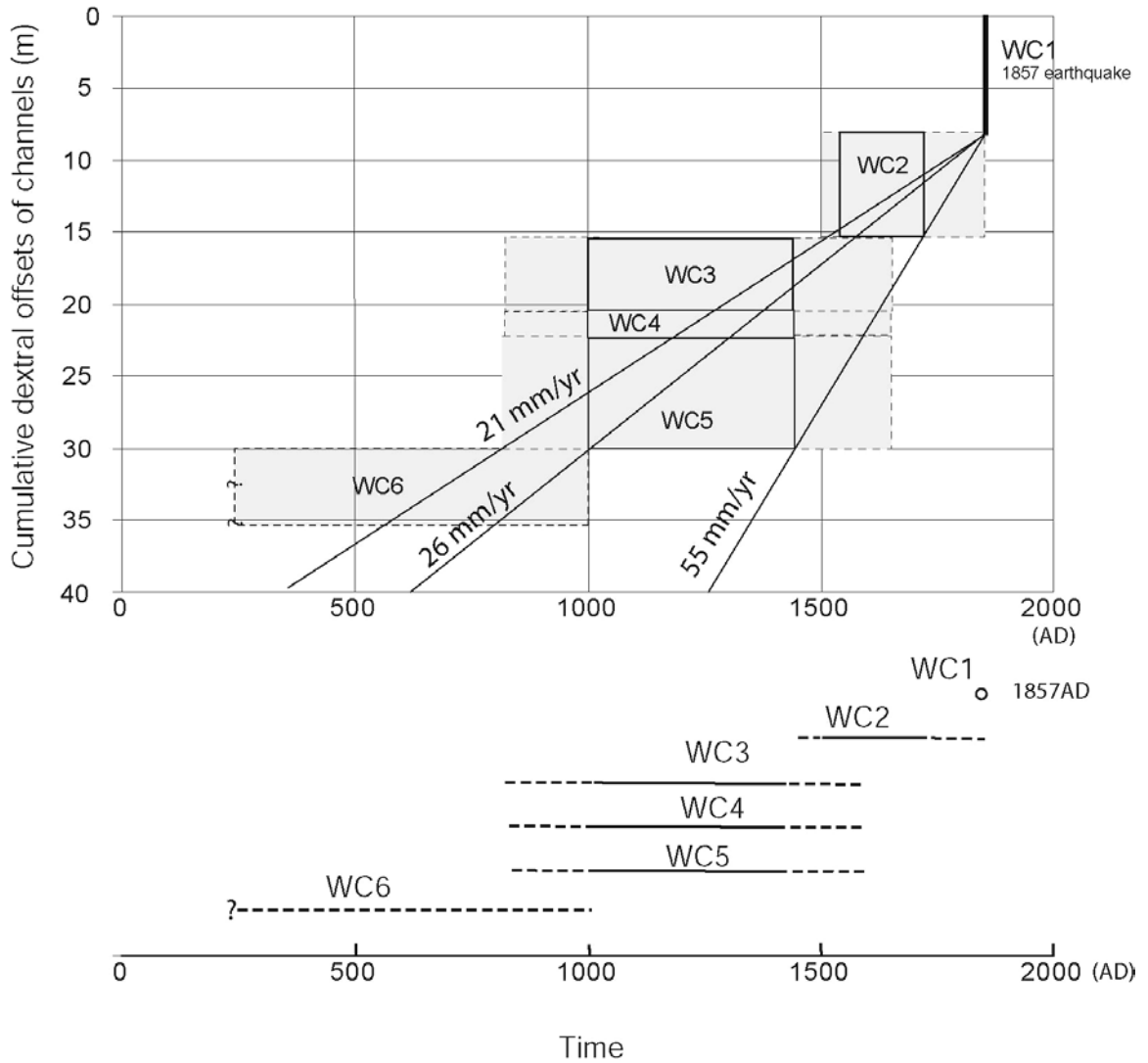


Figure 3.25. Tentative slip history of the Wallace Creek paleoseismic site for the last 1500 year, based solely on data from the site. The vertical dimensions of the boxes indicate the magnitude of slip in each event. Errors in slip magnitude are too small to show clearly at this scale. The horizontal dimensions of the gray boxes represent the age constraints of the events, solid lines denoting 1-sigma uncertainties and dashed lines indicating 2-sigma uncertainties. The average slip rate of 26 mm/yr is shown only for reference. Using only the radiocarbon dates from the site, the dates of the earthquakes are too poorly known to allow useful constraints of long-term slip rate, variations in slip rate or recurrence intervals between the earthquakes.

The constraints on rupture magnitudes and dates appear together graphically in Figure 3.25. The constraints are so poor that we cannot assess any of the important questions about recurrent behavior. Millennially averaged slip rates derived from the data range between 21 and 55 mm/yr, and we have no basis for discussing variability of recurrence within the past two millennia. The great uncertainties in event dates also preclude any tests of models of recurrence, such as time- and slip-predictable models.

### ***3.7.2 Additional constraints from other data***

Fortunately, age control of depositional events and episodes from other sites of late Holocene deposition allow us to offer improvements to the dates of events. These sites include paleoseismic sites just a few kilometers to the southeast and the climatic record from Mono Lake, a few hundred km to the northeast. The improvements in age control that we suggest are not based upon correlation of earthquakes between these sites and Wallace Creek. Rather, they are based upon the correlation of periods of deposition and non-deposition at the sites.

#### **3.7.2.1 Correlation with the Phelan Creeks site**

The Phelan Creeks paleoseismic site lies just 1.5 km southeast of our site (Figure 3.26). It has a series of cuts and fills that may correlate with our channel cuts and fills. If so, we can benefit from the correlations, because the radiocarbon dates from the Phelan Creeks site are more self-consistent and thus appear to be less plagued by problems of inheritance. The Phelan Creeks paleoseismic site was excavated in the 1980s (Sims, 1994, Sims et al., 1994 unpublished paper), although its sequence of offset was first described by Wallace (1968). The site encompasses two active channels, Little Phelan Creek and Large Phelan Creek, which at the time of the study were incised 1.25m and 4m into an alluvial surface at the fault. The morphology of the channels, aided by a few excavations, revealed that Little and Large Phelan Creeks are offset  $15.8 \pm 0.6$  m and  $17.4 \pm 1.6$  m, respectively. Two beheaded channels lie about 100 to 200 m to the northwest of Little Phelan Creek. Both beheaded paleo-channels were offset and abandoned prior to the

entrenchment of the downstream segments of Little and Large Phelan Creeks. Trenches H and C revealed that the nearest abandoned paleochannel bends along the fault.

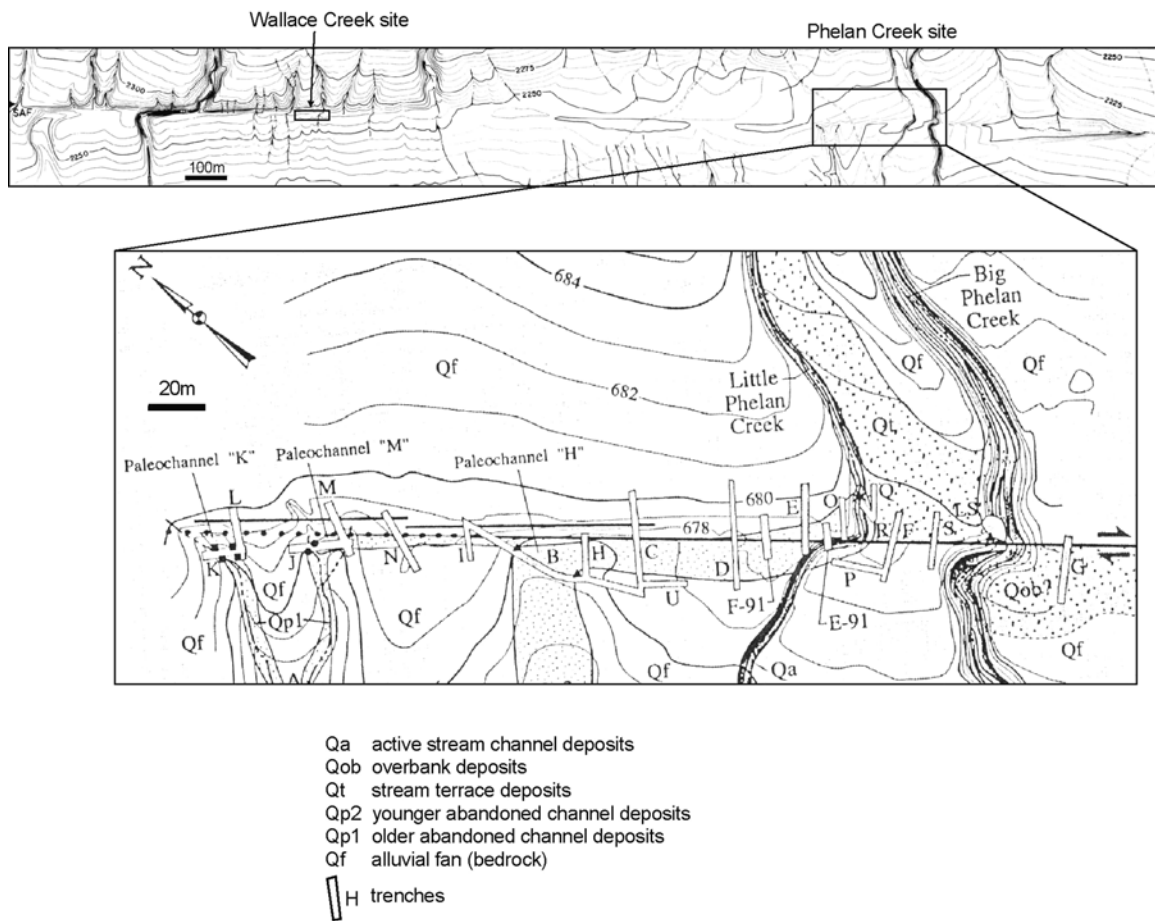


Figure 3.26. A paleoseismic investigation conducted at the Phelan Creeks site, 1.5km southeast of the Wallace Creek by Sims et al. (1989, 1994) provides plausible additional constraints on the dates of cut-and-fill sequences at the Wallace Creek site. The upper panel shows the location of the two sites along the fault (topo from Wallace and Sieh, 1986); the lower panel is the geologic map of the Phelan Creeks site. It shows the topography, basic channel units and trenches cuts to expose the stratigraphy of the offset channels.

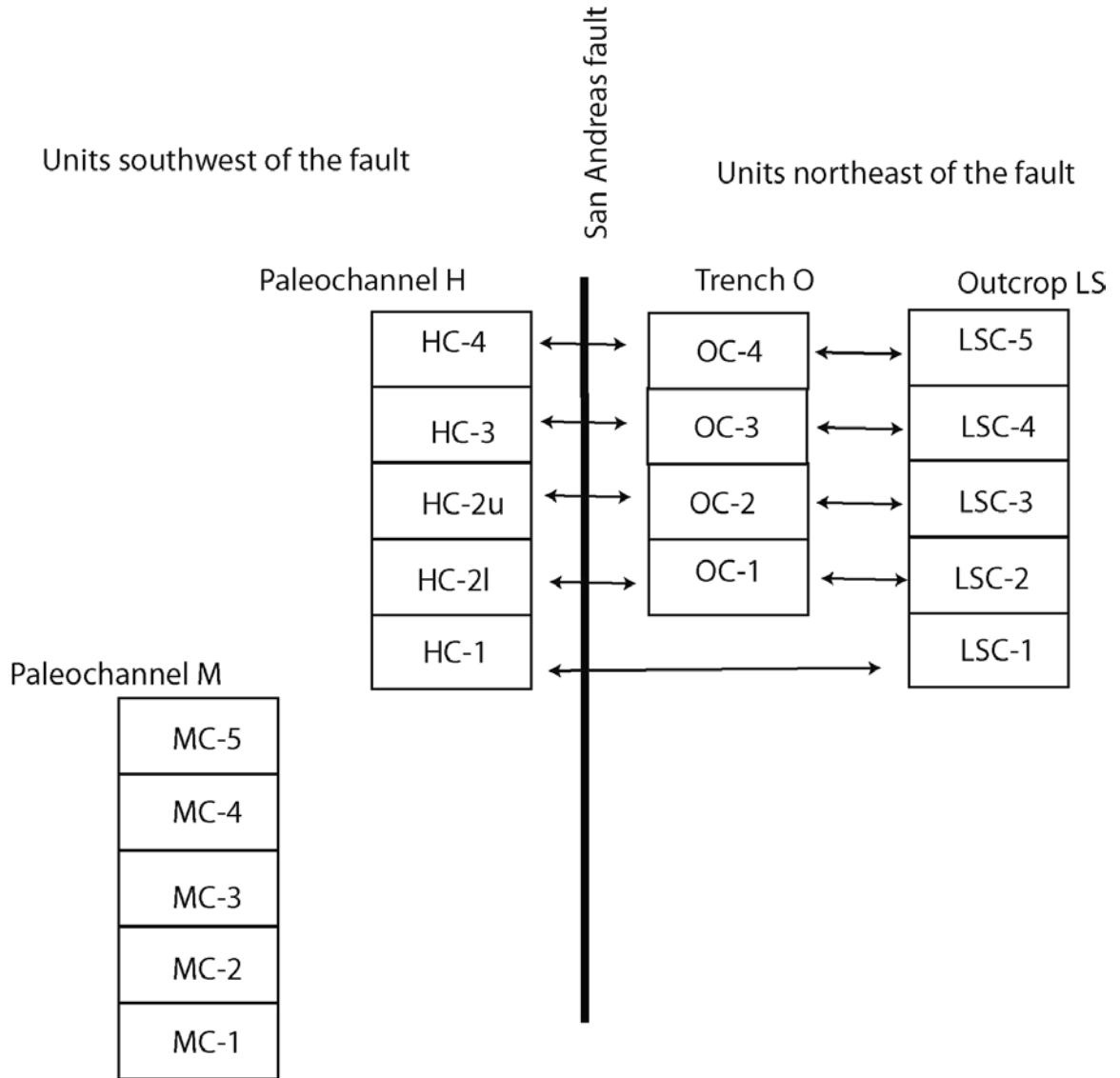


Figure 3.27. Proposed correlation of units east and west of the San Andreas fault at the Phelan Creeks paleoseismic site (modified from Sims et al., 1994a). Letter designations refer to trenches and exposures in Figure 3.26 in which the units were found.

Table 3.2 Radiocarbon samples at the Phelan Creek site

Sample No	Units	Laboratory <sup>14</sup> C ages years BP ± 1σ	Sample ages according to Sims et al. (1994)		Recalculated calendar years		Remarks
			Calib years BP ± 1σ	rated <sup>(1)</sup> years BP ± 1σ	1σ range <sup>(2)</sup>	2σ range <sup>(2)</sup>	
O-1	HC4	565 ± 51	589 ± 38	A.D. 1300 - 1430	A.D. 1300-1440	<i>in-situ</i> burn	
B-49	HC4	1142 ± 144	1064 ± 72	A.D. 710- 1020	A.D. 600-1250	reworked charcoal	
Q-2	HC3	816 ± 51	739 ± 24	A.D. 1180-1280	A.D. 1040-1290		
E-7	HC3	799 ± 53	718 ± 32	A.D. 1190-1285	A.D. 1060-1300		
D-18	HC3	840 ± 200	804 ± 86	A.D. 990-1390	A.D. 700-1450		
B-65	HC3?	1545 ± 100	1441 ± 53	A.D. 420-620	A.D. 250-670		
D-38	HC3	1610 ± 120	1502 ± 66	A.D. 260-600	A.D. 100-700	reworked charcoal	
Q-5	HC2u	1017 ± 50	947 ± 20	A.D. 900-1160	A.D. 890-1160		
F-19	HC2u	1170 ± 65	993 ± 33	A.D. 770-960	A.D. 690-1000		
G-8	HC2u	1210 ± 100	1157 ± 58	A.D. 690-950	A.D. 650-1020		
B-35	HC2l	1639 ± 50	1554 ± 30	A.D. 340-540	A.D. 250-540		
LS-7	HC2l	1662 ± 256	1585 ± 148	A.D. 50-650	B.C. 400- A.D. 1000		
96E-16	HC2l	1827 ± 128	1754 ± 80	A.D. 50-380	B.C. 100- A.D. 550		
LS-4	HC1	2182 ± 208	2144 ± 130	B.C. 500 - A.D.100	B.C. 800- A.D. 300		
D-17	HC1	2415 ± 60	2421 ± 40	B.C. 760 - 400	B.C. 770-390		
D-21	HC1	2374 ± 56	2407 ± 38	B.C. 760 - 380	B.C. 800-350		
I-12	MC4	3475 ± 74	3764 ± 45	B.C. 1890 - 1680	B.C. 2020-1600	reworked charcoal?	
I-5	MC4	4030 ± 130	4557 ± 160	B.C. 2900 - 2350	B.C. 2900-2200	reworked charcoal?	
B-10	MC3	3140 ± 190	3335 ± 129	B.C. 1700 -1100	B.C. 1900-900		

(1) Dendrocorrection of dates < 4000 yr B.P. determined from calibration curve of Stuiver and Pearson (1986); dates > 4000 yr B.P. calculated from calibration curve of Pearson and others (1986).

(2) Assuming laboratory <sup>14</sup>C ages are given with "1σ corrections.

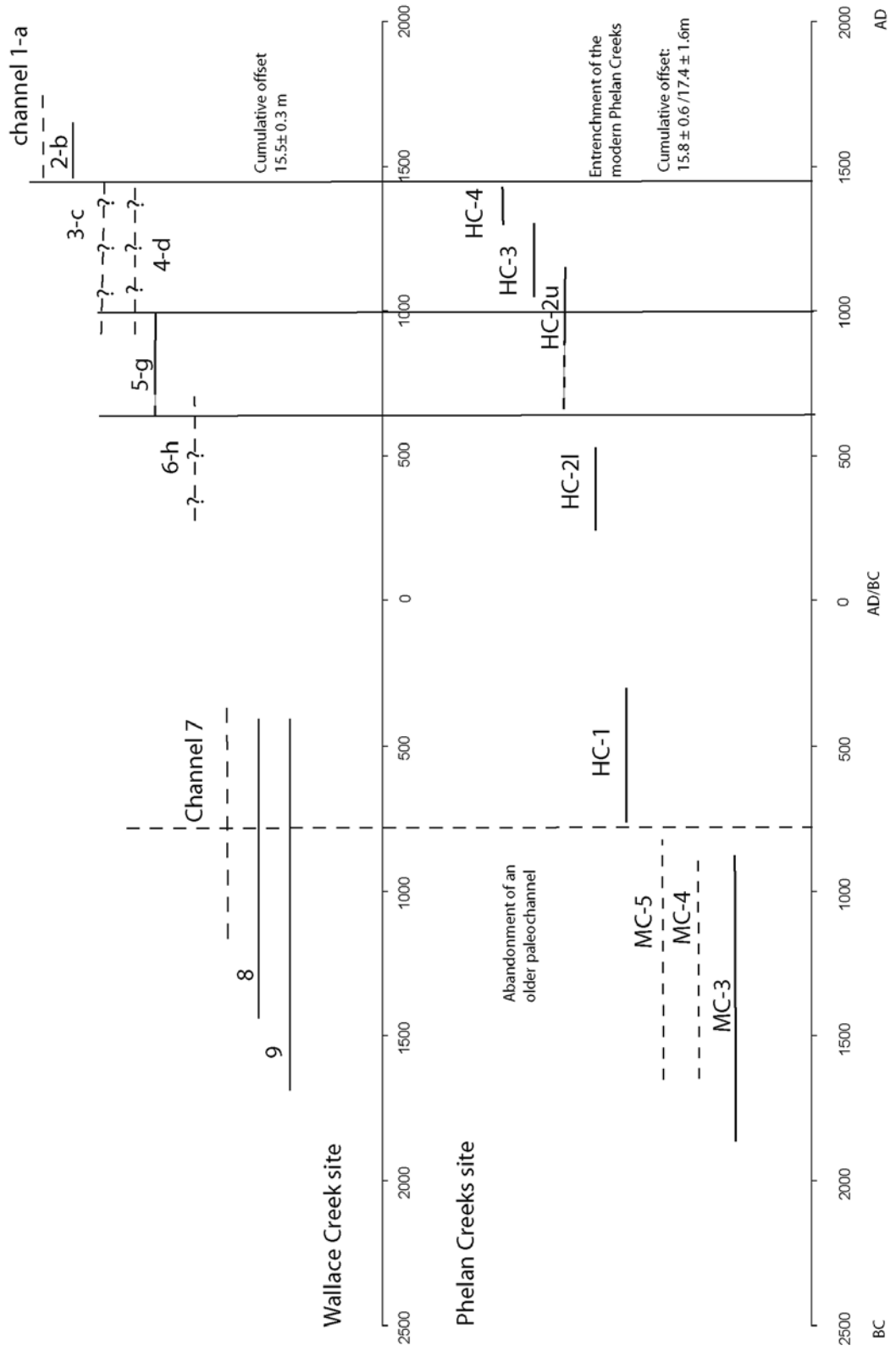
Exposed in trenches H and C within the fault-parallel segment of the paleochannel are five distinct cut-and-fill episodes that occurred immediately prior to abandonment of the channel. These units occur on both sides of the fault zone. Figure 3.27 shows the correlations of units southwest of the fault (HC-1 through HC-4) with those on the northeast side (OC-1 through 4 and LSC-1 through 5). The ages of these units are comparatively well dated (Table 3.2), but the amount of offset of each of these cuts-and-fills were not documented.

Sims et al. (1994) hypothesized that the sedimentary fill within each of the five cuts causally followed five ruptures of the fault. Thus he argued that the dates of the channel fills constrain the dates of earthquakes. We don't subscribe to this interpretation, but we are intrigued by the fact that the alluviation history of the last three thousands years at Phelan Creeks is remarkably similar to the channel history at the Wallace Creek site (Figure 3.28). The resemblance is manifested in several aspects.

First, both the timing and amount of offset of the Phelan Creeks are consistent with those of channel 2-b at the Wallace Creek site. Channel 2-b was incised shortly before a date within the range A.D. 1460 – 1600 and is offset 15.4 m. The beheaded channel at the Phelan Creeks site was abandoned at the time of incision of the Little and Large Phelan Creeks, which subsequently have been offset 16 and 17 m, respectively. Coarse deposition ceased in the abandoned channel at that time. The time of the abandonment was shortly after a date within the range A.D. 1300 – 1440. Thus, the maximum bound on the age of the 16- and 17-m offsets are constrained by these youngest dates in unit HC-4 within the abandoned channel.

The record of sedimentation before the 15- to 17-m offset is also similar at the two sites. Both the Phelan Creeks and at Wallace Creek sites exhibit four cuts and fills between about A.D.

Figure 3.28. (Next page) A proposed correlation of the alluviation history at the Wallace Creek site with that at the Phelan Creeks. Vertical lines represent synchronous alluvial events, which are less certain where dashed. The six cut-and-fill events of the past 1500 years at both sites could well be correlative, as could the long hiatus in alluviation and incision centered on AD zero.



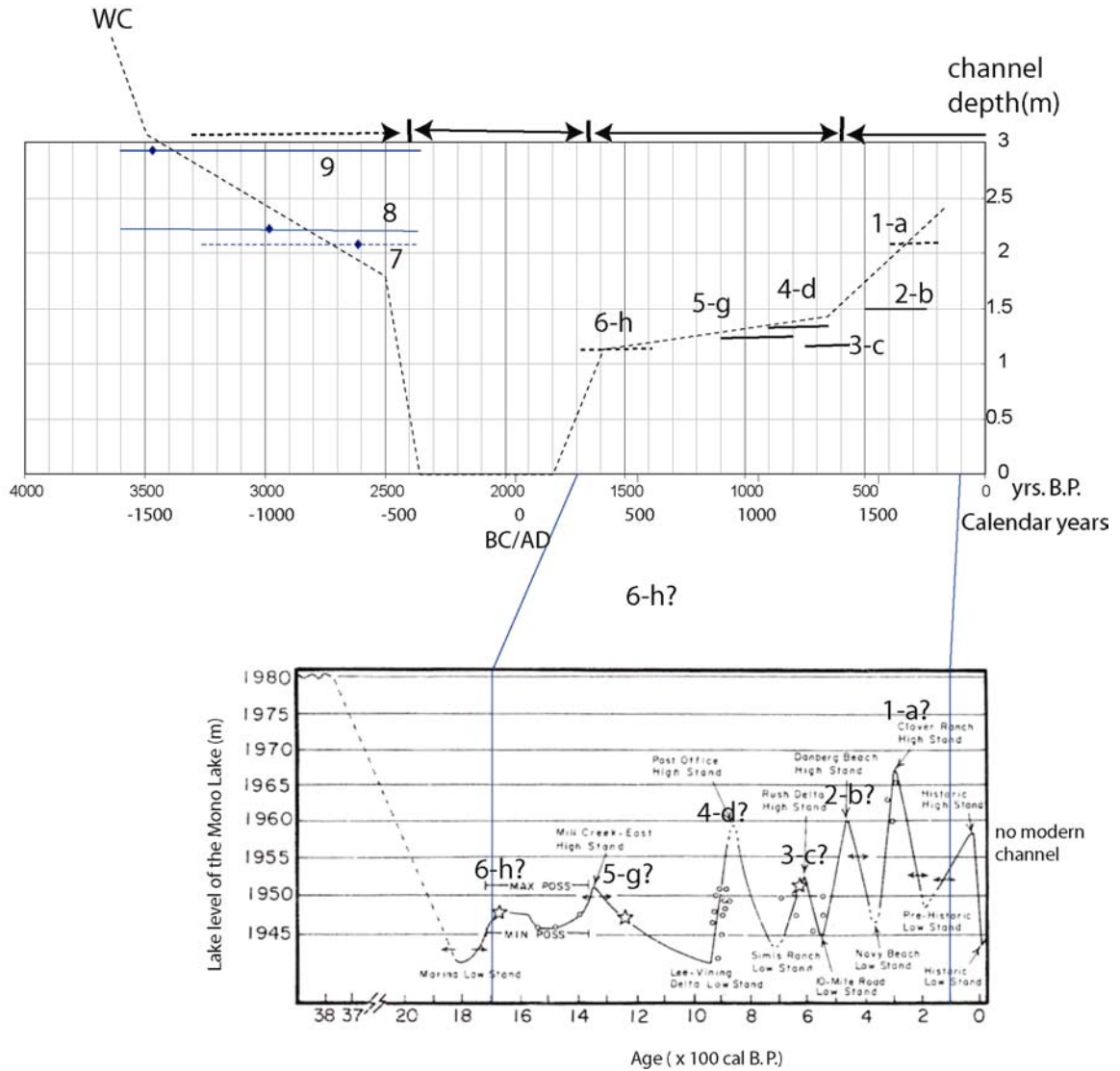


Figure 3.29. The similarity of the record of rises and falls in of the Mono Lake in eastern California with cuts and fills at the Wallace Creek and Phelan Creeks sites suggest the alluvial histories have been climatically regulated. The upper panel shows the incision events at Wallace Creek as a function of time and depth of incision. The lower panel is Stine's (1990) record of lake fluctuations.

300 and 1450. At Phelan Creeks, these are the 4 unconformity-bounded sedimentary units in paleochannel HC. At Wallace Creek, these are channels 3 through channel 6. Figure 3.28 illustrates the compatibility in the ages of these two sequences.

A third similarity between the Phelan Creeks and Wallace Creek records is the existence of a long hiatus in erosion and deposition in the centuries before and after A.D. zero. At Phelan Creeks, this is a 500- to 1000-year hiatus prior to HC-21. At the Wallace Creek site, the hiatus occurred prior to incision of channel 6-h and after cutting and filling of upstream channel 7. This hiatus corresponds to the long downstream stretch that lacks downstream channels between channels  $\underline{h}$  and  $\underline{i}$  (Figure 3.4a).

This hiatus appears to exist at late Holocene sites elsewhere in southern California, as well. Excavations across the Garlock fault, southeast of the Carrizo Plain, show an extremely low sedimentation rate and more infrequent flooding events during the same period (McGill and Rockwell, 1998). Also during the same time period, Walker Lake in northeastern California and west-central Nevada became shallow and probably desiccated (Benson et al., 1991).

### **3.7.2.2 Correlation of cut and fill with climatic variability**

The similarity of the Wallace Creek and Phelan Creeks records to the record of fluctuation in the level of Mono Lake in eastern California suggests that the cut-and-fill history of the two sites in the Carrizo Plain is probably forced by regional changes in climate. Stine (1990) recovered an exquisite record of lake-level fluctuations from lake-bottom sediments that were exposed during partial dessication of the lake in the late 1980s. He showed that higher lake levels correspond to wetter periods and that lower lake levels correspond to warmer and drier periods. These fluctuations at Mono Lake probably correspond to shifts to the north and south in the average position of the jet stream, because the jet stream controls the degree to which Pacific storms are able to penetrate southward.

The prominent features of the Mono Lake record are a peak in lake level about 3700 years ago and 5 cycles of lake level in the past millennium (Figure 3.29). The 3700-year-old high stand is coincident with a rapid filling of the now-beheaded channel of Wallace Creek and resultant cutting of the current channel straight across the fault (Sieh and Jahns, 1984). Also, the dates of fill in our oldest upstream channel (9) immediately post-date this period (3380 yrs. B.P. to 2520 yrs. B.P. in Figure 3.21 and Table 3.1). This suggests that the upstream channel was

incised its deepest at the time of the Mono Lake 3700-year-BP high-stand and filled soon thereafter. These correlations with the 3700-years-BP high stand suggest that cuttings and fillings in the Carrizo Plain occurred during wetter conditions. The coincidence in the number of high stands of Mono Lake and cuts and fills at Wallace and Phelan Creeks suggests that modest climatic changes have forced the cuts and fills of the past millennium as well.

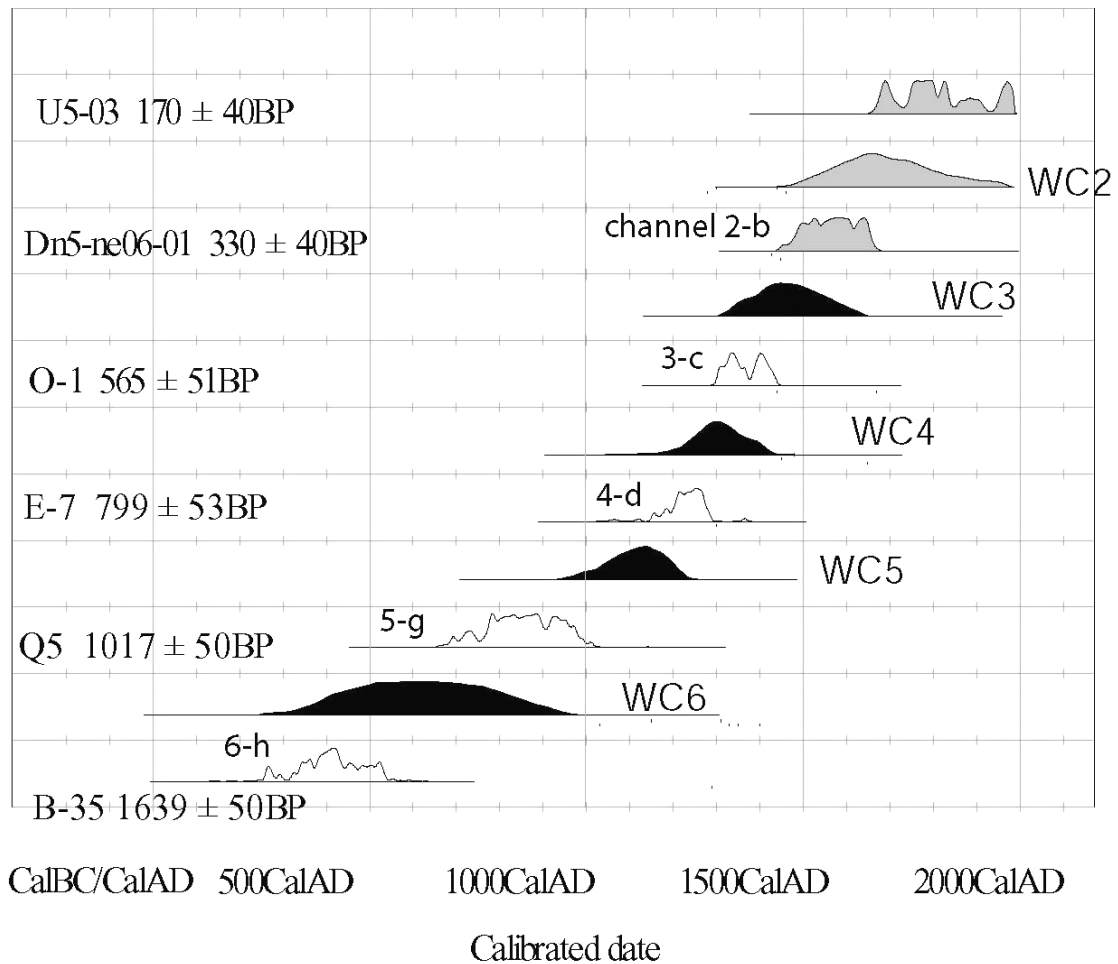


Figure 3.30. Revised dates of offset events using Phelan Creek dates. Open curves of date ranges represents inferred ages of channels based on the correlation of alluviation history at the Wallace Creek site and Phelan Creeks site. Solid dark curves are the modified age ranges of offset events. Gray curves indicate unchanged Wallace Creek dates.

Table 3.3 Age constraints of paleoseismic events near Wallace Creek

Dates from the Wallace Creek site only					
Events	Bounding dates			Ages ranges for events	
	After	Sample ID	Before	1 sigma range	3 sigma range
WC1	A.D. 1857		A.D. 1857	A.D. 1857	A.D. 1857
WC2	A.D. 1460-1650	dn5-ne06-01	A.D. 1650 - 1960	A.D. 1560-1770	A.D. 1500-1857
WC3	A.D. 770-1000	dn3-03	A.D. 1460-1650	A.D. 1000-1460	A.D. 850-1600
WC4	A.D. 770-1000	dn3-03	A.D. 1460-1650	A.D. 1000-1460	A.D. 850-1600
WC5	A.D. 770-1000	dn3-03	A.D. 770 - 1000	A.D. 1000-1460	A.D. 770-1000
WC6	B.C. 790-410	U7-20(1)	A.D. 770-1000	B.C. 400- A.D. 700	B.C. 700-A.D. 1000 B.C. 800 - A.D. 1000

Dates from the Wallace Creek and Phelan Creeks sites combined					
Events	Bounding dates			Age ranges for events	
	After	Sample ID	Before	1 sigma range	3 sigma range
WC1	A.D. 1857		A.D. 1857	A.D. 1857	A.D. 1857
WC2	A.D. 1460-1650	dn5-ne06-01	A.D. 1650 - 1960	A.D. 1560-1770	A.D. 1500-1857
WC3	A.D. 1300-1440	O-1	A.D. 1460-1650	A.D. 1380-1550	A.D. 1320-1610
WC4	A.D. 1060-1300	E-7 and Q-2	A.D. 1300-1440	A.D. 1240-1370	A.D. 1180-1430
WC5 <sup>1</sup>	A.D. 890-1160	Q-5	A.D. 770-1000	A.D. 905-965	A.D. 870-1020
WC5 <sup>2</sup>	A.D. 890-1160	Q-5	A.D. 1060-1300	A.D. 1040-1220	A.D. 970-1270
WC6?	A.D. 250-540	B35	A.D. 890-1160	A.D. 510-950	A.D. 350-1100

1 Age range of WC5 assuming that sample dn3-03 postdated the abandonment of channel 5-g.

2 Age range of WC5 substituting the bounding ages with Phelan Creeks dates.

### **7.2.3 Revised dates of Wallace Creek events using Phelan Creeks dates.**

The constraints from Phelan Creeks indicate that the last 4 events along this portion of the San Andreas fault occurred since A.D. 1240 or A.D. 1180 (The older bounds of the 1  $\sigma$  and 2  $\sigma$  age ranges of event WC4, respectively; Figure 3.30, and Table 3.3). If the correlation is valid, we can infer the ages of some unconstrained channels at Wallace Creek to be the same as those of the correlative unconformity-bounded units at Phelan Creeks. In particular, channel 3-c at the Wallace Creek site was probably incised sometime around A.D. 1300 - 1440, channel 4-d around A.D. 1060 - 1300 (Figure 3.28). Accordingly, offset event WC3 that caused the abandonment of channel 3-c occurred at a date within the 2 $\sigma$  range of A.D. 1320 - 1610, and event WC4 within the 2 $\sigma$  range of A.D. 1180 - 1430 (Figure 3.30 and Table 3.3).

The age of the fifth **event WC5**, however, is still ambiguous. The older bound for the date of event WC5 can be the age of **channel 5**, which is assumed to be similar to the Phelan Creek unit HC-2u, A.D. 890 - 1160. If we further substitute the age of unit HC-3, A.D. 1060 - 1300 for channel 4 as the upper bound, then the combination of these two bounding ages implies that WC5 occurred within the 2 $\sigma$  range of A.D. **970 - 1270** (Figure 3.30).

The correlation in alluvial history at the Wallace Creek and the Phelan Creeks sites gives also credit to the tentative channel match for channel 6-h: channel 6-h could have been incised around A.D. 250 - 540. The age of the subsequent offset event WC6 still has large uncertainty, probably sometime between the 6<sup>th</sup> and 10<sup>th</sup> century (Figure 3.30).

Figure 3.31 shows plots of offset versus time based upon these surrogate dates for the events. The two plots are identical, except that the constraints on event WC5 differ. In the upper plot, the date constraints are strictly from the Phelan Creek site. In the lower plot, we assume that our sample **Dn03-03**, the *in-situ* burn, post-dates the abandonment of channel 5, thus provides an upper-bounding date for WC5. **WC5** would have occurred within the 2 $\sigma$  range of A.D. **870 - 1020** (Figure 3.23 and Table 3.3). Although this age range overlaps with the previous estimation of A.D. 970 - 1270 within the 2 $\sigma$  uncertainty, the second estimation is significantly older than the first, particularly if one considers the corresponding 1 $\sigma$  age range. This ambiguity may have

important implication: the second interpretation of age constraints suggests a slip-time pattern more irregular than the first; it also implies a lower slip rate.

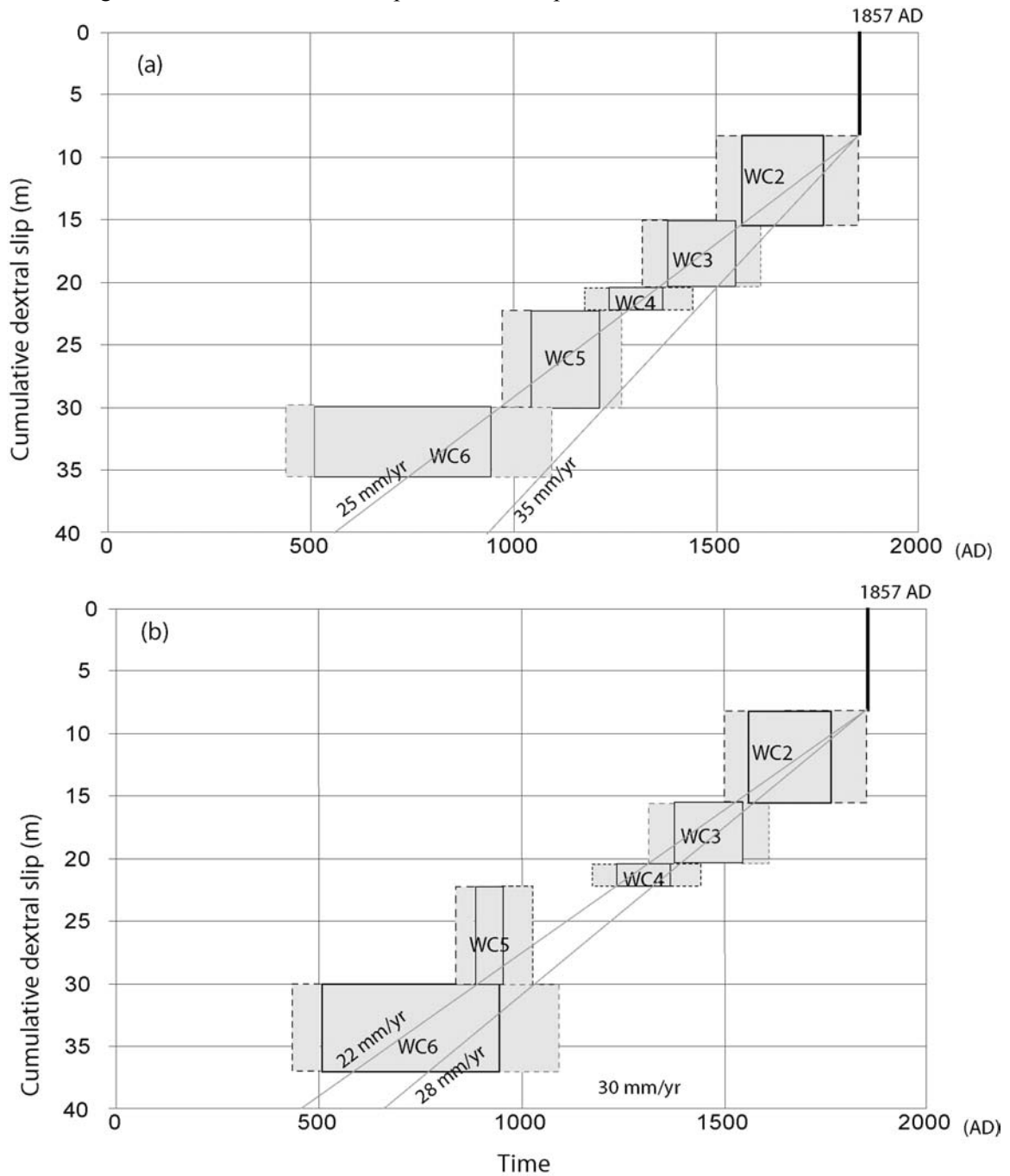


Figure 3.31. A revised slip history at the Wallace Creek site, incorporating the constraints on alluvial events from the Phelan Creeks site. This yields better constraints for the dates of paleoseismic events than

those derived solely from the Wallace Creek dates (Fig. 3.25). The event boxes in the upper and lower graphs are identical except for event WC5. Diagonal lines represent best estimations of average slip rates.

These two plots show much tighter constraints on the dates of the slip events than the plot derived from the Wallace Creek radiocarbon dates (Cf. Figure 3.25).

#### **3.7.2.4 Further constraints from the Bidart fan record**

The Bidart fan paleoseismic site is on an alluvial fan about 5 km southeast of the Wallace Creek site. Grant and Sieh (1994) documented a sequence of 5 ruptures of the San Andreas fault there. All five events occurred after about A.D. 1200. As at our site and the Phelan Creeks sites, the latest two events at the Bidart fan (their events A and B) occurred after a date in the range A.D. 1450 - 1510. Grant and Sieh (1994) concluded that a gully offset 15 to 18 m at the site

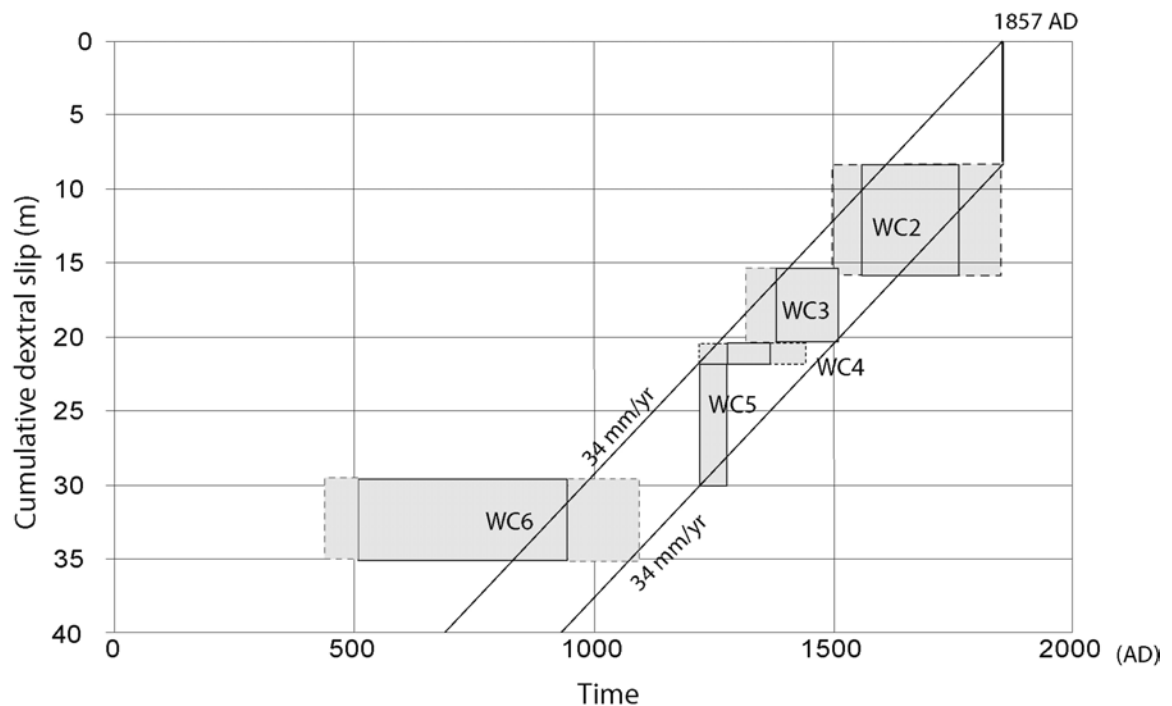


Figure 3.32. Additional constraints on event WC5 from the Bidart fan site (Grant and Sieh, 1994) further improve the precision of the slip history. Two diagonal lines represent the best estimation of average slip rate; the upper one indicates a slip-predictable idealization whereas the lower one indicates a time-predictable idealization.

represented the cumulative offset of these latest two events, and possibly a third event. The similar magnitude of this offset to the 2-event offsets at Wallace Creek and Phelan Creeks suggests that it is the cumulative offset of 2 events. Radiocarbon dates constrain their other three events (C, D and E) to have occurred within the period A.D. 1218 - 1510, with the oldest event (E) being tightly constrained to the period A.D. 1218 – 1276.

The age constraints from the Bidart site may also provide further limits on the dates of the latest five events at Wallace Creek. If the record at the Bidart Fan site is complete for the past five ruptures and if the record at the Wallace Creek site is similarly complete, then their fifth event back (E) would correlate with our event WC5. We would then be able to use the date constraints for event E to bound the date of WC5.

Figure 3.32 shows this modification to the plot of cumulative slip versus time.

## 3.8 Discussion

The data that we have recovered from the 3-dimensional excavation at Wallace Creek provide an unusually well-constrained sequence of ruptures at one location along the San Andreas fault. However, the constraints on the timing of these events from radiocarbon samples within the excavated volumes are poor. Even so, reasonable correlations with better-dated alluvial events and ruptures from the nearby Phelan Creeks and Bidart Fan sites allow us to construct a useful history of rupture that extends back about one millennium. This rupture sequence and tentative history are significant for their value in understanding the physics of sequential earthquake rupture. The rupture sequence, tentative history and their significance are the subjects of the discussion that follows.

### ***3.8.1 Slip behavior of the San Andreas fault at the site***

The most reliable aspect of our data is the sequence of the most recent six ruptures. These appear to have produced the latest 35 m of dextral offset. Although it is certainly possible that smaller events have gone unrecognized in the record, we have found no evidence for them. It is skeptical that additional excavations in alluvial deposits will enable recognition of such cryptic events along this reach of the fault, given the episodic nature and climatic control of alluvial cuts and fills and the coarseness of alluvial stratigraphy. If a young, lacustrine deposit could be found, however, it might have finer resolution than the alluvial sequence we have documented.

If our interpretation of the paleoseismic record for the last 1500 years or so is correct, the dextral slips associated with the latest six events are, from youngest to oldest, 8.0 m, 7.5 m, 5.0 m, 1.5 m, 8.0 m, and 5.5 m. The remarkable feature of this series is that half of the offsets are in the range from about 7 to 8 m. And it is curious that two of the three values that do not fall in this range, 1.5 m and 5.5 m, are sequential and add up to about 7 m.

An interpretation at the extreme end of the spectrum from episodic slip – i.e. continuous creep -- can be rejected easily. Even if climatic oscillations between relatively wet and dry conditions favor the cutting and filling of gullies during some periods, the sharp intersections of most of the gullies with the fault zone render large amounts of creep or numerous small offsets unlikely. This position is bolstered by the observation of undisturbed fences across the fault nearby, which show that no creep or small offsets have occurred since at least the beginning of the 20<sup>th</sup> century. Still, we are hard-pressed to argue against the possibility of some unrecognizable events with dextral slip of a meter or less. It is reasonable, yet conservative, to set the lower detection limit of offset events at the site to be about 1m, as is shown in the size of WC4.

The common occurrence of 7 - 8m offset values in the Wallace Creek record indicates that this offset series does not result from a uniform random process. Of the six offsets, 3 are

between 7 and 8m. While a detailed frequency-size distribution may not be meaningful for only 6 data points, at least we can say that the larger offsets ( $> 4\text{m}$ ) are five times more frequent than the

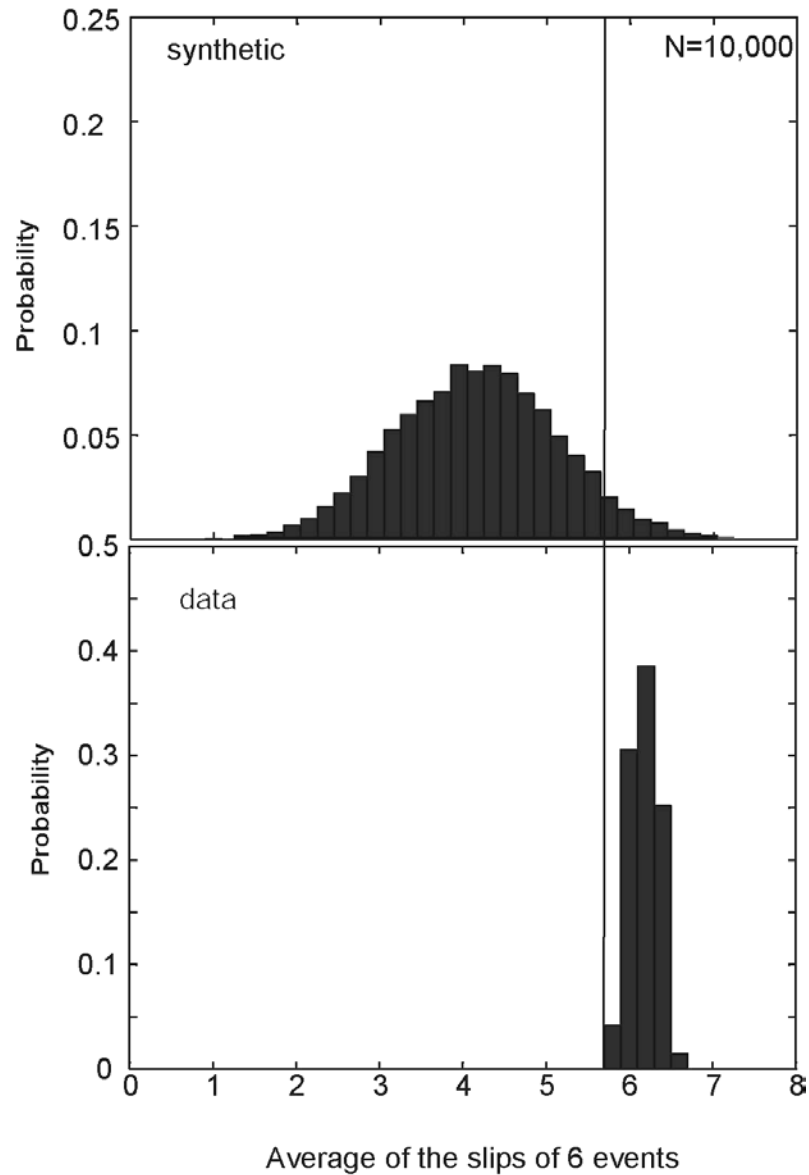


Figure 3.33. A test of the randomness in the offset series of events at the site. Both panels show the average values of samplings of six values from a synthetic data set (a) and the actual data set (b). The probability distribution function of synthetic averages is derived by averaging ten thousand groups of six sequential values drawn randomly from a population of values between 1 and 8.5 m. The probability

distribution function of actual values is created from averages ten thousand groups of six values drawn from within the error limits of each of the six measured offset values.

We conducted a simple statistical test for randomness of this offset series. We generated a synthetic series of 10,000 data points by assuming that each slip value is a random number from between 1 and 8.5 m. We then calculated the average value for each sequence of six data points. smaller one ( $< 4$  m). This asymmetry in the distribution does not prove, but certainly suggests that slips at this location are not randomly drawn from the range of 1-8m.

From this set of about 1500 average values, we plotted the probability distribution of the average slip (Figure 3.33). This synthetic distribution of average slip is a bell-shaped normal distribution with a mean of about 4.0m.

To test for randomness of the data, we can compare this synthetic distribution with the distribution of our data. First, we have to create a family of average offsets from our data. If our offset series is also a random series, then the probability distribution would also be similar to that of the synthetic distribution. To calculate the average slip of the 6 events at the site, we allow each offset value to be a random number within its uncertainty bounds, since each offset is associated with some uncertainties. For example, the slip of the 1857 earthquake (event WC1) can be any value within the range of 7.8 - 8.0 m. So, we generated one average value by picking a value at random from each of the six offsets, summing these six values and dividing by six. Doing this 10,000 times yielded the sharply spiked probability distribution shown in the lower panel of Figure 3.31b. Unlike the broad synthetic function, this has a narrow range of 5.7 to 6.7 m, with a mean of 6.2 m. Clearly, both the mean and standard deviation of the real data differs fundamentally from that of a random process. We may ask, what is the chance of getting a series of 6 consecutive values with a mean larger than 5.8 m (the vertical line in Figure 3.31)? The answer is 3.6%. In actuality, this number is a conservative estimation, because the mean of the distribution based on actual values is very likely to be larger than 5.8m, and the chance of getting a series with higher mean is smaller than 3.6%. Therefore, the hypothesis that the slip data of the latest six events at this location is a random process can be rejected with greater than 95% confidence.

### ***3.8.2 Implications for earthquake recurrence models***

Our observations of magnitude of slip during the last 6 earthquakes provide an opportunity to evaluate earthquake recurrence models. The high occurrence of events with slip of about 7.5 m suggests that the magnitude of slip at a point along the fault is not stochastic. But the slip is not as regular as predicted by characteristic models either. One 1-2 m event and two 5-6 m events are individual violations of characteristic behavior. Thus, data at the site do not support perfectly characteristic behavior, but do show a significant degree of regularity.

The slip sequence at the site is quite different from sequences generated by some numerical models. For example, one would expect that models that generate earthquakes of all sizes on a fault would also predict irregular slip behavior of specific locations along that fault. Models that allow a fault to produce earthquakes of all sizes, with say a power-law frequency-size distribution, then the slip at a point probably also has a power-law distribution. In such a case, slip associated with an  $M = 6$  earthquake would occur 10 times more often than that of an  $M = 7$  event. This conflicts with our observations.

A direct comparison between synthetic models of rupture history and our observations is not straightforward, however, because only a few attempts (e.g. Ward, 1997, 2000; Shaw, 1995, 1997; Shaw and Rice, 2000), explicitly address how slip is accumulated through time at individual locations along the fault.

Some numerical models, however, can predict near characteristic behavior when utilizing smoothing parameters or assumptions, such as a uniform distribution of fault strength, a large critical patch size for rupture preparation and nucleation, or simply a high degree of geometrical or material regularity (e.g., Rice and Ben-Zion, 1996; Ben-Zion, 1996; Ward, 1997). These models produce rupture sequences that more closely resemble our data. Our data may provide further constraints on the parameters of these models that control or modulate regularity of slip.

### **3.8.3 Slip history of the San Andreas fault at the site**

What can we say after we add our timing to the sequence of the events? Figure 3.25 shows that the timing derived just from dates from the site is poor. One cannot resolve the millennial slip rate of the fault or centennial fluctuations to any useful degree. A line fit through about the center of the event boxes has a slope of 25 mm/yr, but the average rate could range from 18 to 55 mm/yr. If we choose to rely on dating only from the site, the most significant contributions are these:

- 1) Offset during the 1857 earthquake is  $7.9 \pm 0.1$  m. This is within the  $8.7 \pm 1.4$  m value measured for channel 1-a from geomorphic evidence alone (Sieh, 1978, site #25). It is a bit higher than the 6.6 to 6.9 m value Grant and Sieh (1993) documented at their 3-d excavations about two kilometers to the south. But this difference in values is well within the range one commonly sees over short distances for modern large strike-slip ruptures (e.g. Rockwell et al., 2002; McGill and Rubin, 1999). The difference between our measured value and the  $11 \pm 2$  m value determined by Grant and Donnellan (1993) may well be due to the fact that their geodetic measurement spans an aperture of about a kilometer, whereas ours spans only 5 m. The 11-m value could well include 3 m or so of off-fault warp.
- 2) The penultimate event, with an offset similar to that of 1857 earthquake, occurred sometime after a date within the range of A.D. 1460 – 1650. This age constraint adds confidence to previous speculations that an event in the mid-fifteenth to mid-sixteenth century may have ruptured the same portion of the fault as in 1857 (e.g. Sieh and Jahns, 1984; Grant and Sieh, 1994; Arrowsmith, 1997; Fumal et al., 2002).

If we use the Phelan Creeks site ages, the history is much more precise (Figure 3.31). Figure 3.31a shows, for example, that the millennially averaged rate of slip on the fault is likely to be somewhere between about 25 and 35 mm/yr, which is equal to or as much as 10 mm/yr lower than the 3700-year average determined from the 130-m offset of Wallace Creek. Even with

the use of the Phelan Creeks ages, however, the dates of individual events are too poorly constrained to resolve fluctuations in rate or in recurrence interval. The average interval between the 6 events is somewhere between about 140 and 260 years.

Use of the Bidart Fan constraint on the age of event WC5 greatly improves the precision of the history (Figure 3.32). First, the average slip rate over the span of the past five events (between 1210 and 1857) has been 34 mm/yr, a rate not resolvably different than the 3700-year average of  $33.9 \pm 3$  mm/yr (Sieh and Jahns, 1984). Second, the average interval between events WC5 and WC1 (1857) is somewhere between about 150 and 160 years. If we also adopt the age constraints on the penultimate event (WC2) that Grant and Sieh (1993) have for the penultimate event (B) at the Bidart Fan site, then we can actually resolve structure within the sequence. They argue that that event occurred shortly after a date within the range A.D. 1450 to 1510. If this is the case, then WC5, 4, and 3 occurred in relatively rapid succession between A.D. 1210 and about 1510.

### ***3.8.4 Correlation of earthquakes along the central and southern San Andreas fault***

During the last couple of decades, paleoseismic investigations at various sites along the San Andreas fault have progressively enriched the paleo-earthquake history of the southern half of the San Andreas fault (Sieh, 1984; Sieh, 1986; Sieh et al., 1989; Fumal et al., 1993, 2002a and b; Grant and Sieh, 1994; Seitz, 1997; Yule and Sieh, 2001; Stone et al., 2002; McGill et al., 2002; Young et al., 2002; Lindvall et al., 2002). Following in this tradition, we now attempt to correlate the past earthquakes at the Wallace Creek site with those documented at other sites along the fault (Figure 3.34). Though still highly speculative, this synthesis of available data, forms a basis for evaluating and updating our present understanding of earthquake recurrence and for guiding future studies.

As with previous attempts to construct an earthquake history for this 600-km-long stretch

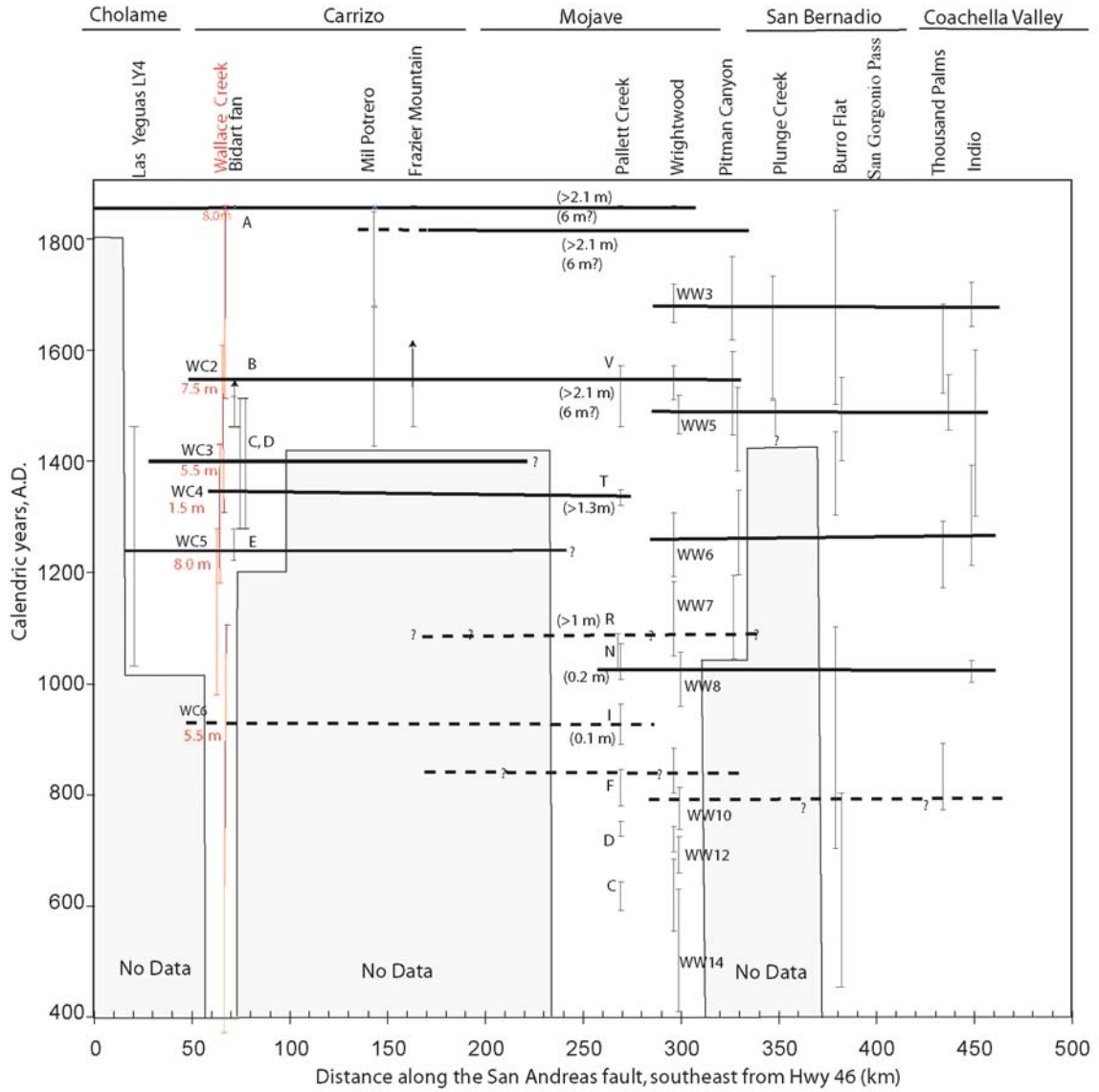


Figure 3.34 Speculative correlation of earthquake ruptures between paleoseismic sites along the southern half of the San Andreas fault. Vertical bars indicate the 2-sigma date ranges for prehistoric events. Horizontal lines are proposed correlations of events. In these correlations, the rupture pattern on the Carrizo and Mojave sections of the San Andreas fault is not simple repetition. Data sources: LY4 site (Stone et al., 2001 and Young et al., 2002), Bidart fan site ( Grant and Sieh, 1994), Mil Potrero (Davis, 1983), Frazier Mountain ( Lindvall et al., 2002), Pallett Creek site (Sieh, 1989, and Biasi et al., 2002), Wrightwood site (Fumal et al., 1993 and 2002a), Pitman Canyon site (Seitz et al., 1997), Plunge Creek site (McGill et al., 2002), Burro Flat site (Yule et al., 2001), Indio site (Sieh, 1986); and the Thousand Palms site (Fumal et al., 2002b).

of the fault, large uncertainties in radiocarbon dates at most sites precludes certainty in our correlations. We adopt the bias of previous speculators toward hypothesizing larger events; that is, if the radiocarbon errors allow a correlation between sites, we make that correlation. This bias is somewhat supported by the known potential for great earthquakes and long ruptures along the San Andreas fault, as demonstrated by the 1857 and 1906 earthquakes.

In addition to the date constraints for correlating the Wallace Creek events, we have the magnitude of slip for the past six events. This may provide additional information for hypothesizing correlations. For instance, an event with the magnitude of slip similar to that of the 1857 earthquake is more likely to have similarly long ruptures and to be correlative to events at sites to the southeast that also recorded the 1857 earthquake. Another constraint that we will use is the fact that just 60 km to the northwest is a 170-km-long reach of the fault that has been dominated by creep during at least the past century. We assume that this behavior has occurred throughout the past millennium and that this creeping section serves as a boundary that separates ruptures of the northwestern and southeastern halves of the 1100-km long fault.

#### **3.8.4.1 The 1857, 1812, and late 17th-century earthquakes**

The extent of the historic 1857 earthquake rupture (Figure 3.32) has been discussed by Sieh (1978), based on observation of the youngest geomorphic offsets, and by Agnew and Sieh (1978), based upon the historical record of shaking. The southern end of the rupture is probably located between the Wrightwood (Meisling and Sieh, 1980; Jacoby et al., 1988; and Fumal et al., 1993, 2002a) and Lost Lake, near Cajon Pass (Weldon and Sieh, 1985; Seitz et al., 1997).

The historic 1812 rupture was shown to involve at least the forested 12 km of the fault near Wrightwood, by virtue of its effects on trees there (Jacoby et al., 1988). Stratigraphic records of rupture that are consistent with a date of 1812 occur at Pallett Creek, Wrightwood and Pitman Canyon (Sieh, et al., 1989; Fumal et al., 1993, 2002a; Seitz et al., 1997). Shaking from the event has been interpreted by Toppazada (2002) to indicate that rupture during the event of December 8<sup>th</sup> extended as far northwest as Mil Potrero. Thus, it appears that the 1812 event rent the entire Mojave section of the San Andreas fault and overlapped with the southern 100 km or so of the 1857 rupture. The northernmost extent of the 1812 event is still in debate, but none of the

sites in the northern Carrizo plain report an event that could correlate with it (this study, Prentice and Sieh, 1989; Grant and Sieh, 1994). Furthermore, no evidence occurs at the Frazier Mountain site (Lindvall et al., 2002). The southeastern end of the 1812 rupture appears to be northwest of the Plunge Creek site (McGill et al., 2002), in the San Bernardino Valley. Thus, the extent of the 1812 rupture is coincident with the southern 170 km the 1857 rupture, but extended a few kilometers farther to the southeast.

An earlier event, late in the 17<sup>th</sup> century, involved rupture of the San Andreas fault from the Wrightwood site (Fumal et al., 1993, 2002a) through the Pitman Canyon, Plunge Creek and Burro Flat site, on the western of the San Gorgonio Pass step-over. This event broke through the step-over and appears as a 2-m thrust event with the San Gorgonio Pass section of the fault (Yule et al., 2001) and extended at least as far southeast as the Indio site (Sieh, 1986).

Together, these three events form a northwestward propagating sequence of large events.

#### **3.8.4.2 Event WC2**

The penultimate event WC2 at the Wallace Creek site can be matched with events along most of the southern half of the fault. Quite plausibly, WC2 is the same as event B at the Bidart fan site (Grant and Sieh, 1994), the penultimate event at the Frazier Mountain site (Lindvall et al., 2002), event V at the Pallett Creek (Sieh 1984; Sieh et al., 1989; Biasi et al., 2002), to event WW4 at the Wrightwood (Fumal et al., 2002), and event Ev-3 at the Pitman Canyon (Seitz et al., 1997). At Pallett Creek, this event is associated with about 6 m of dextral slip, indistinguishable from the amount of slip in 1812 and 1857 there. The date constraints on events at the LY4 site suggest that this event did not rupture as far northwest as the 1857 event (Young et al., 2002).

If these correlations are valid, they indicate a rupture with very similar length and offset magnitudes to the rupture of 1857. Its southeastern end would appear to extend slightly farther than that of 1857.

This correlation, at least down to the Pallett Creek has already been suggested (Sieh and Jahns, 1984; Grant and Sieh, 1994; Fumal et al., 2002). Our study, however, provides additional information to favor this hypothesis. At the Wallace Creek site, the magnitude of slip associated with this event is nearly identical to that of the 1857 earthquake.

If this correlation is valid, then the age of the penultimate event in the Carrizo segment of the San Andreas fault could be narrowed down to the middle of the 16<sup>th</sup> century, as suggested by the well constrained date at sites to the southeast (Biasi et al., 2002; Fumal et al., 2002). Grant and Sieh (1994) showed that this event occurred after a date within the range of A.D. 1450-1510. They went on to argue that the range included the date of the event. This inference has been disputed by Fumal et al. (2002a). Biasi et al. (2002) also dispute the Sieh et al. (1989)'s assignment of a date of A.D.  $1480 \pm 15$  to the event at Pallett Creek.

The presence of another event about A.D. 1500 at the Pitman Canyon and Wrightwood sites first led Fumal et al. (1993) and Seitz et al. (1997) to question Sieh et al.'s (1989) assignment of a date of  $1480 \pm$  to the mid-1500s event. This earlier rupture of the fault, southeast of Pallett Creek appears to be event WW5 at Wrightwood, event Ev-2 at Pitman Canyon (Seitz et al., 1997), event W at Plunge Creek (McGill et al., 2002), and an event at Burro Flat (Yule and Sieh, 2001), at Thousand Palms (Fumal, 2002), and at Indio (Sieh, 1986).

Until recently, uncertainty in the timing of event WW4 and WW5 at the Wrightwood site, the penultimate event in the Carrizo Plain had been speculated to extend southeastward through San Gorgonio pass, and through the Indo site (Grant and Sieh, 1994). With a rupture length of over 400 km, this hypothetical event would have had a magnitude of about  $M_w 8$  (Wells and Coppersmith, 1994). Recent studies at the Wrightwood site (Fumal et al., 2002), as well as a later study at the Pitman Canyon (Seitz et al., 1997), however, suggest these ruptures represent it is a separate event that occurred shortly before our penultimate WC2 event. These two events also appear to involve a northward progression in large events.

#### **3.8.4.3 Event WC3 and WC4**

By virtue of their stratigraphic positions, Event WC3 at Wallace Creek appears to be correlative to Event C at the Bidart site and WC4 to event D (Grant and Sieh, 1994).

Correlations for events WC3 and WC4 to are more ambiguous. Either of WC3 and WC4 can be correlative to Event T at the Pallett Creek, if we use 2 sigma age ranges constrained by Phelan Creek dates. If we use 1 sigma age range, WC4 would appear more likely than WC3 to correlate to Pallett Creek T. WC4 has a 1-sigma range of A.D. 1240 – 1370, which brackets the

A.D. 1343 – 1370 age range of Pallett Creek T (Biasi et al., 2002). However, if we take in consideration the amount of offset in correlating events, WC3 seems more plausible to correlate with T, because WC3 has larger offset.

Certainly, there is no double rupture in the 13<sup>th</sup> or 14<sup>th</sup> centuries at Pallett Creek, so we cannot run both WC3 and 4 through Pallett Creek (Figure 3.34).

We speculate that event WC4 correlates with Event T at the Pallett Creek (Sieh, 1984; Sieh et al., 1989). This leaves WC3 to be a local event. This choice of correlations is the same as in Grant and Sieh (1994).

#### **3.8.4.4 Event WC5**

The correlation of older events at the Wallace Creek site with other sites is more speculative, due to the larger uncertainties in ages.

The date of event WC5 at the Wallace Creek site is poorly constrained, probably at a date within  $2\sigma$  range AD 870 – 1020 or AD 970 - 1210 (Table 3.3). At both the Pallett Creek site and the Wrightwood site, there are multiple events falling into this time window. WC5 may be the same earthquake as event N or R at the Pallett Creek, which suggests an occurrence date around mid-11<sup>th</sup> century (Biasi et al., 2002).

But if we consider the event WC5 to be 5<sup>th</sup> Bidart event E, then the tight constraint of this event, A.D. 1218-1270, do not allow us to correlate WC5/E to any event at Pallett Creek.

It is interesting that there is a Wrightwood event, WW6, roughly correlative with our WC5/E. This event plausibly rent the fault for at least 150 km, between Wrightwood and Indio. But the tight constraint on the date of event T at Pallett Creek bars this large rupture from having continued farther to the northwest. Thus event WC5/E and the plausibly contemporaneous event far to the southeast cannot be contiguous. Probably the gap was subsequently filled by the Pallett Creek event T.

Within the date constraints, only one of events WC3, 4 and 5 can be extend to the LY4 site, about 50 km to the northwest (Young et al., 2002). We extend WC5 through the LY4 site in Figure 3.34, rather than extending WC3 or WC4 through it, because WC5 has larger offset.

### 3.9 Conclusions

Data on the earthquake history of the San Andreas fault form the basis of numerous models of fault behavior and calculations of seismic hazard. Our recent 3-D paleoseismic excavations at a site along the Carrizo segment of the San Andreas fault attempt to address a fundamental question: how similar is the fault slip per event through time? At this site, several small channels, roughly perpendicular to the fault, are offset dextrally from the source channel and have been sequentially abandoned. The geometrically simple fault trace and the geomorphic configuration of tiny gullies have enabled us to determine the slip associated with the past several ruptures with small uncertainties. The dextral slips associated with the latest 6 events are, from youngest to oldest,  $7.9 \pm 0.1$  m,  $7.6 \pm 0.4$  m,  $5.2 \pm 0.55$  m,  $1.4 \pm 0.5$  m,  $8.0 \pm 0.5$  m, and  $5.4 \pm 0.6$  m. The high occurrence of events with slip of about 7.5 m suggests that the magnitude of slip at a point along the fault does not result from a random process. But the slip is not as regular as predicted by characteristic models either. Thus, data at the site do not support perfectly characteristic behavior, but do show a significant degree of regularity. Unfortunately, age constraints for these events are not very tight at the site, but additional age constraints from previous studies at sites within 6 km seems to suggest that the millennial slip rate is about 34 mm/yr, indistinguishable from the late Holocene rate (Sieh and Jahns, 1984).

### 3.10 References

- Agnew, D.C., and K.E. Sieh, A documentary study of the felt effects of the great California earthquake of 1857, *Bull. Seism. Soc. Am.*, 68, 1717-1729, 1978.
- Arrowsmith, J.R., K. McNally, and J. Davis, Potential for earthquake rupture and M 7 earthquakes along the Parkfield, Cholame, and Carrizo segments of the San Andreas Fault, *Seism. Res. Lett.*, 68, 902-916, 1997.
- Ben-Zion, Y., Stress, slip, and earthquakes in models of complex single-fault systems incorporating brittle and creep deformations, *J. Geophys. Res.*, 101, 5677-5706, 1996.
- Benson, L.V., P.A. Meyers, and R.J. Spencer, Change in the size of Walker Lake during the past 5000 years, *Palaeogeography, Palaeoclimatology, Palaeoecology*, 81, 189-214, 1991.
- Biasi, G.P., R.J. Weldon, II, T.E. Fumal, and G.G. Seitz, Paleoseismic event dating and the conditional probability of large earthquakes on the southern San Andreas fault, California, *Bull. Seism. Soc. Am.*, 92, 2761-2781, 2002.
- Blong, R.J., and R. Gillespie, Fluvially transported charcoal gives erroneous 14C ages for recent deposits, *Nature*, 271, 739-741, 1978.
- Brown, R.D., Jr., and R.E. Wallace, Current and historic fault movement along the San Andreas fault between Paicines and Camp Dix, California, in *Proceedings of conference on geologic problems of San Andreas fault system*, edited by W.R. Dickinson, and A. Grantz, Stanford University Publications in Geological Sciences, Stanford, California, 1968.
- Fumal, T.E., S.K. Pezzopane, R.J. Weldon, II, and D.P. Schwartz, A 100-year average recurrence-interval for the San Andreas Fault at Wrightwood, California, *Science*, 259, 199-203, 1993.
- Fumal, T.E., R.J. Weldon, II, G.P. Biasi, T. Dawson, G.G. Seitz, W.T. Frost, and D.P. Schwartz, Evidence for large earthquakes on the San Andreas fault at the Wrightwood, California paleoseismic site: A.D. 500 to present, *Bull. Seism. Soc. Am.*, 92, 2726-2760, 2002.
- Fumal, T.E., M.J. Rymer, and G.G. Seitz, Timing of large earthquakes since A.D. 800 on the Mission Creek strand of the San Andreas fault zone at Thousand Palms Oasis, near Palm

- Springs, California, *Bull. Seism. Soc. Am.*, 92, 2841-2860, 2002.
- Grant, L.B., and K. Sieh, Stratigraphic evidence for seven meters of dextral slip on the San Andreas Fault during the 1857 earthquake in the Carrizo Plain, *Bull. Seism. Soc. Am.*, 83, 619-635, 1993.
- Grant, L.B., and K. Sieh, Paleoseismic evidence of clustered earthquakes on the San Andreas Fault in the Carrizo Plain, California, *J. Geophys. Res.*, 99, 6819-6841, 1994.
- Grant, L.B.a.A.D., 1855 and 1991 surveys of the San Andreas Fault; implications for fault mechanics, *Bull. Seism. Soc. Am.*, 84, 241-246, 1994.
- Jacoby, G.C., P.R. Sheppard, and K.E. Sieh, Irregular recurrence of large earthquakes along the San Andreas Fault; evidence from trees, *Science*, 241, 196-199, 1988.
- Lindvall, S., T.K. Rockwell, T. Dawson, J.G. Helms, and K.W. Bowman, Evidence for two surface ruptures in the past 500 years on the San Andreas fault at Frazier Mountain, California, *Bull. Seism. Soc. Am.*, 92, 2689-2703, 2002.
- McGill, S., T. Rockwell, Ages of late Holocene earthquakes on the central Garlock Fault near El Paso Peaks, California, *J. Geophys. Res.*, 103, 7265-7279, 1998.
- McGill, S.F., and C.M. Rubin, Surficial slip distribution on the central Emerson Fault during the June 28, 1992, Landers earthquake, California, *J. Geophys. Res.*, 104, 4811-4833, 1999.
- McGill, S., and others, Paleoseismology of the San Andreas fault at Plunge Creek, near San Bernadino, southern California, *Bull. Seism. Soc. Am.*, 92, 2803-2840, 2002.
- Meisling, K.E., and K.E. Sieh, Disturbance of trees by the 1857 Fort Tejon Earthquake, California, *J. Geophys. Res.*, 85, 3225-3238, 1980.
- Nelson, A.R., Discordant 14C ages from buried tidal-marsh soils in the Cascadian subduction zone, southern Oregon coast, *Quaternary Research*, 38, 74-90, 1992.
- Prentice, C.S., and K. Sieh, A paleoseismic site along the Carrizo segment of the San Andreas fault, central California, *EOS, Trans. Amer. Geophys. Union*, 70, 1349, 1989.
- Ramsey, C.B., Radiocarbon calibration and analysis of stratigraphy: the OxCal program, *Radiocarbon*, 37, 425-430, 1995.
- Ramsey, C.B., OxCal Program Ver. 3.5, Radiocarbon Accelerator4 Unit, University of Oxford, U.K., [http://units.ox.ac.uk/departments/rlaha/orau/06\\_01.htm](http://units.ox.ac.uk/departments/rlaha/orau/06_01.htm), 2000.

- Rice, J.R., and Y. BenZion, Slip complexity in earthquake fault models, *Proceedings of the National Academy of Sciences of the United States of America*, 93, 3811-3818, 1996.
- Rockwell, T.K., S. Lindvall, T.E. Dawson, R.M. Langridge, W. Lettis, and Y. Klinger, Lateral offsets on surveyed cultural features resulting from the 1999 Izmit and Duzce earthquakes, Turkey, *Bull. Seism. Soc. Am.*, 92, 79-94, 2002.
- Rubin, C.M., and K. Sieh, Long dormancy, low slip rate, and similar slip-per-event for the Emerson Fault, eastern California shear zone, *J. Geophys. Res.*, 102, 319-15, 1997.
- Schwartz, D.P., and K.J. Coppersmith, Fault behavior and characteristic earthquakes; examples from the Wasatch and San Andreas fault zones, *J. Geophys. Res.*, 89, 5681-5698, 1984.
- Seitz, G.G., R. Weldon, II, and G.P. Biasi, The Pitman Canyon paleoseismic record; a re-evaluation of southern San Andreas Fault segmentation, *Journal of Geodynamics*, 24, 1-4, 1997.
- Shaw, B.E., Frictional weakening and slip complexity in earthquake faults, *J. Geophys. Res.*, 100, 239-18, 1995.
- Shaw, B.E., Model quakes in the two-dimensional wave equation, *J. Geophys. Res.*, 102, 367-27, 1997.
- Shaw, B.E., and J.R. Rice, Existence of continuum complexity in the elastodynamics of repeated fault ruptures, *J. Geophys. Res.*, 105, 791-23, 2000.
- Sieh, K.E., Slip along the San Andreas fault associated with the great 1857 earthquake, *Bull. Seism. Soc. Am.*, 68, 1421-1448, 1978.
- Sieh, K.E., and R.H. Jahns, Holocene activity of the San Andreas Fault at Wallace Creek, California, *Geol. Soc. Am. Bull.*, 95, 883-896, 1984.
- Sieh, K.E., Lateral offsets and revised dates of large prehistoric earthquakes at Pallett Creek, Southern California, *J. Geophys. Res.*, 89, 7641-7670, 1984.
- Sieh, K., Slip rate across the San Andreas Fault and prehistoric earthquakes at Indio, California, *Eos, Transactions, American Geophysical Union*, 67 (44), 1200, 1986.
- Sieh, K.E., and R.E. Wallace, The San Andreas Fault at Wallace Creek, San Luis Obispo County, California, *Geological Society of America Centennial field guide-Cordilleran Section*, 1987.

- Sieh, K., M. Stuiver, and D. Brillinger, A more precise chronology of earthquakes produced by the San Andreas Fault in Southern California, *J. Geophys. Res.*, *94*, 603-623, 1989.
- Sieh, K., The repetition of large-earthquake ruptures, *Proceedings of the National Academy of Sciences*, *93*, 3764-3771, 1996.
- Sims, J.D., and J.C. Hamilton, Tectonic control of Pleistocene drainage patterns by the San Andreas Fault, Central California, *Abstracts with Programs Geological Society of America*, *21*, 1989.
- Sims, J.D., Stream channel offset and abandonment and a 200-year average recurrence interval of earthquake on the San Andreas fault at Phelan Creeks, Carrizo Plain, California., *Proceedings of the workshop on paleoseismology, U S Geological Survey Open-file Report 94-568, C. S. Prentice, D. P. Schwartz and R. S. Yeats (editors)*, 170-172, 1994.
- Sims, J.D., T. Ito, J. Hamilton, A. J. Foss, C. D. Garvin and D. B. Meier, A 200-year average recurrence interval of earthquakes on the San Andreas fault at Phelan Creeks, Carrizo Plain, California: reconstruction from paired offset paleochannels, *unpublished manuscript*, 1994.
- Stone, E.M., L.B. Grant, and J.R. Arrowsmith, Recent rupture history of the San Andreas Fault southeast of Cholame in the northern Carrizo Plain, California, *Bull. Seism. Soc. Am.*, *92*, 983-997, 2002.
- Stone, E.M., L.B. Grant, and J.R. Arrowsmith, Recent rupture history of the San Andreas fault southeast of Cholame in the northern Carrizo Plain, California, *Bull. Seism. Soc. Am.*, *92*, 983-997, 2002.
- Stuiver, M.P., Henry A, Discussion; reporting of C-14 data, *Radiocarbon*, *19*, 355-363, 1977.
- Stuiver, M., P.J. Reimer, E. Bard, J.W. Beck, G.S. Burr, K.A. Hughen, B. Kromer, G. McCormac, J. van der Plicht, and M. Spurk, INTCAL98 radiocarbon age calibration, 24,000-0 cal BP, *Radiocarbon*, *40*, 1041-1083, 1998.
- Topozada, T.R., D.M. Branum, M.S. Reichle, and C.L. Hallstorm, San Andreas fault zone, California:  $M \geq 5.5$  earthquake history, *Bull. Seism. Soc. Am.*, *92*, 2555-2601, 2002.
- Vaughan, P.R., K.M. Thorup, and T.K. Rockwell, Paleoseismology of the Elsinore Fault at Agua Tibia Mountain, southern California, *Bull. Seism. Soc. Am.*, *89*, 1447-1457, 1999.

## **Chapter 4**

# **A Structural Interpretation of the Aftershock "Cloud" of the 1992 $M_w$ 7.3 Landers Earthquake**

By Jing Liu, Kerry Sieh and Egill Hauksson

Seismological Laboratory and  
Division of Geological and Planetary Sciences 100-23  
California Institute of Technology  
Pasadena, CA 91125

*In Press*

*Bulletin of the Seismological Society of America*

## **Abstract**

We analyze the spatial relationship of relocated aftershocks to the principal rupture planes of the  $M_w$  7.3 1992 Landers mainshock from a structural point of view. We find that the aftershocks constitute primarily a several-km-wide damage zone centered on the mainshock rupture planes. Intensity of damage decreases away from the principal faults. Less than half of aftershocks occurred within 1km of the mainshock planes, and perhaps only 5% of the aftershocks are candidates for re-rupture of the mainshock faults. Moreover, it seems that aftershocks along the Landers rupture have b values that correlate well with the complexity of the mainshock rupture. Low b values occur along segments that are simple, whereas higher b values correlate with sections that are more complex. Thus, structural complexity appears to correlate with a greater relative abundance of small earthquakes. These observations imply that aftershock populations reflect fault populations in the medium surrounding the principal faults rather than the behavior of the mainshock planes themselves.

## 4.1 Introduction

Aftershock sequences of moderate to large crustal earthquakes provide information about rupture processes of fault zones. Their spatial and temporal distributions have been exploited to understand better their relationship to mainshocks. Previous studies show that aftershocks generally form a cloud around the principal fault ruptures (e.g. Mendoza and Hartzell, 1988). However, location errors often result in uncertainties as to whether the aftershocks occur on the fault that slipped to produce the mainshock or within the volumes on either side of the rupture surface.

Aftershocks are often considered, either implicitly or explicitly, to have occurred on the mainshock rupture plane. For instance, aftershock hypocenters are widely used to identify the length, depth, dip, and geometric complexities of the mainshock rupture (e.g. Kanamori and Anderson, 1975; Fehler and Johnson, 1989; Dietz and Ellsworth, 1990; Nakamura and Ando, 1996; Shaw and Shearer, 1999; Rubin and Gillard, 2000). For these purposes, aftershock hypocenters are assumed to occur on (or at least very near) the mainshock rupture planes. Recent improvements in location accuracy generally support this assumption, in that they commonly show a reduction in the dimension of the aftershock “cloud” perpendicular to the principal fault planes (Richards-Dinger and Shearer, 2000; Waldhauser and Ellsworth, 2000).

However, there is reason to suspect that most aftershock hypocenters are not, in fact, located on the mainshock rupture plane. Instead, aftershocks form a zone or “cloud” surrounding the mainshock rupture. For example, evidence has accumulated in support of the notion that stress changes and viscous flow in the lower crust induced by the mainshock rupture trigger off-plane aftershocks, even at great distances from the mainshock rupture plane (e.g. Das and Scholz, 1981; Stein and Lisowski, 1983, Reasenber and Simpson, 1992; Stein et al., 1994; King et al., 1994; Hill et al., 1995; Gomberg and Davis, 1996; Hardebeck et al., 1998; Deng et al., 1998, 1999).

One question that has seldom been asked is this: What do aftershocks tell us about the geologic structure of fault zones that produce large earthquakes? Their almost universal association with large crustal earthquakes suggests that they must be caused by the stress

perturbations induced by the mainshock rupture. But are they re-ruptures of the mainshock plane, or are they the result of subsidiary faulting in the fault blocks that bound the primary fault? If the latter is true, then aftershocks constitute a structural damage zone around the mainshock ruptures, perhaps reflecting the zone of lesser fracturing around the principal rupture that one commonly sees in a geologic outcrop. The answer to this question has an important bearing on the physics of earthquake faulting. For example, it could help resolve whether irregularities in slip distribution, such as those suggested by seismologic and geodetic inversions (Kanamori et al., 1992; Wald and Heaton, 1994; Hudnut et al., 1994), are smoothed out by re-rupture during aftershocks.

In this paper, we present a detailed analysis of the 1992 Landers earthquake sequence to clarify the relationship of aftershock distribution to mainshock rupture from a structural point of view. The 1992 Landers aftershocks comprise an exceptionally well-recorded sequence. They afford an excellent opportunity to answer the questions listed above because (1) a detailed map of surface rupture places unambiguous constraints on both the location of the rupture plane and a variety of geometric complexities; (2) hundreds of slip measurements constrain the sense and magnitude of fault slip; and (3) there are tens of thousands of aftershocks, with location errors of less than 1 km. Unlike previous studies of Landers aftershock sequence (e.g. Wiemer and Katsumata, 1999), we demonstrate a link between aftershocks and the geologic structure of the fault zones.

## **4.2 Data**

### ***4.2.1 Surface rupture***

The surface rupture of the Landers mainshock that we use, Figure 1, is a compilation of the detailed mapping of several groups. To produce this database, the surface ruptures were mapped onto 1:6000-scale post-rupture aerial photos in the field during the weeks immediately following the Landers earthquake. The results of this mapping were then compiled onto 1:24,000 USGS topographic maps, which had been enlarged to the same scale. Surface ruptures were mapped in greatest detail along the northernmost 35 km of the rupture. This section of the rupture includes the Camp Rock fault, the Emerson fault (McGill and Rubin, 1999), the step-over between the

Emerson and Homestead Valley faults (Zachariassen and Sieh, 1996), and a 3-km long slip gap at

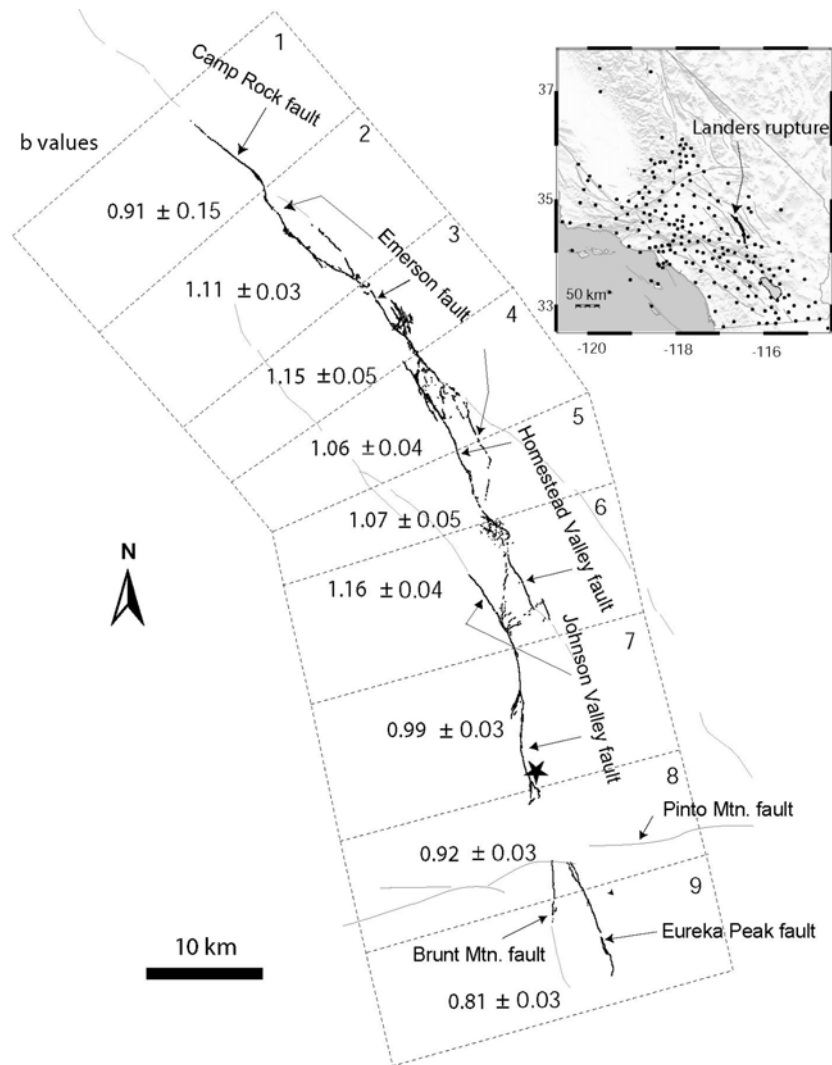


Figure 4.1. Map of the surficial ruptures of the 1992 Landers earthquake. The rupture is divided into 9 sections for an examination of aftershock locations in cross-section views. Aftershock b-values in these sections range from about 0.8 to 1.2. Sections in which the rupture is simple have lower b values, and sections of complex rupture have higher b values. The inset figure shows the distribution of seismicographic stations during the period of the Landers aftershock sequence used in this paper.

the northern end of the step-over between the Homestead Valley and Johnson Valley faults

(Spotila and Sieh, 1995) (segments 1, 2, 3, 4, and 6 in Figure 4. 1). The southern one third of the rupture, although mapped in detail by USGS and CDMG personnel (California Department of Conservation, Division of Mines and Geology, 2000), is not shown in as much detail, but the location of the main surface rupture zones are in the database.

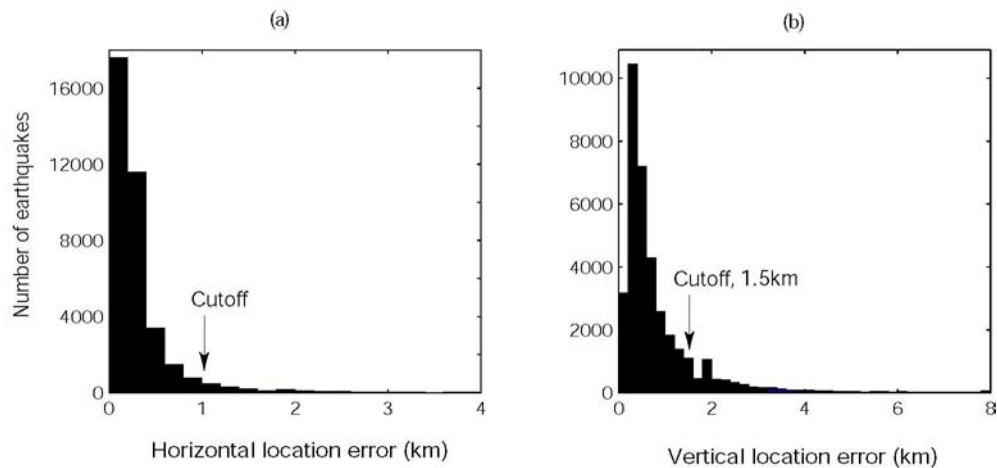


Figure 4.2. Histograms of horizontal and vertical location errors of relocated 1992 Landers aftershocks from June 28, 1992 to May 22, 1998. Relocations by Hauksson (2000). We excluded aftershocks with location errors greater than 1 km in the horizontal and 1.5 km in the vertical, to avoid the use of ill-located aftershocks in our analysis.

### 4.2.2 Aftershocks

We use the relocated aftershock hypocenters of Hauksson (2000) and Richards-Dinger and Shearer (2000). Hauksson (2000) used 3-D ray tracing techniques as well as a 3-D crustal velocity model of southern California that was an improvement over the one used to create the catalog locations. For his relocations, explosions set off for earlier trapped-mode studies provided the calibration for absolute locations. These new locations have average 1-sigma errors of 0.35 km in the horizontal and 0.88 km in the vertical dimension (Figure 4. 2a and b). We used only the 29,399 aftershocks that have horizontal and vertical location errors no greater than 1 km and 1.5

km, respectively, and that occurred in the period from June 28, 1992 to May 22, 1998. We also repeated our analysis using Richards-Dinger and Shearer (2000)'s relocations. Their relocation was done by an L1-norm, grid-search approach on a smooth 1-D velocity model, plus a refining source-specific station term correction. Their relocations have median horizontal and vertical location errors of 0.31 km and 0.75 km, respectively.

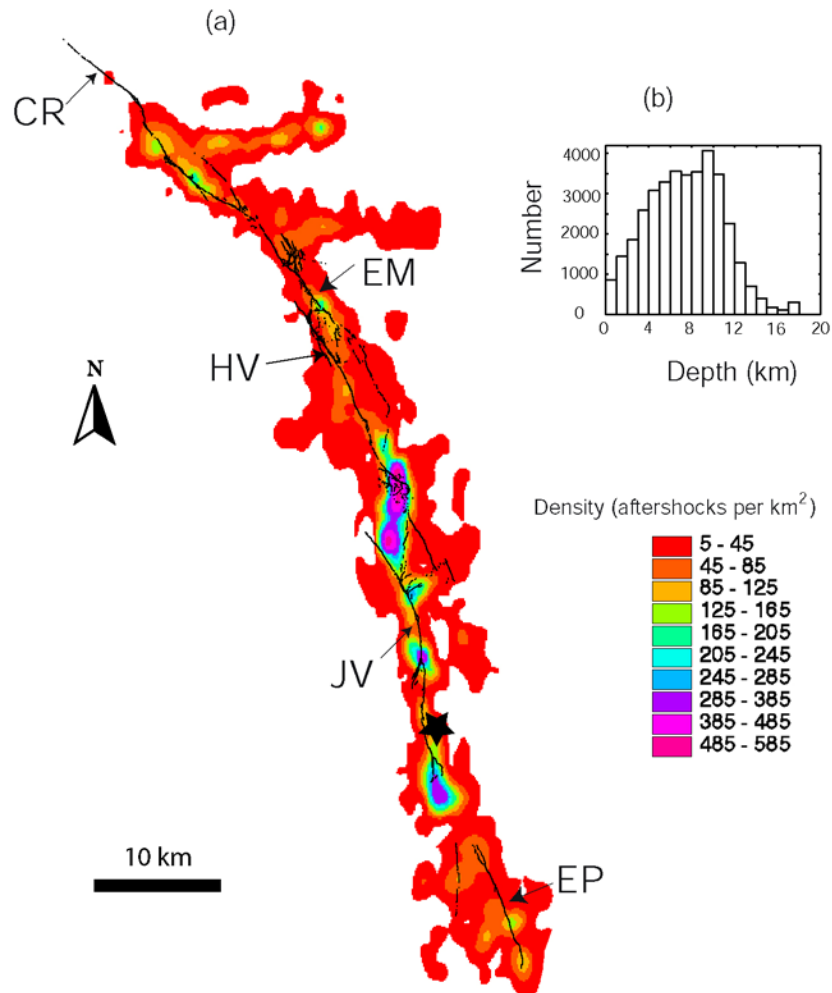


Figure 4.3. (a) Map view of the surficial ruptures of the 1992 Landers earthquake and aftershock density distribution. The contour representing a density of 5 to 45 events per km<sup>2</sup> commonly extends 3 to 8 km from the principal ruptures, distances far greater than the uncertainty in aftershock locations. A star marks the location of the mainshock epicenter. Abbreviations are CR, Camp Rock fault; EM, Emerson fault; HV, Homestead Valley fault; JV, Johnson Valley fault; EP, Eureka Peak fault. (b) Histogram of aftershocks as a function of depth.

## 4.3 Results

### ***4.3.1 The aftershocks occur in a vertically-dipping cloud***

Figure 4.3 shows that Landers aftershocks extend far into the regions surrounding the coseismic rupture planes. Note that the contour representing a density of 5 to 45 events per km<sup>2</sup> commonly extends 3 to 8 km from the mapped surface ruptures, distances far greater than the uncertainty in aftershock locations. Also, near the mainshock rupture, aftershocks cluster locally at fault termini and step-overs. For instance, the Johnson Valley-Homestead Valley step-over has the highest aftershock density of the entire sequence -- up to 585 events/km<sup>2</sup>. Another unusually high concentration occurs at the southern end of the Johnson Valley fault. Another cluster, in the middle of the Johnson Valley fault, is associated with a minor fault splay.

The scatter we see is not the result of viewing a dipping band of aftershocks in plan view. Figure 4.4 shows that the aftershock clouds dip vertically (or nearly so). Furthermore, they do not reflect dipping mainshock fault ruptures, because the clouds do not spread out just to one side of the principal ruptures. Rather, they occur on both sides of the surficial ruptures (Figure 4.3).

To facilitate the examination of the distributions of the aftershocks, we divide the Landers rupture into 9 sections from north to south, and inspect the distribution of  $M \geq 2$  aftershock hypocenters in 9 cross-sectional views perpendicular to the Landers fault zone (Figure 4.1 and 4.4). Along the Camp Rock fault (section 1) aftershocks are too few to delineate a volume surrounding the principal fault. But along the Emerson fault (sections 2 and 3), aftershocks define a nearly vertically-dipping planar structure that is aligned with the surface trace of the Emerson fault and a broad diffuse zone to the east of the fault. The cloud along the Homestead Valley fault (sections 4 and 5) is relatively broad and roughly vertical. In the region of the Homestead Valley/Johnson Valley fault step over (section 6), the aftershock cloud is particularly intense and is a 3-km wide vertical band, particularly well-expressed at depths between 5 and 13 km. Across the Johnson Valley fault (section 7), the 1-2 km wide aftershock zone sharply delineates the mainshock fault plane. Although a surface rupture and surface fault are absent in the gap between the Johnson Valley and Eureka Peak faults (section 8), aftershocks form a well defined vertically

elongate cluster. The most scattered aftershock zone occurs across the Eureka Peak fault section (section 9).

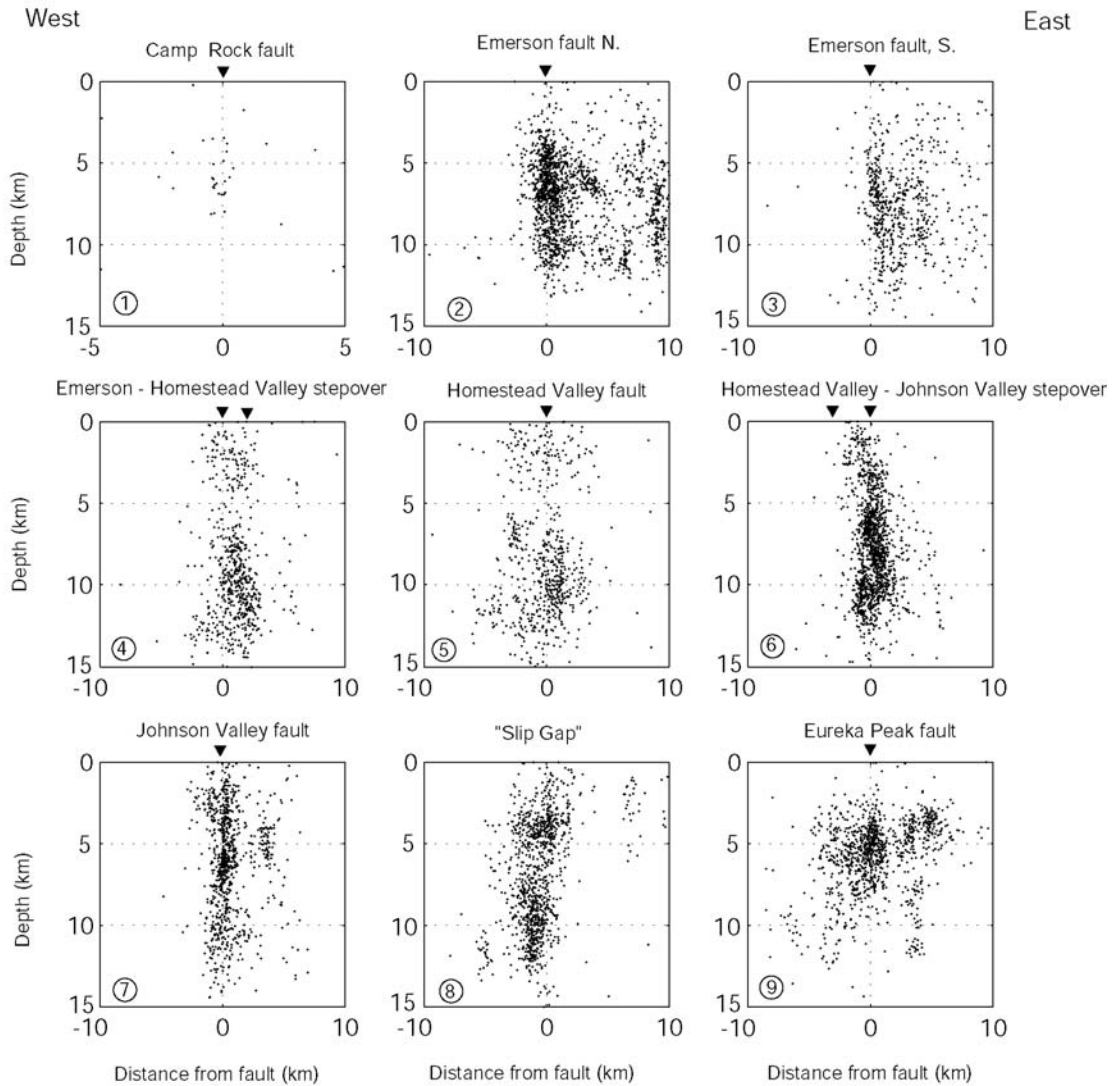


Figure 4.4. Cross-sectional views of aftershock locations ( $M_L \geq 2$ ) for the 9 sections shown in Figure 4.1. The inverted solid triangles denote traces of the principal mainshock ruptures. Aftershock clouds suggest nearly vertically dipping mainshock fault planes, because the clouds do not spread out just to one side of the principal ruptures.

### 4.3.2 Most aftershocks occur off the mainshock fault planes

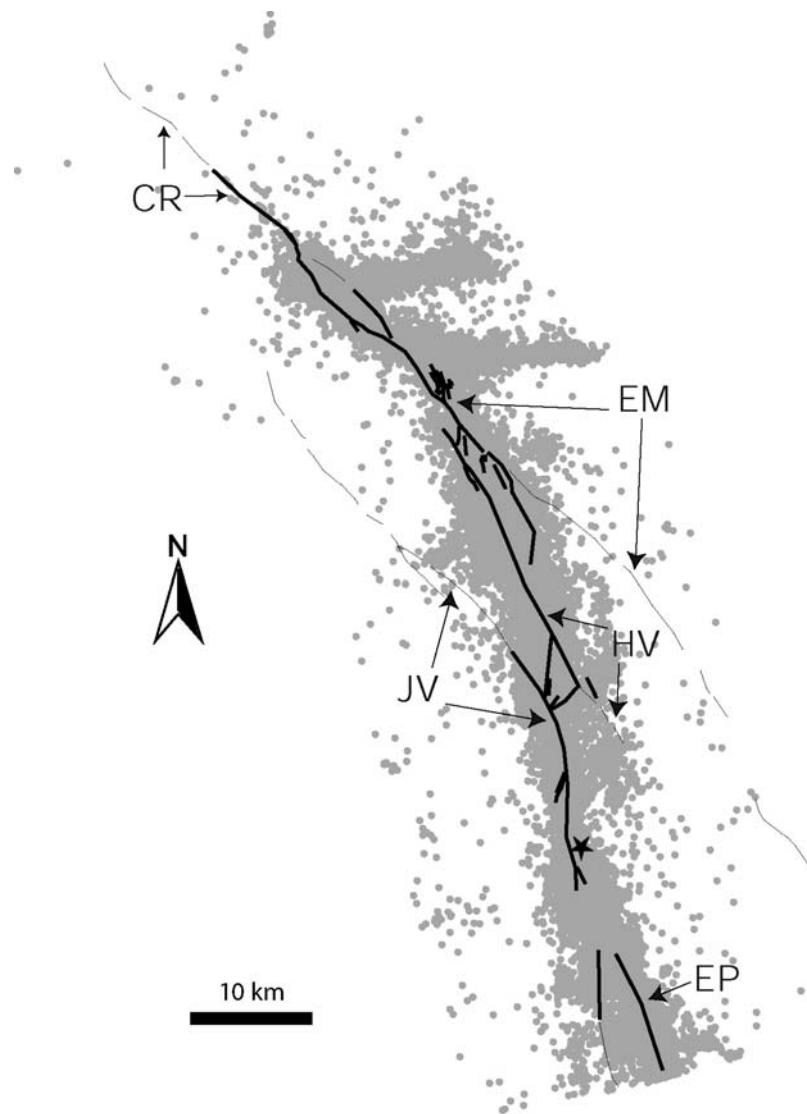


Figure 4.5. Map view of the surface traces of the mainshock fault planes and aftershock locations. Simplified surface ruptures, shown as thick lines, represent the fault planes that failed during the mainshock; fault planes beyond the ends of the mainshock ruptures are shown as thin lines. Abbreviations of the faults are the same as in Figure 4.3.

Overall, the vertical dip of the aftershock clouds and their symmetry about the mainshock

ruptures suggest strongly that the mainshock faults dip vertically. This interpretation is consistent with the focal mechanism of the Landers mainshock (Kanamori et al., 1992; Hauksson et al., 1993). Now that we are confident that the mainshock rupture planes are vertical or nearly so, we may proceed to estimate how many aftershocks might have occurred on the mainshock planes.

We simplify the mapped surface ruptures as references to the parts of faults that failed in the mainshock. The modification is made mainly by fitting straight lines through the alignments of *en echelon* cracks; the lengths of fitted lines vary depending on how straight the *en echelon* cracks are aligned. But if the cracks extend no more than 500m, such as those in the step-over between Homestead Valley fault and Emerson fault, we choose to ignore them. Nonetheless, the simplified faults match closely with the mapped ruptures (Figure 4.5, thick lines). Another major modification is made at the 4.5 km-long section immediately north of the step-over between Homestead Valley fault and Johnson Valley fault, where surface ruptures were reportedly northward thrust faults at shallow depth (Spotila and Sieh, 1995). There, we consider that the Homestead Valley fault at depth has the same orientation as that outside the structure knot.

We also consider faults beyond the ends of the rupture, because a large earthquake sometimes does not rupture the entirety of a fault and aftershocks can still fall on the fault plane in the portions outside the bounds of the mainshock rupture. Parts of four major faults that did not break in the 1992 Landers earthquake are shown in Figure 4. 5 as thin lines; these include the northern half of the Camp Rock fault, the southern two-thirds of the Emerson fault, the northern two-thirds of the Johnson Valley fault, and the southern end of the Homestead Valley fault (Jennings, 1994; California Department of Conservation, Division of Mines and Geology, 2000).

Figure 4.6a shows how both the number of Landers aftershocks and the moment for 0.5-km-wide bins vary as a function of distance from the surface traces of the mainshock fault planes defined in Figure 4.5. Both the numbers of aftershocks and moment attenuate symmetrically out from the principal fault planes. This fault-normal distribution is independent of the time period sampled. For example, the ratios of near-fault to total aftershocks are similar for the periods encompassing six months and six years after the mainshock (Table 4.1). The distributions are not sensitive to the choice of minimum magnitude cutoff ( $M_L \geq 0$  or  $M_L \geq 2$ ) or location method

either. Use of the Richards-Dinger and Shearer (2000) catalog yields similar results (Table 4.1). Nor do relocations using a double difference method (Hauksson and Michael, in preparation, 2002) change the results significantly.

The distributions of moment and number of events in Figure 4.6 indicate that the majority of aftershocks resulted from fault ruptures well away from the principal fault planes. Only about 40% of the aftershocks occurred within 0.5 km of the main fault zone, the approximate uncertainty in horizontal location; but about 60- 65 % occurred within 1 km of the mainshock fault zone (Table 4.1). A slightly more rigorous determination of those aftershocks that would be candidates for re-rupture appears in Figure 4. 6b. It yields a similar result. There, we consider the location error distribution normal to the faults. If we shift all aftershocks toward the nearest mainshock rupture by the amount of their  $2\sigma$  location errors, we find a conservative upper bound to the number of aftershocks that might have occurred on the mainshock faults. These aftershocks are those between the two diagonal dashed lines in the figure. They constitute about 44% of aftershocks with  $M \geq 0$ .

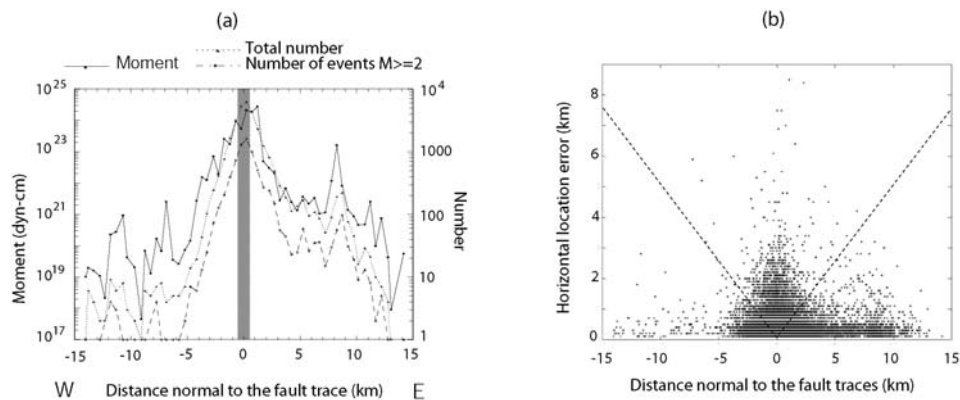


Figure 4.6. (a) Distributions of Landers aftershocks and (b) their horizontal location errors as a function of distance normal to the mainshock faults as shown in Figure 4.5, using relocated data set by Hauksson (2000). Only about 40% of the aftershocks occurred within 0.5km of the mainshock faults. If we shift all aftershocks toward the nearest mainshock faults by the amounts of their  $2\sigma$  location uncertainties, 44% of aftershocks might have occurred on the faults (those between the two diagonal dashed lines in Figure 4.6b).

	Data source	Time period	Number of earthquakes $M_L \geq 0$	Number of earthquakes $M_L \geq 2$	Summed moment
Within 0.5 km of the mainshock fault planes	Hauksson (2000)	6/28/92-5/28/98	0.40	0.40	0.29
		6/28/92-12/31/92	0.41	0.41	0.30
	Richards-Dinger and Shearer (2000)	6/28/92-3/18/98	0.36	0.35	0.56 [0.36]
		6/28/92-12/31/92	0.36	0.36	0.63 [0.38]
Within 1km of the mainshock fault planes	Hauksson (2000)	6/28/92-5/28/98	0.65	0.64	0.60
		6/28/92-12/31/92	0.64	0.64	0.62
	Richards-Dinger and Shearer (2000)	6/28/92-3/18/98	0.62	0.61	0.77
		6/28/92-12/31/92	0.61	0.61	0.85

Table 4.1. Ratios of near-fault to the total population of aftershocks during different time periods. Mainshock faults are defined in Figure 4.5. The ratios of summed moment from Richards-Dinger and Shearer (2000)'s data set are higher because an  $M=5.7$  aftershock is excluded in the analysis due to its large location uncertainty. If we include this event, the ratios, shown in brackets, are comparable to those from Hauksson (2000).

Among the aftershocks that occurred within half a km of the main fault zone and that are candidates of re-rupture of mainshock fault planes, only about 1-2% of the total aftershocks fell beyond the rupture ends on the Camp Rock fault, the Emerson fault, the Homestead Valley fault and the Johnson Valley fault. This is in contrast with Rubin and Gillard (2000)'s studies of the micro-earthquakes in the central San Andreas fault, where they found that majority of aftershocks occurred on the mainshock fault plane, but beyond the termini of the mainshock rupture.

### ***4.3.3 Aftershock focal mechanisms further limit which aftershocks can represent re-rupture of the mainshock fault planes***

The Landers aftershocks have diverse focal mechanisms (Hauksson, 1994; Hardebeck et

al., 1998). This further constrains the number of aftershocks that are candidates for re-rupture of the mainshock ruptures, since slip along most of the mainshock ruptures was right-lateral. First-motion lower hemisphere focal mechanisms of the relocated aftershocks are determined for events that had twelve or more first motions. We use the grid-searching algorithm and computer programs by Reasenberg and Oppenheimer (1985). Since the first motion solutions do not decide on which of the two planes, in order to exclude left-lateral motion we choose planes with either a right-lateral component or pure dip slip.

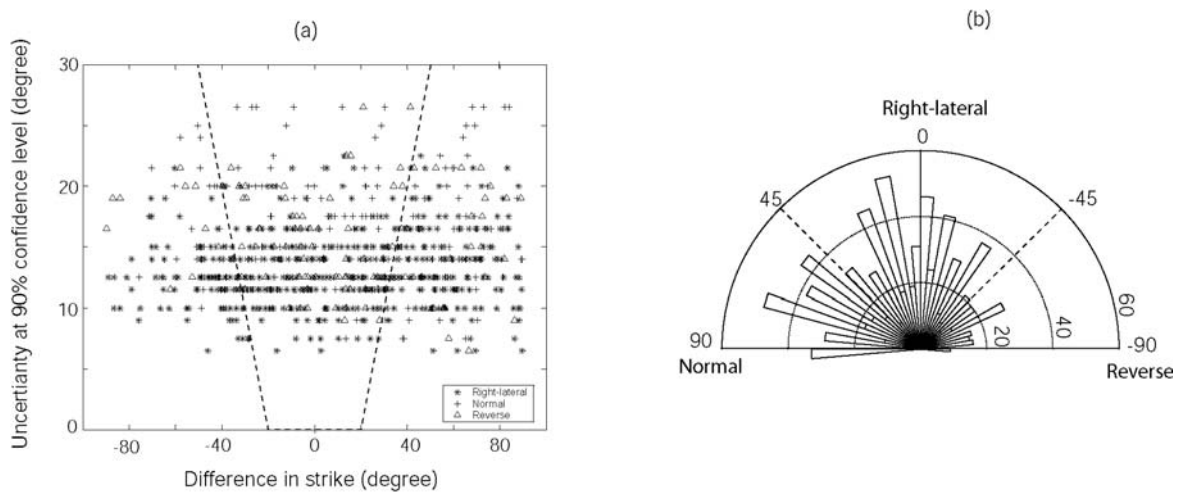


Figure 4.7 (a) The difference in strike of aftershock focal plane with that of the local mainshock fault is plotted against the uncertainty in strike of aftershock focal plane. We include only the 751 aftershocks that fall within 0.5km of the mainshock rupture and have reliable first motion solutions. 42% of these aftershocks are within  $20^\circ$  of the local strike at the 90% confidence level (those between the two dashed lines). (b) The histogram of the sense of motion (rake) on the chosen plane. Right-lateral refers to those that have larger horizontal component than in vertical.

Out of the 751 aftershocks that originated within half a km of mainshock ruptures and have reliable first-motion solutions with the 90% confidence range of less than  $60^\circ$  in strike, only 25% have a focal plane with a right-lateral component of motion that is within  $20^\circ$  of the strike of the local mainshock rupture plane (Figure 4.7a), or 42% are within  $20^\circ$  of the local strike at the 90%

confidence level. However, in either case, only about half of the aftershocks have a dominant horizontal component of motion on the chosen plane (Figure 4. 7b), whereas the mainshock rupture was predominantly right-lateral. Even within the step-overs, the right-lateral component of the mainshock rupture was larger than the vertical component (Spotila and Sieh, 1995; Zachariassen and Sieh, 1996). The focal mechanism statistics within 1km of the main fault zone is nearly identical. Out of the 1225 aftershocks that occurred within 1km of the mainshock ruptures and that satisfy the same criteria as above, 26% are within 20° of the strike of the local mainshock rupture plane, or 43% at the 90% confidence level but half of these aftershocks do not have a right-lateral focal mechanism.

This suggests that of all 11,564 aftershocks with hypocenters within half a kilometer of the mainshock rupture plane, far fewer than half were produced by shear in directions consistent with the mainshock rupture. Taking proximity to the mainshock rupture and consistency of focal mechanism together, no more than about 15% of the total population of aftershocks are strong candidates for re-rupture of the mainshock ruptures.

#### ***4.3.4 Aftershock b values correlate with mainshock fault complexity***

The relationship between mainshock rupture geometry and aftershocks is also manifest in the correlation of b values of the aftershock sequence and mainshock rupture complexity. To calculate b values and their uncertainties in each of the 9 volumes outlined in Figure 1, we used the maximum likelihood method of Aki (1965). The b value for aftershocks with  $M \geq 2.0$  appears in Figure 1 within each of the 9 rectangles.

Aftershock b-values range along strike from about 0.8 to 1.2 and vary with the complexity of the mainshock rupture. Low b-values occur in sections where the rupture is the simplest, specifically along the southern third of the rupture (Johnson Valley and Eureka Peak faults) and along the northernmost segment (Camp Rock fault). The slip gap between Johnson Valley and Eureka Peak fault, where no surface rupture was found, also has low b-values. The sections 12 to 50 km north of the mainshock epicenter, where the mainshock rupture was geometrically more complex than elsewhere (as evidenced by more minor faults and branches and a wider rupture

zone), have high  $b$ -values. This correlation is consistent with previous observations that greater material heterogeneity and crack density correlate with higher  $b$  values (Mogi, 1962; Mori and Abercrombie, 1997). Although we show here the  $b$  values with a lower cut-off magnitude of  $M_2$ , repeated analysis shows that the spatial pattern in  $b$  values between sections is independent of choices of magnitude cut-off. Moreover, these spatial variations in  $b$ -value agree with the results of Wiemer and Katsumata (1999), who found that  $b$  values are high along the northern section ( $b > 1.2$ ) and low on the southern section ( $b < 0.9$ ) of the Landers rupture. They concluded that lower  $b$  values resulted from lesser mainshock slip (Wiemer and Katsumata, 1999). Whereas this correlation is true for sections 1, 8 and 9, it is not true for section 7.

## 4.4 Discussion

The Landers aftershocks are manifestations of a broad structural damage zone astride the mainshock faults. The width of the aftershock zone, the increase in aftershock moment release as one approaches the mainshock ruptures and the correlation of  $b$ -values with fault complexity are all consistent with what one commonly sees in exposures of natural fault zones.

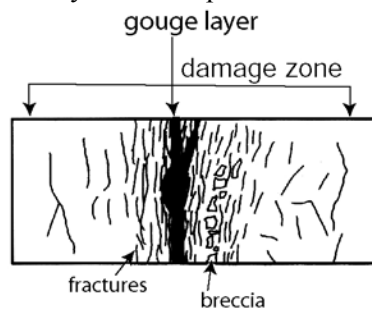


Figure 4.8. Schematic model of the gouge layer-damage zone morphology of a natural fault. It consists of a narrow gouge layer bounded by a broad damaged zone of subsidiary faults. The fracture density in the damage zone generally decreases with distance away from the center (Modified from Wallace and Morris, 1986).

Exposures of large natural faults commonly consist of a narrow band of intensely sheared material (a gouge layer) surrounded by a broad swath of subsidiary faults (a damage zone)

(Figure 4.8, Chester and Logan, 1986; Wallace and Morris, 1986). The broader swath of damage commonly displays a progressive decrease in deformation intensity away from the principal fault,

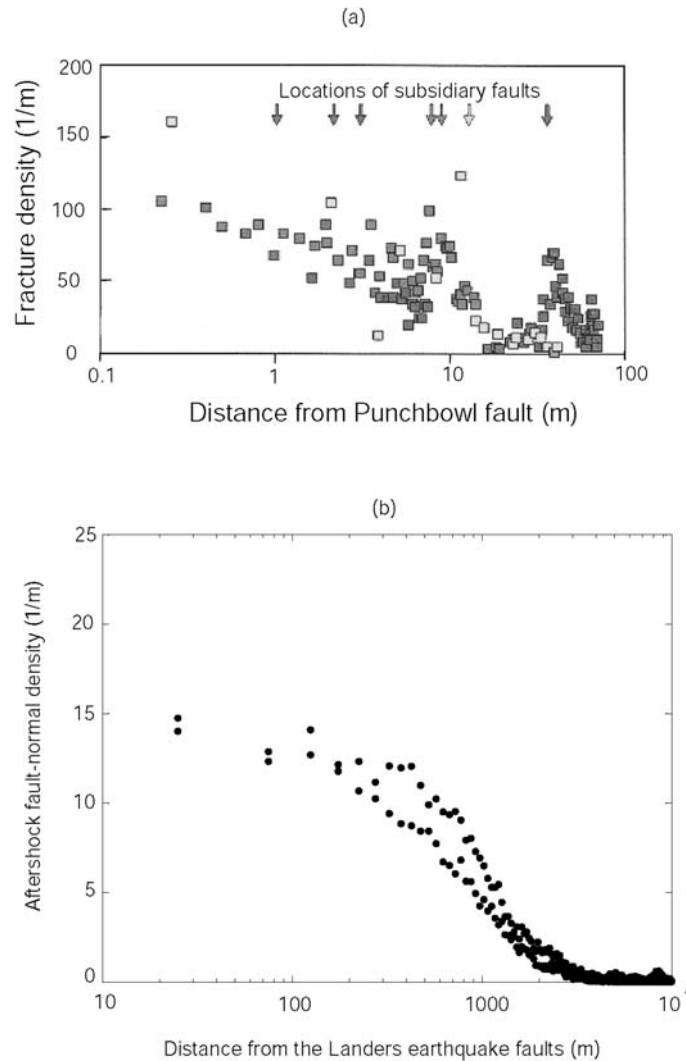


Figure 4.9. Density distributions of (a) mesoscopic fractures of the Punchbowl fault (Chester and Logan, 1986) and (b) Landers aftershocks as a function of distance normal to the principal fault plane. The fault-normal density of Landers aftershocks is summed over the entire length of the mainshock surface ruptures. The aftershock density at the center of the fault is 15 aftershocks per meter of distance perpendicular to the fault.

and the transition from the fault zone to undeformed host rock is gradual (Figure 4.8, Chester and

Logan, 1986; Wallace and Morris, 1986). Chester and Logan (1986) documented that fracture density in the damage zone generally decreases with distance away from the fault surface (Figure 4.9a).

Aftershock sequences may provide exceptional opportunities to quantify strain distribution across crustal fault zones – information that is exceedingly difficult to obtain from the outcrop. The gouge layer-damage zone morphology of fault zones indicates that most of the displacement is accommodated within the gouge layer, supplemented by distributed cataclasis in the surrounding region (Chester and Logan, 1986; Chester et al., 1993; Chester and Chester, 1998; Schulz and Evans, 1998). But it is difficult to evaluate quantitatively the strain distribution across a fault zone in outcrop, because reference features that can be traced across an entire fault zone are rare. Chester and Chester (1998) attempted to address this issue, however, in their study of the Punchbowl fault, an exhumed member of the San Andreas fault zone. They speculated that less than 100 m of the 40 km of dextral offset across the Punchbowl fault, a mere 0.25%, has been accommodated by faults outside of the 0.5-m wide gouge layer.

How does this compare with deformation across the Landers mainshock and aftershock zone? For the mainshock rupture, we have a direct measure of slip on the surface traces of the faults. For the aftershocks, we must estimate slip indirectly, using the relationship between seismic moment and slip. We can calculate a hypothetical sum of aftershock slip,  $d$ , by using the conventional equation,  $d = \sum M_o / (\mu A)$ , where  $\mu = 3.0 \times 10^{11}$  dyn/cm,  $\sum M_o$  is the summed moment of aftershocks projected to their closest locations on the mainshock rupture planes, and  $A$  is the area of mainshock fault plane onto which the aftershocks are projected. We make the calculation for the Johnson Valley fault, because it is representative of the other principal faults of the rupture. The average slip on the Johnson Valley fault during the Landers mainshock was 2m, and the nominal aftershock slip across the Johnson Valley fault averages about 1cm. Thus, aftershock slip is about 0.5% of mainshock slip. This value is not all that different from the 0.25% value estimated by Chester and Chester (1998) for the ratio of slip across the Punchbowl gouge zone and the surrounding fault zone. Thus it is plausible and even likely that the Landers aftershocks are merely the manifestation of a broad damage zone of small faults that extend out from narrow gouge zones that contains the principal ruptures of the mainshock.

What are the implications of adopting Chester and Chester (1998)'s model of a fault zone for the Landers mainshock rupture and aftershock zone? Their observations, as well as others (Chester and Logan, 1986; Chester et al., 1993; Schulz and Evans, 1998; Brune, 2001), show that the majority of displacement normally occurs in a band that ranges from a couple of meters to about 40 m in thickness. If displacements are accommodated by rupture during individual earthquakes, then this gouge layer, just a few tens of meters or less in width, which includes the mainshock rupture planes. Such gouge layers are three orders of magnitude narrower than the Landers aftershock cloud.

If we know the aftershock density within this gouge layer, then we can estimate how many aftershocks occurred within it. For the Landers rupture, Figure 4.9b shows that the aftershock density at the center of the fault is 15 aftershocks per meter of distance perpendicular to the fault, summed over the entire length of the ruptures. For gouge layers 2 to 40 meters wide, this would yield just 30 to 600 aftershocks. This is equivalent to just 0.1 to 2% of the total aftershock population. We have already shown that very few of the aftershocks occurred as re-ruptures of the mainshock rupture surfaces. This calculation suggests that in addition, very few of the aftershocks of the Landers earthquake occurred within the gouge layers associated with the main ruptures. Furthermore, if mainshock rupture only occurred on single or multiple discrete surfaces, rather than involved the entire gouge layer volume, the number of aftershocks falling on mainshock rupture planes would be even less.

But is the Landers aftershock sequence unusual? Recent improvements in locating earthquakes have revealed tighter clustering of aftershocks and clearer structural lineation of seismicity than could be resolved previously (e.g. Shearer, 1997; Shaw and Shearer, 1999; Fehler et al., 2000; Richards-Dinger and Shearer, 2000; Rubin and Gillard, 2000; Waldhauser and Ellsworth, 2000). It is often observed that many aftershocks following major earthquakes appear to coincide with the parts of faults that slipped during the mainshock. However, it is still unclear that these tighter clusters of aftershocks occur on the same surfaces that moved in the mainshock or reflect activation of subsidiary faults in the surrounding volume. Although current earthquake-location technology does not enable resolution of individual aftershock locations to within or immediately outside of a mainshock rupture surface, geological observations provide important

structural constraints that considerable percentages of aftershocks, if not most, must occur in the volume surrounding the zone of principal displacement. Exhumed fault zones show that there are numerous secondary fractures in the vicinity of the layer of fault gouge, with no or negligible offsets. These fractures quite plausibly originate during aftershocks.

Thus, rather than being an artifact of location error, the aftershock “cloud” may reflect a fundamental property of a fault zone. The discrete mainshock slip surfaces could appear remarkably planar, but cannot be perfectly or continuously planar. Geometric irregularities on the fault plane could give rise to locally large stresses and trigger off- fault aftershocks (Segall and Pollard, 1980; Das and Scholz, 1982). Structural complexities exist in all scales (e.g. Tchalenko, 1970; Aviles et al., 1987; Okubo and Aki, 1987; Power et al., 1988); meters-scale irregularities could be responsible for the aftershocks that are in the meters vicinity of mainshock rupture planes but in fact off-plane in the tabular surrounding volume. Hence, the characteristic complexity and network of faults of many sizes makes the wide distribution of aftershocks very expected. In this general sense, the Landers aftershock sequence is not that unusual.

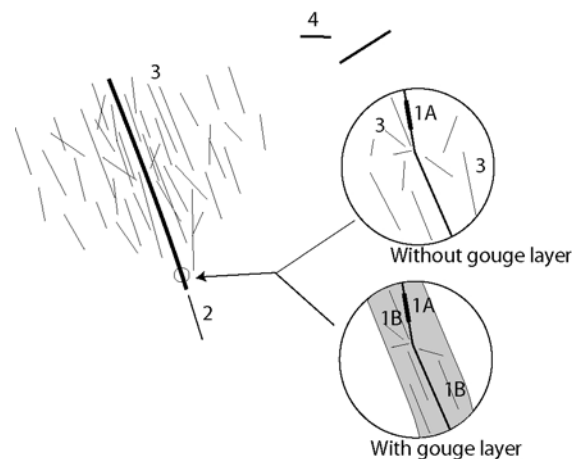


Figure 4.10. Schematic diagram illustrates the classification of aftershocks with respect to their locations relative to mainshock fault planes. See text for the definition for each class of aftershocks.

To understand better the implications of these observations and hypotheses, we should distinguish at least five types of aftershocks, classifying them with respect to their locations relative to mainshock fault planes (Figure 4.10). There are (1) class 1A aftershocks: those that occur on the same surfaces that slipped during the mainshock; and class 1B aftershocks: those that occur in the gouge layer but off the planes that slipped during the mainshock; (2) class 2 aftershocks: those that occur on the same faults, but beyond the rupture termini of the mainshock; (3) class 3 aftershocks: those that occur on the subsidiary faults in the volume of damage zone surrounding the mainshock fault planes; and (4) class 4 aftershocks: remotely-triggered aftershocks on faults farther from the principal faults of the mainshock rupture. Kisslinger (1996) proposed three similar classes of aftershocks, but combined our category 1A, 1B and 3 into a single category. Even though it might be beyond the limit of earthquake location technology, the distinction between classes 1B and 1A aftershocks is mechanically important, because they occur on different surfaces. Only class 1A aftershocks among all types represent truly the re-ruptures of the mainshock rupture plane. Although class 3 aftershocks appear to be the spatial extension of class 1B aftershocks into the bounding region, the distinction between class 1B and 3 aftershocks could also be significant if the gouge material will lower the frictional strength (Byerlee, 1978) than the surrounding medium and the boundary between the gouge layer and the surrounding host rock is general sharp (e.g. Chester and Logan, 1986; Cowan, 1999).

Perhaps aftershock sequences of major earthquakes are a combination of different classes, but that the relative portion of each type varies among ruptures. In this paper, we show that Landers aftershock sequence has a small percentage of class 1 and 2 aftershocks. In contrast, Rubin and Gillard (2000) demonstrated that aftershocks of the earthquakes they studied occurred on the mainshock fault plane, but beyond the termini of the mainshock rupture. Thus, the aftershocks of the earthquakes in their study were predominantly class 2 aftershocks. Common in both studies, however, is that class 1A and 1B aftershocks are rare; aftershocks in Rubin and Gillard (2000) did not tend to occur on the parts of the faults that slipped during the mainshock either.

The difference in manifestation of aftershock types may be due to factors such as the magnitude of the mainshock and the different degrees of geometric irregularity of the principal

faults, or the cumulative slip of the fault if fault trace complexity decreases with large cumulative slip (Wesnousky, 1988). The larger the mainshock magnitude is, the wider the aftershock “cloud” would be, if keeping all other parameters fixed. If the mainshock principal faults are geometrically more irregular or fragmented, then more aftershocks would be off-plane. For example, in Rubin and Gillard (2000), the earthquakes are micro-earthquakes, and are located in the creeping section of the San Andreas fault. The wide Landers aftershock “clouds” may indicate the great complexity of the Landers principal faults.

An important implication of our analysis is that aftershock populations reveal the nature of the fractured medium around principal faults. This is consistent with another observation that higher  $b$  values are associated with segments of mainshock rupture of more cracks. This is compatible with previous results that higher material heterogeneity or crack densities are associated with higher  $b$  values for background seismicity (Mogi, 1962), and also in volcanic areas (Wyss et al., 1997; Wiemer et al., 1998). Thus, the ubiquitously observed Gutenberg-Richter power-law relationship of regional seismicity would not arise from the dynamics of failure of a single smooth and planar fault with particular frictional properties, as claimed in some numerical models (e.g. Burridge and Knopoff, 1967; Carlson and Langer, 1989; Langer et al., 1996).  $B$ -value statistics would, instead, be a measure of the complexity of the broader fault zone or a network of faults (Wesnousky, 1994; Stirling et al., 1996; Ben-Zion, 1996).

## 4.5 Conclusions

We have observed three things about the aftershock sequence of the 1992 Landers earthquake and its relationship to the ruptures of the mainshock. First, the aftershocks occur in a cloud surrounding the mainshock fault ruptures. But, this cloud is far too wide to be due to erroneously located events generated by re-rupture of the mainshock rupture planes. This implies rupture of hundreds of secondary faults within a zone of failure that is kilometers in width.

Furthermore, the focal mechanisms of most of the aftershocks that originated close to the mainshock ruptures are inconsistent with generation by the mainshock ruptures. Less than a third of the aftershocks that are within a half-kilometer of the mainshock rupture planes exhibited

orientations and senses of motion consistent with the principal ruptures.

Finally, b-values are higher along those parts of the principal rupture where rupture complexity at the surface is greater. This further suggests that the aftershock population is controlled by the structure of the fault zone, rather than by the physical properties of the principal fault planes.

One important implication of this work is that the Gutenberg-Richter relationship that characterizes most seismic regions and most aftershock sequences reflects the population of faults in a region or within a broad fault zone, not the behavior of a planar active fault.

## 4.6 Acknowledgments

We thank A. Rubin, M. Fehler, and an anonymous reviewer for their constructive reviews of this paper, and K. Richards-Dinger and P. Shearer for sharing their relocated Landers aftershock dataset. Discussions with Eric Cowgill help to improve Figure 4.10. This research was supported by the Southern California Earthquake Center. SCEC was funded by NSF Cooperative Agreement EAR-8920136 and USGS Cooperative Agreements 14-08-0001-A0899 and 1434-HQ-97AG01718. This research was also partially supported by US Geological Survey Grant 99HQGR0039 to Caltech. This paper is Southern California Earthquake Center contribution 635 and Caltech Seismological Laboratory contribution number 8855.

## 4.7 References

- Aki, K. (1965). Maximum likelihood estimates of b in the formula  $\log N = a - bM$  and its confidence limits, *Bull. Earthquake Res. Inst. Univ. Tokyo*, **43**, 237-239.
- Aviles, C. A., C. H. Scholz, and J. Boatwright (1987). Fractal analysis applied to characteristic segments of the San Andreas Fault, *J. Geophys. Res.* **92**, 331-344.
- Ben-Zion, Y. (1996). Stress, slip, and earthquakes in models of complex single-fault systems incorporating brittle and creep deformations, *J. Geophys. Res.* **101**, 5677-5706.

- Brune, J. N. (2001). Fault-normal dynamic unloading and loading: An explanation for “non-gouge” rock powder and lack of fault-parallel shear bands along the San Andreas fault, EOS Trans. AGU **82**, F854.
- Byerlee, J. D. (1978). Friction of rocks, PAGEOPH **116**, 615-626.
- Burridge, R. and L. Knopoff (1967). Model and theoretical seismicity, Bull. Seism. Soc. Am. **57**, 341-371.
- California Department of Conservation, Division of Mines and Geology. (2000). Digital images of official maps of Alquist-Priolo earthquake fault zones of California, southern region, DMG CD 2000-003.
- Carlson, J. M. and J. S. Langer (1989). Properties of earthquakes generated by fault dynamics, Phy. Rev. Lett. **62**, 2632-2635.
- Chester, F. M., J. P. Evans and R. L. Biegel (1993). Internal structure and weakening mechanisms of the San Andreas fault, J. Geophys. Res. **98**, 771-786.
- Chester, F. M. and J. M. Logan (1986). Implications for mechanical properties of brittle faults from observations of the Punchbowl Fault zone, California. PAGEOPH **124**, 79-106.
- Chester, F. M. and J. S. Chester (1998). Ultracataclasite structure and friction processes of the Punchbowl fault, San Andreas system, California, Tectonophysics, **295**, 199-221.
- Cowan, D. (1999). Do faults preserve a record of seismic slip? a field geologist's opinion, J. of Struct. Geology, **21**, 995-1001.
- Das, S. and C. H. Scholz (1981). Off-fault aftershock clusters caused by shear stress increase? Bull. Seism. Soc. Am. **71**, 1669-1675.
- Deng, J., M. Gurnis, H. Kanamori, and E. Hauksson (1998). Viscoelastic flow in the lower crust after the 1992 Landers, California, earthquake, Science, **282**, 1689-1692.

- Deng, J., K. Hudnut, M. Gurnis, and E. Hauksson (1999). Stress loading from viscous flow in the lower crust and triggering of aftershocks following the 1994 Northridge, California, earthquake, *Geophys. Res. Lett.* **26**, 3209-3212.
- Dietz, L. D. and W. L. Ellsworth (1990). The October 17, 1989, Loma Prieta, California, earthquake and its aftershocks: geometry of the sequence from high-resolution locations, *Geophys. Res. Letters.* **17**, 1417-1420.
- Fehler, M., and P. Johnson (1989). Determination of fault planes at Coalinga, California by analysis of patterns in aftershock locations, *J. Geophys. Res.* **94**, 7496-7506.
- Fehler, M., W. S. Phillips, L. House, R. H. Jones, R. Aster and R. Charlotte (2000). Improved relative locations of clustered earthquakes using constrained multiple event location, *Bull. Seism. Soc. Am.* **71**, 775-780.
- Freed, A. and J. Lin (1998). Time-dependent changes in failure stress following thrust earthquakes. *J. Geophys. Res.* **103**, 24393-24409.
- Gomberg, J. and S. Davis (1996). Stress/strain changes and triggered seismicity following the Mw 7.3 Landers, California, earthquake, *J. Geophys. Res.* **101**, 751-764.
- Hardebeck, J. L., J. J. Nazareth, and E. Hauksson (1998). The static stress change triggering model: Constrains from two southern California aftershock sequences. *J. Geophys. Res.* **103**, 24427-24437.
- Hauksson, E. (1994). State of stress from focal mechanisms before and after the 1992 Landers earthquake sequence. *Bull. Seism. Soc. Am.* **84**, 917-934.
- Hauksson, E., L. M. Jones, K. Hutton, and D. Eberphart-Phillips (1993). The 1992 Landers earthquake sequence: Seismological observations. *J. Geophys. Res.* **98**, 19835-19858.
- Hauksson, E. (2000). Crustal structure and seismicity distribution adjacent to the Pacific and North America plate boundary in Southern California. *J. Geophys. Res.* **105**, 13,875-13,903.

- Hauksson, E., and Michael (2002). (in preparation).
- Hill, D. P., M.J.S. Johnston, J. O. Langbein and R. Bilham (1995). Response of Long Valley caldera to the Mw=7.3 Landers, California, earthquake, *J. Geophys. Res.* **100**, 12985-13005.
- Hudnut, K. W. and 16 others (1994). Co-seismic displacements of the 1992 Landers earthquake sequence, *Bull. Seism. Soc. Am.* **84**, 625-645.
- Jennings, C. W. (1994). Fault activity map of California and adjacent areas, Department of Conservation, Division of Mines and Geology geologic map no. 6, scale 1:75000.
- Kanamori, H., H. -K., Thio, D. Dreger, E. Hauksson and T. Heaton (1992). Initial investigation of the Landers California earthquake of 28 June 1992 using TERRAScope. *Geophys. Res. Lett.* **19**, 2267-2270.
- Kanamori, H. and D. L. Anderson (1975). Theoretical basis of some empirical relations in seismology, *Bull. Seism. Soc. Am.* **65**, 1073-1096.
- King, G.C. P., R. S. Stein, and J. Lin (1994). Static stress changes and the triggering of earthquakes. *Bull. Seism. Soc. Am.* **84**, 935-953.
- Kisslinger, C. (1996). Aftershocks and fault-zone properties. *Advances in Geophysics*, 38, 1-36.
- Langer, J. S., J.M. Carlson, C.R. Myers, and B.E. Shaw (1996). Slip complexity in dynamic models of earthquake faults. *Proc. Natl. Acad. Sci. U. S. A.* **93**, 3825-3829.
- McGill, S. F. and C. M. Rubin (1999). Surficial slip distribution on the central Emerson fault during the June 28, 1992, Landers earthquake, California. *J. Geophys. Res.* **104**, 4811-4833.
- Mendoza, C. and S. H. Hartzell (1988). Aftershock patterns and main shock faulting. *Bull. Seism. Soc. Am.* **78**, 1438-1449.

- Mogi, K. (1962). Magnitude-frequency relation for elastic shocks accompanying fractures of various materials and some related problems in earthquakes, *Bull. Earthquake Res. Inst., Univ. Tokyo*, **40**, 831-853.
- Mori J. and R. Abercrombie (1997). Depth dependence of earthquake frequency-magnitude distributions in California: Implications for the rupture initiation, *J. Geophys. Res.* **102**, 15081-15090.
- Nakamura, M. and M. Ando (1996). Aftershock distribution of the January 17, 1995 Hyogo-ken earthquake determined by the JHD method. *J. Phys. Earth*, **44**, 329-335.
- Okubo, P. and K. Aki (1987). Fractal geometry in the San Andreas Fault system. *J. Geophys. Res.* **92**, 345-355.
- Power, W. L., T. E. Tullis, S. R. Brown, G. N., Boitnott, and C. H. Scholz (1987). Roughness of natural fault surfaces, *Geophys. Res. Lett.* **14**, 29-32.
- Resenberg P. and D. H. Oppenheimer (1985). FPFIT, FPLOTT and FPPAGE: Fortran computer programs for calculating and displaying earthquake fault-plane solutions. U. S. G. S. Open-file Rep. OF **85-0739**, 109.
- Reasenberg, P.A. and R.W. Simpson (1992). Response of regional seismicity to the static stress change produced by the Loma Prieta earthquake. *Science*, **255**, 1687-1690.
- Richards-Dinger, K B. and P. M. Shearer (2000). Earthquake locations in southern California obtained using source-specific station terms. *J. Geophys. Res.* **105**, 10939-10960.
- Rubin, A.M. and D. Gillard (2000). Aftershock asymmetry/rupture directivity among central San Andreas fault microearthquakes. *J. Geophys. Res.* **105**, 19095-19109.
- Schulz, S. E. and J. P. Evans (1998). Spatial variability in microscopic deformation and composition of the Punchbowl fault, southern California: implications for mechanisms, fluid-rock interaction, and fault morphology. *Tectonophysics*, **295**, 223-244.

- Segall, P. and D. D. Pollard (1980). Mechanics of discontinuous faults. *J. Geophys. Res.* **85**, 4337-4350.
- Shaw, J. H. and P.M. Shearer (1999). An elusive blind-thrust fault beneath metropolitan Los Angeles. *Science*, **283**, 1516-1518.
- Shearer, P. (1997). Improving local earthquake locations using the L1 norm and waveform cross correlation: Application to the Whittier Narrow, California, aftershock sequence, *J. Geophys. Res.* **102**, 8269-8283.
- Sieh, K. E. and 19 others (1993). Near-field investigations of the Landers earthquake sequence, April to July, 1992. *Science*, **260**, 171-176.
- Stein, R.S., G.C.P. King, and J. Lin (1994). Stress triggering of the 1994 M = 6.7 Northridge, California earthquake by its predecessors. *Science*, **265**, 1432-1435.
- Stirling, M. W., S. G. Wesnousky and K. Shimazaki (1996). Fault trace complexity, cumulative slip, and the shape of the magnitude-frequency distribution for strike-slip faults: a global survey, *Geophys. J. Int.* **124**, 833-868.
- Spotila, J. A. and K. Sieh (1995). Geologic investigations of a "slip gap" in the surficial ruptures of the 1992 Landers earthquake, southern California, *J. Geophys. Res.* **100**, 534-559.
- Stein, R. S. and M. Lisowski (1983). The 1979 Homestead Valley earthquake sequence, California: Control of aftershocks and postseismic deformation, *J. Geophys. Res.* **88**, 6477-6490.
- Tchalenko, J. S. (1970). Similarities between shear zones of different magnitudes, *Bull. Geol. Soc. Am.* **81**, 1625-1640.
- United States Geological Survey/California Divisions of Mines and Geology Staff (1992). Pattern of surface ruptures associated with the June 28, 1992, Landers earthquake (abstract). *Trans. Am. Geophys. Union*, **73**, 357-358.

- Waldhauser, F. and W. L. Ellsworth (2000). A double-difference earthquake location algorithm: Method and application to the northern Hayward Fault, California. *Bull. Seism. Soc. Am.* **90**, 1353-1368.
- Wald, D.J. and T.H. Heaton (1994). Spatial and temporal distribution of slip for the 1992 Landers, California, Earthquake, *Bull. Seism. Soc. Am.* **84**, 668-691.
- Wallace, E. W. and H. T. Morris (1986). Characteristic of faults and shear zones in deep mines. *PAGEOPH*, **124**, 107-125.
- Wesnousky, S. G. (1988). Seismological and structural evolution of strike-slip faults, *Nature*, **335**, 340-342.
- Wesnousky, S. G. (1994). The Gutenberg-Richter or characteristic earthquake distribution, which is it? *Bull. Seism. Soc. Am.* **84**, 1940-1959.
- Wiemer, S. and K. Katsumata (1999). Spatial variability of seismicity parameters in aftershock zones. *J. Geophys. Res.* **104**, 13135-13151.
- Wiemer S., S. R. McNutt, and M. Wyss (1998). Temporal and three-dimensional spatial analysis of the frequency-magnitude distribution near Long Valley Caldera, California. *Geophys. J. Int.* **134**, 409-421.
- Wyss, M. K. Shimazaki, and S. Wiemer (1997). Mapping active magma chambers by b value beneath Off-Izu volcano, Japan. *J. Geophys. Res.* **102**, 20413-20433.
- Zachariassen, J. and K. E. Sieh (1995). The transfer of slip between en echelon strike-slip faults: A case study from the 1992 Landers earthquake, southern California. *J. Geophys. Res.* **100**, 15281-15301.

- Wallace, R.E., Notes on stream channels offset by the San Andreas fault, in *Proceedings of conference on geologic problems of the San Andreas fault*, edited by W.R.D.a.A. Grantz, Stanford University Publications in the Geological Sciences, 1968.
- Ward, S.N., Dogtails versus rainbows; synthetic earthquake rupture models as an aid in interpreting geological data, *Bull. Seism. Soc. Am.*, 87, 1422-1441, 1997.
- Ward, S.N., San Francisco Bay area earthquake simulations; a step toward a standard physical earthquake model, *Bull. Seism. Soc. Am.*, 90, 370-386, 2000.
- Weldon, R.J., II, and K.E. Sieh, Holocene rate of slip and tentative recurrence interval for large earthquakes on the San Andreas Fault, Cajon Pass, Southern California, *Geol. Soc. Am. Bull.*, 96, 793-812, 1985.
- Wells, D.L., and K.J. Coppersmith, New empirical relationships among magnitude, rupture length, rupture width, rupture area, and surface displacement, *Bull. Seism. Soc. Am.*, 84, 974-1002, 1994.
- Wood, H.O., The 1857 earthquake in California, *Bull. Seism. Soc. Am.*, 45, 47-67, 1955.
- Young, J.J., J.R. Arrowsmith, L. Colini, L.B. Grant, and B. Gootee, Three-Dimensional excavation and recent rupture history along the Cholame segment of the San Andreas fault, *Bull. Seism. Soc. Am.*, 92, 2670-2688, 2002.
- Yule, D., K. Sieh, and K. Aki, Neotectonic and paleoseismic investigation of the San Andreas fault system, San Geronio Pass [Monograph] The 1996 SCEC annual report; progress reports from SCEC scientists; volume II, 1997.
- Yule, D., K. Seih, P.W. Weigand, and J. Shellebarger, The paleoseismic record at Burro Flats; evidence for a 300-year average recurrence for large earthquakes on the San Andreas Fault in San Geronio Pass, Southern California, *Abstracts with Programs Geological Society of America*, 33 (3), 2001.

## **Appendix A**

### **Field Data**

This appendix includes three parts: a digital copy of field data, a description of hierarchy of folders that contain the field data and the procedure for digitizing the trench logs.

## A.1 Digital field data

See CD attached

## A.2 Folder description of digital field data

- **dn\_all** ----files and folders created for all downstream logs
  - 3d\_tru\_coor - folder containing point shape files of digitized logs in true xyz coordinates.
  - orig\_srvey\_data – original surveyed data of all down stream trenches.
  - rectified\_logs – all scanned trench log tiff's used for digitizing rectified to cross sectional coordinates and the associated world files (\*.tfw).
  - srvey\_rot – original survey data rotated parallel to the x or y axis in map view.
  - wall\_sfc – surfaces made from the rotated original survey data in cross sectional view.
  - xs\_line\_2d – line shape files in cross sectional view digitized from down stream trench logs.
  - xs\_pts2d – point shape files in 2d cross sectional coordinates that are made of 1 cm spaced points along all digitized lines.
  - xs\_pts\_3d - point shape files in 3d cross sectional coordinates that were made by projecting the shape files in xs\_pts\_2d onto the trench wall surfaces in wall\_sfc.

- 2000\_mod – 2000\_mod – files and folders modified from the work completed during 2000.
  - re-rectifiedLogs – scanned trench log tiff's used for digitizing rectified to cross sectional coordinates and the associated world files (\*.tfw).
  - srvey\_rot – original survey data rotated parallel to the x or y axis in map view.
  - wall\_sfc – surfaces made from the rotated original survey data in cross sectional view.
  - xs\_line\_2d – modified line shape files in cross sectional view digitized from down stream trench logs in 2000.
  - xs\_pts\_2d – point shape files in 2d cross sectional coordinates that are made of 1 cm spaced points along all digitized lines.
  - xs\_pts\_3d - point shape files in 3d cross sectional coordinates that were made by projecting the shape files in xs\_pts\_2d onto the trench wall surfaces in wall\_sfc.
- **up\_all** --- files and folders created for all downstream logs
  - 3d\_tru\_coor – folder containing point shape files of digitized logs in true xyz coordinates.
  - orig\_srvey\_data – original surveyed data of all down stream trenches.
  - rectified\_logs – all scanned trench log tiff's used for digitizing rectified to cross sectional coordinates and the associated world files (\*.tfw).
  - srvey\_rot – original survey data rotated parallel to the x or y axis in map view.
  - wall\_sfc – surfaces made from the rotated original survey data in cross sectional view.
  - xs\_line\_2d – line shape files in cross sectional view digitized from down stream trench logs.

- xs\_pts2d – point shape files in 2d cross sectional coordinates that are made of 1 cm spaced points along all digitized lines.
- xs\_pts\_3d - point shape files in 3d cross sectional coordinates that were made by projecting the shape files in xs\_pts\_2d onto the trench wall surfaces in wall\_sfc.
- **trenchsite** --- useful ArcView shape files containing information of the trench site: survey points and 20 cm contour topographic map, locations of trench volumes and trench lines.
- **fault\_lines** --- fault locations (point shape files in **real** x, y and z coordinates.)
- **channel\*** --- folders containing point shape files of major units and the outline of each channel (pair), in **real** x, y and z coordinates.
  - Substitute \* with the name of channel pair, 1 for channel 1-a, 2 for channel 2-b, ect.
  - Files that contain “bottom” in the name represent **lower portion** of a feature in each exposure; files that contain “min” are the shape files of the **deepest point** of a feature (thalweg).

Notes:

- Key to attribute table for digitized lines and points:
  - Id = Field that Arc adds automatically. This field was not used.
  - Trench = indicates what trench the points or lines belong
  - Cut = indicates what direction the trench cut the points or lines belong to is facing and what number cut of that particular trench.
  - Rel\_age = indicates what channel the points or lines belong to. 1 is the youngest 11 is the oldest

- Depo\_id = indicates level of the stratigraphy within the channel. 10 is the base of the channel and each digitized layer above the base was numbered ten greater than the previous layer.
- Conf = indicates the confidence of the digitized feature: d = dashed (inferred), s = solid (certain).
- X\_COOR different for files:
  - In rotated map view coordinates
  - In cross sectional view coordinates
  - In true coordinates
- Y\_COOR different for files:
  - In rotated map view coordinates
  - In cross sectional view coordinates
  - In true coordinates
- Z\_COOR different for files:
  - In rotated map view coordinates
  - In cross sectional view coordinates
  - In true coordinates

### **A.3 Procedure for digitizing trench logs in ArcView**

(Initially edited by Clay Stevens July, 2001)

1. Open ArcView
  - a. On windows machines the location of the ArcView shortcut can be found in Start>Programs>ESRI>ArcView GIS 3.2>ArcView GIS 3.2 (Fig 1).
2. Open a new view
  - a. Select the View icon on the left portion of the project window and click on the new button or just double click on the View icon (Fig. 2).

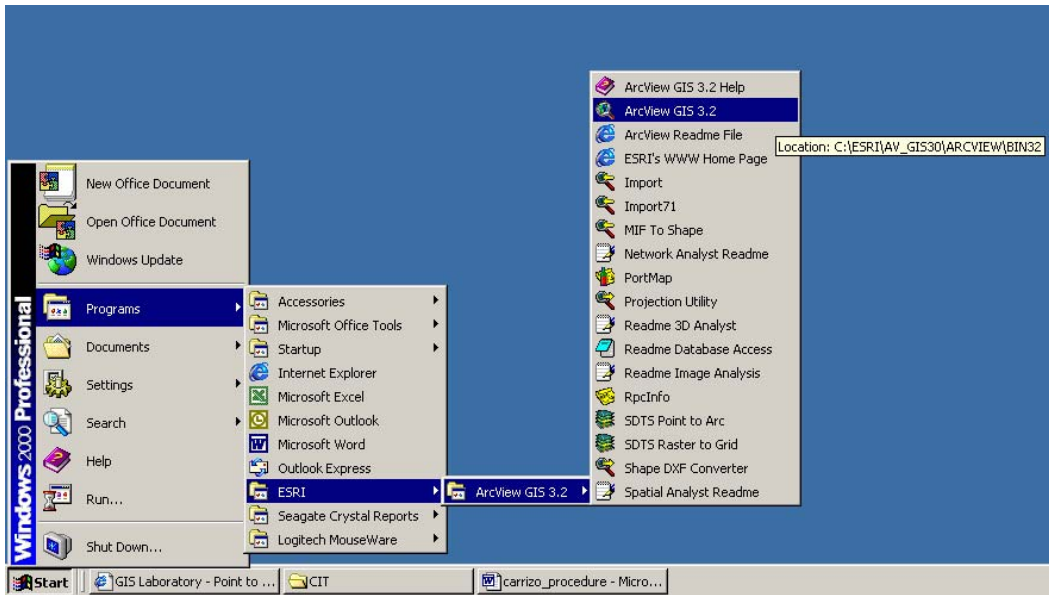


Figure 1. Opening ArcView program.

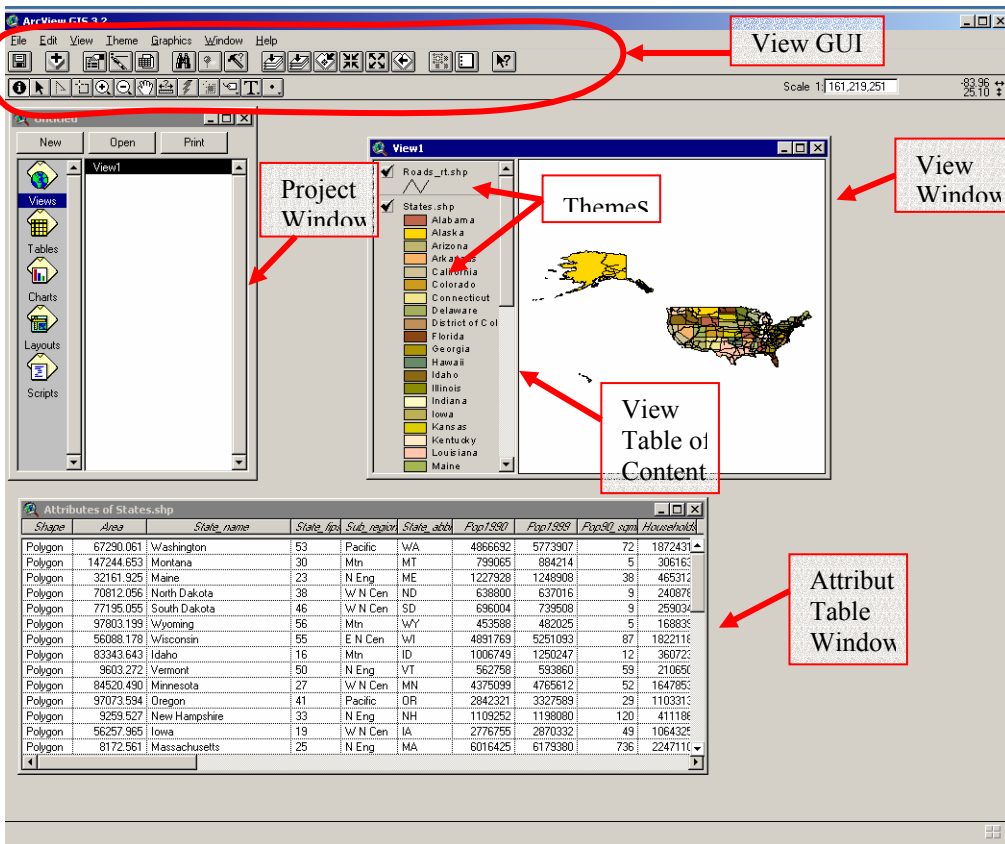


Figure 2. Main windows and elements of ArcView 3.2

3. Name the view.
  - a. Make the project window active.
  - b. Left click on the view icon.
  - c. Select the view you just created (“View 1”) in the right portion of the project window.
  - d. Select the rename option in the Project Menu or press the [control+r] keys together.
  - e. Type in a name of the view that will reflect what kind of data will be displayed in this view
    - i. For these types of projects I named this first view “orig surveyed data”.
  - f. Press OK.
4. Set the working directory. GIS projects generate a lot of files it would be wise to make a folder specifically for this project.
  - a. Make the view window active.
  - b. Select the “Set Working Directory” option in the File menu.
  - c. Type in the full path to the folder that you created for this project.
    - i. A quick way to do this, if the path is really long, is to use Explorer to navigate to your new project folder and copy the path of the folder shown in the address tool bar and press [control] and [c] keys together to copy the text to the clipboard then make ArcView active again and paste the path into the Set Working Directory dialog box by pressing [control] and [v] keys together.
    - ii. DO NOT use spaces in any of the folder names in the path of your working directory!!!
  - d. Press OK.
5. Bring in all survey data of individual trench walls into ArcView as event themes, (x.y plot), in map view and convert into shape files.
  - a. A good extension that plots the points as shape files or event themes for multiple files automatically is the “Batch Point Loader” by Christopher O'Connor.
    - i. Go to [ESRI's arcscripts](#) web site and search for “batch point loader”.
    - ii. Download the extension.

- iii. Put the .avx file into the Ext32 folder in ArcView's home directory.
  - The default ArcView home directory for computers running Windows is C:\ESRI\AV\_GIS30\ARCVIEW.
  - If you are using winzip to open the compressed files you do not need to unzip them. Just open the archive with winzip and drag the .avx file from the winzip program into the EXT32 folder. You can also open any other type of file, with the exception of executables (.exe), directly from the winzip program without unzipping them
    - The downloaded extension comes with a detailed set of instructions.
  - Note: When importing as shapefiles with this extension it automatically places the created shapefiles in the system temp directory. Once you import them as shapefiles into the view delete them from the view and move all of the files associated with each shapefile (all the files with the same name as the shapefile) to the directory you will use for these files. Make sure you have the option to see hidden files in the folder browser you use to move the files or else you may not see all of the files associated with each shapefile.
6. Use available scripts or extensions to rotate surveyed data of the trench walls so that the trend of the trench wall is parallel (or as close as possible) to the x or y axis when in map view.
  - a. A good script that does this for multiple themes at a time is the "Rotate Features" script by Abdelhakim AMMARI. This script only works on shape files.
    - i. Search for the script at [ESRI's arcscripts](#) web site.
    - ii. Download the script from [ESRI's arcscripts](#) web site.
    - iii. Open the .ave file in a text editor such as word pad and copy the text to the clipboard.
    - iv. Open a new script window in ArcView

1. Select the Script icon on the left portion of the project window and click on the new button or just double click on the Script icon.
  - v. Paste the text into the new script window in the ArcView project
  1. With the cursor in the new script window press [control] and [v] keys simultaneously.
    - vi. Compile the script by clicking on the compile button (the one with a check mark) of the Script GUI, the Graphical User Interface (e.g. buttons and menus) that is viewable when a script window is active.
    - vii. Rename the script with following the same steps described in step 3 for renaming a View.
    - viii. Select all of the themes that you want to rotate in the Table Of Contents of the View.
    - ix. Run the script by clicking on the script window and click the “run” button of the script GUI, the button that looks like a man running.
      - Whenever you run any script make sure that the window that was active just prior to selecting the script window was the type of window (view, or table) that you want to run the script on. You will receive an error message if you try to run the script on any other type of window other than the type of window the script was programmed to run on.
      - If you want to rotate all of the features of the theme then make sure that none of the features are selected by clicking on the “unselect all features” button of the View GUI before running the script. Otherwise the script will only rotate the selected features.
7. Use script or extension to get the new x,y coordinates of the rotated points.
  - a. A script that can do this is available in ArcView’s help files.
    - i. Go to the contents of the help files and navigate through the Sample Scripts and Extensions book to the Sample Scripts book to the Views book to the Data Conversion/ Alteration book.

- ii. Select and display the “Adds X and Y coordinates of features to Attribute Table” help topic.
  - iii. Read the instructions on the use of the script and then click on the “source code” link at the top of the help page.
  - iv. Select all of the text by highlighting it with the cursor
  - v. Copy this text to the clipboard by using the copy choice under Options menu or by pressing the [control] and [v] keys simultaneously..
  - vi. Paste the text from the clipboard into a new script window and compile as before.
  - vii. Run the script on each of the themes that you want to get the rotated coordinates for.
    - Unfortunately, this script does not have a batch option and hence will not run on multiple themes, so size and position the script and view windows so that running the script sequentially on multiple themes takes the least amount of mouse movement and therefore the least amount of time.
8. Plot the trench wall in cross sectional view.
- a. Make the theme that you want to plot in cross sectional view active.
    - i. Click on the themes legend in the views Table of Contents.
  - b. Turn on the themes Attribute Table.
    - i. Select the Table option in the Theme menu, or click the Open Theme Table button of the View GUI.
  - c. Make a new view for the cross sectional data
    - i. Create and name the view as described in steps two and three.
  - d. Plot the data in cross sectional view.
    - i. Make the view you just created active
    - ii. Select the Add Event Theme option in the View menu.
    - iii. Choose the table name of the theme you want to plot in cross sectional view from the Table combo box of the Add Event Theme dialog box.

- iv. Plot the coordinates obtained in the previous step that are parallel to one of the axis vs. the surveyed elevation. For example, if the surveyed data of the trench was rotated so that the trend was parallel to the x axis then plot the x coordinate that you obtained in the previous step vs. the surveyed elevation.
    - v. Choose the X coordinate field you want to plot from the x field combo box of the Add Event Theme dialog box.
    - vi. Choose the Y coordinate field you want to plot from the y field combo box of the Add Event Theme dialog box.
9. Scan the trench logs into the computer as a tiff image.
  - a. DO NOT use spaces in any of the names of files you are going to use in ArcView!!! Use a dash or underscore.
10. Rectify the scanned image of the trench log.
  - a. Turn on the Image Analyst Extension for ArcView. Note: There are many image manipulation scripts and extensions of various qualities available from [ESRI's arcscripts](#) web site. Any equivalent script or extension that can move, rotate, mirror, scale, and generate a world file for the scanned image of the log will work.
    - i. Make the View window active.
    - ii. Select the Extensions option under the File menu.
    - iii. Place a check for the Image Analysis.
  - b. Add the scanned trench log as a Image Analysis Data Source theme1
    - i. Make the View window you want to add the log to active.
    - ii. Click the add theme button of the View GUI, or select the Add Theme option from the View menu, or press the [control] and [t] keys simultaneously.
    - iii. Select the Image Analysis Data Source option under the Data Source Types combo box of the Add Theme dialog box.
    - iv. Navigate to the location of the scanned trench log.
    - v. Select the log you want to rectify.
    - vi. Click OK.

- c. Set the extents of the viewable area of the view to the same extents as the theme you want to rectify the log to.
  - i. Make the theme that you want to rectify the trench log to active.
    1. Click on the themes legend in the views Table of Contents.
  - ii. Select the Zoom to Theme option in the View menu of the View GUI, or click on the Zoom to Active Theme(s) button of the View GUI.
- d. Make the theme of the scanned trench log active.
- e. Click on the align tool of the Image Analyst Extension for ArcView (Fig. 3).
- f. Click on a point on the scanned image of the trench wall and then click on the corresponding point of the plot you made in step 8.
- g. Repeat this as many times as necessary to rectify the trench logs so that the pattern of surveyed points marked on the log of trench wall match the pattern that you plotted in step 8.
- h. Save rectified image as a new image.
  - i. Select the Save Image As option in the Theme menu.
  - ii. Select the Tiff option in the List Files of Type combo box.
  - iii. Save in new folder with a name to indicate that it has been rectified.
  - iv. Add the rectified image to the view.



Figure 3. Align tool location in the View GUI.

11. Create a new line theme and begin digitizing over the selected contacts.
  - a. Select the New theme option in the View menu of the View GUI.

- b. Choose line in the Feature Type combo box of the New Theme dialog box.
  - c. Navigate to the folder you want to save the new theme in.
    - i. It would be wise to create a folder just to contain these new themes.
  - d. Type in the name of the new theme.
    - i. It is a good idea to come up with a file-naming scheme to keep track of all of your files.
    - ii. DO NOT use spaces in any of the names of files you are going to use in ArcView!!! Use a dash or underscore.
  - e. Click OK.
  - f. Set the snapping tolerance.
    - i. Right click the view area of the view you are digitizing in.
    - ii. Select the Enable General Snapping from the pop up dialog box.
    - iii. Select the Snap Tolerance button from the tool bar.  
The icon is a square button with a black background and a white double-headed arrow pointing vertically.
    - iv. Click a point on the view and drag a circle to the size you want the snap tolerance to be set at. This will be a distance such that a line you drawing this distance or less away from another line will automatically connect with that other line.
  - g. Select the Draw Line tool from the group of drop down graphic tools.
  - h. Begin drawing lines over the selected lines on the scanned image.
  - i. Save edits as you go.
    - i. Select the Save Edits option in the Theme menu of the View GUI.
  - j. Stop editing when you are finished.
    - i. Select the Stop Editing option in the Theme menu of the View GUI.
    - ii. A quick way to stop editing and save your last edits is to click the Save Project button of the View GUI, or press [control] and [s] simultaneously.
12. Create more columns in the attribute table for all of the attributes that you want to associate with each individual line. Then attribute each line so that you can later distinguish it from the other lines.

- a. A good extension that can add multiple columns to an attribute table is in the Compiled Table Tools, which is a collection of useful tools for manipulating attribute tables put together by Charles Herbold.
    - i. This extension adds a button with a blue diamond to the Table GUI.
    - ii. Click the button to display a floating tool bar for manipulating tables.
    - iii. Place the mouse pointer over the buttons to get a description of each tool.
  - b. A good extension for filling in the attributes of the theme is the Data Editing Extension by David Kimball.
  - c. Both of these extensions can be downloaded from [ESRI's arcscripts](#) web site and they both come with detailed instructions.
13. Convert the lines into points with a script or extension that will preserve and transfer the attributes to the new point shape file.
- a. A good extension that does this is the extension poly2pts by William Huber available from [ESRI's arcscripts](#) web site.

This extension adds a menu item to the Theme menu called "Convert to Points".
  - c. With the line theme that you want to convert to points active select this menu item.
  - d. Follow the on screen instructions.
  - e. Save these files in a new folder for all of the cross sectional view 2D point shapefiles.
14. Make a surface of the trench wall with either a TIN or a spline grid.
- a. Using the axial values obtained in step 7 that are perpendicular to the trend of the rotated survey data as the z values for the surface. For example, if the surveyed data of the trench was rotated so that the trend was parallel to the x axis then use the y values obtained in step 7 as the z values for the surface.
  - b. Load the 3d Analyst Extension.
  - c. Select "Create TIN From Features" or "Interpolate Grid" from the Surface menu to create the surface of your choice.
15. Create a 3d shape file from the points created in step 13.
- a. Make the point theme you created in step 13 active.

- b. Using the surface of the trench wall created in the previous step as the source for the z values.
  - c. Select the Convert to 3D Shapefile option in the theme menu of the View GUI.
  - d. Save file in new folder for all cross sectional view 3D point shapefiles.
16. Get the rotated, cross sectional view, xyz coordinates of all of the points of the 3d shape file created in the previous step.
- a. A script that does this for 3d shape files is the addxyz.ave script by Yuan Ming Hsu which is available from [ESRI's arcscripts](#) web site.
    - i. Works just like the xy script suggested in step 7, but only on 3D shapefiles.
17. Plot the digitized points of the trench wall in the rotated-map view.

IMPORTANT NOTE: ROTATION ANGLES ARE DIFFERENT FOR SOME EXPOSURES, AND DIFFERENT FROM THE 2000 SUMMER DIGITIZING WORK AS WELL:

Exposures	Rotation angle around (0,0) from East-North system	Cross-sectional plot vs. rotated mapview plot
Dn2-ne00 to dn2-ne10	45 degree counterclockwise	$X_{xs} = X_{rot}$ ; $Z_{xs} = Y_{rot}$
Dn2-ne11 to dn2-ne15 Dn2-se exposures Dn1, Dn3, Dn4 (including ne and se exposures) Dn5	47 degree counterclockwise	NE exposures: $X_{xs} = X_{rot}$ ; $Z_{xs} = Y_{rot}$ SE exposures: $X_{xs} = Y_{rot}$ ; $Z_{xs} = X_{rot}$
Up-nw04 to nw12	55 degree clockwise	$X_{xs} = X_{rot}$ ; $Z_{xs} = Y_{rot}$

Up-nw00 to nw03	45 degree clockwise	$X_{xs} = X_{rot}; Z_{xs} = Y_{rot}$
Up-sw00 to sw05	47 degree counterclockwise	$X_{xs} = X_{rot}; Z_{xs} = Y_{rot}$
Up-sw06 to sw14	40 degree counterclockwise	$X_{xs} = Y_{rot}; Z_{xs} = X_{rot}$

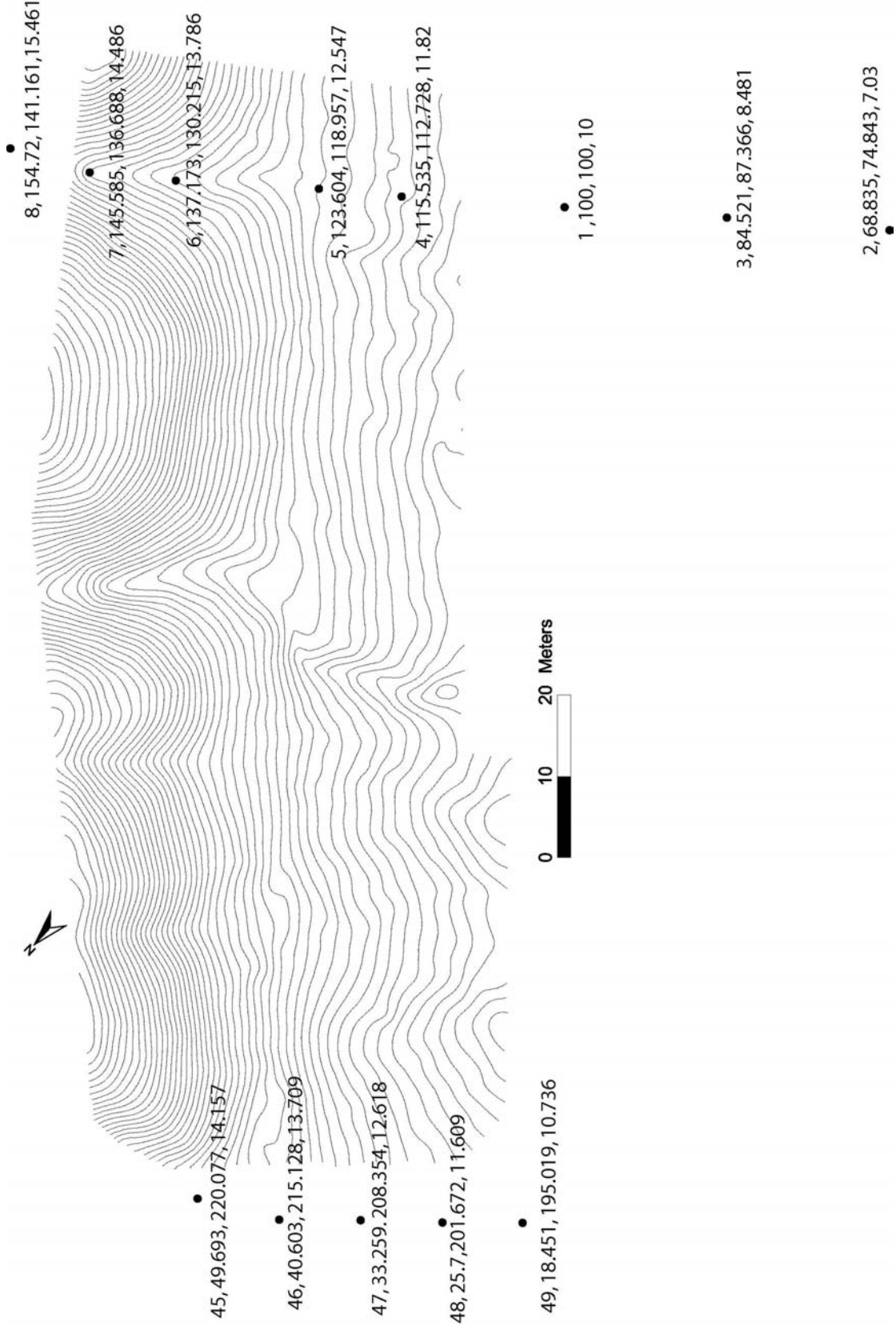
- a. Plot the x-coordinate obtained in the previous step as the axial value that the trend of the trench wall was rotated parallel to in step 6 vs the z value. For example, if the surveyed data of the trench was rotated in step 6 so that the trend was parallel to the x-axis then plot the cross-sectional x coordinate obtained in the previous step as the map-view x coordinate and the cross-sectional z coordinate as the map-view y coordinate.
  - b. Convert this into a shapefile if you did not use the option to do so with the Batch Point Loader.
    - i. Make the theme of plotted points (Event Theme) active.
    - ii. Select the convert to shapefile option in the Theme menu.
    - iii. Save in a new folder for all of the map view 2D shapefiles.
18. Rotate the digitized data back into the original map view position of the trench.
- a. Script suggested in step 6.
  - b. Use the negative of the angle you used in step 6.
19. Create a 3d shape file of the map view digitized data.
- a. Use the y coordinate attribute obtained in step 16 as the z value.
  - b. Save in new folder for all of the map view 3D shapefiles.
20. Delete the xyz coordinates obtained in step 16 from the attribute table.
- a. Extension suggested in step 12.
21. Get the true map view xyz coordinates of all of the points of the 3d shape file created in step 19.
- a. Script suggested in step 16.

b. If you did not delete the xyz fields you created in step 16 select yes if prompted to overwrite these fields. However, the script may not prompt you to overwrite these fields but just append the table with new xyz fields. In order to avoid confusion, you should delete these fields as step 20 suggests.

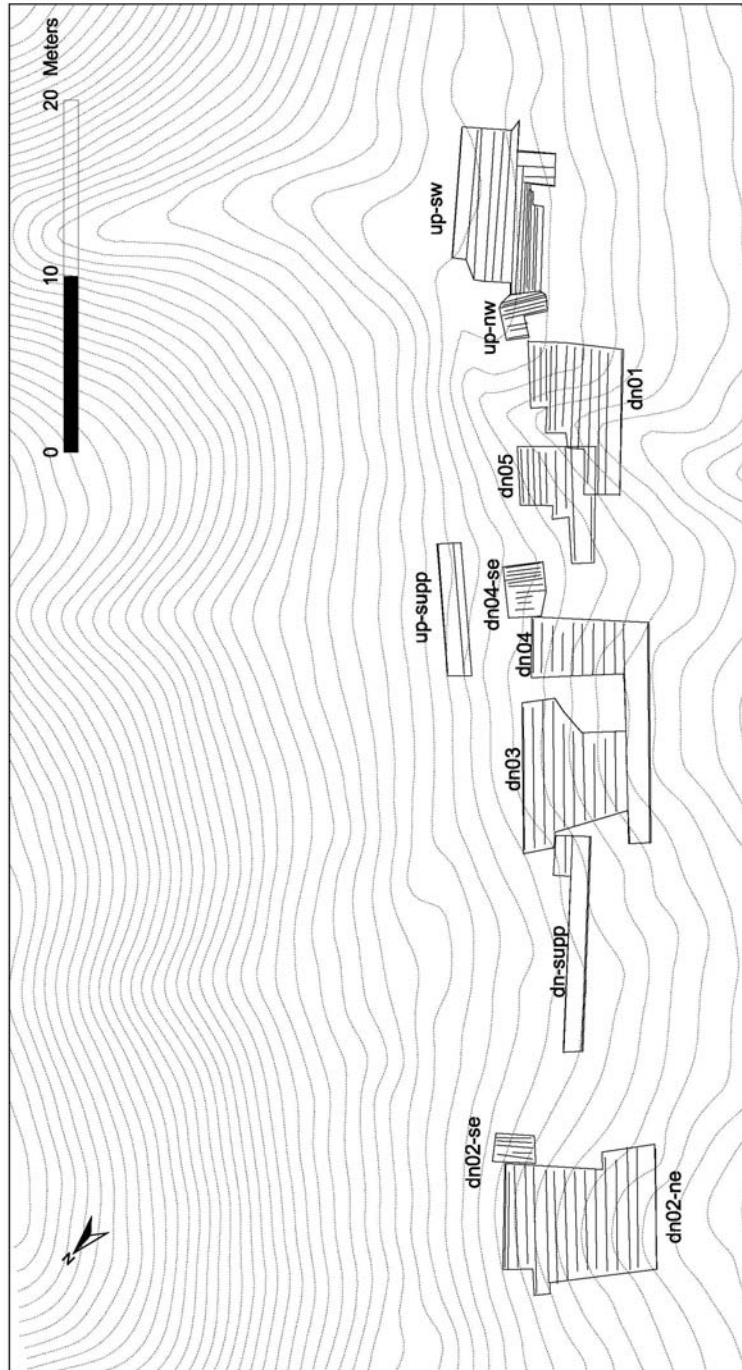
## **Appendix B**

### **Reference Frame for Surveying**

We built the reference frame of surveying at our trench site by utilizing two lines of survey benchmarks deployed by USGS (?). We used one of the nails as the base (1, 100, 100, 10 as point id, east, north, and elevation; in meters), and surveyed only the nails that are close to the site. The southern line of nails was initially surveyed in March, 1998; the northern line was surveyed the first time in January, 1999.



Map view of trench lines



## **Appendix C**

### **Original <sup>14</sup>C Dating Reports**









**CENTER FOR ACCELERATOR MASS SPECTROMETRY**  
Lawrence Livermore National Laboratory

<sup>14</sup>C results

Submitter: Liu/ SCEC      DATE: #####

CAMS #	Sample Name	Other ID	<sup>13</sup> C	fraction Modern	±	D <sup>14</sup> C	±	<sup>14</sup> C age	±
81173	U5-04		-25	0.7939	0.0044	-206.1	4.4	1855	45
81174	U9-08		-25	0.9360	0.0043	-64.0	4.3	530	40
81175	U5-01		-25	0.7155	0.0034	-284.5	3.4	2690	40
81176	U7-19		-25	0.7033	0.0037	-296.7	3.7	2830	45

1) <sup>13</sup>C values are the assumed values according to Stuiver and Polach (Radiocarbon, v. 19, p.355, 1977) when given without decimal places. Values measured for the material itself are given with a single decimal place.

2) The quoted age is in radiocarbon years using the Libby half life of 5568 years and following the conventions of Stuiver and Polach (ibid.).

3) Radiocarbon concentration is given as fraction Modern, D<sup>14</sup>C, and conventional radiocarbon age.

4) Sample preparation backgrounds have been subtracted, based on measurements of samples of <sup>14</sup>C-free coal. Backgrounds were scaled relative to sample size.